



University of Lille

Doctoral School ED SMRE

Department of Physics

PhLAM: Laboratory of Physics of Lasers, Atoms, and Molecules

Building P5 – 2 Avenue Jean Perrin – 59655 Villeneuve d’Ascq – Cedex – France.

Cerla: Center for Laser Studies and Research Applications

Cité scientifique – 59655 Villeneuve d’ascq – Cedex – France.

Thesis defended by **Rabih EL SOKHEN**

Defended on **20 December 2024**

To become a Doctor from the University of Lille

Academic Field **Physics**

Specialty **Diluted Media And Fundamental Optics**

Two-dimensional topological properties of photonic mesh lattices subject to discrete step walks

Thesis supervised by:	DR Alberto Amo Garcia	Director
	PR Stéphane Randoux	Co-Director
President of the jury	PR Gaëtan Lévêque	University of Lille
Jury composition		
<i>Referees</i>	DR Vincent Couderc	XLIM Research Institute
	PR Tomoki Ozawa	University of Tohoku
<i>Examiner</i>	PR Gaëtan Lévêque	University of Lille
<i>Director</i>	DR Alberto Amo Garcia	University of Lille

Two-dimensional topological properties of photonic mesh lattices subject to discrete step walks, © 20 December 2024



Université de Lille

École doctorale ED SMRE

Département de physique

PhLAM: Laboratoire de Physique des Lasers, Atomes et Molécules

Building P5 – 2 Avenue Jean Perrin – 59655 Villeneuve d'Ascq – Cedex – France.

Cerla: Centre d'Études et de Recherches Lasers et Applications

Cité scientifique – 59655 Villeneuve d'Ascq – Cedex – France.

Thèse présentée par **Rabih EL SOKHEN**

Soutenue le **20 décembre 2024**

En vue de l'obtention du grade de docteur de l'Université de Lille

Discipline **Physique**

Spécialité **Milieux dilués et optique fondamentale**

Propriétés topologiques bidimensionnelles des réseaux photoniques soumis à des marches discrètes

Thèse dirigée par:	DR Alberto Amo Garcia	Directeur
	PR Stéphane Randoux	Co-Directeur
Président du jury	PR Gaëtan Lévêque	Université de Lille
Composition du jury		
<i>Rapporteurs</i>	DR Vincent Couderc	Institut de Recherche XLIM
	PR Tomoki Ozawa	Université de Tohoku
<i>Examineur</i>	PR Gaëtan Lévêque	Université de Lille
<i>Directeur</i>	DR Alberto Amo Garcia	Université de Lille

Propriétés topologiques bidimensionnelles des réseaux photoniques soumis à des marches discrètes, © 20 décembre 2024

TABLE OF CONTENT

Table of Content	v
Abstract	ix
Acknowledgments	xi
Declaration of Authorship	xiii
Publications	xv
Introduction	1
1 DOUBLE RING PHOTONIC LATTICE	5
1.1 Photonic lattices	5
1.1.1 Light diffraction in 1D photonic lattice	5
1.1.2 Floquet-Bloch theorem	8
1.1.3 Topological system	10
1.2 Introduction to the double ring photonic lattice	15
1.2.1 Discrete-step walk platforms overview	15
1.2.2 Conceptual model of the double ring	16
1.2.3 Evolution equation and band structure	21
1.3 Two-dimensional synthetic photonic lattice	28
1.3.1 Two-step model	28
1.3.2 Four-step model	36
1.4 Review: Double rings & topological properties	40
1.4.1 Berry curvature via anomalous transport	40
1.4.2 Stability of edge states in nonlinear regime	42
1.4.3 Observation of the non-Hermitian skin effect	43
1.5 Conclusion	44
2 EXPERIMENTAL SETUP	47
2.1 Overview of the optical setup	47
2.1.1 Double ring configuration	47
2.1.2 Local oscillator	52
2.2 Electronic: Automation and control	55
2.2.1 Optical fiber ring stabilization	55
2.2.2 Arduino: central controller and ring stabilization	57
2.2.3 Sequence generation	59
2.3 Conclusion	63

3	EIGENSTATE AND EIGENVALUE ANALYSIS	65
3.1	Measurement of eigenvalues	65
3.1.1	Impulse response	65
3.1.2	Spatiotemporal diagrams	67
3.1.3	Measuring the band structure	68
3.2	Measurement of eigenstates	71
3.2.1	Numerical eigenstate analysis	71
3.2.2	Experimental eigenstate analysis	74
3.3	Conclusion	77
4	BULK TOPOLOGICAL PROPERTIES OF THE TWO-STEP MODEL	79
4.1	Computing the Berry curvature	79
4.2	Two-step model bulk topological invariants	80
4.3	Topological charge associated with the phase transition	84
4.3.1	Phase transition	84
4.3.2	Topological charge	87
4.4	Interface State	91
4.5	Conclusion	94
5	EDGE DEPENDENT TOPOLOGY OF THE TWO-STEP MODEL	95
5.1	Edge dependent topological invariant	95
5.1.1	Bulk topology	96
5.1.2	Reference frames and open boundary conditions	98
5.2	Extrinsic topology	103
5.2.1	Edge unitary	103
5.2.2	Edge state engineering	107
5.3	Conclusion	115
6	TOPOLOGICAL PROPERTIES OF THE FOUR-STEP MODEL	117
6.1	Four steps model bulk topology	117
6.2	Bulk-edge correspondence	124
6.3	Extrinsic topology	125
6.4	Conclusion	128
7	CONCLUSION & PERSPECTIVE	129
7.1	Conclusion	129
7.2	Perspective	130
A	TWO-STEP MODEL	133
a.1	Eigenvector computation	133
a.2	Eigenvalue computation	137
B	FOUR-STEP MODEL	141
b.1	Eigenvector computation	141
b.2	Eigenvalue computation	145

C	COMPONENT POSITION	151
c.1	Phase modulator placement relative to beamsplitter	151
c.1.1	Phase modulator before the beamsplitter	151
c.1.2	Phase modulator after the beamsplitter	152
D	DATA SMOOTHING	157
E	QUASI PERIODIC MODULATION	163
e.1	Quasi periodic modulation in space	163
e.2	Quasi periodic modulation in time	167
F	QUADRA-RING SYSTEM	171
f.1	Quadra-ring temporal response	171
f.2	Quadra-ring dispersion relation	174
f.2.1	Numerical characterization of the band structure	174
f.2.2	Analytical characterization of the band structure	178
	BIBLIOGRAPHY	183

Abstract

Two-dimensional topological properties of photonic mesh lattices subject to discrete step walks.

This thesis presents experimental and numerical investigations into bulk and edge invariants within a 2D synthetic photonic lattice subjected to discrete step walks. The lattice is engineered by time-multiplexing light pulses in two unequal-length optical fiber rings coupled with a variable beam splitter (VBS). In this configuration, one dimension exhibits real-space dynamics, while the other is governed by an external phase modulator (PM). Employing heterodyne detection, we access spectral information and measure eigenvalues and eigenvectors, enabling the extraction of bulk invariants, such as the Chern number, from the Berry curvature associated with the photonic bands. Furthermore, we derive an expression for the winding number and demonstrate that the emergence of edge states is tied to specific geometric boundaries. Finally, we highlight the impact of edge topology on the overall system topology, which can either suppress or induce the presence of edge states.

Keywords: *Photonic lattices, coupled fiber rings, Discrete step walk, Eigenvalue, Eigenstates, Topological invariants.*

Résumé

Propriétés topologiques bidimensionnelles des réseaux photoniques soumis à des marches discrètes.

Cette thèse explore expérimentalement et numériquement les invariants de volume et de bord dans un réseau photonique synthétique 2D soumis à des marches discrètes. Le réseau est réalisé par multiplexage temporel d'impulsions lumineuses dans deux anneaux de fibres optiques de longueurs inégales, couplés à un coupleur variable (VBS). Dans cette configuration, une dimension présente une dynamique dans l'espace réel, tandis que l'autre est gouvernée par un modulateur de phase externe (PM). En utilisant la détection hétérodyne, nous accédons aux informations spectrales et mesurons les valeurs propres et les vecteurs propres, ce qui permet d'extraire les invariants de volume tel que le nombre de Chern à partir de la courbure de Berry associée aux bandes photoniques. De plus, nous dérivons une expression pour le nombre d'enroulement et démontrons que l'émergence des états de bord est liée à des frontières géométriques spécifiques. Enfin, nous soulignons l'impact de la topologie des bords sur la topologie globale du système, qui peut soit supprimer soit induire la présence d'états de bord.

Mots-clés : *Réseaux photoniques, Anneaux de fibres couplés, Marche discrète, Valeur propre, États propres, Invariants topologiques.*

ACKNOWLEDGMENTS

This achievement wouldn't have been attainable without the assistance and support generously given by so many. During my stay in France. I was privileged to encounter a multitude of fascinating individuals, many of whom have become dear friends. To each one of you, I express my deepest gratitude: Thank you for everything! This journey would have been impossible without your presence. Nevertheless, there are a few individuals who merit special recognition.

A special thanks to my PhD director Professor Alberto Amo Garcia and my Co-director Stéphane Randoux for their priceless support and guidance throughout my PhD journey. Their mentorship helped shape my research path and pushed me to reach new heights. Their dedication, feedback, and encouragement have been crucial in improving my ideas and my research skills. With their expertise, I had the opportunity to present my work at international conferences, engage in curriculum projects at the university level, and publish my first paper [1].

I also want to thank Professor Pierre Suret, Dr. François Copie, and Dr. Clement Hainaut for their valuable advice and willingness to share their deep knowledge. Their teaching skills and engaging discussions have played a key role in deepening my understanding of key concepts and greatly improving my research.

A very special thank you goes to the previous postdoc, Albert Adiyatullin. His amazing teaching skills, precision, and clarity have been truly inspiring. Albert's dedication, and ability to simplify complex concepts have set a high standard for me to aim for in my academic and professional pursuits. His constant support and mentorship have played a key role in my development, for which I am deeply thankful.

I wish to express my gratitude to Gaetan Leveque from the University of Lille, Tomoki Ozawa from the University of Tohoku, and Vincent Couderc from the Research Institute XLIM. Thank you for accepting and dedicating your time to review and examine my manuscript and for your willingness to be a part of my jury.

I am deeply thankful to Professor Christophe Szwaj, Professor Dominique Derozier and Professor Jihane Jabbour. The collaboration between the University of Lille and the Lebanese University enabled me to secure an internship scholarship at the University of Lille and pursue my PhD application. Despite the challenges presented by the COVID-19 pandemic, your efforts were key in helping

me complete my master's degree during an extraordinary and difficult period. The solid academic foundation, opportunities for growth, resources, facilities, and vibrant academic communities provided by the University of Lille and the Lebanese University have greatly enriched my learning experience, for which I am truly thankful.

I want to thank the administrative teams, the P5 team, the CERLA team, the electronic department, and the PhLAM team for their encouragement, support, and warm welcome. Their work behind the scenes was crucial in creating a smooth and supportive environment for my research.

I'm really grateful for the friendship and teamwork with my colleagues. During my PhD, our discussions, celebrations, and working together have been crucial. Whether we're debating research or just having fun at social events, each moment has made my experience richer and our academic environment stronger. Your support has been so important, keeping me motivated through the ups and downs of doctoral studies. Your presence has been a real source of strength and inspiration. I genuinely value the friendships I've made and the support I've received from all of you. It's made my PhD journey so much better and helped me grow as both a researcher and a person.

I also want to extend a heartfelt thank you to Dr. Corentin Lechevalier. His previous work as a PhD student laid the essential groundwork for my project. His willingness to share his vast knowledge and experiences has been a major factor in my academic progress. It was Corentin who passed the torch to me, entrusting me with the continuation of this important work. Now, it's my turn to pass that same torch to the new PhD student Rajesh Asapanna. I have the utmost confidence in his abilities and motivation, and I am certain he will make significant contributions and achieve remarkable discoveries in this field.

Most importantly, I want to thank my family. Your constant support, encouragement, and faith in me have been my greatest source of strength. Through the ups and downs of this journey, your love and support have been constant, and I couldn't have reached this point without you.

A special thank you to Chalimar Salameh. Words cannot express my gratitude for her unwavering love and belief in me, which have been instrumental in my success and a constant source of motivation and strength throughout my PhD and life.

Finally, I want to take a moment to thank myself for my determination, hard work, and belief in my potential, and for pushing through the challenges of this PhD. I am proud of my growth and accomplishments along the way.

Thank you all from the bottom of my heart !!!

DECLARATION OF AUTHORSHIP

I, Rabih EL SOKHEN, born in Kartaba, Lebanon, on October 15, 1998, declare that all the material in this thesis, entitled '*Two-dimensional topological properties of photonic mesh lattices subject to discrete step walks*', is the product of my work. I certify that I conducted this research primarily while pursuing a research degree at the University of Lille from October 2021 to December 2024.

Except for instances explicitly cited within the thesis, I have not incorporated any material previously published or sourced from another thesis for any degree or diploma. All contributions from other individuals have been duly acknowledged within the body of the thesis. Furthermore, this thesis has not been presented for the attainment of any other degree or diploma from any other educational institution.

Signature: Rabih EL SOKHEN

20 December 2024

PUBLICATIONS

This thesis entitled '*Two-dimensional topological properties of photonic mesh lattices subject to discrete step walks*' contains the author's work, some of which has been previously published or is awaiting publication. The author has permission from the original publishing journal to include these publications for academic purposes and to use the work within this thesis.

In particular, certain data, concepts, views, and figures in this thesis may appear in future publications after the submission of this thesis:

- **Rabih El Sokhen**, Álvaro Gómez-León, Albert F. Adiyatullin, Stéphane Randoux, Pierre Delplace, and Alberto Amo. Edge-dependent anomalous topology in synthetic photonic lattices subject to discrete step walks, *Physical Review Research*, vol. 6, p. 023 282, 2 Jun. 2024. doi: [10.1103/PhysRevResearch.6.023282](https://doi.org/10.1103/PhysRevResearch.6.023282).
- **Rabih El Sokhen**, Rajesh Asapanna, Albert F. Adiyatullin, Clément Hainaut, Pierre Delplace, Álvaro Gómez-León, and Alberto Amo. Observation of extrinsic topological phases in Floquet photonic lattices. The draft is in preparation for submission.

Aside from the references mentioned in this thesis, no other content has been sourced, either entirely or partially, from a thesis that was previously approved for any other degree or diploma. The main content of the thesis does not include any uncredited references to the work of others. This thesis has not been submitted to any other higher education institution for the purpose of obtaining a degree or diploma.

INTRODUCTION

Topology is a branch of mathematics that focuses on properties preserved under continuous deformations. For instance, a donut and a teacup are topologically equivalent, as they can be continuously deformed into each other without cutting or gluing while preserving the number of holes [2].

In the realm of photonics, topological photonics leverages geometrical and topological concepts to enable unique, robust unidirectional propagation of light. This field draws inspiration from exciting developments in solid-state materials, including new phases of matter known as topological insulators [3–5]. Even in the presence of substantial impurities, the latter exhibit insulating behavior in their bulk and conduct electricity on their surfaces without backscattering or dissipation. A prime example of this is the quantum Hall effect [6], discovered in 1980 in condensed matter, which demonstrates quantized Hall conductance in two-dimensional electron systems at low temperatures and under strong magnetic fields [6]. In this phenomenon, electrons are confined to move along the edges of the material, creating exceptionally robust edge states. This quantization of the Hall conductance is linked to topological invariants called Chern numbers, which ensure stability against impurities and disorder.

Recent studies revealed that systems with parameters varied periodically over time (periodically driven systems or Floquet systems), can exhibit unusual properties, known as anomalous topological phases [7–9]. These systems are specifically referred to as Floquet anomalous topological phases. Furthermore, quantum walks systems, which involve discrete-step time evolution, yield richer topological phases due to their discrete time evolution, and highlight that both the bulk topology (the overall properties of the internal structure of the system) and the edge topology (properties of a system that arise at boundaries or the edge of a material) are essential for the formation of chiral edge states [10], a unidirectional, robust, localized quantum states located at the boundary or the edge of a material. Experimentally, Floquet anomalous topological phases, have been realized in one-dimensional discrete step walks [11–14] and in two-dimensional photonic lattices with continuous time evolution [15, 16]. However, no previous work has studied the anomalous topological phases in a two-dimensional discrete step walk.

In this dissertation, we investigate the bulk and edge properties of anomalous and trivial topological phases in a two-dimensional synthetic discrete step-walk photonic lattice. The lattice is implemented using time multiplexing of light pulses in two coupled fiber rings. In this system, one of the dimensions displays real space

dynamics and the other one is defined by an external phase applied to the rings. Through a two-dimensional Fourier transform of the stroboscopic spatiotemporal diagram of the system's impulse response, we examine both eigenvectors and eigenvalues from spectral information [17]. We focus on the relation between the bulk invariants and the presence of topological edge states and demonstrate important differences with anomalous topological phases in Floquet systems with a Hamiltonian description (i.e. under continuous time evolution). In particular, we show that the specific choice of boundaries affects the existence of edge states. Our results are well described by suitably defined winding numbers which we directly measure in the experiment, and open the door to the engineering of extrinsic topological phases [10]. In these phases, the number of topological edge modes can be varied through the appropriate design of unitary operators at the edges of the lattice. The implementation of such a configuration could be useful to switch on and off edge transport via local modifications.

Chapter. 1: Starting with photonic lattices and the concept of topological systems, we introduce the photonic lattice model utilized in this study, achieved through the temporal multiplexing of two coupled fiber loops of different lengths. Light pulse evolution in this model is governed by two mathematical equations. Applying a Fourier transform to the stroboscopic spatiotemporal diagram of the system's impulse response, we can access spectral information and extract the eigenstate and eigenvalue. Following that, we present the two-step and four-step models, which exhibit distinct topological properties and form the basis for investigating anomalous phases in our two-dimensional synthetic photonic lattice subject to Floquet-driven discrete step walk. Finally, we review the relevant literature and outline the key problems addressed by the thesis.

Chapter. 2: The experimental setup is presented in this chapter along with the role, precise lengths, and timings of the components. The setup consists of two primary parts: First, the electronic section, managed by an Arduino, and a fast arbitrary waveform generator (AWG7000B), which stabilizes the optical fiber lengths and generates precise waveform sequences to control the setup. Secondly, the optical section incorporates two coupled fiber rings along with a local oscillator, enabling access to spectral information via the heterodyne method.

Chapter. 3: Presents a comprehensive characterization of the double-ring system eigenvalues and eigenvectors (from both power and phase spectral distributions) within a single measurement. This is achieved by leveraging a heterodyne method and analyzing the spectral information of the system's impulse response through a 2D Fourier transform of the stroboscopic spatiotemporal diagram.

Chapter. 4: The bulk properties are analyzed by calculating the Berry curvature and identifying a trivial Chern number for the two-step model. We also explored the topological phase transition and extracted the topological charge Q from the

difference in the Berry flux before and after the gap-closing point. The non-trivial topological charge directly results in an interface state between two distinct topological regions.

Chapter. 5: Anomalous topological phases in a two-dimensional discrete step walk were examined through two distinct approaches. The first approach highlighted the significance of lattice geometry in establishing the presence of edge states. The second approach concentrated on extrinsic topology, demonstrating how the topological characteristics of the boundaries can impact the system's global topology, ultimately resulting in the suppression or emergence of gapless boundary states.

Chapter. 6: Examines the four-step model bulk and edge topology. We present various methods for calculating the Chern number and uncover a richer phase diagram characterized by both trivial and non-trivial Chern numbers. Finally, we explore the impact of the influence of the extrinsic topology on the overall topological system in both trivial and non-trivial Chern bands scenarios, and reveal the potential to close and open specific gaps.

DOUBLE RING PHOTONIC LATTICE

1.1 Photonic lattices

1.1.1 Light diffraction in 1D photonic lattice

Over the past two decades, photonic lattices [18, 19] or waveguide arrays focus on examining the behavior of light when it encounters a pattern of periodically arranged waveguides. Despite the challenges, limitations, and fabrication constraints [20, 21], a diverse range of waveguides, such as fiber optics [22], planar waveguides [23], photonic crystals [18], micro-cavities [24], coupled micro-resonators [25], and micro-pillars [26, 27], have facilitated the emergence of innovative photonic lattice platforms. These platforms have found extensive applications in various physics fields, including cold atoms [28], topology [29], and mechanics [30, 31].

Photonic lattices unveil a mix of allowed and forbidden photonic energy bands, similar to electronic band structures in semiconductors [32]. Additionally, they have proven invaluable in the study of complex light phenomena, including light diffraction [33], Bloch oscillations [34, 35], Rabi oscillations [36], Anderson localization [37], and discrete solitons [38, 39], among others. This progress has been facilitated by the control of various factors such as site coupling, phase modulation, gain, loss, and non-linearities [40–42].

Periodic structures are commonly found in nature. In optics, periodicity is associated with materials that exhibit a refractive index modulation, allowing for the control of light flow in a manner very similar to electrons in electronic devices [33]. Generally, a light beam propagates continuously and undergoes diffraction throughout a homogeneous medium that has a uniform refractive index, meaning that the cross-sectional area of the beam spreads, as represented in Fig. 1.1.a. This behavior can be controlled by modulating the refractive index of the optical material. Recently, researchers have followed this approach and realized that light can propagate discretely in photonic lattices.

Imagine light being channeled into photonic lattices. These lattices consist of coupled one-dimensional or two-dimensional optical waveguides. For example, op-

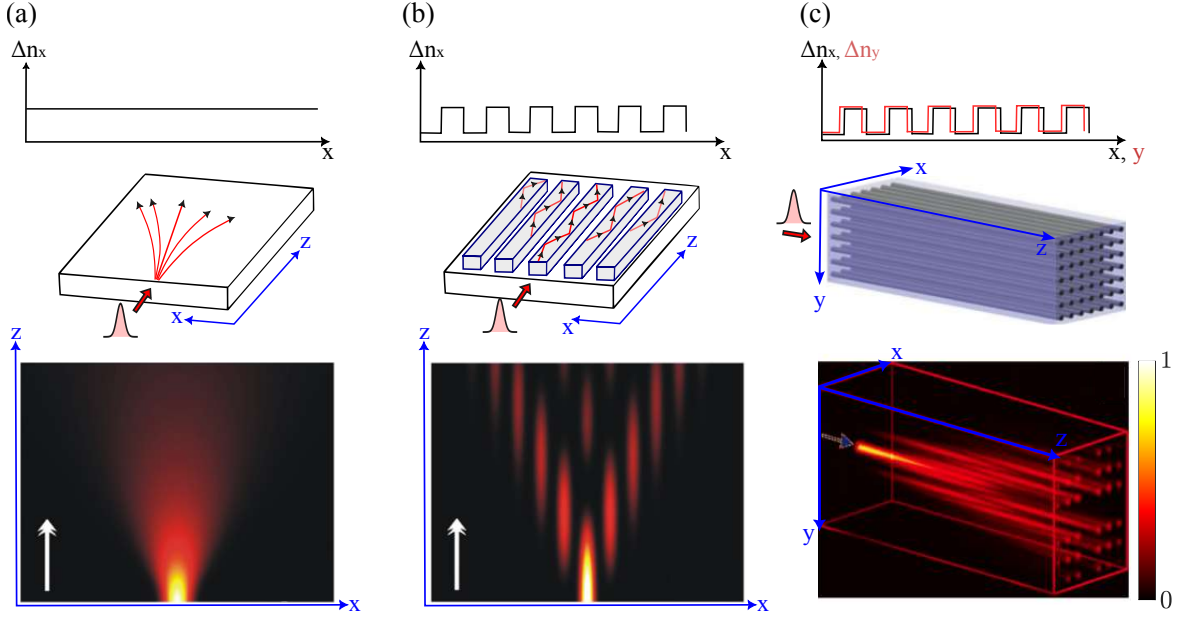


Figure 1.1: Diffraction of light. (a) Diffraction of light in a homogenous medium with a continuous index profile. (b) One-dimensional discrete diffraction is achieved when light is introduced into a waveguide network of planar structures, juxtaposed next to each other to achieve an overlap between the modes propagating in the guides. Light becomes localized to specific points and interacts with neighboring guides during its transition between channels, facilitated by evanescent optical coupling while propagating along the z -axis direction. (c) Two-dimensional discrete diffraction of light in a heterogeneous medium with index profile n_x and n_y along the x and the y direction respectively, while the propagation is along the z -axis. [48, 49]

tical fibers or three-layer planar structures juxtaposed next to each other, as presented in Fig. 1.1.c and Fig. 1.1.b, respectively. In an isolated waveguide, light becomes confined, following a specific path within the central layer. This is achieved through continuous total reflections on the two edges of a waveguide [43], as illustrated in Fig. 1.1.b.

In photonic lattices, the modes confined in adjacent waveguides overlap [44] and couple with neighboring guides as they propagate along the z -axis through evanescent optical coupling [45, 46], as depicted in Fig. 1.1.b and Fig. 1.1.c. This results in widening the spatial distribution of the light beam [39] and profoundly altering the diffraction characteristics. The light beam becomes localized to specific points of high energy far from the center with several secondary peaks between them, see Fig. 1.1.b and Fig. 1.2.b. This so-called discrete diffraction opens up new possibilities for controlling the flow of light that would have otherwise been impossible in other systems [41]. Two complementary approaches can be implemented to study these photonic lattices, the first deals with coupled individual waveguides, and the second is the Floquet-Bloch analysis that treats the photonic arrays as a periodic structure [47].

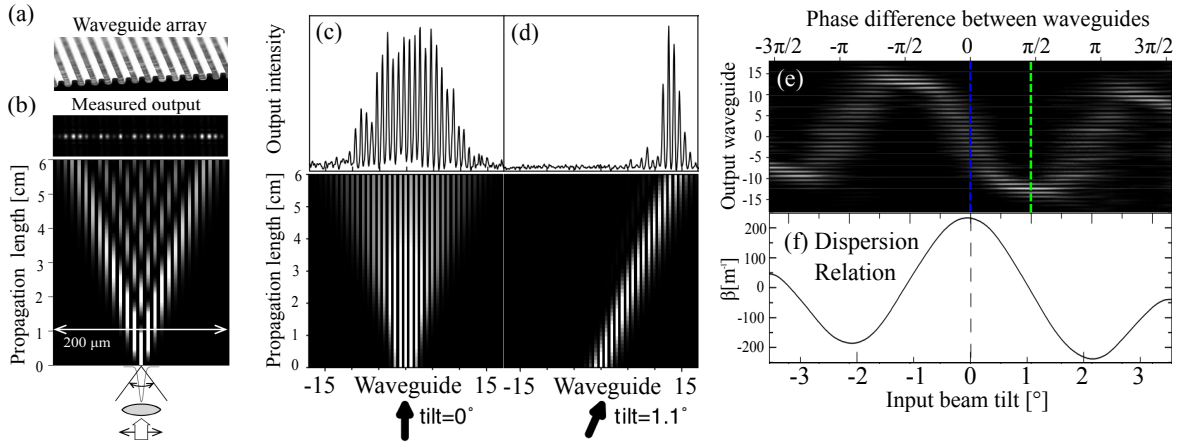


Figure 1.2: (a) 1D Photonic lattice composed of coupled waveguides. (b) Discrete diffraction is achieved when a narrow pulse is injected into the lattice. (c)-(d) Discrete diffraction is depicted when a broad pulse with an inclination angle of 0° and 1.1° is respectively introduced. (e) The output intensity profiles of this one-dimensional lattice are determined by the inclination angle of the injected beam. The blue (green) dashed line corresponds to the input beam tilt of 0° (1.1°) and mirrors the scenarios presented in images (c) and (d) respectively. (f) The dispersion relation of the photonic lattice. Those figures are extracted from [20]

The genesis of experiments on photonic lattices can be traced back to the early 1970s. This was the era when S. Somekh and his team pioneered the design of planar waveguides [50]. Their groundbreaking research demonstrated light coupling across Gallium Arsenide guides, marking the first observation of a discrete diffraction type. The subject of waveguide arrays was revived in the 1980s by Haus and his team, who demonstrated their unique discrete imaging properties of the photonic network [51]. This concept has been further validated with optical fibers [52] and has been broadly adopted in many studies [48, 53, 54].

For instance, F. Lederer's team [20] embarked on an intriguing exploration into the behavior of light pulses within a one-dimensional photonic network made of 75 discrete coupled waveguides, as illustrated in Fig. 1.2.a. They observed how a narrow pulse, equivalent in size to a basic waveguide, navigates through the network, transitioning from one guide to another, a process during which interference may occur, as depicted in Fig. 1.2.b. In contrast, they found that injecting a wide pulse covering several guides disperses in a unique pattern across the photonic lattice, as showcased in Figs. 1.2.c-d. This pattern is influenced by the specific excitation conditions and dispersion properties of the photonic lattice. Various wave packets with different widths and inclination angles within a one-dimensional photonic lattice were examined. This provides insights into the dispersion relationship and distinctly illustrates the spatial progression of light pulses within the photonic lattice. The lower panels of Figs. 1.2.c-d showcase the injection of a broad pulse into the arrays at angles of 0° and 1.1° respectively, It's noticeable that a minor tilt of 1.1° allows the light to maintain its form while propagating through the lattice, giv-

ing the appearance of a solitonic¹ structure. This conservation of shape, however, was not observed when the angle was set to 0° . The upper panels of Figs. 1.2.c-d displays the output intensity after it has moved through the entire lattice.

Figure. 1.2.e depicts the pulse's dispersion as a function of its incidence angle in the waveguide array. The pulse's final central position can shift based on the entry angle, as represented by the blue dashed line (0°) and the green dashed line (1.1°), mirroring the scenarios in Fig. 1.2.c and Fig. 1.2.d, respectively. The study explores how the pulse's width can either expand or contract depending on the angle of injection. The photonic band in Fig. 1.2.f reveals a dispersion relationship that governs the path and spread of a light pulse within a photonic lattice. This relationship not only dictates how light will propagate through the lattice but also unveils topological properties characterized by topological invariants [55].

1.1.2 Floquet-Bloch theorem

A convenient way to understand the eigenmodes of a spatially periodic lattice is to examine the periodicity of the lattice itself. This line of reasoning can be extended to lattices that experience periodic time modulations. In this context, we will delve into the details of such eigenmodes. The motivation is that they will be useful to describe the photonic lattices at the core of this work. We start our discussion with the Floquet and Bloch theorems, we will shed light on the behavior of states in periodic systems across both time and space. Subsequently, we investigate in the next section periodic driving for Floquet systems and quantum walks, emphasizing unique characteristics such as anomalous topological phases.

1.1.2.1 Bloch Theorem

In 1928, Lyapunov [56] and F. Bloch [57] came up with the "Bloch theorem" for systems with spatial periodicity, it describes the behavior of electrons in a crystal lattice with periodic potential energy by decomposing the wave function $\psi(\vec{k}, \vec{r})$ of electrons into a plane wave term $e^{i\vec{k}\vec{r}}$ and a spatial periodic function $\phi(\vec{k}, \vec{r})$ as represented by equation. 1.1, such that $\phi(\vec{k}, \vec{r} + \vec{a}) = \phi(\vec{k}, \vec{r})$, with \vec{a} being the spatial period of the crystal lattice, \vec{k} is the quasimomentum, which is defined in terms of modulo 2π and \vec{r} is the position vector

$$\psi(\vec{k}, \vec{r}) = e^{i\vec{k}\vec{r}} \phi(\vec{k}, \vec{r}) \quad (1.1)$$

Using the Bloch theorem to solve the Schrödinger equation in a periodic lattice reveals the allowed energy levels and corresponding electronic states.

¹ **Soliton:** a localized wave that travels without changing shape and speed while traveling through a medium due to a balance between nonlinearity and dispersion in the medium.

1.1.2.2 Floquet theorem

In 1883, G. Floquet discovered the "Floquet theorem" [58], which was further shaped by G. Hill [59]. Floquet theory deals with differential equations whose coefficients are periodic functions of time. For instance, let's consider a physical system described by a time-periodic Hamiltonian $H(t)$ with a period T , such that $H(t + T) = H(t)$. As time progresses from $t_0 \rightarrow t$, the system evolves, as described by the evolution operator $U(t_0 \rightarrow t)$ from an initial state, denoted as $|\psi(t_0)\rangle$, into a new state given by $|\psi(t)\rangle$, such that $|\psi(t)\rangle = U(t_0 \rightarrow t)|\psi(t_0)\rangle$, which satisfies the Schrödinger equation. 1.2.

$$i\frac{\partial}{\partial t}|\psi(t)\rangle = H(t)|\psi(t)\rangle \quad (1.2)$$

The solutions to such periodic differential equations can be decomposed into a phase factor e^{iEt} (with E being the quasienergy, which is defined in terms of modulo 2π) and a periodic function $|\phi(t)\rangle$ with a period T such that: $|\phi(t + T)\rangle = |\phi(t)\rangle$, as represented by equation. 1.3:

$$|\psi(t)\rangle = e^{iEt}|\phi(t)\rangle \quad (1.3)$$

One can view the Floquet theorem as the temporal counterpart of the Bloch theorem. Substituting this solution back into the Schrödinger equation, we find the time-dependent eigenvalue equation.

$$-(H(t) - i\frac{\partial}{\partial t})|\phi(t)\rangle = E|\phi(t)\rangle \quad (1.4)$$

1.1.2.3 Floquet-Bloch Theorem

Blending the two previous theorems together, the Floquet-Bloch theorem was born [60], it describes systems that exhibit a double periodicity, in space (period of \vec{a}) and in time (period of T). Thus, the Floquet-Bloch theorem deals with Hamiltonians periodic in both space and time and satisfies the following:

$$\begin{cases} H(\vec{r} + \vec{a}, t) = H(\vec{r}, t) \\ H(\vec{r}, t + T) = H(\vec{r}, t) \end{cases} \quad (1.5)$$

The Schrödinger equation in its time-dependent form for a wavefunction $|\psi(\vec{r}, t)\rangle$ is given by:

$$i\frac{\partial}{\partial t}|\psi(\vec{r}, t)\rangle = H(\vec{r}, t)|\psi(\vec{r}, t)\rangle \quad (1.6)$$

The solutions to the Schrödinger equation for such systems can be written as:

$$\psi(\vec{k}, \vec{r}, t) = e^{i\vec{k}\vec{r}}e^{iEt}\phi(\vec{k}, \vec{r}, t) \quad (1.7)$$

Where \vec{k} & E being the quasimomentum and the quasienergy respectively, both of which are defined in terms of modulo 2π and $\phi(\vec{k}, \vec{r}, t)$ being periodic both in space and time. As we will see later, the Floquet-Bloch theorem, which is perfectly suited for our time and space periodic system, identifies the system's eigenstates.

1.1.3 Topological system

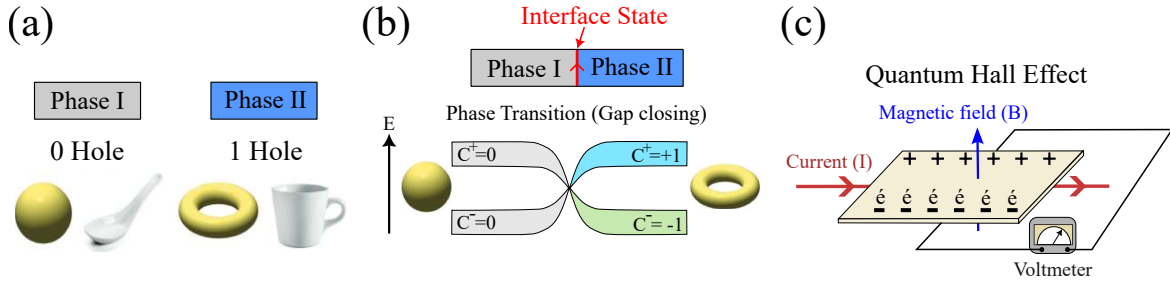


Figure 1.3: (a) Mathematical examples showcasing that various objects are considered to be in the same topological phase if they share the same topological invariant (in this example, the number of holes). (b) Topological phase transition gives rise to an interface state between two distinct topological phases (phase I and phase II). The transition occurs by continuously deforming the band structure, which causes energy gaps to close and reopen into a new topological region distinguished by unique bulk topological invariants (the Chern number C). (c) Quantum Hall effect, showcases the localization of electrons at the boundary of the material when a strong magnetic field is applied, thus forming unique electronic edge states. [61–63]

Topology is a mathematical discipline that emphasizes a space's connectivity rather than its geometric form. It is characterized by topological invariants, which are properties that persist even under continuous deformations [2]. Different objects are considered to be in the same topological phase and thus topologically identical if they share the same topological invariant. For example, a yellow sphere and the surface of a white spoon do not have any holes, they are topologically equivalent. Similarly, despite their distinct shapes, the surface of a donut and a teacup are topologically equivalent, they can be reshaped into each other through continuous deformation without altering their fundamental property, which in this case, is the number of holes, as illustrated in Fig. 1.3.a. We can apply a similar description to the structure of eigenmodes forming an electronic band in a solid. This structure can be described by a topological invariant, which we will introduce later. When the solid is continuously deformed, the eigenmodes change but the topological invariant is preserved as long as the gap between the considered band and the nearest one remains open.

Figure. 1.3.b illustrates a topological phase transitions between two distinct topological phases (trivial and non-trivial) give rise to interface states. To accomplish

this transition, the band structure is continually deformed, which causes energy gaps to close and reopen into a new topological region marked by different bulk topological invariants (Chern number C).

In the field of physics, topological photonics enables a robust unidirectional propagation of light. This feature draws inspiration from condensed matter, materials science, and topological insulators [3–5, 64]. Systems with topological properties provide a framework for understanding new phases of matter that exhibit unique properties with a large number of practical applications [65–69]. A prime example of this is the quantum Hall effect [6] in condensed matter, observed in two-dimensional electron systems subjected to strong magnetic fields, where electrons become confined and travel robustly along the material’s edges rather than the bulk, forming unique electronic edge states, as shown in Fig. 1.3.c.

One characteristic of edge states is their ability to persist without back scattering or dissipation, even in the presence of disorder and significant impurities. This is ensured by the two-dimensional bulk topological invariant (the Chern number C^n) that offers insights into the overall topological properties of a specific band structure n .

$$C^n = \frac{1}{2\pi} \int_{BZ} \nabla_{\vec{k}} \times A(\vec{k})_n d\vec{k}_x d\vec{k}_y. \quad (1.8)$$

The Chern number C^n is obtained by executing an integration of the Berry curvature denoted as $\nabla_{\vec{k}} \times A(\vec{k})_n$, with $\nabla_{\vec{k}}$ being the gradient operator in k -space and $|\psi_n(\vec{k}, t)\rangle$ the Bloch eigenmodes, over the complete Brillouin zone (BZ). The Berry curvature [70] is a geometrical property of the band structure, it is obtained by taking the curl of the Berry connection and provides insights into the topological properties of the system. The Berry connection is given by $A(\vec{k})_n = \langle \psi_n(\vec{k}, t) | i \nabla_{\vec{k}} | \psi_n(\vec{k}, t) \rangle$, it’s a vector field that describes how the quantum state’s phase evolves with respect to parameter variations. The Brillouin zone is a fundamental concept in solid-state physics, particularly for analyzing the electronic properties of periodic materials like crystals [71, 72]. It is defined as a uniquely primitive cell in the reciprocal space, containing all the possible wavevectors \vec{k} that describe the allowed electronic states in a periodic structure. In static lattices, the Chern number of a band dictates the number of edge states traversing the gap when an interface is considered.

1.1.3.1 *Periodically Driven System*

In addition, the extension to the realm of non-equilibrium or dissipative systems has increased the variety of topological phases and their possible uses [73]. A fascinating and fruitful example of this are Floquet topological phases [74–76]. They appear in systems with enriched topology due to the coupling to an external driving field that is periodic in time. In contrast to static systems (Hamiltonian

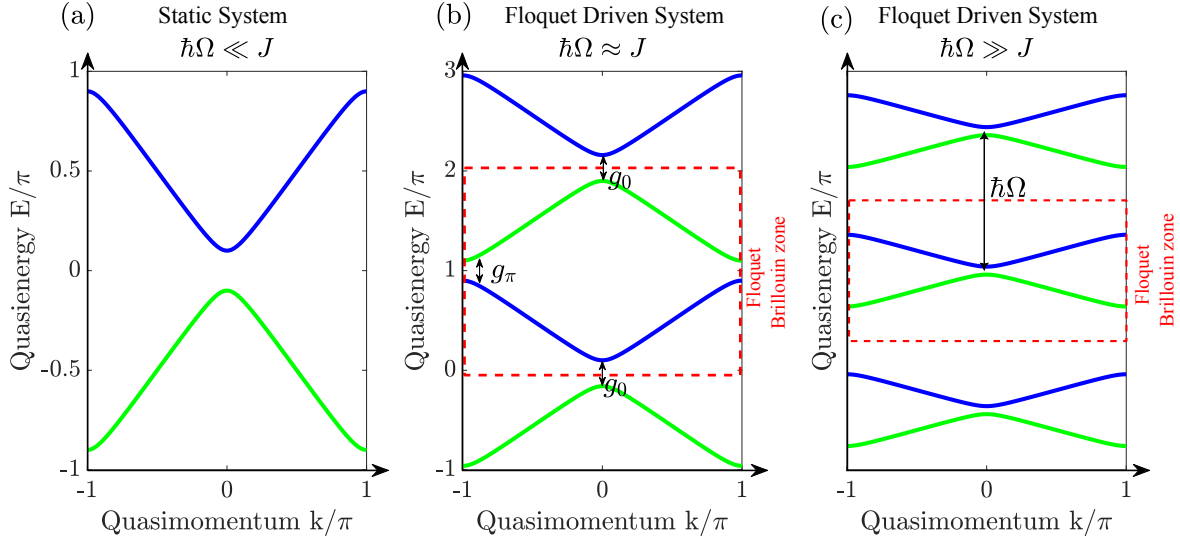


Figure 1.4: External frequency driving. (a) Adiabatic regime occurs when the external driving energy $\hbar\Omega$ is significantly lower than the coupling energy between the waveguides J , such that $(\hbar\Omega \ll J)$, where \hbar is the Planck constant and Ω is the driving frequency. Changes within the system occurs gradually, allowing it to adjust internally while maintaining its equilibrium state. (b) The frequency of the external driving approaches proximity to the coupling frequency $(\hbar\Omega \approx J)$, and there is a small energy gap between the periodic quasienergies. Consequently, these bands interact with each other. (c) High-frequency regime when external driving dominates the system energy $(\hbar\Omega \gg J)$, a notable energy gap between the periodic quasienergies. This gap is substantial enough that the repeated bands remain separated by an energy equivalent to the driving field $(\hbar\Omega)$, consequently, these bands do not interact or exert influence on each other.

is independent of time) where the zero bulk topological invariant links to the trivial phase with no edge state. Periodically driven lattices exhibit a spectrum of modes that are both periodic in space and quasienergy, with a period of $2\pi/T$. This phenomenon introduces intriguing characteristics, like the presence of anomalous topological phases. This feature opens the possibility of having bands with topological Chiral (unidirectional) edge states traversing a specific energy gap (μ) even while exhibiting trivial Chern indices ($C = 0$) [77]. Since their discovery, Floquet anomalous topological phases have been realized in one-dimensional discrete step walks [11–14] and in two-dimensional photonic lattices with continuous time evolution [15, 16]. However, the absence of spectral information in these systems has prevented both the identification of the gap in which the anomalous edge modes are present and access to the bulk topological invariants.

1.1.3.2 Externally Driven Static System

Let us first consider static systems, for our purposes a static system can be driven by external energy in time with an energy of the external drive $\hbar\Omega$ significantly lower than the coupling energy between the waveguides J of the system $(\hbar\Omega \ll J)$, where \hbar is the Planck constant and Ω is the driving frequency.

In this case, changes within the system occur gradually, allowing it to adjust internally while maintaining its equilibrium state. This condition is often referred to as the adiabatic case [78]. In this context, the dispersion bands within the system demonstrate a unique pattern, lacking any repetitive periodicity (see Fig. 1.4.a). An example of this is the Thouless charge pump [79, 80], which describes a process where an integer amount of charge is transported across a system during one period of an adiabatic (slowly changing) cycle.

Recently, both Floquet systems and quantum walks have attracted increasing interest due to the topological phenomena. Floquet systems are characterized by periodic time-dependent Hamiltonians $H(\vec{k}, t + T) = H(\vec{k}, t)$, where T denotes the period of one cycle, undergoes continuous time evolution, The corresponding one-cycle time-evolution operator known as the Floquet operator associated with a time-dependent Hamiltonian is given by: $U_F(\vec{k}, t_0 \rightarrow T) = \tau e^{-i/\hbar \int_{t_0}^T dt H(\vec{k}, t)}$, where τ denotes time ordering. In contrast, split-step walk systems, commonly referred to as quantum walks, are characterized by the discrete-time evolution of unitary operators $U_j(\vec{k})$ that describe their dynamics rather than a time-dependent Hamiltonian. In this context, the one-cycle time evolution operator U_{QW} is delineated by the sequential multiplication of unitary operators $U_j(\vec{k})$ such that $U_{QW}(\vec{k}) = \prod_j U_j(\vec{k})$. Furthermore, any Floquet operator U_F can be interpreted as a quantum walk operator U_{QW} [10].

1.1.3.3 Floquet-driven systems

Two distinct cases for Floquet-driven systems (where the Hamiltonian is time-dependent) arise regarding the dynamics of external driving. First of all, in the high-frequency regime where the driving is smooth and continuous, the coupling energy between the waveguides J is lower than the energy of the external driving $\hbar\Omega$ such as ($\hbar\Omega \gg J$). An example of such a scenario is demonstrated in the work of M. Rechtsman et al. on a two-dimensional array of waveguides forming a honeycomb lattice [81]. In the high-frequency regime, a notable energy gap exists between the periodic quasienergies. This gap is substantial enough that the repeated bands remain separated by an energy equivalent to the driving field ($\hbar\Omega$). Consequently, these bands do not interact or exert influence on each other (see Fig. 1.4.c). A stroboscopic effective Hamiltonian can describe the system. Additionally, the primary effect of the drive is that it enables the effective Hamiltonian to incorporate magnetic and electric fields that were absent in the original Hamiltonian. This allows photons to be engineered within the effective Hamiltonian framework, mimicking the behavior of charged particles under the influence of electric and magnetic forces. For every band, the topological description of its two-dimensional band structure is determined by the Chern number.

Secondly, when the frequency of the external driving approaches proximity to the coupling frequency ($\hbar\Omega \approx J$), the periodic quasienergies are separated by a

small gap g_0 and g_π at energy level 0 and 2π respectively, leading to an interaction between these bands (see Fig. 1.4.b). The system can no longer be accurately described by an effective Hamiltonian and stroboscopic dynamics alone prove inadequate, necessitating explicit consideration of the evolution dynamics within a single driving period, referred to as micromotion. In this regime, the topology of Floquet systems becomes fundamentally different from that of static ones, and one can find anomalous topological phases with chiral edge states in systems with topologically trivial bands [11, 82–92]. Micromotion plays a significant role in the system’s dynamics [42, 93]. These lattices can exist in one dimension [42, 94, 95], or in two dimensions [15, 16], as exemplified by the research of Rudner et al. [96]. The latter shows that it is possible to generate anomalous Floquet topological phases [11, 82–93]. Interestingly, in these cases, the Chern number no longer describes the topological system. Instead, it is defined by another topological invariant known as the winding number (W) [4] that determines the number of Floquet edge modes.

$$W[U] = \frac{1}{8\pi^2} \int_0^T \int_{\text{BZ}} dt d\vec{k}_x d\vec{k}_y \times \text{Tr}(U^{-1} \partial_t U [U^{-1} \partial_{\vec{k}_x} U, U^{-1} \partial_{\vec{k}_y} U]) \quad (1.9)$$

The winding number denoted as $W[U]$ it is fundamentally different from the Chern number. It is dependent on the complete time evolution throughout the driving cycle, as dictated by the unitary evolution operator $U(t)$.

1.1.3.4 *Floquet discrete-step systems*

Anomalous phases have also been found in systems with a discrete-step time evolution, known as quantum walks [11–16, 97]. One of their particular features is the absence of an intrinsic time coordinate due to their discrete time evolution. This implies that the topological characterization of Floquet phases with a Hamiltonian description, which requires an explicit time-coordinate [83, 85], is not suitable for quantum walks. Recent theory works have shown [98–100] that quantum walks result in a richer topological phase diagram due to their discrete time evolution, and that in two-dimensional lattices subjected to discrete splitting events, the number of edge states cannot be solely explained by the bulk invariants of the lattice (i.e., the Chern number and the Floquet winding number), as would be the case in static lattices or lattices subject to smooth modulations. Instead, the number of edge states is also influenced by a topological invariant associated with the winding of the discrete-step unitary operators acting at the lattice edges, a phenomenon referred to as “*Extrinsic topology*” [10]. The total number of edge states within a given gap is given by: $N = C + \nu_{\text{Edge}}$, where C represents the Chern number of the band below the gap, and ν_{edge} defined in equation. 1.10 denotes the winding of the edge unitary operator U_{edge} .

$$\nu_{\text{edge}} = \frac{1}{2\pi} \int_0^{2\pi} d\varphi \text{Tr}[U_{\text{edge}}(\varphi)^{-1} i \partial_\varphi U_{\text{edge}}(\varphi)]. \quad (1.10)$$

Experimentally, Floquet topological phases in discrete step walks have been realized in photonic lattices [11–16, 88, 101, 102]. However, the characterization of anomalous phases in these experimental systems has been constrained either to chiral symmetric lattices in one-dimension [11–14] or to two-dimensional lattices in the limit of a continuous time evolution [15, 16] employing the invariants discussed by Rudner and co-workers [83, 85], which do not take into account the crucial discrete-step aspect of the time evolution.

Our objective is to uncover the bulk and edge properties to topologically characterize the anomalous phases in a two-dimensional synthetic discrete-step photonic lattice. In the following sections, we introduce the conceptual model of our double-ring system.

1.2 Introduction to the double ring photonic lattice

As we proceed, our discussion will follow the evolution of random walk from the Galton board to the double-ring synthetic photonic lattice. We will explore how temporal multiplexing and coupled rings form a photonic lattice, allowing light to evolve discretely in both time and space. Employing numerical simulations and mathematical models, our exploration will focus on studying the dynamics of light in the double-ring configuration. Our first objective will be to obtain the eigenvalues and eigenvectors through the analysis of impulse responses.

1.2.1 Discrete-step walk platforms overview

Back in 1894, Francis Galton proposed the "Bean Machine" to demonstrate the principles of probability and the normal distribution [103, 104]. This machine consists of a vertical board with a series of regularly spaced obstacles. At the top of the board, particles are released one by one. As they descend through each level of the board, they are randomly deflected left or right by the obstacles until they eventually settle into one of several slots at the bottom of the board, following a binomial distribution, refer to Fig. 1.5.a. The unpredictable stochastic bouncing motion, either left or right, encountered at each obstacle demonstrates the Galton board as a prime model of a random walk [104, 105]

In 1999, a novel optical implementation of the Galton board, known as the 'Pyramid of Beam Splitters', was proposed by Bouwmeester and co-workers [106]. The innovative setup substitutes the solid obstacles of the Galton board with 50/50 optical beam splitters and the walker with a laser beam (refer to Fig. 1.5.b). At each beam splitter, the optical beam splits into two counterparts of equal amplitude: the transmitted and reflected parts, where the phase of the reflected field is shifted by $\frac{\pi}{2}$, and the output amplitudes of the electrical field of a single 50/50 beam

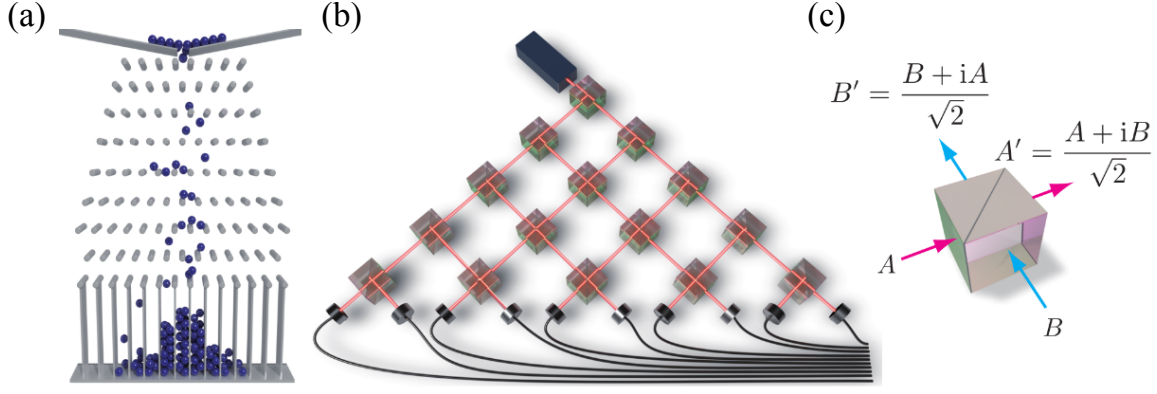


Figure 1.5: (a) The Galton Board [103] demonstrates the normal distribution as particles deflect left or right while descending past obstacles into slots. (b) Bouwmeester et al. [106] suggest an optical Galton board, substituting the particles with a laser beam and the obstacles with 50/50 beam splitter cubes. (c) The output amplitudes of the electrical field A' and B' of a single 50/50 beam splitter resulting from the combination of the two input amplitudes field A and B . [107]

splitter A' and B' are given by two coupled linear equations. 1.11 resulting from the combination of the two input amplitude fields A and B (see Fig. 1.5.c) [107].

$$\begin{pmatrix} A' \\ B' \end{pmatrix} = \frac{1}{\sqrt{2}} \begin{pmatrix} 1 & i \\ i & 1 \end{pmatrix} \begin{pmatrix} A \\ B \end{pmatrix} \quad (1.11)$$

As a result, the accumulated phase shifts at each reflection, along with the resultant interference pattern, play a crucial role in describing the evolution of the optical field and shaping its propagation. This phenomenon is commonly referred to as a 'Light Walk' distribution [104, 107, 108]. The numerous components needed for a spaced-apart pyramid of beam splitters make it difficult to maintain a stable path length between couplers, crucial for preserving coherence and visibility of interference patterns [109]. This requires active interferometric stabilization, significantly raising experimental complexity [110]. Andreas Schreiber and Christine Silberhorn's team proposed that employing a time multiplexing method is crucial for overcoming the requirement for numerous components, but it also ensures constant system stability against external noise [111, 112]. Their experimental quantum optical version serves as a reliable platform for both one dimensions [112, 113] and even two spatial dimensions [114].

1.2.2 Conceptual model of the double ring

In line with the concept of time multiplexing [113], Ulf Peschel's team originally developed the double-ring synthetic configuration in 2011, which serves as a simplified version of the pyramid beam model and forms the basis of our study [115]. This configuration primarily consists of three main components: a long-ring optical

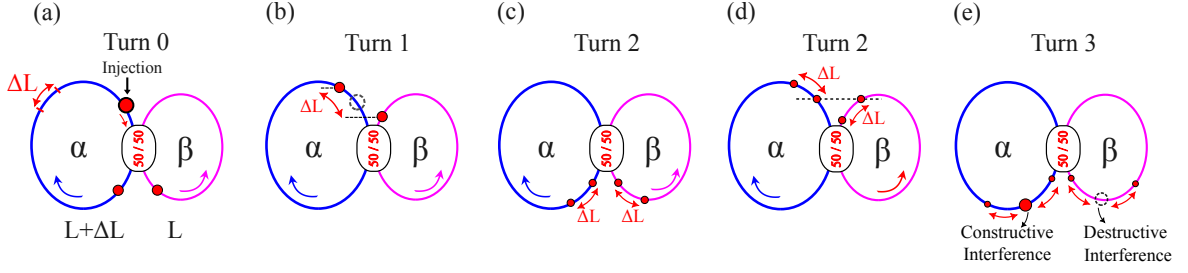


Figure 1.6: (a) A simplified pyramid beam model consists mainly of a 50/50 coupled fiber and two rings: ring α (in blue), which is longer than ring β (in pink) by a length difference of ΔL . (a) to (e) Illustrate the evolution of light dynamics in the double-ring setup. (a) The injected light in the long loop splits into two smaller pulses with equal amplitude within each ring once it reaches the 50/50 fiber coupler. (b) These pulses traverse their respective loops until they reach the beam splitter again at different moments due to the length differential ΔL , (c) where they split once more into two smaller pulses with equal amplitude within each ring. This cyclical process continues, generating multiple pulses with consistent time intervals during each round trip. Occasionally, pulses arriving simultaneously from the different loops at the beam splitter, as shown with a dashed line in (d) will undergo constructive interference in one ring while being destructive interference in the second one and vice versa (e).

fiber called α with a length L_α , a short-ring optical fiber called β with a length L_β , and a 50/50 beam splitter. The beam splitter connects the short loop (β) to the long one (α) as indicated by different colors in Fig. 1.6.a, thus significantly reducing the required components. The term "synthetic" implies two key concepts. The first one is the use of multiple fictitious beam splitters, while in reality, only one single fiber coupler is employed to reconstruct the entire pyramid of beam splitters. The operational principle involves using pulsed signals instead of continuous waves and employing a single fiber coupler for the entire pyramid of beam splitters. This is achieved by connecting the input fibers of a two-by-two 50/50 fiber coupler to the output fiber ports through two optical fibers of different lengths. The second notion, rearranging the pulse time from a time dimension to a spatial one, the setup maintains a small length difference ΔL between the loops, such that $\Delta L = L_\alpha - L_\beta$, which provided the foundation for time multiplexing [115, 116] and caused pulses to shift spatially, corresponding to left or right movements with temporal delays [107], representing optical round trips in shorter or longer loops, as we will see now.

Let's begin by examining the overall pulse dynamics within the double-ring configuration. Initially, a pulse injected into the α ring divides into two smaller pulses with equal amplitude within each ring once it reaches the 50/50 fiber coupler, as depicted in Fig. 1.6.a. These pulses journey through their respective loops until they reunite at the beam splitter at different moments due to the length differential ΔL between the two rings. The pulse in the shorter loop reaches the beam splitter first. Meanwhile, the pulse in the longer loop is relatively delayed by a distance of ΔL with respect to the pulse in the shorter loop, as illustrated in Fig. 1.6.b. Once

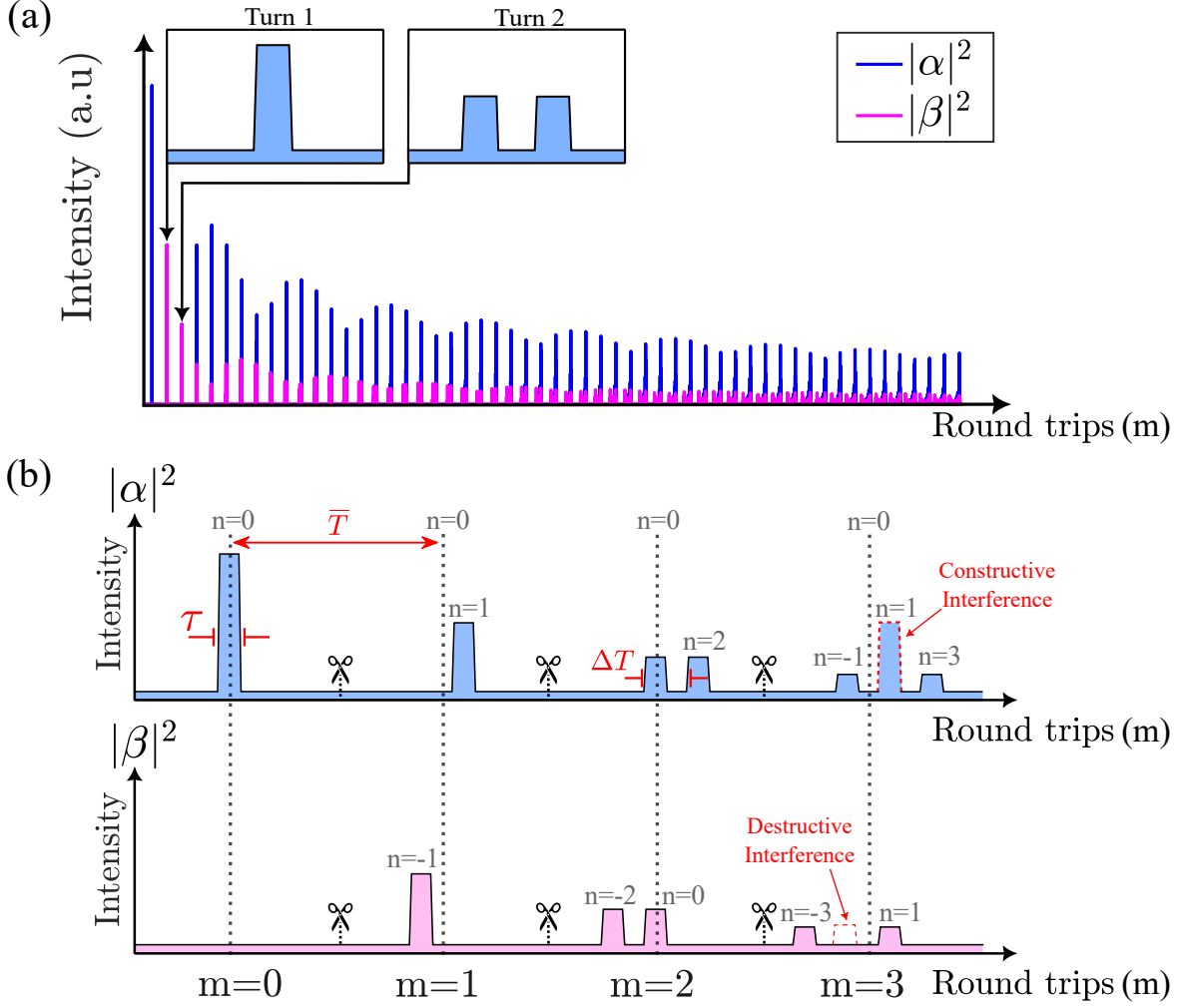


Figure 1.7: (a) Numerical simulation illustrating the temporal evolution of intensity as a function of time in the long (short) ring, represented in blue (pink). (b) Zoom on the first 4 turns of the signal.

again, each of the pulses within each ring split into two smaller pulses, illustrated in Fig. 1.6.c. Consequently, this continuous cyclic process generates multiple pulses with consistent time intervals during each round trip (red double arrows). Eventually, when pulses from different loops arrive simultaneously at the beam splitter, as indicated by a dashed line in Fig. 1.6.d, they undergo constructive interference in one ring while experiencing destructive interference in the other, as denoted by Fig. 1.6.e.

In the double-ring setup, the dynamics of light progress discretely, as splitting occurs only at specific time intervals when pulses reach the fiber coupler. This characteristic makes our system periodic in time. Furthermore, due to the length difference in the loops, the adjacent pulses within the same round trip in each ring are consistently temporally separated, leading to their detection at specific physical times [117]. We assign an integer number to each pulse to represent a particular time coordinate, which can be equated to a position in space. This approach makes our system spatially periodic. For a better understanding of this

concept, we present in Fig. 1.7.a a numerical simulation of the temporal response of the double ring system for the case of a 50/50 beam splitter, illustrating the distribution of signal intensity as a function of time at the output of the long (short) ring, represented in blue (pink).

Figure. 1.7.b provides a closer look at the initial four round trips within each of the rings from Fig. 1.7.a that allows us to notice several aspects. Initially, a narrow pulse with a temporal width of τ is introduced in the α ring at round trip $m = 0$ and position site $n = 0$. Upon reaching the 50/50 coupler, this pulse splits into two diminished pulses, each with half the intensity of the original. One of these pulses is found in the short ring β at round trip time $m = 1$ and position $n = -1$, indicating that it is detected one site earlier than the original pulse. Conversely, the other pulse travels in the longer ring α at round trip time $m = 1$ and position $n = +1$, signifying a one-site delay compared to the original pulse. The length difference ΔL between the two rings causes pulses in the long ring to be detected later than the short one. As a direct consequence, the spatial expansion on the horizontal axis (n) is increased by a positive step of (+1) to the right for the long ring α and a negative step of (-1) to the left for the reduced ring β . As a result, the length difference between the two loops ΔL causes a spatial separation of two site positions n , every round trip m . Alongside this, interference can take place when pulses from both rings reunite the fiber coupler at the same time. For instance, in Fig. 1.7.b at the third round trip $m = 3$, constructive interference occurs at site $n = 1$ in the long ring α . Conversely, destructive interference happens in the short ring β at site $n = -1$.

The average time of one period is $\bar{T} = \bar{L}/v$, with \bar{L} representing the average length of the rings, $\bar{L} = (L_\alpha + L_\beta)/2$ and v is the speed of light in the optical fiber. In addition, for a specific round trip (m), the adjacent pulses in the same sequence are separated by a time interval $\Delta T = \Delta L/v$ which corresponds to the duration associated with the difference in length between the two optical fiber loops. Also, if the number of pulses per round trip exceeds the maximum number of pulses n_{max} , such that $n_{max} = \bar{T}/(\Delta T/2)$ with $\Delta T/2$ the duration of a single site position, each of the two loops are fully filled with pulses, a situation that we aim to avoid in practice. To observe sequences of separated pulses clearly and avoid any overlap, the duration width of each pulse must be smaller than one single site position ($\tau < \frac{\Delta T}{2}$).

By cutting the signal of Fig. 1.7.a into equal durations of \bar{T} and superimposing these signal samples on top of each other, we obtain the spatiotemporal diagram represented in Fig. 1.8.a that describes the progression of light from one turn to another as a function of position n (a numerical simulation will be presented in the next section for better clarification). In the spatiotemporal diagram, the light's behavior from turn to turn is impacted by the length differences of the rings, leading to an interference pattern that shapes the propagation of the field into an inver-

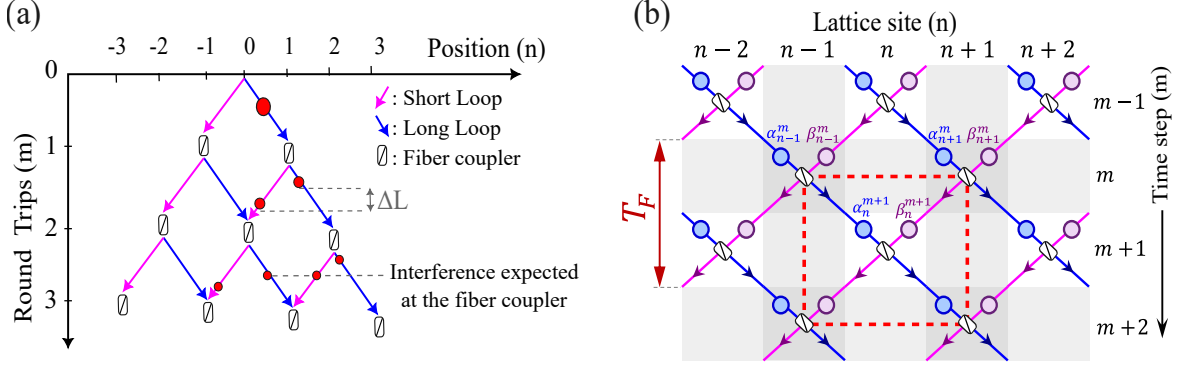


Figure 1.8: (a) A spatiotemporal diagram of synthetic photonic lattices illustrates the progression of light from one turn to another. This progression is impacted by differences in length ΔL , leading to an interference pattern that shapes the light's propagation into an inverted pyramid pattern. Blue (pink) arrows represent the rings α (β), respectively, while rectangle nodes depict the fiber couplers. (b) Synthetic split step lattice.

ted pyramid pattern, whereas the blue (pink) arrows represent the long (short) ring while the connection nodes are symbolized by white rectangles representing the fiber coupler that connects the two rings. Moreover, the inverted pyramid in Fig. 1.8.a exhibits a slight tilt. This is because the right (left) edge of the pyramid, in line with the blue (pink) arrows, represents the light propagation exclusively in the long (short) ring. Thus, the light propagating along the left border of the pyramid does not travel the same distance compared to that on the right, and eliminates the possibility of interference patterns at the couplers situated on the pyramid's edge.

Figure. 1.8.b represents the corresponding synthetic photonic lattices of the system which is spanned by the discrete time m and position n . To simplify and more effectively illustrate the mesh lattice, all of its paths are shown with the same length. The splitting process occurs discretely at the beam splitter during each round trip, emphasizing the periodic nature in time. However, one Floquet period T_F corresponds to the complete light propagation in both the long and short rings, effectively comprising two round trips, one in α and one in β .

As illustrated in Fig. 1.8.b, the two sublattices sites, depicted in blue (pink) corresponding to the complex amplitudes α_n^m (β_n^m) for a specific round trip m and position n , return to the same site position after two-time steps. Similarly, the spatial periodicity is highlighted by the time-multiplexing of pulses, which are consistently temporally separated due to the length difference between the rings. At a specific round trip, the two sublattices manifest by a spatial periodicity every two site positions. Thus, our system exhibits dual periodicity in both time and space, with a period corresponding to two round trips in time $m \rightarrow m + 2$ and two site positions in space $n \rightarrow n + 2$. This defines the unit cell, which is delineated by a dashed red line.

1.2.3 Evolution equation and band structure

1.2.3.1 *Evolution equation*

The amplitude and phase dynamics of light pulses in the rings can be represented as a coherent step evolution in the one-dimensional synthetic lattice depicted in Fig. 1.8.b. The evolution of the field is governed by two coupled linear equations. 1.12 discretized in position (n) and time (m) [115]. Here, (n) denotes the position along the horizontal axis, representing a specific physical time, while (m) indicates the vertical time axis, signifying the number of round trips in the loops.

$$\begin{cases} \alpha_n^{m+1} = \frac{1}{\sqrt{2}} (\alpha_{n-1}^m + i\beta_{n-1}^m) \\ \beta_n^{m+1} = \frac{1}{\sqrt{2}} (i\alpha_{n+1}^m + \beta_{n+1}^m) \end{cases} \quad (1.12)$$

Equations. 1.12 show that the output complex amplitudes of the wavefield α_n^{m+1} and β_n^{m+1} in the left and right rings, respectively, at time step ($m + 1$) at lattice site (n) result from a linear combination of the transmitted and reflected input amplitude fields at round trip (m). The imaginary factor (i) denotes the phase shift of the reflected field at the fiber coupler by $\frac{\pi}{2}$, and the term $\frac{1}{\sqrt{2}}$ describes the amplitude splitting angle of the transmitted and reflected fields of the 50/50 fiber coupler.

1.2.3.2 *Spatiotemporal diagram*

Throughout our research, our primary focus will be on analyzing the impulse response of the photonic lattice by injecting a short pulse smaller than the size of a single site ($\tau < \frac{\Delta T}{2}$). However, it's important to acknowledge that previous studies have investigated various phenomena, such as injecting a broad pulse [118–121]. While this aspect is undoubtedly interesting, it is not within the scope of our work. Exploring the impulse response of our system is straightforward; we conduct numerical simulations by employing equations. 1.12 and injecting a narrow pulse into the long ring α , ensuring it satisfies the conditions specified in the equation. 1.13.

$$\begin{cases} \alpha_{n=0}^{m=0} = 1 \\ \beta_n^{m=0} = 0 \quad \forall n \end{cases} \quad (1.13)$$

In Figs. 1.9.a-b, a pyramid-like shape emerges from the dispersion of the field evolution intensity during its propagation from one turn to another as a function of position n , as evidenced in the spatiotemporal diagram for each ring. A gray-scale color scheme represents the optical power of the pulses, where black signifies maximum power and white represents zero power. In the case of the short ring β , the intensity distribution is uniform and symmetrical with regard to a vertical axis.

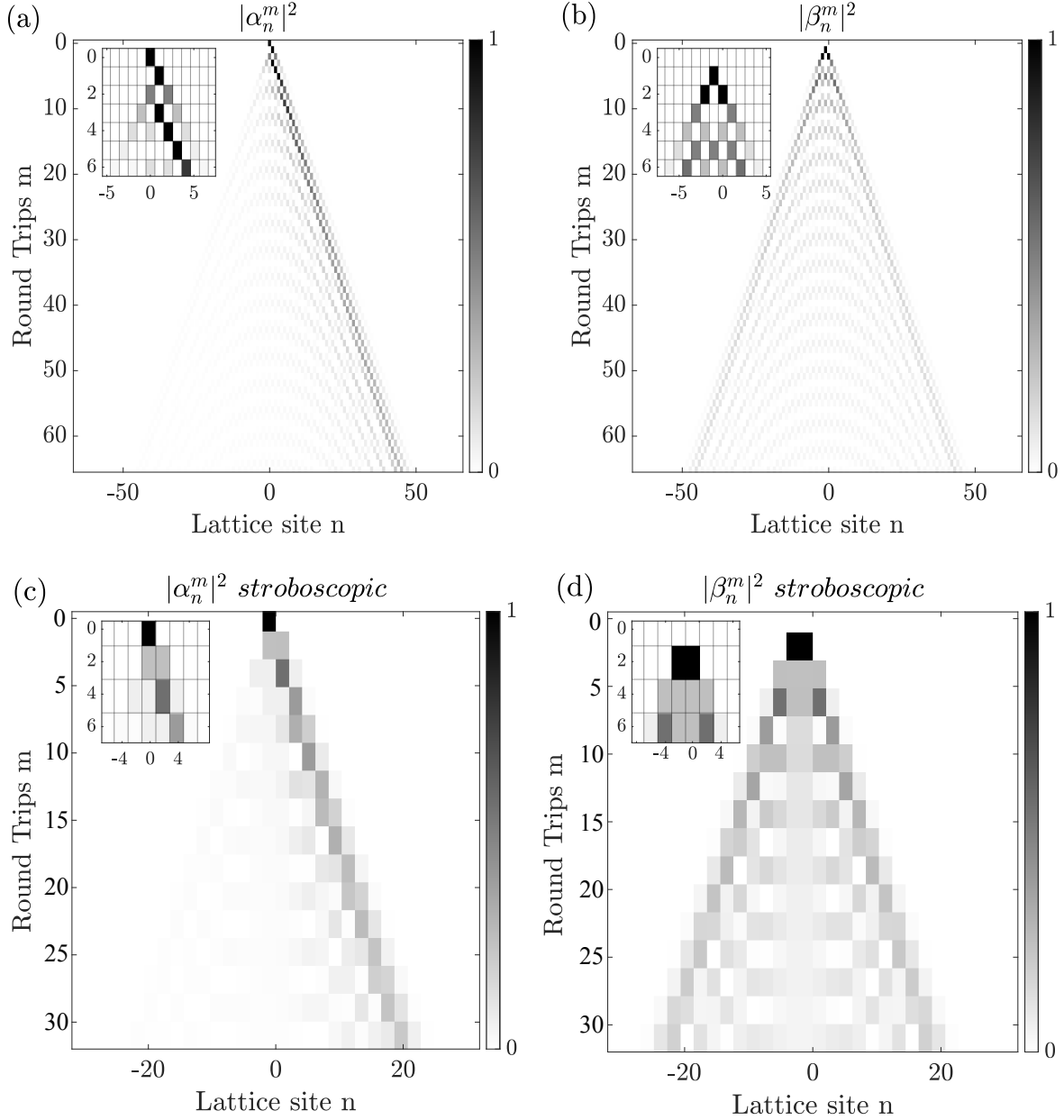


Figure 1.9: (a)-(b) Numerical simulation illustrating the photonic network's impulse response through the spatiotemporal intensity evolution within the short and long loops when a short pulse is introduced to the long loop. (c)-(d) Numerical simulation of the stroboscopic spatiotemporal dynamics of each ring by selecting only even round trips with even site positions.

On the other hand, we introduced the initial condition into the α ring where the pulses mostly follow one direction, resulting in an asymmetrical intensity distribution of pulses. As was indicated in the preceding section, the absence of interference at the pyramid's edges explains why the light intensity distribution in the spatiotemporal diagram is primarily localized in two main lobes along the edge of each diagram, with several secondary maxima in between.

The eigenmodes of our Floquet-Bloch lattice have a periodicity of two-time steps and two sites. To study these modes, it is more convenient to consider the stroboscopic dynamics, rather than the amplitude of pulses at every Floquet and Bloch period only. These are the amplitudes that will be later correctly described by the Floquet-Bloch formalism.

Figures. 1.9.c-d presents a numerical simulation of the stroboscopic spatiotemporal dynamics of each ring. This is achieved by keeping even time steps ($m = 0, 2, 4, \dots$) with even site positions ($n = \dots, -4, -2, 0, 2, 4, 6, \dots$), while disregarding the micromotion in between. This approach is due to the double periodicity of our system, characterized by two-site spatial periodicity and two-time step temporal periodicity. However, it is possible to select odd Floquet periods ($m = 1, 3, 5, \dots$) with odd site position ($n = \dots, -3, -1, 1, 3, \dots$). The choice of unit cell outlined with a dashed red line in Fig. 1.8.b to start with an even or odd round trip does not affect the main properties of the system.

1.2.3.3 Eigenvector and eigenvalue

Analyzing the eigenmodes of the system described by the coupled equations. 1.12 and examining the dispersion relation are essential for interpreting the observed behaviors. Due to the system's double periodicity, equations. 1.12 can be solved using the Floquet-Bloch ansatz equation. 1.14.

$$\begin{pmatrix} \alpha_m^n \\ \beta_m^n \end{pmatrix} = \begin{pmatrix} \tilde{\alpha}(k) \\ \tilde{\beta}(k) \end{pmatrix} e^{i\frac{Em}{2}} e^{i\frac{kn}{2}} \quad (1.14)$$

The Bloch momentum k and the quasienergies E are the conjugate variables corresponding to spatial (n) and temporal (m) parameters, respectively. Equation. 1.14 emphasizes: first, the system's double periodicity in both directions, with a period of two discrete steps. This is reflected in the exponents term of the ansatz equation by a factor of $1/2$ along both E and k . Secondly, Due to the system's periodicity, the temporal evolution of the sublattices complex amplitudes (α_m^n & β_m^n) at any stroboscopic time in real space can be expressed as a superposition of all the eigenmodes in reciprocal space, with $\tilde{\alpha}(k)$ and $\tilde{\beta}(k)$ is the complex amplitude of the eigenmodes at the sites corresponding to the α and β rings respectively.

Incorporating this formulation into equations. 1.12 allows us to derive the analytical dispersion relation characterizing light propagation within the photonic lattice, as described by equation. 1.15. The system's dispersion relation consists of two photonic bands characterized by the eigenvalues $E(k)^+$ and $E(k)^-$, representing the upper and lower bands, respectively. Additionally, the normalized eigenvectors $|\psi(k)^+\rangle$ and $|\psi(k)^-\rangle$, corresponding to each of the eigenvalues $E(k)^+$ and

$E(k)^-$, are represented by the complex amplitudes $\tilde{\alpha}$ and $\tilde{\beta}$ of the two sublattices are given by equation. 1.16 and 1.17:

$$E(k)^\pm = \pm \cos^{-1}\left[\frac{1}{2}(\cos(k) - 1)\right] \quad (1.15)$$

$$|\psi(k)\rangle^\pm = \begin{pmatrix} \tilde{\alpha}(k) \\ \tilde{\beta}(k) \end{pmatrix}^\pm = \frac{1}{\sqrt{1 + |R(k)^\pm|^2}} \begin{pmatrix} 1 \\ |R^\pm| e^{i\Phi_{\alpha\beta}^\pm} \end{pmatrix} \quad (1.16)$$

$$R(k)^\pm = |R^\pm| e^{i\Phi_{\alpha\beta}^\pm} = \frac{e^{iE(k)^\pm} + \frac{1}{2}(1 - e^{-ik})}{\frac{1}{2}i[1 + e^{-ik}]} \quad (1.17)$$

Equations. 1.15, 1.16, and 1.17 are all derived from the two-step model equations described in the Appendix. A, and correspond to the case of a photonic lattice made with a 50/50 fiber coupler. Using equation. 1.18, the numerical dispersion relation $|\tilde{\beta}(k, E)|^2$ and $|\tilde{\alpha}(k, E)|^2$ presented in Fig. 1.10 for each of the loops can be extracted by performing a two-dimensional Fourier transform analysis on both α and β spatiotemporal diagram shown in Fig. 1.9 [17, 118].

$$\begin{cases} \mathcal{F}\mathcal{F}\mathcal{T}2[\beta(n, m)] = \tilde{\beta}(k, E) = \frac{1}{NM} \sum_{n=-\frac{N}{2}}^{\frac{N}{2}} \sum_{m=1}^M \beta(n, m) e^{-i2\pi(\frac{Kn}{N} + \frac{Em}{M})} \\ \mathcal{F}\mathcal{F}\mathcal{T}2[\alpha(n, m)] = \tilde{\alpha}(k, E) = \frac{1}{NM} \sum_{n=-\frac{N}{2}}^{\frac{N}{2}} \sum_{m=1}^M \alpha(n, m) e^{-i2\pi(\frac{Kn}{N} + \frac{Em}{M})} \end{cases} \quad (1.18)$$

The quantities N and M represent the number of points used in the numerical simulation of the equation. 1.12 on the n and m axes, respectively. The resolution of the numerical dispersion relation depends on both the number of round trips (m) and the size of the lattice (n). Thus, the more turns the light circulates, the smaller the linewidth of the band structure becomes in Fig. 1.10.

Figures. 1.10.a-b show dispersion relations for long and short rings, derived from spatiotemporal diagrams of Figs. 1.9.a-b. Figures. 1.10.c-d present the corresponding dispersion relations for the stroboscopic case of Figs. 1.9.c-d obtained via a two-dimensional Fourier transform.

Analyzing Figs. 1.10.a-b, the lattice periodicity in both time (m) and space (n) ensures that the band structure displays a double periodicity in the range of $[-\pi; \pi]$ along their respective conjugate variables (k) and (E). This defines our Brillouin zone in the same range of $[-\pi; \pi]$ in both the quasimomentum k and quasienergy E directions, as depicted by the white dashed square.

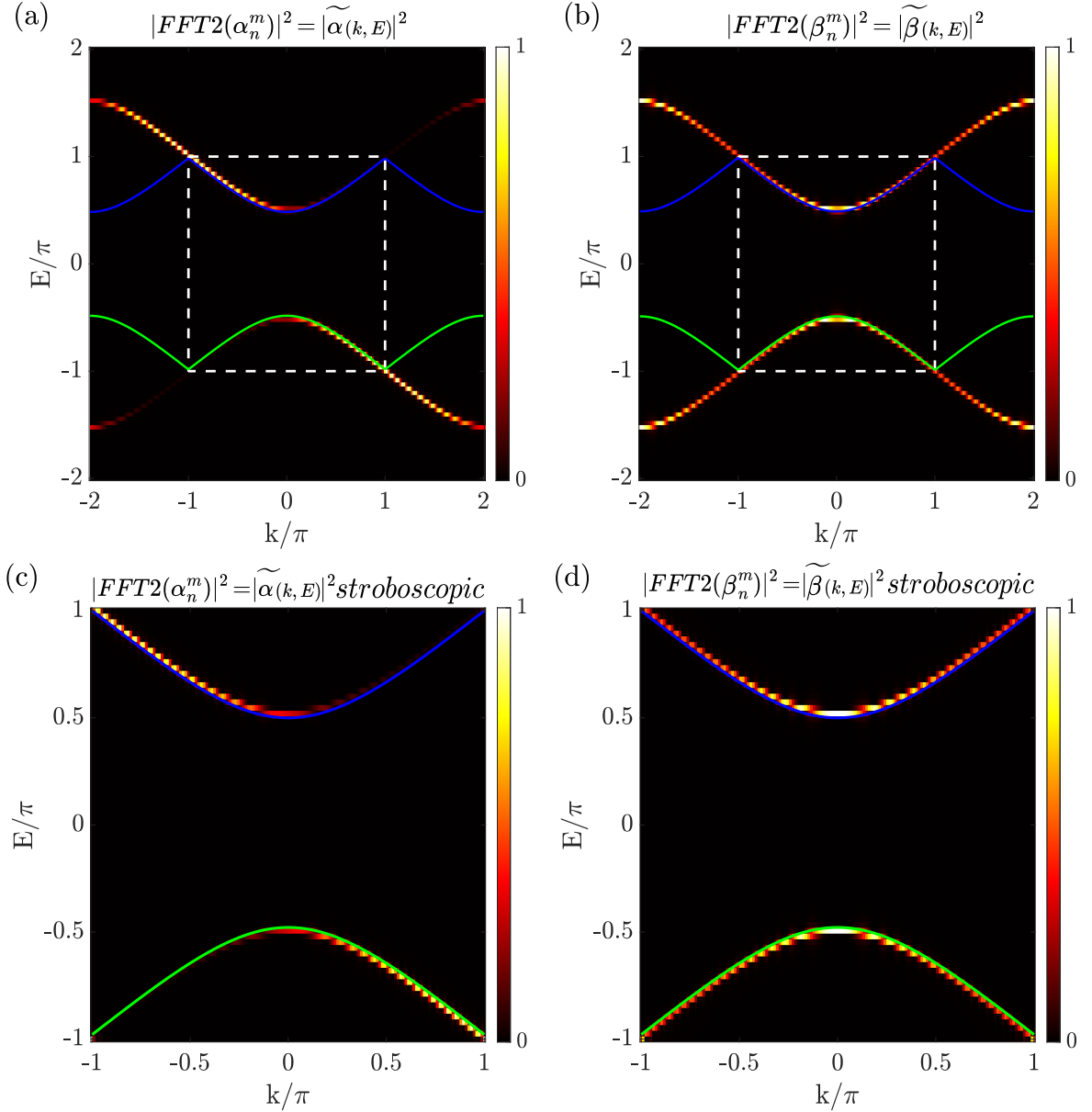


Figure 1.10: (a)-(b) and (c-d) Numerical dispersion relations for the long and short rings, extracted via two-dimensional Fourier transform of their corresponding spatiotemporal diagram presented in Figs. 1.9.a-b and Figs. 1.9.c-d, respectively. The results show excellent agreement between the numerically obtained dispersion relations and the analytical upper (blue) and lower bands (green) of equation. 1.15 within the Brillouin zone (dashed white square).

The two-dimensional numerical Fourier transform equation. 1.18 has a period of (n, m) as opposed to the $(\frac{n}{2}, \frac{m}{2})$ period of Floquet-Bloch equation. 1.14. The factor $1/2$ in the exponents of the ansatz takes into account the two sites' spatial periodicity and the period of two-time steps in equation. 1.12. This difference causes the numerical dispersion relation to be distributed throughout two Brillouin zones as opposed to just one, emphasizing the importance of considering the stroboscopic case presented in Figs. 1.10.c-d. **For this reason, we will henceforth focus exclusively on the stroboscopic dynamics for the remainder of this thesis.**

Figures. 1.10.c-d, highlights several insights. Firstly, it showcases a remarkable agreement between the analytical dispersion relation in equation. 1.15 (upper band in blue and lower band in green) and the numerically extracted one within the Brillouin zone with an energy gap separating the band at the energy level $E = 0$. The bands are identical in form but have different curvatures, the lower band is concave while the upper band is convex. The second derivation of the photonic band structure $\partial^2 E(k)/\partial k^2$ depicts the group velocity dispersion as zero at the four corners of the Brillouin zone. This is equivalent mathematically to an inflection point (a shift in curvature form from concave to convex or vice versa). On the second hand, the first derivatives of the dispersion relation describe the effective group velocity, $v_g = \partial E(k)/\partial k$. This analysis is particularly relevant when a broad Gaussian pulse is injected into the lattice, exciting a few modes within the spectrum. The dispersion relation is crucial for understanding nonlinear phenomena in the photonic lattice [17].

Secondly, the values at $(k, E) = (-\pi, \pi)$ on the higher band coincide with the value at $(k, E) = (\pi, -\pi)$ on the lower band, as well as between $(k, E) = (-\pi, -\pi)$ and $(k, E) = (\pi, \pi)$, because of the energy's degeneration. Thus, there is no energy gap at the Brillouin zone's corners. The two bands touch at the corners of the Brillouin zone.

Thirdly, upon introducing a narrow pulse that meets the conditions of equation. 1.13, the long and short rings exhibit distinct patterns of eigenstate excitation in their numerical band structures. The entire short-ring energy spectrum is fully excited symmetrically, as displayed in Fig. 1.10.d, whereas the long-ring energy spectrum is partially excited in an asymmetrical way, as presented in Fig. 1.10.c. Therefore, the symmetrical (asymmetry) intensity distribution observed in the spatiotemporal diagram in Fig. 1.9 is directly reflected in the spectral distribution in the band structure Fig. 1.10, as determined by the system's eigenstates described in equation. 1.16. The reason for this disparity is the asymmetry in the initial condition, which injects light in one of the rings only.

Numerically and experimentally, the eigenstates in equation. 1.16 are established by analyzing the power and the phase of their spectral distributions in each ring. This methodology is further detailed in Chapter. 3. The eigenstates of a specific band structure can be described by $|R(k)^\pm| = |\tilde{\beta}^\pm(k, E(k)^\pm)|^2 / |\tilde{\alpha}^\pm(k, E(k)^\pm)|^2$, representing the ratio of amplitudes, and $\Phi(k)_{\alpha\beta}^\pm = \arg(\tilde{\beta}^\pm(k, E(k)^\pm)) - \arg(\tilde{\alpha}^\pm(k, E(k)^\pm))$, denoting the phase difference between the two sublattice sites associated with the eigenvector with quasimomentum k within the first Brillouin zone. Figures. 1.11.a-b displays, respectively, the absolute value and the phase of the amplitude ratio described in equation. 1.17, it shows a good agreement between the analytical and numerical eigenstates corresponding to the upper band in the case of a 50/50 fiber coupler connecting the two fiber loops. In Fig. 1.11.a A noticeable asymmetry can be observed in the analytical (numerical) amplitude ratio

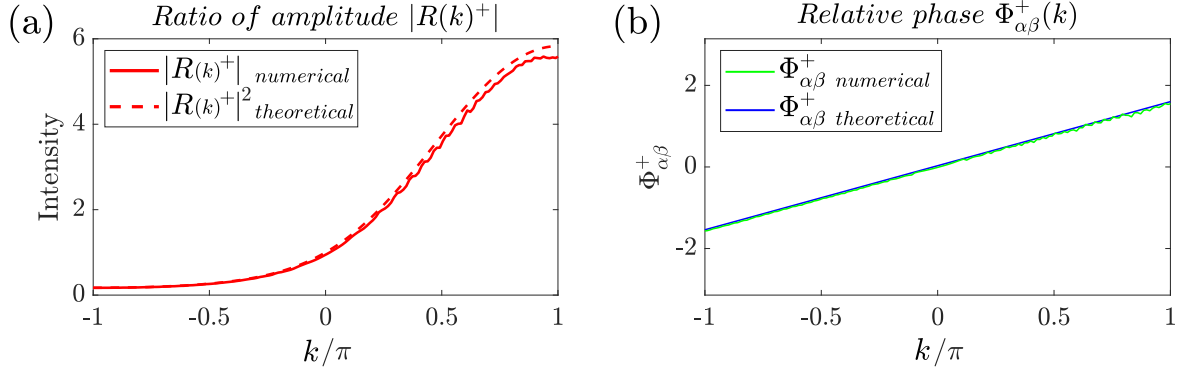


Figure 1.11: Analytical (numerical) representations of (a) the amplitude ratio of the eigenstate corresponding to the upper band, shown in red dashed (solid) lines, and (b) the relative phase, depicted in blue (green).

$|R^+(k)|$ depicted by a red dashed (solid) line. On the other hand, the analytical (numerical) relative phases, represented in blue (green) in Fig. 1.11.b follow a linear distribution such that $\Phi_{\alpha\beta}^+(k) = \frac{k}{2}$. The absolute value and the phase of the lower band's amplitude ratio are presented in Chapter. 3.

It is vital to acknowledge that measuring the phase of the optical field over short time scales in optical experiments is challenging but crucial for Fourier transformation to obtain the dispersion relation, unlike the simulations. Later in the thesis, we delve into how to effectively address these complexities in Chapter. 2.

1.3 Two-dimensional synthetic photonic lattice

Building upon our comprehension of the dynamics of the double-ring system in the one-dimensional framework presented in the previous section, we now introduce the two-step and four-step models. These models provide a foundational basis for our investigation into topological phases within a two-dimensional synthetic photonic lattice. Within this model, we will examine the bulk and edge properties in later chapters. The bulk can be studied from the direct measurement of the eigenvectors of the Floquet operator [118] and via the measurement of anomalous transport [122], which give access to the Berry curvature of the Floquet bands over the whole first Brillouin zone. The implementation of physical edges in the setup can be done via the onsite control of the splitting angle in the step evolution.

1.3.1 Two-step model

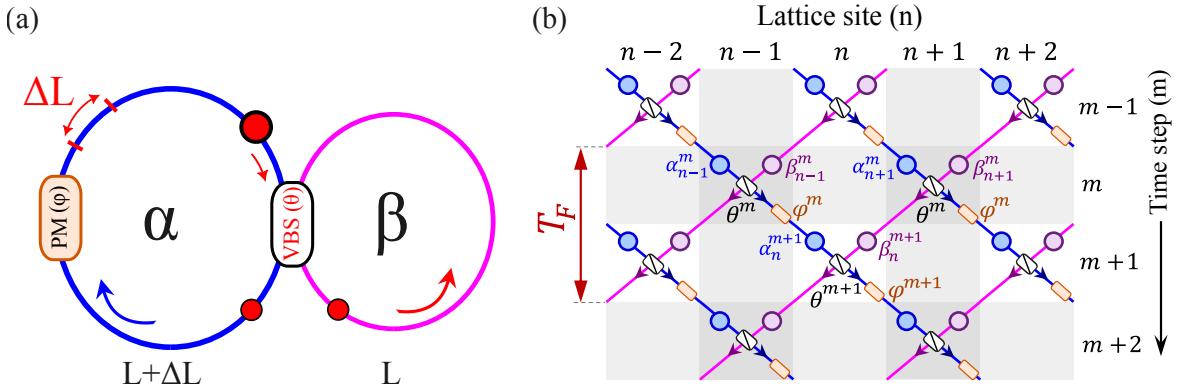


Figure 1.12: (a) Scheme of the double ring system presenting the long (short) ring in blue (pink) arrows, coupled via a variable beamsplitter VBS (white rectangle), the longer loop α incorporates an external phase modulator (orange rectangle). (b) Synthetic split step lattice that spans in discrete steps along the position site (n) and time step (m).

Building on the two-loop system introduced in Section. 1.2, let's delve deeper into its dynamics when a variable beam splitter and a phase modulator are incorporated within the loops, as shown schematically in Fig. 1.12.a.

The dynamics of the amplitude and phase of light pulses in the rings can be mapped into a coherent step evolution in the one-dimensional synthetic lattice depicted in Fig. 1.12.b, governed by the following equations [14, 123]:

$$\begin{cases} \alpha_n^{m+1} = (\cos \theta_m \alpha_{n-1}^m + i \sin \theta_m \beta_{n-1}^m) e^{i\varphi_n^m} \\ \beta_n^{m+1} = i \sin \theta_m \alpha_{n+1}^m + \cos \theta_m \beta_{n+1}^m \end{cases} \quad (1.19)$$

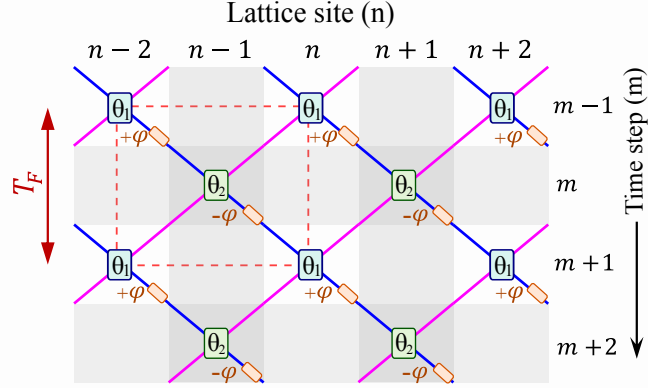


Figure 1.13: A synthetic split-step lattice demonstrating a two-step periodic modulation of the beam splitter's coupling angle, alternating between θ_1 and θ_2 , and the phase modulator's applied phase φ , switching between $+\varphi$ and $-\varphi$ at odd and even steps, the unit cell is presented in a dashed red square.

α_n^m and β_n^m being the complex amplitude of the light pulses in the left and right rings, respectively, at lattice position (n) and round trip time step (m). The splitting amplitude angle at the variable beamsplitter is $\theta_m \in [0, \pi/2]$. When θ_m equals 0, the transmission term, represented by $\cos \theta_m$, results in a value of 1, while the reflectance term, denoted by $\sin \theta_m$, reduces to 0. In this case, we witness total transmission, and the pulses continue to propagate within the same loops. On the other hand, when θ_m equals $\pi/2$, we observe total reflectance. In this scenario, the pulse alternates between the two rings without any splitting. Finally, when θ_m equals $\pi/4$, it represents the case of a 50/50 beam splitter. To get the second synthetic dimension, a phase modulator adds a controlled phase in the form of periodic potentials φ_m to the α ring with a value that alternates between two values, $\varphi_1 = +\varphi$ and $\varphi_2 = -\varphi$ at odd and even steps.

$$\varphi_n^m = \begin{cases} \varphi_1 = +\varphi & \forall n \text{ if } m \text{ is odd} \\ \varphi_2 = -\varphi & \forall n \text{ if } m \text{ is even} \end{cases} \quad (1.20)$$

The lattice sites (n) provide a spatial dimension along which dynamics can take place with an associated conjugated momentum k , while the external phase φ acts as a generalized quasimomentum resulting in a second parametric dimension ($\varphi \in (-\pi, \pi]$).

Alternating the coupling angle θ between two values, θ_1 and θ_2 , and the phase modulator between $\varphi_1 = +\varphi$ and $\varphi_2 = -\varphi$ at odd and even steps, the system exhibits a spatial periodicity of two sites and a time-step periodicity of two steps, as shown by the red dashed unit cell in Fig. 1.13. The lattice system has two sublattices corresponding to the α and β rings (blue and purple circles) in Fig. 1.12.b and a Floquet period of two-time steps. Substituting the Floquet-Bloch ansatz equation. 1.14 into equation. 1.19, we obtain the general formula for the eigenvalues of the two bands as a function of k and, φ as described in equation. 1.21. Detailed

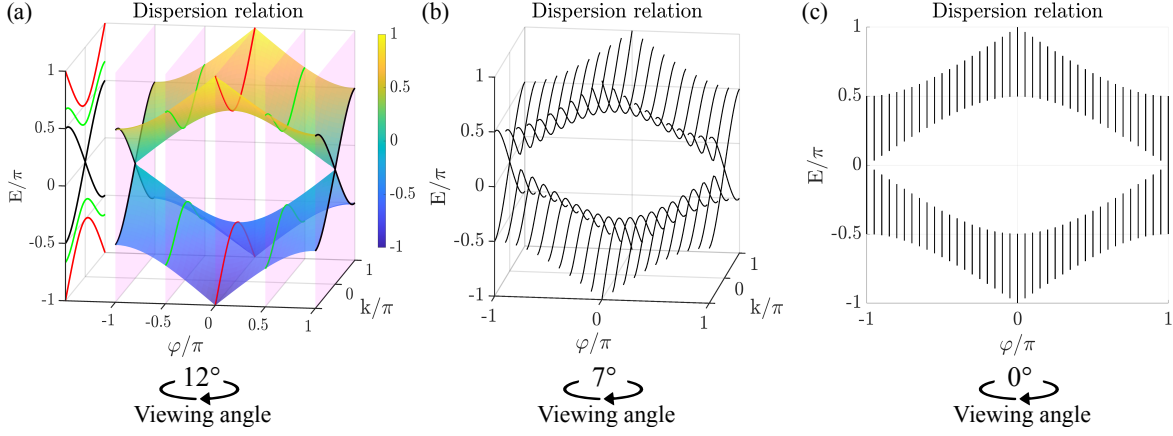


Figure 1.14: 3D view of the two-dimensional analytical dispersion relation of equation. 1.21 for $\varphi \in [-\pi, \pi]$, $\varphi_1 = +\varphi$, $\varphi_2 = -\varphi$ and $\theta_1 = \theta_2 = \pi/4$. (a) Perspective view at a 12° , with slices highlighting specific values of $\varphi(-\pi, -\pi/2, 0, \pi/2, \pi)$ in the (k, E) plane. A projection of these slices is shown on the left. (b)-(c) Perspective views at 7° and 0° angles, respectively.

calculations can be found in Appendix. A. I present the general dispersion relation of the two-step model as a function of φ_1 and φ_2 , irrespective of their opposite signs. This is crucial for the engineering of edge states, as will be discussed in the later chapters.

$$E^\pm(k, \varphi_1, \varphi_2, \theta_1, \theta_2) = \pm \cos^{-1} \left[\cos \theta_2 \cos \theta_1 \cos \left(\frac{\varphi_1 + \varphi_2}{2} - k \right) - \sin \theta_2 \sin \theta_1 \cos \left(\frac{\varphi_1 - \varphi_2}{2} \right) \right] + \frac{\varphi_1 + \varphi_2}{2} \quad (1.21)$$

The evolution of the two-dimensional analytical dispersion relations of equation. 1.21 for $\varphi \in [-\pi, \pi]$, $\varphi_1 = +\varphi$, $\varphi_2 = -\varphi$ and $\theta_1 = \theta_2 = \pi/4$ is illustrated in Fig. 1.14.a in 3D at a viewing angle of 12° with a period of 2π along (E, K, φ) , one of the dimensions displays real space dynamics k , and the other one is a parametric dimension defined by an external phase modulator φ . Specific values $\varphi(-\pi, -\pi/2, 0, \pi/2, \pi)$ are represented by slices through the (k, E) plane. A projection of these slices is shown on the left side of the figure. Figures. 1.14.b-c depict the same dispersion relations from different viewing angles of 7° and 0° , respectively.

1.3.1.1 Phase modulator effect

Figure. 1.15 illustrates numerical simulation of the stroboscopic spatiotemporal diagrams for various φ values in the context of a 50/50 beam splitter ($\theta_1 = \theta_2 = \pi/4$), by employing equations. 1.19 and introducing a narrow pulse into the long ring α at round trip $m = 0$ at site $n = 0$ that satisfies the conditions specified in equation. 1.13. Figures. 1.15.a-c depict the scenarios for $\varphi = 0$, $\varphi = \pi/2$, and $\varphi = \pi$,

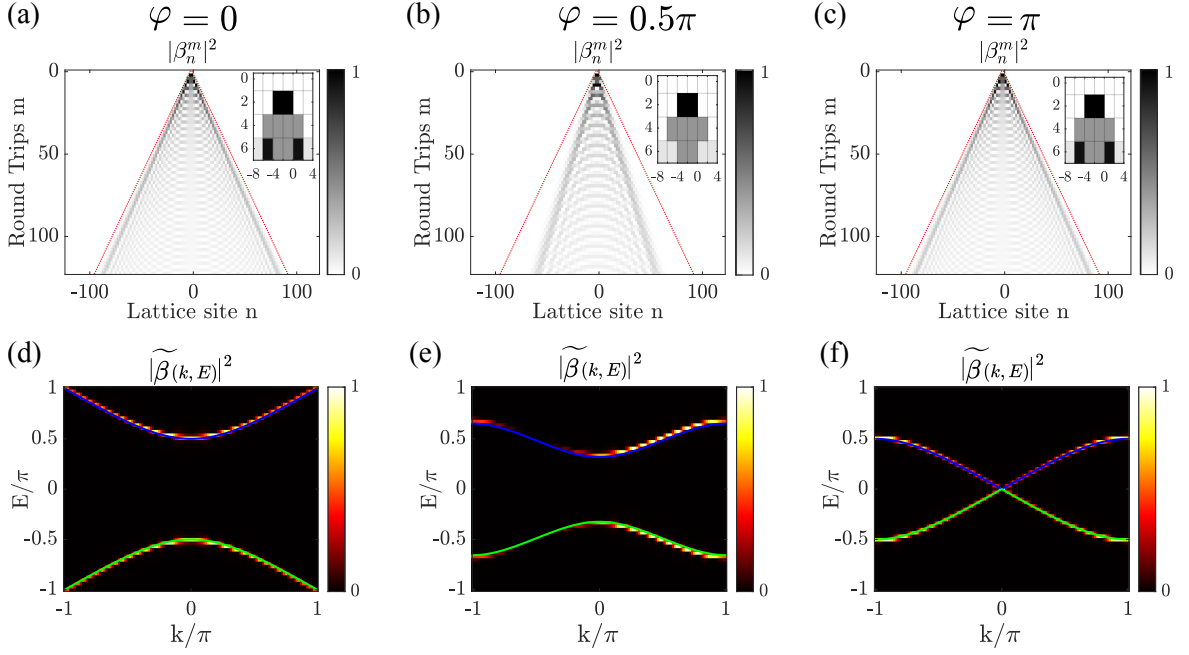


Figure 1.15: (a-c) Numerical simulation depicting stroboscopic spatiotemporal diagrams for phase values of $\varphi(0, \pi/2, \pi)$ for the case of a 50/50 beam splitter. (d-f) Alongside each diagram (a-c), the respective numerical and analytical (blue and green) dispersion relations of equation. 1.21 are presented in the first Floquet Brillouin zone.

respectively. Underneath each diagram, the respective numerical and analytical dispersion relations are also presented in the first Floquet Brillouin zone.

Examining the spatiotemporal diagrams located in the left column of Fig. 1.15, Figure. 1.15.b compares the pulse movement within the short ring when a phase modulation of $\varphi = \pi/2$ is applied versus the $\varphi = 0$ case depicted in Fig. 1.15.a. A noticeable reconfiguration of intensity distribution is seen on the spatiotemporal diagram, as shown in the zoom of Fig. 1.15.a and Fig. 1.15.b. There is a reduction in the spatial dispersion of pulses in the lattice when compared to the red line. The latter signifies the maximum pulse expansion in the pyramid pattern. However, comparing the spatial distribution of the case $\varphi = \pi$ depicted in Fig. 1.15.c to the $\varphi = 0$ scenario, they appear identical.

In the lower row of Fig. 1.15, we can follow the gradual deformation of the bands as the phase modulation parameter φ varies. Notably, the analytical photonic band structure in equation. 1.21 for the upper and lower bands presented in blue and green, respectively, exhibits good agreement with the numerical simulations within the first Brillouin zone. Figure. 1.15.d depicts the band structure within the first Brillouin zone for the previously discussed 50/50 case with $\varphi = 0$ in Section. 1.2.3. Notably, the two photonic bands exhibit a gap centered at energy $E = 0$, signifying the forbidden energy range for light propagation. However, at the Brillouin zone edges ($k = \pm\pi$), the bands become degenerate, implying that

the upper and lower bands coincide at the four corners of the Brillouin zone. Figure 1.15.e highlights that by modulating φ from 0 to $\pi/2$, the two bands no longer exhibit degeneracy at $k = \pm\pi$, thus eliminating any points of contact. As a result, a new forbidden energy band forms around $E = \pm\pi$.

As the phase modulation value increases and reaches $\varphi = \pi$, the two bands gradually approach each other until they intersect at the center of the Brillouin zone ($k = 0$). At this point, the energy gap at $E = 0$ closes, while the gap at $E = \pm\pi$ widens, resembling the Dirac cones commonly found in two-dimensional lattices [124]. Despite the identical intensity distribution in the spatiotemporal diagrams for $\varphi = 0$ and $\varphi = \pi$ shown in Fig. 1.15.a and Fig. 1.15.c, the respective numerical and analytical dispersion relations are different, as illustrated in Fig. 1.15.d and Fig. 1.15.f. The disparity is caused by alternating the additional phase incorporated within the long ring at each time step.

Periodic phase modulation introduces significant alterations to the structure of photonic bands. This technique enables the exploration of novel photonic band configurations and the generation of edge states, as we will discuss later. The phase modulator with periodic modulation $+\varphi$ and $-\varphi$ can be seen as a way of modifying the one-dimensional bands, as illustrated in Fig. 1.15. It can also be seen as a parametric dimension in a two-dimensional model, with a two-dimensional Brillouin zone, as displayed in Fig. 1.14. We will focus our description on this second approach, as it will allow us to explore two-dimensional topological properties.

1.3.1.2 Coupling modulation

Manipulating the coupling angle between two values, θ_1 and θ_2 , and the phase modulator between $+\varphi$ and $-\varphi$ at odd and even steps, give rise to the two-step model topological phase diagram. This diagram features two distinct gapped topological phases with different topological invariants, presented in white and orange, as seen in Figs. 1.16.a-e, that we will characterize later their topological properties. These phases are separated by black lines, which indicate the simultaneous closure of the 0- and π -gaps. This occurs when $\theta_1 \pm \theta_2 = n\pi$, with $n \in \mathbb{Z}$.

In phase I, a red point is pinpointed within the white region for a coupling set of $(\theta_1, \theta_2) = (0.1, 0.4)\pi$, as depicted in Fig. 1.16.a. This coupling configuration corresponds to a two-dimensional analytical dispersion relation $E(k, \varphi)^\pm$ (as a function of φ and k perpendicular to the plane (E, φ)) that reveals two distinct energy gaps centered around $E = 0$ and $E = \pi$ with $\varphi \in [-\pi, \pi]$, as seen in Fig. 1.16.f. By smoothly tuning the coupling parameters until they reach $(\theta_1, \theta_2) = (0.25, 0.25)\pi$ (see Fig. 1.16.c), the two bands start to converge until they intersect. At this point, both the energy gap at $E = 0$ and $E = \pi$ close simultaneously, as depicted in Fig. 1.16.h. Subsequently, the energy gap reopens in the orange phase. As the red dot for a specific coupling set (θ_1, θ_2) deviates further from the black line repres-

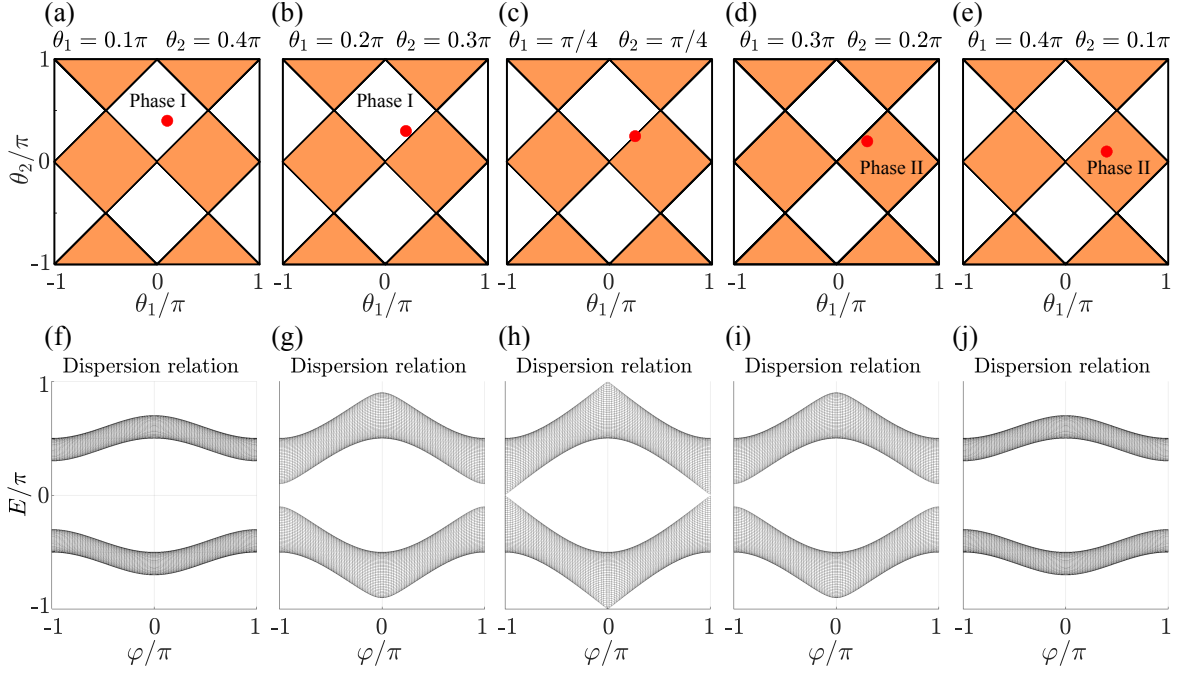


Figure 1.16: (a-e) Two-step model topological phase diagram, showcasing different sets of coupling angles (θ_1, θ_2) . It highlights a topological phase transitions from a gapped topological Phase I (in white) to another distinct Phase II (in orange) by gradually altering the splitting angle. (f-j) The corresponding two-dimensional analytical dispersion relations as a function of φ for each set of the splitting angles (θ_1, θ_2) of panels (a-e). The transition occurs through the closing and reopening of an energy gap.

entering the boundary between the two regions toward phase II, the band structure progressively flattens, leading to an increase in the energy gap, as demonstrated in Fig. 1.16.j.

Analogous to periodic phase modulation, adjusting the coupling parameter of the variable beam splitter modifies the photonic band structure. This method allows for transitions between different topological phases and the creation of edge and interface states, as discussed in later chapters.

1.3.1.3 *Eigenstate of the two-step model*

Our previous work focused on determining the eigenstate of a 50/50 beam splitter without any phase modulator (see Section. 1.2.3), within a one-dimensional discrete step walk system. Now, we aim to expand our exploration to the realm of a two-dimensional synthetic photonic lattice. To do this, we start by comparing the analytic with the numerical result of Fig. 1.17 and Fig. 1.18.

The general normalized eigenvectors formula of the two-step model $|\psi^+(k)\rangle$ and $|\psi^-(k)\rangle$, corresponding to each of the eigenvalues $E^+(k)$ and $E^-(k)$ in equation. 1.21, respectively, are represented by the complex amplitudes $\tilde{\alpha}$ and $\tilde{\beta}$ of the two sublattices in equation. 1.22:

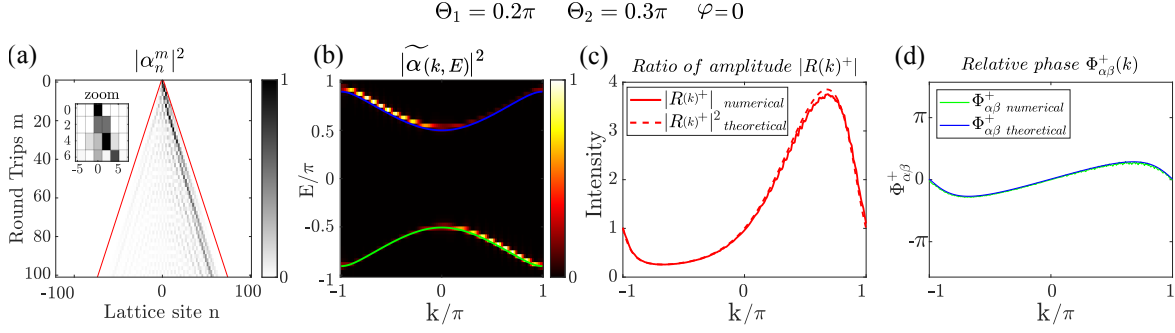


Figure 1.17: (a) Numerical simulation presenting a stroboscopic spatiotemporal diagram when a narrow pulse is introduced into the long loop α for $(\theta_1, \theta_2) = (0.2, 0.3)\pi$ and $\varphi = 0$. The solid red line describes the maximum pulse dispersion when $\theta_1 = \theta_2 = \pi/4$ and $\varphi = 0$. (b) Fourier transformation of panel (a) presenting the numerical and analytical (blue and green) photonic band structure. (c) Analytical and numerical representations of the amplitude ratio $|R|^+$ of the eigenstate corresponding to the upper band in dashed and solid red lines, respectively. (d) Numerical and analytical demonstration of the relative phase $\Phi_{\alpha\beta}^+$, depicted in blue and green, respectively.

$$|\psi^\pm(k)\rangle = \begin{pmatrix} \tilde{\alpha}(k) \\ \tilde{\beta}(k) \end{pmatrix}^\pm = \frac{1}{\sqrt{1 + |R^\pm|^2}} \begin{pmatrix} 1 \\ |R^\pm| e^{i\Phi_{\alpha\beta}^\pm} \end{pmatrix} \quad (1.22)$$

$$R(k)^\pm = |R^\pm| e^{i\Phi_{\alpha\beta}^\pm} = \frac{[e^{iE(k)^\pm} - \cos \theta_2 \cos \theta_1 e^{-ik} e^{i(\varphi_1 + \varphi_2)} + \sin \theta_2 \sin \theta_1 e^{i\varphi_2}]}{[i \cos \theta_2 \sin \theta_1 e^{-ik} e^{i(\varphi_1 + \varphi_2)} + i \sin \theta_2 \cos \theta_1 e^{i\varphi_2}]} \quad (1.23)$$

Figure. 1.17 shows a one-dimensional cut at $\varphi = 0$ represented by the white dashed line in panels (b) and (c) of the two-dimensional tomography of Fig. 1.18 where φ ranges across $[-\pi, \pi]$ for a set of splitting angles $(\theta_1, \theta_2) = (0.2, 0.3)\pi$.

Beginning with the one-dimensional scenario depicted in Fig. 1.17. After introducing a narrow pulse into the system that satisfies the condition of equation. 1.13. Figure. 1.17.a displays a numerical simulation of the stroboscopic spatiotemporal diagram over 100 Floquet even time steps in the long ring α , showing a reduction in the spatial dispersion of pulses in the lattice compared to the red line that describes the maximum dispersion for the case $\theta_1 = \theta_2 = \pi/4$ and $\varphi = 0$. The corresponding analytical photonic band structure, highlighted in green for the lower band and blue for the upper band, shows a strong agreement with the numerical results, as seen in Fig. 1.17.b. Figures. 1.17.c-d demonstrate an excellent match between the numerical and the analytical results for the amplitude ratio $|R|^+$ and the relative phase $\Phi_{\alpha\beta}^+$ of the upper band, respectively. Clearly showing an asymmetrical intensity distribution along the k axis in panel(c) and a phase oscillation in panel (d).

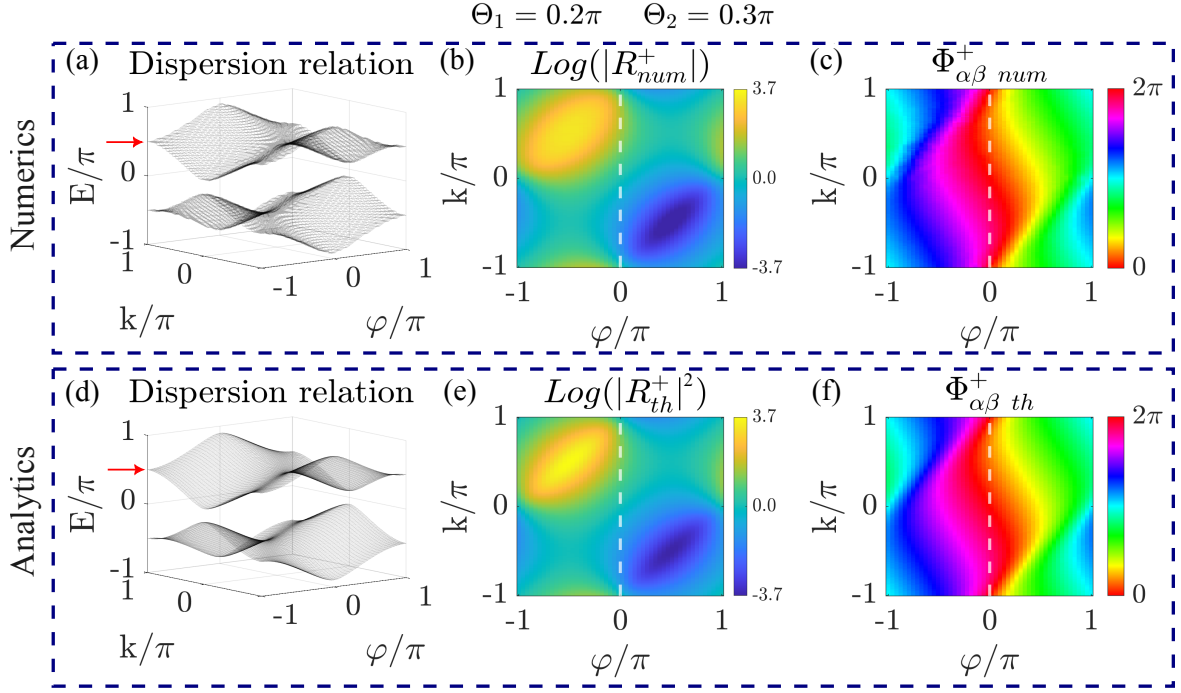


Figure 1.18: Comparison between the numerical simulation and the analytical results of the upper band with $(\theta_1, \theta_2) = (0.2, 0.3)\pi$ and for $\varphi \in [-\pi, \pi]$, represented in the first and second rows, respectively. (a, d) Illustrate the two-dimensional dispersion relation. (b, e) Depict the two-dimensional amplitude ratio. (c, f) Show the two-dimensional relative phase.

Figure 1.18 characterizes the two-dimensional eigenvectors through the amplitude ratio $|R|$ and the phase $\Phi_{\alpha\beta}$. Our numerical and analytical two-dimensional eigenvector results presented in the first and second rows of Fig. 1.18, respectively, align perfectly. The latter is obtained by computing the tomography along φ . This means that for each value of φ in the range of $[-\pi, \pi]$, we extract the eigenvector along k of a specific band (as we did in Fig. 1.17) and store these values in a matrix. The two-dimensional quasienergy bands present two distinct gapped bands in Fig. 1.18.a. The second and third panels in Fig. 1.18.b and Fig. 1.18.c display the tomography of the eigenvectors of the upper band (indicated by a red arrow in Fig. 1.18.a,d) via the ratio of amplitudes $|R|^+$ in log scale and the phase difference $\Phi_{\alpha\beta}^+$ between the two sublattices for each point in the Brillouin zone. The values of $|R|^+$ present a dipole shape, with a high weight in the upper-left corner of the Brillouin zone, and a low weight in the lower-right corner.

Having explored the two-step model in this section, we will now delve into the four-step model, which offers a new phase diagram with richer topological properties.

1.3.2 Four-step model

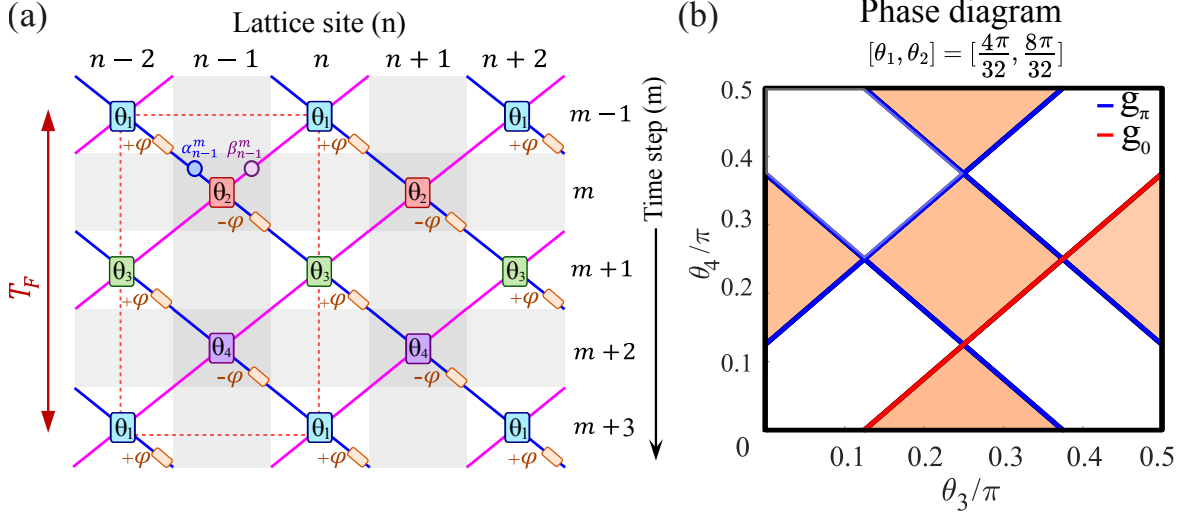


Figure 1.19: Four-step model. (a) Synthetic photonic lattice possesses a double-periodic structure with a spatial period of two sites and a temporal period of four steps. (b) Phase diagram obtained by setting the value of $[\theta_1, \theta_2] = [\frac{4\pi}{32}, \frac{8\pi}{32}]$ while θ_3 and θ_4 in the range of $[0, \pi/2]$. White and orange regions represent different topological phases with trivial and nontrivial Chern numbers, respectively. The energy gap closure at the energy level 0 and π is represented by the red and blue lines, respectively.

Much like the two-step model, the system in the four-step model possesses a double-periodic structure with a spatial period of two sites and a temporal period of four steps, as illustrated by the red dashed unit cell in Fig. 1.19.a. The coupling angle and phase modulator exhibit a cyclic behavior, alternating between four distinct values during one single Floquet period. Each round trip features a unique value, as presented in equation. 1.24, where $m \bmod 4$ gives the remainder of m divided by 4.

$$\varphi_n^m = \begin{cases} \varphi_1 = +\varphi \\ \varphi_2 = -\varphi \\ \varphi_3 = +\varphi \\ \varphi_4 = -\varphi \end{cases} \quad \theta_n^m = \begin{cases} \theta_1 & \forall n \text{ if } m \bmod 4=1 \\ \theta_2 & \forall n \text{ if } m \bmod 4=2 \\ \theta_3 & \forall n \text{ if } m \bmod 4=3 \\ \theta_4 & \forall n \text{ if } m \bmod 4=0 \end{cases} \quad (1.24)$$

Tuning the phase modulator between two values $+\varphi$ and $-\varphi$ during odd and even time steps and setting the coupling parameter $[\theta_1, \theta_2] = [4\pi/32, 8\pi/32]$, while $[\theta_3, \theta_4]$ are kept within the range of $[0, \pi/2]$ as presented in the synthetic photonic lattice in Fig. 1.19.a, allows a unique phase diagram to emerge, featuring distinct gapped topological phases, as shown in Fig. 1.19.b. These phases are shown in white and orange regions, corresponding to trivial and non-trivial Chern numbers, respectively (detailed discussion in Chapter. 6). The boundaries between these re-

gions are marked by red and blue lines, which indicate the closure of the 0-gap and π -gap, respectively. The gaps at energy 0 and π do not necessarily close simultaneously. This behavior contrasts with the two-step model, which demonstrates higher symmetry and features a phase diagram where phases are separated by black lines where both gaps close simultaneously, as shown in Fig. 1.16.b.

1.3.2.1 *Eigenstates and eigenvalues of the four-Step Model*

The Floquet-Bloch ansatz for the four-step model, given by equation. 1.25, encodes both spatial and temporal periodicity in the exponent term. The terms $1/4$ and $1/2$ reflect the time periodicity of four round trips and the spatial periodicity of two site positions, respectively.

$$\begin{pmatrix} \alpha_m^n \\ \beta_m^n \end{pmatrix} = \begin{pmatrix} \tilde{\alpha}(k) \\ \tilde{\beta}(k) \end{pmatrix} e^{i\frac{Em}{4}} e^{i\frac{kn}{2}} \quad (1.25)$$

The lattice system has two sublattices corresponding to the α and β rings (blue and purple circles in Fig. 1.19.a). By expressing the sublattice state in equation. 1.19 after one Floquet period at round trip $(m+4)$ as a function of the sublattice state at time step m and substituting the Floquet-Bloch ansatz presented in equation. 1.25, we arrive at the general formula of the eigenvalues and eigenvectors describing the four-step model, as presented in equations. 1.26, 1.27 and 1.28, respectively. Detailed calculations are given in Appendix. B. To simplify the calculation, we introduce a few abbreviations:

$$\begin{cases} T_m = \cos \theta_m \\ R_m = i \sin \theta_m \end{cases} \quad \begin{cases} \varphi_{ij} = \varphi_i + \varphi_j \\ \varphi_{ijz} = \varphi_i + \varphi_j + \varphi_z \\ \phi = \sum_{i=1}^4 \varphi_i = \varphi_1 + \varphi_2 + \varphi_3 + \varphi_4 \end{cases}$$

$$\begin{aligned} E^\pm(k, \varphi_{1 \rightarrow 4}) = & \pm \cos^{-1} [T_1 T_2 T_3 T_4 \cos\left(2k - \frac{\phi}{2}\right) + R_1 R_2 R_3 R_4 \cos\left(\varphi_{13} - \frac{\phi}{2}\right) \\ & + R_1 R_3 T_2 T_4 \cos\left(\varphi_{12} - \frac{\phi}{2}\right) + R_2 R_4 T_1 T_3 \cos\left(\varphi_{14} - \frac{\phi}{2}\right) \\ & + R_1 R_2 T_3 T_4 \cos\left(\varphi_1 + k - \frac{\phi}{2}\right) + R_2 R_3 T_1 T_4 \cos\left(\varphi_2 + k - \frac{\phi}{2}\right) \\ & + R_3 R_4 T_1 T_2 \cos\left(\varphi_3 + k - \frac{\phi}{2}\right) + R_1 R_4 T_2 T_3 \cos\left(\varphi_4 + k - \frac{\phi}{2}\right)] + \frac{\phi}{2} \end{aligned} \quad (1.26)$$

$$|\psi(k)\rangle^\pm = \begin{pmatrix} \tilde{\alpha}(k) \\ \tilde{\beta}(k) \end{pmatrix}^\pm = \frac{1}{\sqrt{1 + |R^\pm|^2}} \begin{pmatrix} 1 \\ |R^\pm| e^{i\Phi_{\alpha\beta}^\pm} \end{pmatrix} \quad (1.27)$$

$$R(k)^\pm = |R^\pm| e^{i\Phi_{\alpha\beta}^\pm} = \frac{e^{iE(k)^\pm} - A}{B} \quad (1.28)$$

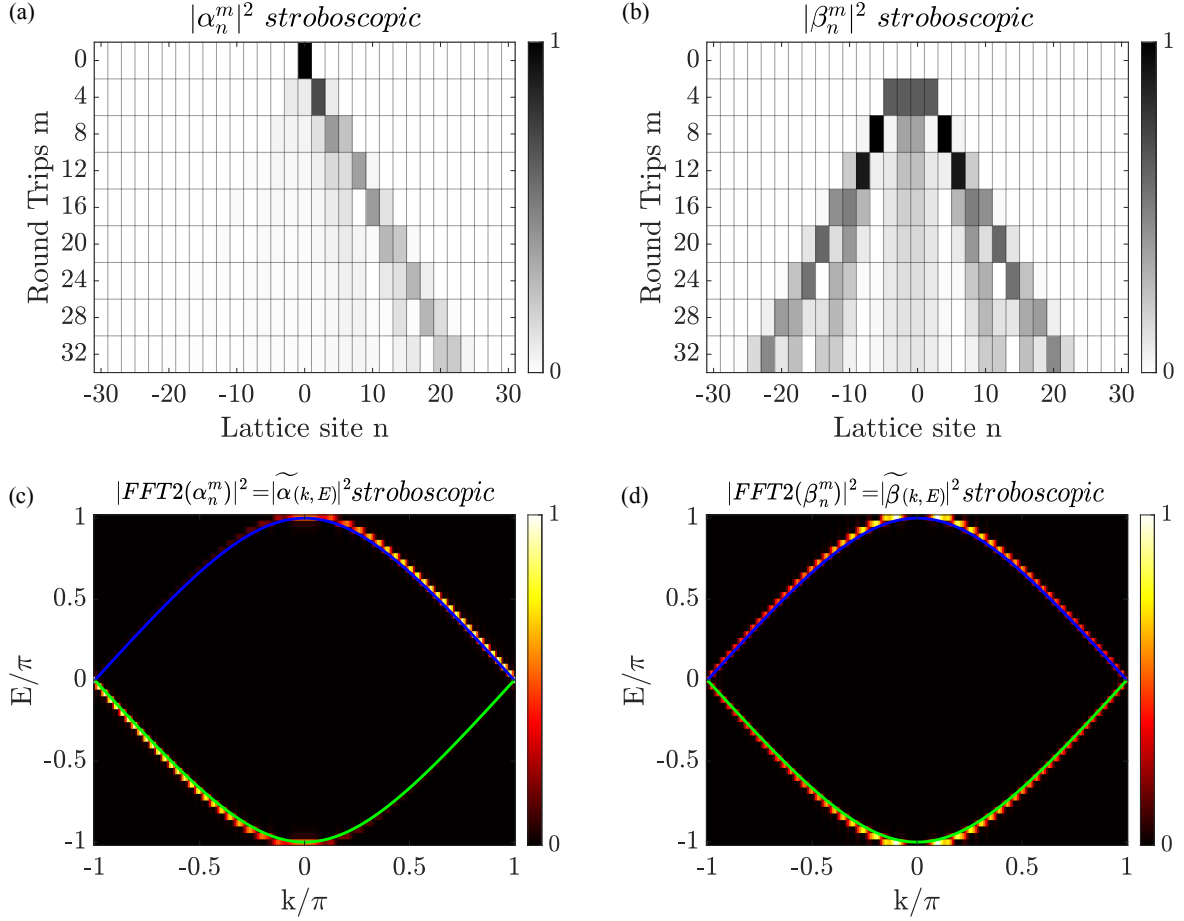


Figure 1.20: (a-b) Numerical simulation showcasing the stroboscopic spatiotemporal diagrams for the rings α and β , respectively, within the 50/50 four-step model when a narrow pulse is introduced in ring α . (c-d) Corresponding dispersion relations of the rings α and β , respectively.

$$\begin{aligned}
 A = & [T_4 T_3 T_2 T_1 e^{i(-2k+\phi)} + T_4 T_3 R_2 R_1 e^{i(-k+\varphi_{234})} + T_4 R_3 T_2 R_1 e^{i\varphi_{34}} + T_4 R_3 R_2 T_1 e^{i(-k+\varphi_{134})} \\
 & + R_4 T_3 T_2 R_1 e^{i(k+\varphi_4)} + R_4 T_3 R_2 T_1 e^{i\varphi_{14}} + R_4 R_3 T_2 T_1 e^{i(-k+\varphi_{124})} + R_4 R_3 R_2 R_1 e^{i\varphi_{24}}]
 \end{aligned} \tag{1.29}$$

$$\begin{aligned}
 B = & [T_4 T_3 T_2 R_1 e^{i(-2k+\phi)} + T_4 T_3 R_2 T_1 e^{i(-k+\varphi_{234})} + T_4 R_3 T_2 T_1 e^{i\varphi_{34}} + T_4 R_3 R_2 R_1 e^{i(-k+\varphi_{134})} \\
 & + R_4 T_3 T_2 T_1 e^{i(k+\varphi_4)} + R_4 T_3 R_2 R_1 e^{i\varphi_{14}} + R_4 R_3 T_2 R_1 e^{i(-k+\varphi_{124})} + R_4 R_3 R_2 T_1 e^{i\varphi_{24}}]
 \end{aligned} \tag{1.30}$$

Using equation. 1.19, Figs. 1.20.a-b presents a numerical simulation of the stroboscopic spatiotemporal dynamics within the four-step model for the rings α and β , respectively, by introducing a narrow pulse that satisfies the conditions specified in the equation. 1.13. The coupling angles are uniformly set to $\theta_1 = \theta_2 = \theta_3 = \theta_4 = \pi/4$, while the phase modulators remain inactive $\varphi_1 = \varphi_2 = \varphi_3 = \varphi_4 = 0$, a situation correspond to the 50/50 case. In this stroboscopic simulation, we retain only even site positions at every second site and even round trips every four turns. Figures. 1.20.c-d showcases the gapless dispersion

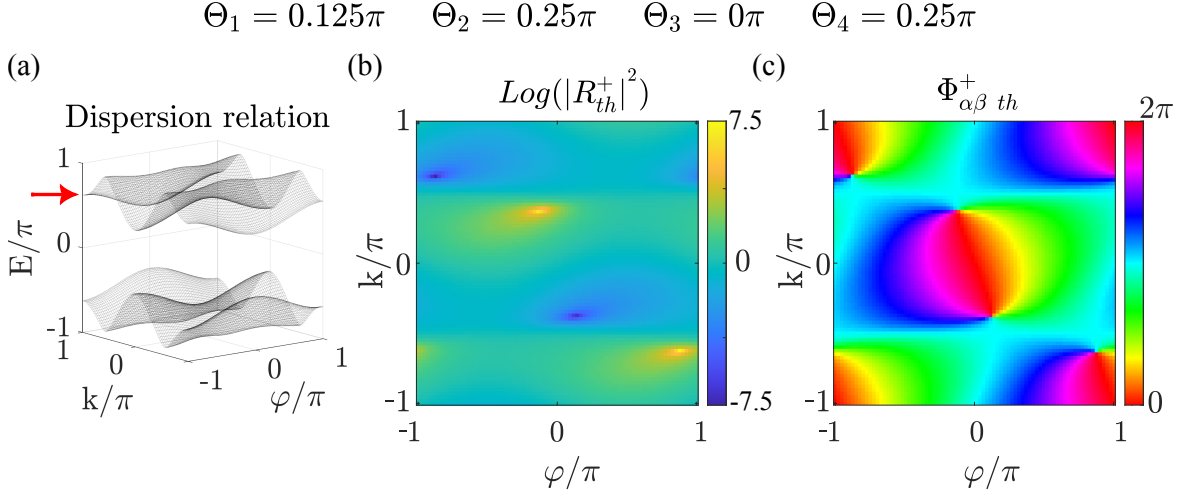


Figure 1.21: Two-dimensional analytical result for $\varphi \in [-\pi, \pi]$ with a coupling angles of $[\theta_1, \theta_2, \theta_3, \theta_4] = [4\pi/32, 8\pi/32, 0, 8\pi/32]$. (a) Two-dimensional Dispersion relation. (b-c) Two-dimensional tomography of the (b) amplitude ratio and (c) relative phase.

relation of the 50/50 case within the four-step model for each of the rings α and β , respectively, obtained by applying a two-dimensional Fourier transform to the stroboscopic spatiotemporal diagrams in Figs. 1.20.a-b. The upper and lower bands coincide at $(E, K) = (0, \pm\pi)$ & $(E, K) = (\pm\pi, 0)$. Additionally, an excellent agreement between the analytical dispersion relation of the upper and lower bands, given by equation. 1.26 and depicted in blue and green, respectively, and their corresponding numerical results.

This chapter primarily emphasizes the 50/50 case for $\theta = \pi/4$ & $\varphi = 0$ in the two- and four-step models, which we refer to as the ‘calibration shot’. This serves as a reference model, providing a benchmark for understanding more complex ‘science shots,’ covered in later chapters.

Following the approach used for the two-step model illustrated in Fig. 1.18, we characterize the four-step model two-dimensional eigenvectors $R^+(k)$ given by equation. 1.28, of the analytical upper band $E(k, \varphi)^+$ denoted by a red arrow in Fig. 1.21.a, via the amplitude ratio $|R|$ and the relative phase $\Phi_{\alpha\beta}$. The phase modulator value $\varphi \in [-\pi, \pi]$ with a set of the splitting angles $[\theta_1, \theta_2, \theta_3, \theta_4] = [4\pi/32, 8\pi/32, 0, 8\pi/32]$, corresponding to a point in the orange region of the phase diagram. The two-dimensional quasienergy bands exhibit two gaps centered at energy 0 & π as shown in Fig. 1.21.a. The second and third panels Fig. 1.21.b and Fig. 1.21.c illustrate the tomography of the upper band’s eigenvectors through the amplitude ratio $|R|^+$ (in logarithmic scale) and the relative phase $\Phi_{\alpha\beta}^+$. $|R|^+$ present two high and low weights amplitude presented in yellow and blue, respectively, corresponding precisely to the positions of the two pairs of vortex-antivortex structures in the relative phase tomography $\Phi_{\alpha\beta}^+$.

Note: One can also characterize the two-dimensional eigenvector of the lower band in the same way, as will be discussed in subsequent chapters.

1.4 Review: Double rings & topological properties

The double ring platform stands out for its efficiency in adding physical elements and applying various modulations, such as gain, loss, and phase modulation, which is challenging to achieve in other experimental platforms [17]. The temporal multiplexing renders our platform periodic in both space and time. It provides an elegant framework for investigating complex phenomena, including the formation of solitons in parity-time symmetric lattices [125, 126], Bloch oscillations [127], anomalous transport [125], artificial gauge fields [128], the non-hermitian skin effect [129], superfluidity [130], nonlinearity [17, 131] and Floquet winding bands [121], and many more. Reflecting on the past, we've seen remarkable work conducted using the double-ring configuration that achieved significant results. It's worth revisiting these accomplishments, as they underline the potential of our setup and its potential for demonstrating certain topological properties.

1.4.1 Berry curvature via anomalous transport

M. Wimmer's research [120] achieved the first complete characterization of the theoretical and experimentally measured Berry curvature, as represented in Figs. 1.22.e-f. This was accomplished by analyzing the anomalous displacement of a coherent classical wavepacket within a two-fiber loop system subjected to a periodic phase modulation φ . In this context, the phase modulator serves as a second parametric dimension with a period of 2π in the two-dimensional dispersion relation, as illustrated in Fig. 1.22.c. The field evolution in the presence of a phase modulator is as follows:

$$\begin{cases} \alpha_n^{m+1} = \frac{1}{\sqrt{2}} (\alpha_{n-1}^m + i\beta_{n-1}^m) e^{i\varphi(m)} \\ \beta_n^{m+1} = \frac{1}{\sqrt{2}} (i\alpha_{n+1}^m + \beta_{n+1}^m) \end{cases} \quad (1.31)$$

To achieve this, a designed Gaussian envelope with the correct phase information is injected into the system to locally excite a superposition of states within the j th band structure at specific values of k , as depicted by the orange and yellow dots in Fig. 1.22.c. Next the magnitude of the phase modulator is slowly tuned from $0 \rightleftharpoons 2\pi$. First, by a gradual phase ramp increase of $+\varphi_0 = +0.01\pi$ from $0 \rightarrow 2\pi$ followed by a reversal decrease of $-\varphi_0 = -0.01\pi$ from $2\pi \rightarrow 0$ over 200 round trips, as illustrated in green and red arrows in Fig. 1.22.a and Fig. 1.22.b, respectively. Figures. 1.22.a-b describes the propagation of wavepackets, along the

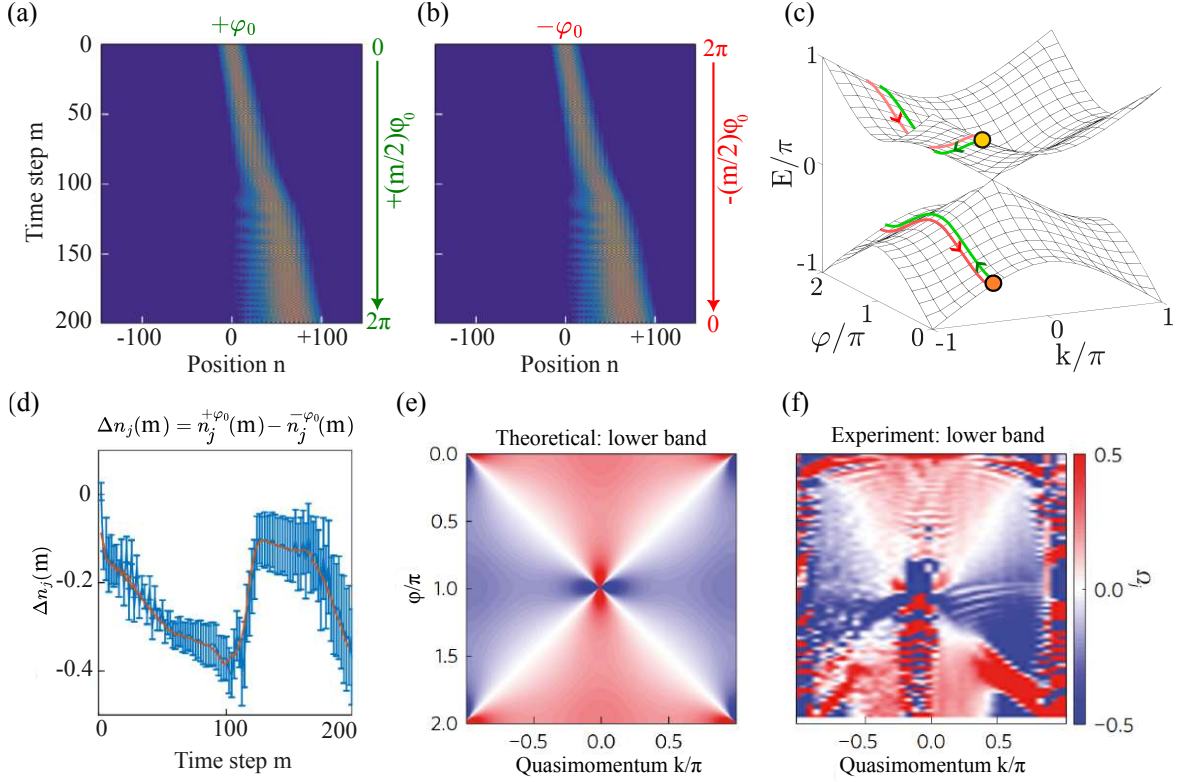


Figure 1.22: (a)-(b) Wavepacket propagation measurement in real space when exiting a superposition of states in the j th band at $k = -0.5\pi$ and $\varphi_0 = 0.01\pi$ with gradual ramping of the phase modulation over 200 round trips m . (a) Gradual increase of the phase from $0 \rightarrow 2\pi$, shown by the green arrow. (b) Gradual decrease of the phase from $2\pi \rightarrow 0$, depicted by the red arrow. (c) In a two-dimensional dispersion relation, one of the dimensions displays real space dynamics k , and the other one is a parametric dimension defined by an external phase modulator φ , the green (red) line traces a gradual ramp from $0 \leftrightarrow 2\pi$ along the φ direction, originating from a superposition of excited states at $k = -\pi/2$ and $\varphi_0 = 0.01\pi$, as represented by the yellow (orange) dots. (d) Discrete differentiation of the lateral shift in the center-of-mass of the wave packet's propagation along the position n as a function of the time steps m . Comparison of the Berry curvature of the lower band in (e) theoretical results with (f) the experimental results. [120]

one-dimensional lattice. During this process, the sign of the phase modulation alternates between $+\varphi$ and $-\varphi$ during odd and even time steps, such that:

$$\varphi(m) = \begin{cases} +\varphi(m) = +m \cdot 0.01\pi & \text{if } m \text{ is odd} \\ -\varphi(m) = -m \cdot 0.01\pi & \text{if } m \text{ is even} \end{cases} \quad (1.32)$$

The anomalous velocity depicted in Fig. 1.22.d is determined by computing a discrete differentiation of the lateral shift in the center-of-mass of the Gaussian

envelope in real space. This shift $\Delta n(m) = n^{\varphi_0}(m) - n^{-\varphi_0}(m)$ is calculated along the position n as a function of the time steps m of the wavepackets propagation.

After extracting the anomalous displacement for a locally excited state along the k -direction, this process is repeated for all relevant states to reconstruct the Berry curvature piece-by-piece. Subsequently, the Chern number can be obtained by integrating the Berry curvature over the entire Brillouin zone.

One of the primary objectives of this thesis is to analyze and measure topological invariants such as the Berry curvature, Chern number, and winding number. Experimentally, this is accomplished by measuring the eigenstate and the dispersion relation using a heterodyne method within a single-shot measurement. This method, developed in my thesis and in the work of C. Lechevalier [17, 118], is completely different from that of M. Wimmer. Detailed explanations will be provided in the Chapter. 2 and Chapter. 3.

1.4.2 Stability of edge states in nonlinear regime

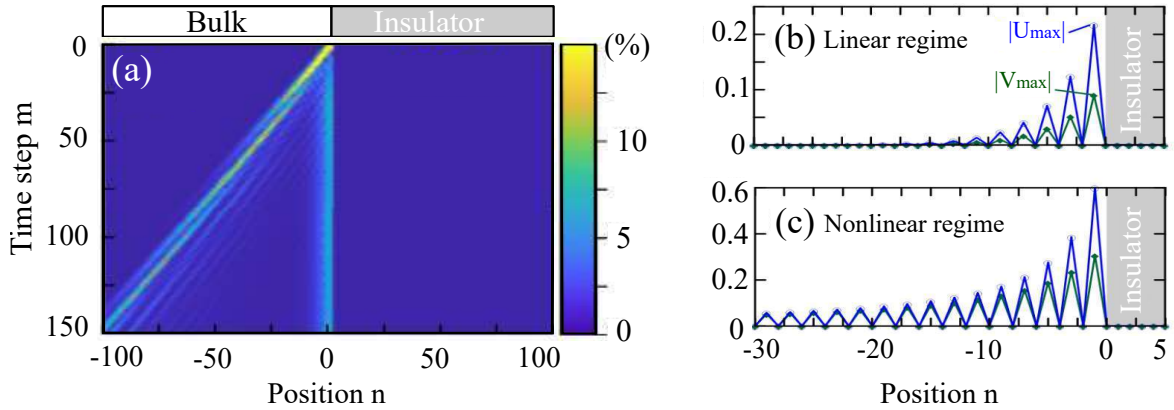


Figure 1.23: (a) Numerical simulation displays chiral edge states when a narrow pulse is introduced at the boundary of two distinct phases. (b)-(c) Profile of the edge mode's amplitude in (b) linear and (c) nonlinear regime. [14]

An intriguing study was undertaken by A. Bisianov and his team [14] in 2019. They explored the persistence of topological chiral edge states within a one-dimensional discrete quantum walk, specifically in the context of Kerr nonlinearity. This is achieved by using loops with long lengths and injecting high powers. The field evolution in the presence of nonlinearity is as follows:

$$\begin{cases} \beta_n^{m+1} = (t_{n+1}^m \beta_{n+1}^m + i r_{n+1}^m \alpha_{n+1}^m) e^{ik |t_{n+1}^m \beta_{n+1}^m + i r_{n+1}^m \alpha_{n+1}^m|^2} \\ \alpha_n^{m+1} = (t_{n-1}^m \alpha_{n-1}^m + i r_{n-1}^m \beta_{n-1}^m) e^{ik |t_{n-1}^m \alpha_{n-1}^m + i r_{n-1}^m \beta_{n-1}^m|^2} \end{cases} \quad (1.33)$$

Where $t_n^m = \cos(\theta)$ and $r_n^m = i \sin(\theta)$ represent the transmitted and the reflected pulse energy, θ is the coupling angle of the variable beam splitter and κ is the effective nonlinear coefficient of the dispersion compensating fibers.

In their study, they realized an insulator that blocks light within a certain frequency by adjusting the splitting angle to full reflectance ($t/r = 0/1$) at a specific site n_{edge} . A narrow pulse injection at the interface reveals persistent edge states in the linear regime, see Fig. 1.23.a. The power of localized edge modes in the linear regime at a given time step (m) is predominantly concentrated in the (α or β) ring, signifying the state's chirality, as demonstrated in Fig. 1.23.b. However, instability and radiation into the bulk modes occur in strongly nonlinear regimes, as depicted in Fig. 1.23.c.

1.4.3 Observation of the non-Hermitian skin effect

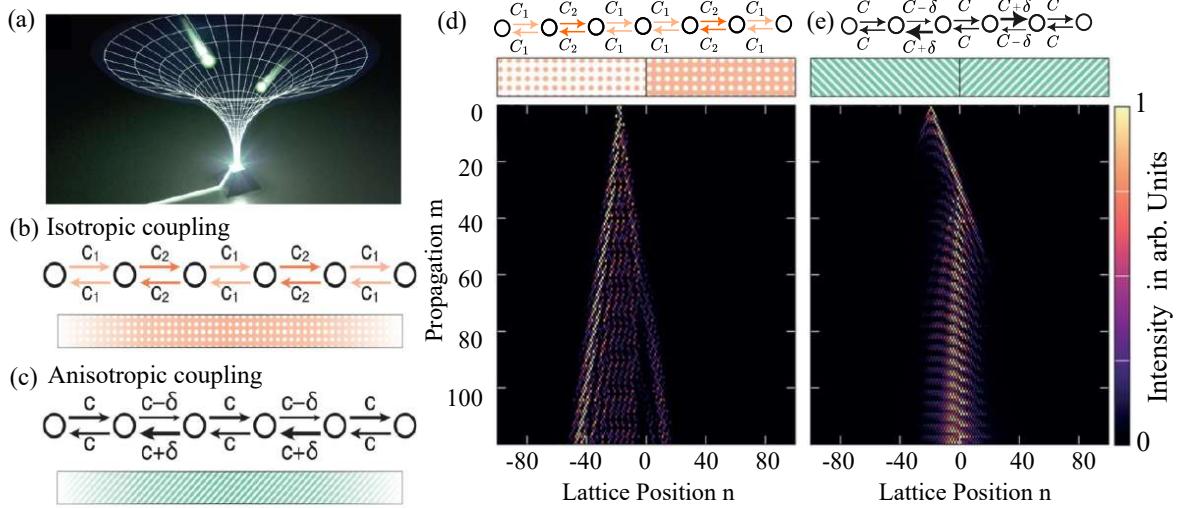


Figure 1.24: (a) Light funneling concept. (b) A linear sequence of linked states with alternating isotropic coupling C_1 and C_2 i.e. the coupling strengths from one site to its neighbor in a certain direction are identical to those in the reverse direction, the variations in the coupling strength are symbolized by the dotted orange ribbon. (c) A linear sequence of linked states that features alternating anisotropic coupling i.e. unequal coupling strengths back and forth from one site to its neighbor site, The ribbon with green stripes describes the anisotropic modulation. (d) One mode localization at the interface when two opposing isotropic lattices are connected, the inverted ribbon represents the reversed coupling angle. (e) All eigenmodes are confined to the interface when attaching two opposite anisotropic lattices.[129]

In the year 2020, A. Szameit et al. showcased a funnel for light [129] as illustrated in Fig. 1.24.a, a phenomenon called the "Non-Hermitian skin effect" where all eigenmodes localize at an interface [132, 133]. Thus, any light field in the lattice regardless of its form and injection position is driven towards the interface. They

achieved this by specifically engineering an anisotropic coupling between the two rings. The system dynamics is described by the following equations:

$$\begin{cases} \beta_n^{m+1} = G[\cos(\theta)\beta_n^{m+1} + i \sin(\theta)\alpha_{m+1}^n]e^{i\varphi} \\ \alpha_{m+1}^n = G[i \sin(\theta)\beta_m^{n-1} + \cos(\theta)\alpha_n^{m-1}]. \end{cases} \quad (1.34)$$

Where θ denotes the splitting angle of the coupler and G describes the attenuation and amplification.

In their research, they compare two models. First, the Hermitian Su-Schrieffer-Heeger (SSH) model [134, 135] which consists of a linear sequence of linked states with alternating isotropic coupling i.e. the coupling strengths C_1 or C_2 from one site to its adjacent one in a certain direction are identical to those in the reverse direction, as depicted in Fig. 1.24.b. An interface is introduced by flipping the splitting angle at a specific site, as depicted by the inverted ribbon in Fig. 1.24.d. Consequently, only one state becomes localized at the interface.

Secondly, the skin effect model features alternating anisotropic coupling, i.e. unequal coupling strengths back and forth from one site to its neighbor site as represented in Fig. 1.24.c. To achieve anisotropic hopping in the system, an amplification-attenuation modulation is implemented before and after the fiber coupler by using an acoustic-optical modulator (AOM), the system exhibits differential loop gain, with one loop amplifying and the other attenuating the signal. Introducing an interface within the system is achieved by reversing the anisotropy at a specific location and flipping the amplification and attenuation. This modification drives all eigenmodes towards the interface, leading to their complete confinement there (see Fig. 1.24.e). Consequently, all previously delocalized bulk modes become localized at the interface, transforming into boundary modes.

These works show, that our double-ring platform conceals a multitude of intriguing topological properties and features. These can be manipulated by adjusting external parameters such as gain, loss, and phase modulation. In the realm of Floquet topological phases, experiments have been conducted in one-dimensional chiral symmetric lattices [11–14] or two-dimensional lattices with continuous time evolution [15, 16]. However, the exploration of anomalous topological phases in a two-dimensional discrete step walk remains uncharted territory. This presents the central problem that our thesis aims to address

1.5 Conclusion

In this chapter, after reviewing the related literature, we pose the following questions that will serve as the objectives of our thesis:

What are the topological properties of a two-dimensional discrete step walk system?

To answer this, our methodology involves utilizing temporal multiplexing of two coupled optical fiber loops of unequal lengths. Our platform is a synthetic photonic lattice in two dimensions, characterized by discrete step walks. One dimension displays real space dynamics, while the external phase applied to the longer ring defines the other. The evolution of light pulses within this model is defined by two mathematical discrete coupled equations. The time multiplexing of light gives our platform a periodic nature in both space and time. This is perfect for studying the eigenstate and constructing the band structure, which is achieved through a two-dimensional Fourier transform of the stroboscopic spatiotemporal diagram of the system's impulse response.

Finally, we have introduced the two-step and four-step models, which exhibit distinct topological properties. These models serve as the foundation for our thesis, for investigating of anomalous and trivial topological phase properties in our two-dimensional synthetic photonic lattice under Floquet-driven discrete step walks.

EXPERIMENTAL SETUP

Building upon the work of former PhD student Corentin Lechevalier [118], the former postdoctoral researcher Albert Adiyatullin automated and upgraded the double ring experimental setup, significantly enhancing its robustness and stability against fluctuations [121].

Chapter. 2 details this experimental setup developed by A. Adiyatullin, depicted in Fig. 2.1, for creating the photonic lattice. It outlines the roles of each component, their specific lengths, and relevant timescales. The experimental setup comprises two main sections: the optical section, illustrated in Fig. 2.1.b, and the electronic section, shown in Fig. 2.1.a, which we will examine in detail.

2.1 Overview of the optical setup

The optical section, shown in Fig. 2.1.b, consists of two fiber rings, α and β , outlined in a black dashed rectangle, and a local oscillator enclosed in an orange dashed rectangle, enabling access to spectral information via a heterodyne method.

2.1.1 Double ring configuration

The experiment utilizes a continuous wave (CW) single-frequency laser source (Koheras MIKRO, NKT Photonics) that operates at a wavelength of 1550 nm with a maximum power of 16 dBm (40 mW). The line width of the laser is < 0.1 kHz which estimates a coherence length ≈ 3000 kilometers (km) in the vacuum (according to the manufacturer). Upon passing through the 50/50 beam splitter, the laser output splits into two equal fields with identical amplitudes, as depicted in Fig. 2.1.b. One continuous part is directed toward the local oscillator, while the other part is chopped into narrow pulses of duration $\tau = 1.4$ ns using an electro-optical modulator (EOM, iXblue MXER-LN-10), which is controlled by an arbitrary waveform generator (AWG 7000B, Tektronix) with a bandwidth of 25 GHz. The EOM has a bandwidth of 10 GHz and an extinction ratio of ≈ 30 dB that suppresses the light for some duration of time ≈ 1 ms.

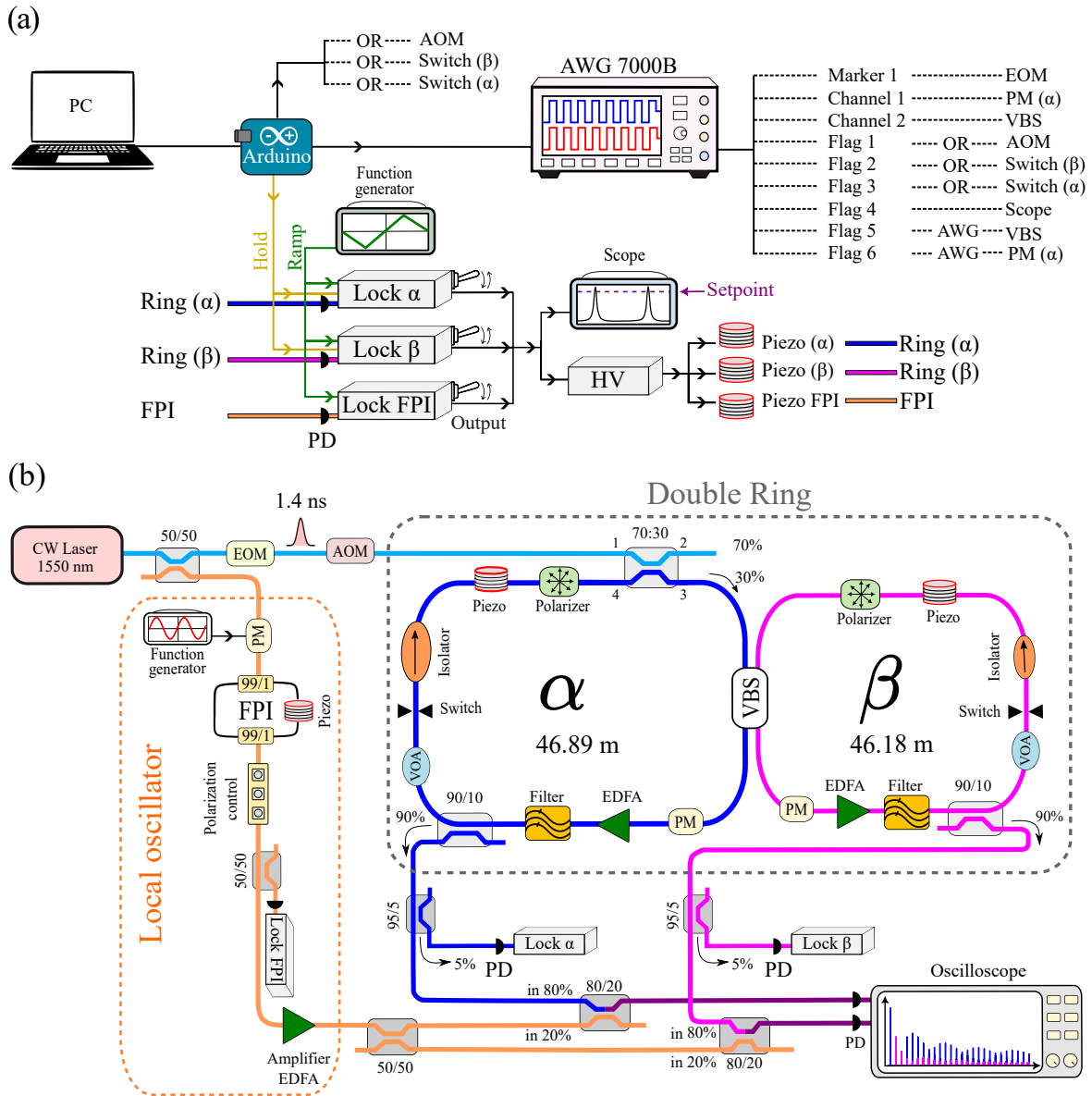


Figure 2.1: The experimental setup includes an electronic section and an optical section. (a) The electronic section consists primarily of a computer (PC), an Arduino, and an arbitrary waveform generator (AWG 7000B), these components facilitate the triggering and control of the elements within the setup by generating precise waveforms. (b) The optical section consists of two primary parts, the first part, situated on the left and colored orange, represents the local oscillator. The second part is the double ring configuration α and β of unequal length presented in blue and pink, respectively, coupled via a variable beam splitter (VBS). Some abbreviations of the components: acoustic optics modulator (AOM), electro-optic modulator (EOM), erbium-doped fiber amplifier (EDFA), variable optical attenuators (VOA), Fabry-Perot Interferometer (FPI), phase modulator (PM).

To further suppress residual transmission and eliminate low-frequency components in the off state of the EOM, we introduced an acoustic optical modulator (AOM, AA Opto-electronic MT110-IIR30-Fio-PM0.5) that shifts the laser frequency by 110 MHz. This frequency shift effectively reduced the residual transmission of the transmission gate to -70 dB, which is precisely centered in time at the shaped by the preceding EOM.

The prepared injection signal is introduced into the long α ring via a 70/30 beamsplitter. The latter includes two input paths (1 & 4) and two output paths (2 & 3) optical fibers, as shown in Fig. 2.1.b. When the light enters via Path 1, 30% of its optical power transmits to Path 3 and 70% to Path 2. Conversely, entering via Path 2 reverses these percentages: 30% of the optical power from Path 4 goes to Path 2, while 70% goes to Path 3.

The short square pulse evolves through the optical components in the rings, following a split step walk each time it reaches the beamsplitter. The two fiber rings α and β are coupled via a high-bandwidth 40 GHz electronically controlled variable beamsplitter (EOSpace AX-2x2-0MSS-20). On each round trip, the 90/10 beam splitter within each ring transmits the majority of light toward the measurement. Yet alone, this is insufficient to obtain the band structure experimentally. Accessing both amplitude and phase information for each of the sublattice α_n^m and β_n^m is essential. This is achieved through a heterodyne measurement: a coherent beating between the extracted shifted wavefield of the double rings, and the narrow bandwidth of the local oscillator's reference field that is shifted by 3 GHz from the laser frequency.

The optical beating signal between the output of the coupled ring configuration and the local oscillator is converted into electrical signals using a fast photodiode (Thorlabs DET08CFC), which operates at 5 GHz, connected to a fast oscilloscope (Tektronix MSO64). This oscilloscope features a 6 GHz bandwidth, a 10-bit vertical resolution providing 2^{10} discrete amplitude levels, a sampling rate of 25 GS/s, which translates to a time interval of 40 ps between two points, and a memory record length of 62.5 Mpts corresponding to 2.5 ms, enabling very detailed signal analysis of the beating.

2.1.1.1 Component role within the double ring

The two identical 1550 nm polarization-maintaining (PM) optical fiber monomode rings, denoted as α and β , consist of identical components organized in the following sequence:

- Electro-optic phase modulator (PM, iXblue MPZ-LN-01) with a 3 GHz bandwidth applies phase modulation to generate the second parametric dimension and investigate topological properties, as elaborated further in Chapter. 4

- Erbium-doped fiber amplifier (EDFA, Keopsys CEFA-C-HG) provides up to 50 dB gain to amplify very weak optical signals of -50 dBm and compensate for the extraction, and absorption losses allowing the circulation of pulses for many round trips in the optical system.
- Tunable wavelength optical filter (EXFO XTM-50) with adjustable bandwidth from 32 pm to 5 nm (According to the manufacturer) to efficiently eliminate spectrum components caused by the EDFA spontaneous emission. The filter introduces significant losses of -5 dB once the filter's central wavelength is set to 1550 nm.
- 90/10 beam splitter from Absys divides the light into two paths: 90% of the light is transmitted towards the measurement, while the remaining 10% continues within the loop. This extraction causes significant losses of -10 dB.
- Manual optical variable attenuator (VOA, Agiltron) to fine-tune the loss rate in each ring up to -30 dB.
- Optical switch (Agiltron, Photonwares NSSW) with an extinction ratio of -20 dB is activated to effectively eliminate residual light signals within each ring between calibrations and scientific measurements, allowing fresh starts for each experiment (as detailed further ahead).
- Isolator from Anylink to ensure the light circulation in one direction.
- Piezoelectric device from PI France to stabilize the ring length against fluctuations, ensuring consistent optical path lengths within the system.
- Polarizer from Thorlab to maintain a consistent polarization state within the optical fiber.

Note: The order of the components is critical. For example, positioning the phase modulator (PM) after the 90/10 beam splitter modifies the phase of the pulses and the evolution equation. 1.19 within the lattice (see Appendix. C).

Each ring has a variety of optical elements with strong extinction powers to either effectively eliminate undesired optical noise or measure the signal. Most of the loss is attributed to the extraction of light through the beam splitter. However, the signal losses that occur during each round trip can be easily compensated for by our EDFA amplifiers, allowing the optical signal to travel over multiple cycles.

Mechanical vibrations, temperature changes, and pressure variations can affect the length of the optical fibers in a setup [136]. To minimize these effects, many components of the double ring are enclosed in a foamed box, placed on a hydraulic table, and kept in an air-conditioned room. However, the key component for ensuring perfect stabilization of the ring length is the piezoelectric device (as detailed in the next section).

Notably, for optimal performance, the ring configuration exclusively utilizes single-mode polarization-maintaining components to guarantee that the waves propagate through the fiber in a linearly polarized state the entire time. Furthermore, all the components are equipped with FC/APC (Fixed Connection-Angled Physical Contact) connectors to ensure secure and stable connections while preventing back reflection of light.

2.1.1.2 *Time and length scale*

Despite their similarities, the long ring α with a length $L_\alpha = 46.89 \text{ m}$ exceeds the shorter ring β with a length of $L_\beta = 46.18 \text{ m}$ by a length difference of $\Delta L = 0.71 \text{ m}$. The latter allows the encoding of the lattice position information at the time of arrival of pulses at the extraction port at each round trip, as described in Section 1.2.2. Additionally, the phase modulator (PM) in the shorter ring will always remain inactive; its presence is solely to maintain an equal amount of loss in both rings.

In the temporal domain, a short pulse takes $T_\beta = 223.24 \text{ ns}$ to travel through the shorter ring, while it takes $T_\alpha = 226.64 \text{ ns}$ to traverse the longer ring. To accurately study optical signal propagation through spatiotemporal representation, two main time intervals should be taken into consideration. First, the time difference between the two pathways, this difference is calculated as $\Delta T = T_\alpha - T_\beta$ and is equal to 3.4 ns. Secondly, the average round-trip travel time within the loops, denoted by \bar{T} , is obtained by averaging T_α and T_β , $\bar{T} = (T_\alpha + T_\beta)/2 = 224.94 \text{ ns}$. The conversion between the two dimensions (time and space) is $l = ct/n$, with $c = 3 \times 10^8 \text{ m/s}$ being the speed of light and $n = 1.45$ the index of reflection of the optical fiber at a wavelength of 1550 nm [137]. Table 2.1 provides a comprehensive overview of the temporal and spatial characteristics of the double-ring configuration.

Upon reaching the beamsplitter every roundtrip, the injected pulse proceeds in a split-step walk, generating two new pulses separated in time by a distance ΔT . From turn to turn, the cycle continues, generating more equally spaced pulses that fill the ring. Eventually, the ring will be completely filled with these pulses after a maximum number of round trips $m_{max} = \bar{T}/\Delta T = 66$ which corresponds to a total traveling duration of 14.85 μs and a distance of $\approx 3 \text{ km}$. The maximum number of excited sites before the pulses start to overlap is, $n_{max} = \bar{T}/(\Delta T/2) = 132$ with $\Delta T/2 = 1.7 \text{ ns}$ being the duration of a single site.

	α	β	Mean	Difference
<i>Time(ns)</i>	$T_\alpha = 226.64$	$T_\beta = 223.24$	$\bar{T} = 224.94$	$\Delta T = 3.4$
<i>Length(m)</i>	$L_\alpha = 46.89$	$L_\beta = 46.18$	$\bar{L} = 46.53$	$\Delta L = 0.71$

Table 2.1: Time and length scale within the double ring configuration.

Polarization-maintaining components ensure that the light's polarization state remains stable throughout the experiment. Additionally, the selected ring lengths ensure that the temporal coherence length of the local oscillator is greater than the distance traveled by the pulses throughout the entire experiment within the coupled loop system. These two conditions maximize and maintain the stability of the beating contrast over many cycles in our experiment [118], as we will see in Section. 3.1.

2.1.2 Local oscillator

A portion of the monochromatic continuous laser source is directed to the local oscillator after passing through a 50/50 beam splitter. The local oscillator is a continuous wave beam that will be mixed with the light coming out of the rings to extract the relative phase between the different pulses in the spatiotemporal dynamics. To do so, as we will explain in detail in the next chapter, the local oscillator needs to have a carrier frequency slightly shifted from the carrier frequency of the pulses in the rings. In our experiments, this shift in the frequency corresponds to 3 GHz. When the local oscillator interferes with the signal coming out of the rings, a beating intensity can be observed in the detected signal. From the beats, the relative phase of the light field between the pulses can be measured.

To engineer the local oscillator field, we use the following elements (see orange dashed rectangle in Fig. 2.1.b):

- Electro-optic phase modulator (PM, iXblue MPZ-LN-10) with a 10 GHz bandwidth, modulated with a sinusoidal electrical signal at a frequency of $\Omega = 3$ GHz with an amplitude of 5 dBm from an Agilent E4421B frequency generator. This process creates sidebands in the optical spectrum shifted by $\pm\Omega$ (i.e., ± 3 GHz) from the laser carrier frequency W .

For example, consider a continuous laser field with an amplitude $V(t)$ and a frequency W , where the phase is modulated over time by the phase modulator (PM) as follows:

$$\begin{cases} V(t) = V_0 \sin[Wt + \phi(t)] \\ \phi(t) = m \sin(\Omega t) \end{cases} \quad (2.1)$$

where $\phi(t)$ is the applied phase, m the phase modulation index, Ω the angular frequency of the modulating signal and V_0 represents the amplitude. equation. 2.1 can be decomposed into a Bessel function [138].

$$V(t) = V_0 \sum_{n=-\infty}^{+\infty} J_n(m) \sin[(W + n\Omega)t] \quad (2.2)$$

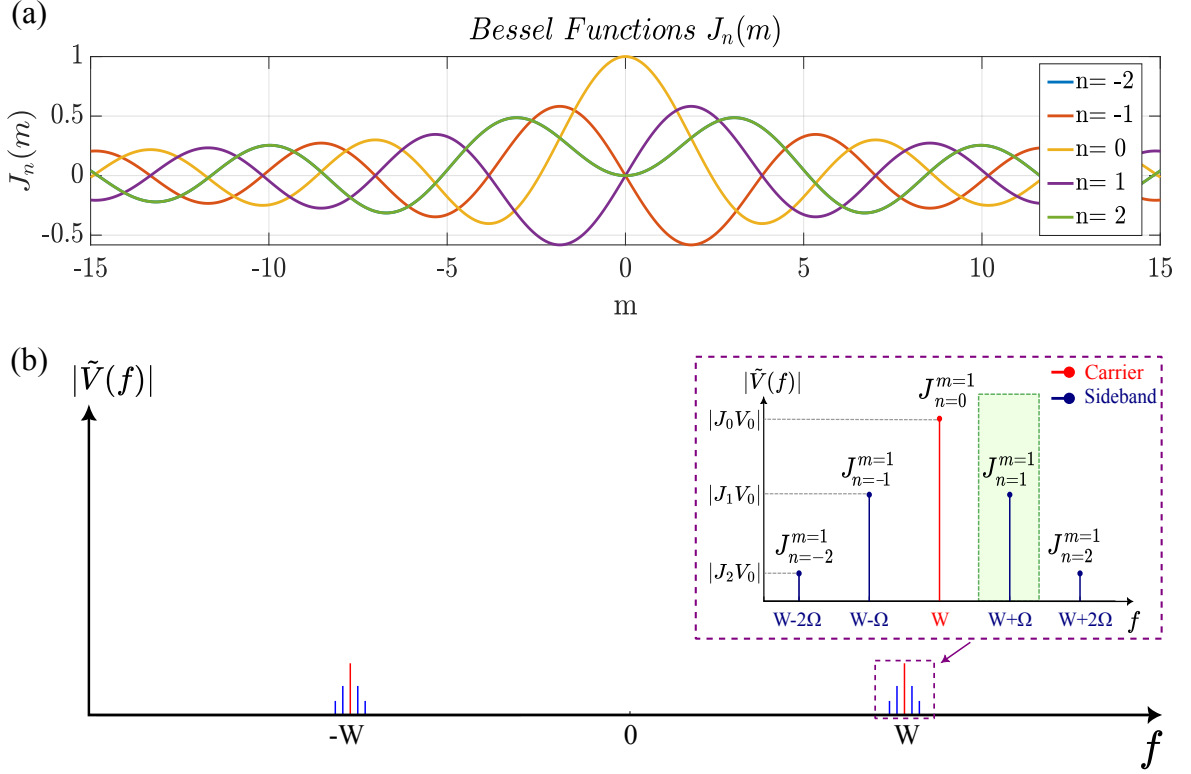


Figure 2.2: (a) Bessel function $J_n(m)$ for orders $n \in [-2:2]$. (b) The optical spectrum $|\tilde{V}(f)|$ of a phase-modulated signal with a modulation index $m = 1$ features an infinite number of symmetrical spectral components (blue sidebands) at frequencies $W \pm n\Omega$, centered around the carrier frequency W (red). The green area indicates the filtered-out sideband at the frequency $W + \Omega$.

The Bessel function $J_n(m)$, as a function of m , and order n is represented in Fig. 2.2.a and given by equation.2.3:

$$\left\{ \begin{array}{l} J_n(m) = \sum_{k=0}^{\infty} \frac{(-1)^k}{k!(n+k)!} \left(\frac{m}{2}\right)^{2k+n} \\ J_{-n} = (-1)^n J_n \\ \sum_{n=-\infty}^{\infty} |J_n(m)|^2 = 1 \end{array} \right. \quad (2.3)$$

The optical spectrum $|\tilde{V}(f)|$ of a phase-modulated signal $V(t)$ produces two sets of lines in the frequency domain, centered at positive and negative frequencies $\pm W$. Each set comprises an infinite series of symmetrically distributed spectral components (sidebands) at a frequency $W \pm n\Omega$ arranged around the carrier frequency (W), these sidebands occupy a specific position with equal weight for a given order n , as illustrated in the purple dashed square of Fig. 2.2.b when the modulation index $m = 1$. We focus exclusively on the first-order spectral components $n = 1$ (where $\Omega = 3$ GHz) since our goal is to design a local oscillator with a frequency shifted by 3 GHz from the original laser.

- A custom single-mode fiber-optic ring cavity interferometer, constructed with a pair of high-reflectance 99/1 beam splitters and a piezoelectric device, acts as a tunable spectral filter. Operating on the Fabry-Perot interferometer (FPI) principle [139], it selectively filters a specific sideband at a specific frequency $W + \Omega$ in the optical spectrum, as depicted by the green rectangle in Fig. 2.2.b.
- Polarization Controller: enables precise adjustment and control of the polarization state of light traveling through it by manually rotating the polarization axes of the polarization-maintaining fiber (PMF). This is necessary because the optical elements in the local oscillator section of the setup do not maintain polarization, and the fiber used is a non-polarization maintaining single-mode fiber.
- Lockbox FPI: the filtered-out light field used as a local oscillator, passes through a 50/50 beam splitter. Half of this light is directed toward a lockbox. This lockbox maintains the stability of the FPI ring cavity by continuously monitoring the output signal. It automatically adjusts the voltage sent to the piezoelectric device, which slightly stretches or relaxes the fiber. This continuous feedback loop ensures optimal stability of the filtering of the first sideband, more details in Section. 2.2.1.
- Amplifier: Erbium-doped fiber amplifier (EDFA, Keopsys CEFA-C-HG), with a maximum output power of 15.5 dBm (30 mW), offers up to 50 dB of gain to compensate the losses.

2.1.2.1 *Heterodyne measurement of the amplitude and phase of the loops pulses:*

The filtered and amplified light from the local oscillator serves as a reference beam. It is split into two equal parts using a 50/50 beam splitter, with each part directed to an 80/20 beam splitter to perform the beating with the output light from the two coupled rings. The band structure can be reconstructed thanks to the phase and amplitude information found in the observed beating, as discussed in Section. 3.1 of Chapter. 3.

From a mathematical standpoint, the phase information is encoded within the beating intensity, as described in the equation. 2.4.

$$\begin{aligned}
 I &= |A_{\alpha\beta} e^{i\omega t} e^{i\phi} + A_{LO} e^{i(\omega+\Omega)t}|^2 \\
 &= A_{\alpha\beta}^2 + A_{LO}^2 + 2A_{\alpha\beta} A_{LO} \cos(\Omega t + \phi)
 \end{aligned} \tag{2.4}$$

With $A_{\alpha\beta}$ denote the laser amplitude within the two coupled rings, with ω and ϕ representing the laser frequency and field phase, respectively. Additionally, A_{LO} and $\omega + \Omega$ correspond to the amplitude and frequency of the local oscillator's narrow laser beam.

In this section, we provided an overview of the optical part within the experimental setup illustrated in Fig. 2.1.b. We detailed the function of each element, specifying their respective lengths and the relevant timescales associated with the double-ring system. Furthermore, we offered an in-depth explanation of the local oscillator, emphasizing its critical role as a reference beam within the experiment.

2.2 Electronic: Automation and control

In this section, we will provide a detailed explanation of the electronic section of the experimental setup depicted in Fig. 2.1.a. The electronic section, primarily managed by a microcontroller (Arduino) and an arbitrary waveform generator (AWG7000B), focuses on ring stabilization and control of the electronic components.

2.2.1 Optical fiber ring stabilization

Variations in temperature and pressure can cause changes in the laser wavelength and the fiber's length of each ring by less than a few percent of a wavelength on a short timescale of 10 ms. From shot to shot, variations in laser wavelength and fiber length can be represented as an extra optical phase that the light passing through each fiber ring acquires, which leads to a shift in the band structure by a random amount in the energy domain (δE) and the wavevector domain (δk) [121].

Stabilizing a fiber ring is crucial to counteract the effects of ring elongation over time. To ensure lasting stability, lockboxes are positioned after the extraction signals of the α and β rings, as well as the Fabry-Perot interferometer (FPI) of the local oscillator, as illustrated in Fig. 2.1.b. The goal of the stabilization protocol is to adjust the length of the two rings to a fixed value that corresponds to an integer multiple of the laser wavelength. For the Fabry-Perot interferometer of the local oscillator, the stabilization protocol ensures filtering of the first sideband. The lockboxes utilize a feedback loop that consists of three primary steps: (Measurement - Decision - Action).

Measurement: a feedback loop ensures system stability by continuously adjusting the optical fiber length according to the output signal that is monitored by a photodiode (PD) positioned before the lockbox, as depicted in Figs. 2.1. The photodiode converts light into an electrical signal to send to a programmable card within the lockboxes. A function generator (FG2, Circuitmate) delivers a continuous peak-to-peak ramp voltage¹ $V_{pp} = 4\text{ V}$ at 1 kHz, as illustrated by the green triangular line in Fig. 2.1.a and Fig. 2.3. This voltage is transferred to the cylindrical piezoelec-

¹ **Ramp voltage:** an electrical signal where the voltage increases or decreases linearly with time.

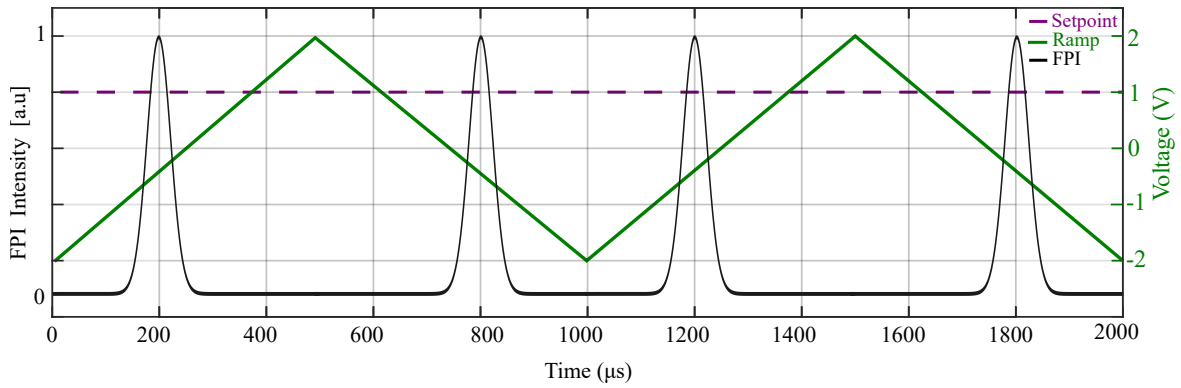


Figure 2.3: The Fabry-Perot interferometer (FPI) transmission spectrum of the local oscillator and the double ring system is shown as a black line, accompanied by the green trace representing the continuous ramp voltage applied via the function generator. The purple line indicates the setpoint value for locking.

tric device after passing through the initially unlocked lockbox. The piezoelectric element, wrapped with a 10-turn, 0.6-meter optical fiber ring, induces a physical stress on the fiber by stretching or compressing it based on the applied voltage by the lockbox, reaching a maximum radial deformation of $15.6 \mu\text{m}$. This technique facilitates the analysis of the Fabry-Perot interferometer (FPI) transmission spectrum from both the local oscillator and the two rings α and β , as illustrated by the black line on the scope in Fig. 2.1.a and Fig. 2.3. Additionally, it compensates for fiber deformations of up to 10 wavelengths, ensuring that the observed transmission line is detected when the piezoelectric device adjusts the optical fiber length to an integer multiple of the laser wavelength, corresponding to a ramp signal voltage of -0.5 V , as illustrated in Fig. 2.3. The local oscillator, along with each of the rings α and β , individually operate as Fabry-Perot interferometers (FPIs), with further details provided in the following subsection.

Decision: By analyzing the signal's spectrum, a desired frequency can be selected. This selection involves locking the lockbox at a specific setpoint value from the spectrum information (purple line in Fig. 2.3). A programmable card calculates the error (the difference between the desired setpoint value and the measured output). If the error signal is not zero, at its output, it applies a correction current, which is amplified by a high voltage amplifier (HV) to a piezoelectric element.

Action: Upon securing the lockbox, the piezoelectric element experiences only the correction voltage and no longer encounters the continuous ramp voltage from the function generator. As a result, the piezo only reacts to the lockbox's correction current, providing the appropriate amount of physical stress to preserve fiber stabilization.

This iterative process continues until the error between the desired setpoint and the measured output signal converges to zero, establishing a stable state.

2.2.2 Arduino: central controller and ring stabilization

Figure 2.1.a shows that the switches located in the α and β ring, along with the Acousto-Optic Modulator (AOM) are connected to the AWG 7000B and the Arduino via logical OR². This design choice reflects the central role of the Arduino. It manages the overall electronic processes, which can be broadly categorized into two stages: (1) ring stabilization and (2) sequence generation using the AWG 7000B, as illustrated in Fig. 2.4.

The first stage, ring stabilization, consists of two equal 20 ms sub-stages (lock β and lock α). Within those two sub-stages, the AOM (green) and the EOM (red) operate at high voltage, which means that light is continually being injected into the double-ring system.

Sub-stage 1: Focus on stabilizing the short ring β . To achieve this, the optical switch in the long ring α (purple) is set to high voltage while in the short ring β (blue) is set to low voltage, see Fig. 2.4. This effectively cuts off the CW laser light within the long ring, allowing light to propagate solely in the short ring. This isolation is critical for achieving a perfect stabilization of the short ring. Here is why: within the short ring cavity, the VBS (Variable Beamsplitter) and the 90/10 beam-splitter work together to form a Fabry-Perot interferometer. This interferometer plays a crucial role in the stabilization process by filtering the desired frequency that corresponds to an integer multiple of the laser wavelength, it can only function properly when the long ring does not interfere with the short ring.

Simultaneously, a function generator (FG2, Circuitmate) generates a ramp voltage applied to the piezo element, as indicated by the green triangular line in Fig. 2.1.a and Fig. 2.3. The information obtained from the spectral analysis of the output signal of the short ring is vital for setting a specific setpoint value to lock the lockbox and stabilize the short ring, as discussed in Section 2.2.1.

Once the lockbox β is secured and the short ring is stabilized, the Arduino ensures this state is maintained by sending a Hold β signal, to its respective lockboxes. This Hold signal mimics a zero-error condition. When set to high voltage, they effectively inform the lockboxes that everything is functioning correctly (zero error) and instruct them to retain the previous correction current. This technique assumes that during the time needed throughout the subsequent steps (locking of the ring α and conducting the calibration and science experiments), the fibers and laser will remain stable. This is indeed the case as far as we can see in our experiments.

² **Logical OR:** ensures a connected component to responds when engaged by either the Arduino or the AWG 7000B.

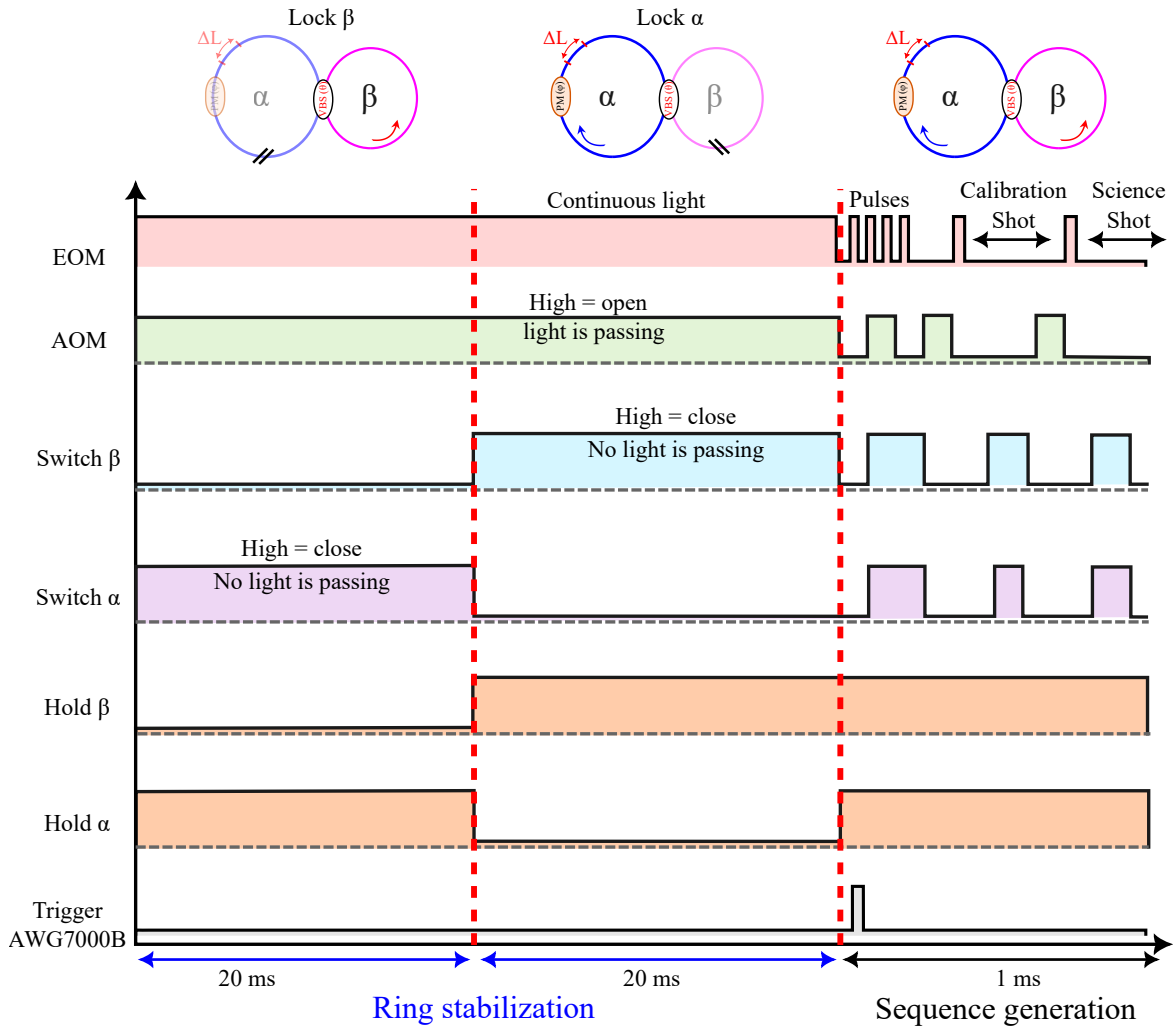


Figure 2.4: The central role of the Arduino is divided into two main stages. The first stage is optical fiber ring stabilization, which includes two equal sub-stages of 20 ms each (lock β and lock α). The second stage is sequence generation, which is carried out using the AWG 7000B.

Sub-stage 2: Building upon sub-stage 1, the focus now shifts to stabilizing the long ring. The Arduino mirrors the strategy used for the short ring by isolating the long ring. It sets the optical switch in the short ring to high voltage and the switches in the long ring to low voltage, effectively cutting off light in the short ring and ensuring no interference during the stabilization of the long ring. Additionally, the previously applied Hold β signal remains active (high voltage) to maintain the short ring's locked state. Upon isolating the long ring, stabilization is achieved by securing the lockbox α at a specific setpoint value.

Once both rings are stabilized and locked, the Arduino takes a final step by triggering the AWG7000B to initiate the sequence generation phase (gray line in Fig. 2.4), as described in Section. 2.2.3. Simultaneously, it sets both Hold signals (α and β) to high voltage, this ensures that the stabilized state of both rings is preserved throughout the entire calibration and science shot.

Note: The Fabry-Perot Interferometer (FPI) of the local oscillator stands apart from the double-ring setup. Unlike the rings α and β , the lockbox FPI doesn't require a continuous Hold signal from the Arduino. This distinction stems from the inherent isolation provided by the FPI's design. It operates independently under continuous (CW) laser light, eliminating the need to block light propagation within its cavity to maintain back its stable state.

2.2.3 Sequence generation

Automation and waveform generation is achieved using the arbitrary waveform generator AWG 7000B, controlled by a custom Python script on a personal computer. The script utilizes the *Broadbean* package for operation. The arbitrary waveform generator AWG 7000B (Tektronix) with a 25 GHz bandwidth (time interval of 40 ps between two points) and a 10-bit mode resolution serves as the central control unit for all electronic components within the setup depicted in Fig. 2.1.b. This instrument features two high-speed channels (Ch1 and Ch2) with a sampling rate of 25 GS/s and an output voltage range of ± 250 mV. Additionally, each channel is associated with two digital masters (M1 and M2) and four slow flags. The master outputs can switch between 0 V and a user-defined high voltage between 500 mV and 1.4 V, while the flags are limited only to two values, 0 V and 3.3 V.

Figure 2.5 depicts the output sequence generated by the AWG 7000B, which controls various elements within the setup in a specific order. The vertical axes represent flags, masters, and channels, each associated with a specific component depending on the required bandwidth. The horizontal axis depicts the temporal sequence of the control signals. This sequence comprises individual waveforms for each component within the setup. Each waveform consists of a series of elements that trigger and dictate the on/off state of the corresponding component.

It is important to note that while Flag 5 and Channel 1 are both connected to the phase modulator (PM), and Flag 6 and Channel 2 are connected to the variable beam splitter (VBS), as illustrated on the vertical axis of Fig. 2.5, only one of these outputs (flag or channel) is used at a time during the experiment. Flags (5 and 6) trigger two separate slow arbitrary waveform generators (Agilent 33250A, 80 MHz). These generators produce a high, symmetrical peak-to-peak voltage of 10 V for a duration longer than the experiment time. Due to their slow rise time, they are only used for experiments in which the bulk properties (like Berry curvature) of the lattice are studied. Such experiments require the VBS and phase modulator PM to change their value only once every round trip. The typical required bandwidth is on the order of one-tenth of the round-trip time.

In contrast to flag outputs, channel outputs (1 and 2) are utilized for the generation of lattice edges in space position (to be discussed later). These channels involve

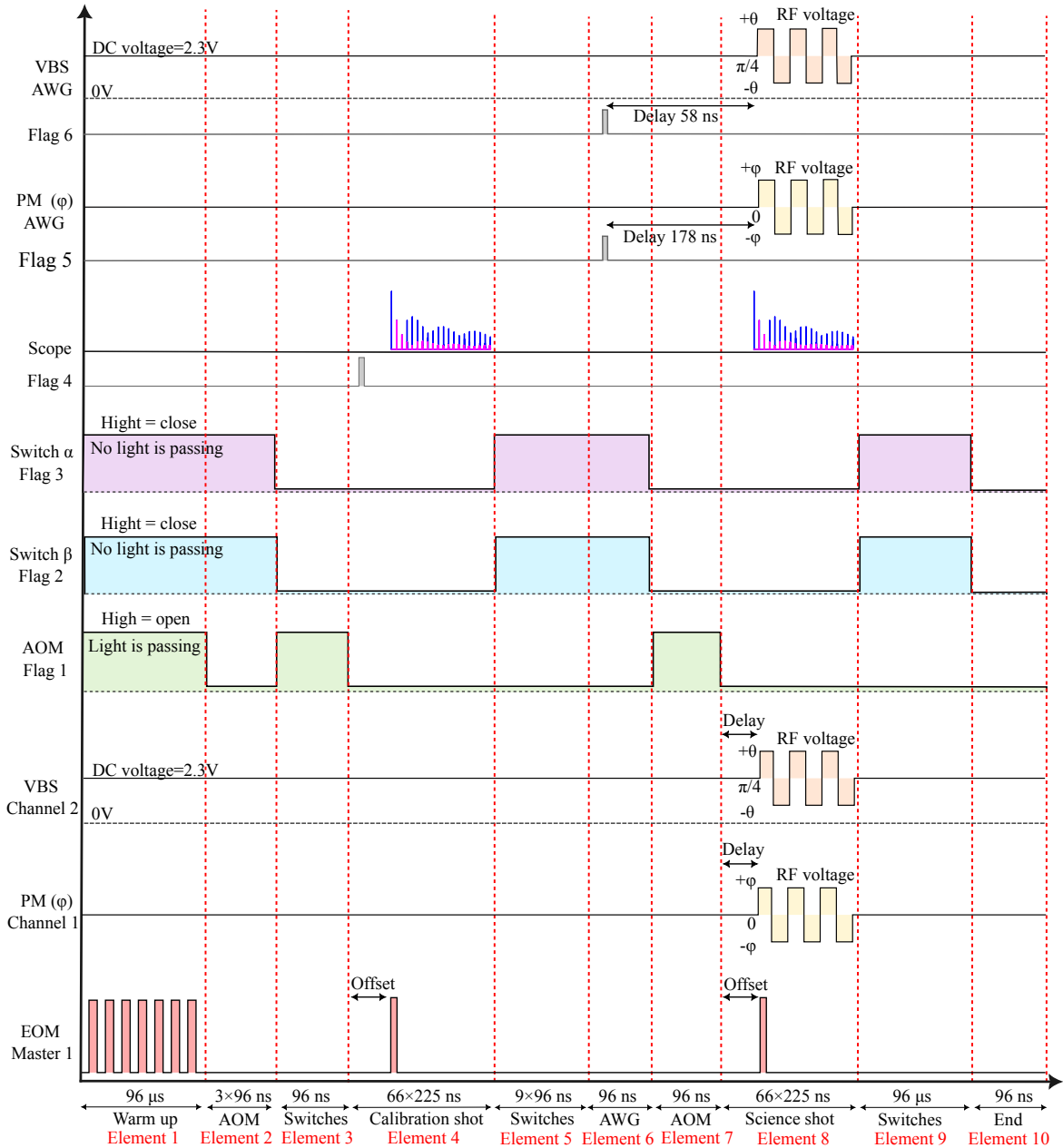


Figure 2.5: Output sequence generated by the arbitrary waveform generator AWG 7000B, which controls various elements within the setup in a specific order.

rapid modulation (10 GHz bandwidth) of both the phase modulator and the variable beam splitter across multiple positions within a single round trip. However, channel outputs are limited in voltage, reaching a maximum of ± 250 mV and the π voltage V_π of the VBS (EOSpace AX-2x2-0MSS-20) and the phase modulator (PM, iXblue MPZ-LN-01) are 9.4 V and 3.55 V, respectively. To overcome this limitation, a voltage amplifier (iXblue DR-DG-12-MO, 12 Gb/s) amplifies the channel signals to a peak-to-peak voltage (V_{pp}) of 8 V. This amplified signal is sufficient for the phase modulator but not for the VBS. Thus, for the VBS, we combine the amplified RF voltage from the channel with a continuous DC voltage of 2.4 V. This DC

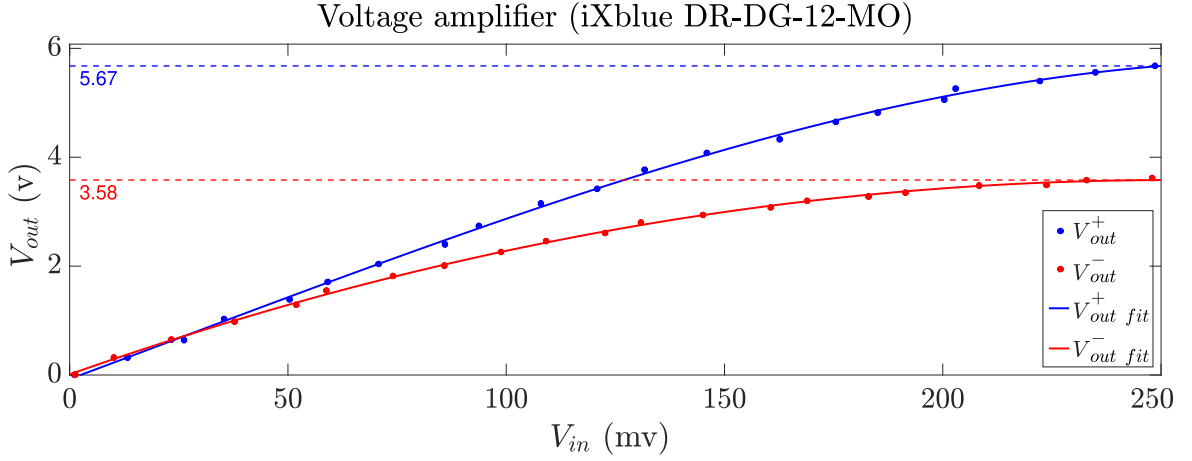


Figure 2.6: The positive (blue) and negative (red) output voltage (V_{out}^{\pm}) in V of the iXblue DR-DG-12-MO amplifier as a function of its input voltage (V_{in}) in mV.

voltage alone sets the angle parameter of the coupling to $\theta = \pi/4$, corresponding to the 50/50 beam splitter scenario.

Figure 2.6 illustrates the positive (blue) and negative (red) output voltage V_{out}^{\pm} in V of the iXblue DR-DG-12-MO amplifier as a function of its input voltage V_{in}^{\pm} in mV. The iXblue amplifier exhibits symmetrical positive and negative voltage amplification for an input signal in the range of 0 to 40 mV. The maximum achievable signal is 3.58 V for the negative output and 5.67 V for the positive output for an input voltage V_{in} of 250 mV (maximum channel output). As the maximum amplified outputs exceed the phase modulator V_{π} , this allows for scanning the PM from $-\pi$ to π without limitation. However, the variable beam splitter V_{π} is 9.4 V exceeds the combined DC voltage of 2.4 V, and the iXblue maximum amplification voltage is 3.58 V. Consequently, the coupling ratio $\cos^2(\theta)$ is limited to a range of 0 to 1, since the angle parameter of the coupling $\theta \in [-\pi/2, \pi/2]$. We consider the maximum amplification voltage for the iXblue to be 3.58 V rather than 5.67 V. Because, when the beam splitter coupling angle is alternated symmetrically between $\pm\theta$, the negative voltages cannot achieve the same amplification value as the positive ones.

The experiments are always performed in a two-pulse sequence: the "calibration" part of the experiment and the "science" part of the experiment. To do so, the AWG7000B generates two consecutive 1.4 ns pulses separated by approximately $70 \bar{T}$, as depicted in Fig. 2.5 in elements 4 and 8, respectively. For the calibration pulse, the beamsplitter is set to $\theta = \pi/4$, which corresponds to a 50/50 coupling angle, and $\varphi = 0$. The time dynamics of this model are quite trivial and well-known [140] and serve as a reference model. The second pulse, referred to as the science pulse, investigates the two-step and four-step models, as well as the edge state engineering, which will be discussed in detail later in this thesis. In contrast to the calibration pulse, the values of the splitting angle θ of the VBS and the phase

modulator value φ within the science pulse change every single round trip according to a predefined value that implements the lattice model we wish to study. The reason for doing the two experiments in the same oscilloscope shot will become clear later in Section. 3.1.3 of Chapter. 3

The control sequence of the AWG7000B shown in Fig. 2.5 will now be further examined step by step:

- **Element 1:** Warmup procedure, this involves sending a series of 100 narrow laser pulses into the ring by alternating the voltage of the Electro-Optic Modulator (EOM) through the Master 1. During these pulses, The Acousto-Optic Modulator (AOM) and both switches in each ring are held in a high-voltage state. The AOM permits the pulses to enter the ring, while both switches block the light propagation once it reaches them. The warm-up phase ensures that all components within the optical system achieve their optimal operating conditions, this process minimizes the transient effects and reduces thermal fluctuations [141], thereby enhancing the overall reliability of the measurements [142].
- **Element 2:** AOM is switched to a low-voltage state, preventing light from reaching the ring to ensure a clean initial condition for the calibration shot.
- **Element 3:** AOM is switched back to high voltage for a short duration of time (minimum element duration of the AWG 7000B is 96 ns), while the switches are set to low voltage to allow the prepared narrow pulse in element 4 to enter the ring and propagate. Taking into account the delay caused by the electronic cable length, the AOM is activated just before the injection.
- **Element 4:** The EOM is rapidly switched from low voltage to high voltage and back to low voltage, enabling the injection of a 1.4 ns narrow light pulse into the double ring, which then evolves following a split-step walk for 66 round trips. Simultaneously, Flag 4 triggers the oscilloscope to start data recording. This element corresponds to the calibration shot, where the PM value is set to 0 and the angle of the coupling is set to $\theta = \pi/4$.
- **Element 5:** The switches are set back to high voltage to make sure that no residual light from the calibration experiment remains within the ring cavity during the subsequent science experiment. The reason for recording the two experiments in the same oscilloscope shot is given in Section. 3.1.
- **Element 6:** Flags (5 and 6) trigger the AWG (Agilent 33250A) using short pulses. This triggering occurs in Element 6 due to the slower response time of the AWG (Agilent 33250A) and the delays introduced by the electrical cables connecting the electronics to the experiment.
- **Element 7:** Similar to element 3, AOM is switched back to high voltage for a short duration of time (96 ns), while the switches are set to low voltage to

allow the prepared narrow pulse of the science shot in element 8 to be injected into the long ring and propagate. Taking into account the delay caused by the electronic cable length, the AOM is activated just before the injection.

- **Element 8:** Similar to element 4, the EOM introduces a narrow pulse of 1.4 ns into the long ring. In contrast to the calibration shot of element 4, the PM and the VBS can be controlled either by (ch1 and ch2) or (flag 5 and flag 6), respectively. This element corresponds to the science shot.
- **Element 9:** Similar to element 5, The switches are set back to high voltage for an extended duration of 96 μ s to make sure that no residual light from the science experiment remains within the ring cavity.
- **Element 10:** Marks the conclusion of the experiment, all control signals are switched to low voltage to prepare the setup for its resting state.

To achieve precise synchronization between all the components, we adjust the offset of the pulses entering the system and add digital delays specifically for each waveform of the VBS and PM.

Note: Reconstruction of the two-dimensional dispersion relation relies on extracting the eigenvalues for various values φ of the phase modulator, which varied from $-\pi$ to π in successive experiments, as we will see in Chapter. 4. The AWG 7000B generates a corresponding sequence with the appropriate waveforms to manipulate the system and induce the desired dynamics at that particular φ value.

2.3 Conclusion

This chapter starts with an overview of the experimental setup, outlining the function and specifications of each component, including their lengths and relevant timescales. The system is divided into electronic and optical sections. The optical section comprises two coupled fiber rings of different lengths connected via a variable beam splitter, and a local oscillator, which enables spectral information acquisition through a heterodyne method. The electronic section is controlled by an Arduino and a fast arbitrary waveform generator (AWG7000B). This section stabilizes the optical fiber lengths through a feedback loop by continuously adjusting them based on the output signal. Additionally, it generates precise waveform sequences and manages the triggering and control of various components within the setup.

EIGENSTATE AND EIGENVALUE ANALYSIS

Chapter. 3 describes the procedure for extracting the eigenvalues of the double-ring system. This process involves using a heterodyne method for precise phase determination (see Chapter. 2) and analyzing the spectral information from the system's impulse response through a 2D Fourier transform of the stroboscopic spatiotemporal diagram. Notably, it is worth mentioning that this method was initially been proposed by *A.M. Tikan* et al. for measuring the dispersion relation [143], and it has been successfully implemented for the first time by *C. Lechevalier* [17, 118]. Subsequently, we discuss how to extract the eigenstates. The methods to be discussed in this chapter will be applied only to the calibration shot within the two-step model for illustrative purposes. However, the underlying concepts apply to all model and shot configurations.

3.1 Measurement of eigenvalues

3.1.1 Impulse response

To determine the excited eigenvectors and eigenvalues, we need to know the pulse phase at various spatial positions (n) and time steps (m) within the rings, as presented by the equation. 3.1

$$\begin{bmatrix} \alpha_n^m \\ \beta_n^m \end{bmatrix} = \frac{1}{\sqrt{1 + |R|^2}} \begin{bmatrix} 1 \\ |R|e^{i\Phi_{\alpha\beta}} \end{bmatrix} e^{ikn/2} e^{iE(k,\varphi)m/2}. \quad (3.1)$$

Since the photodiodes only detect intensity, we extract phase information by interfering the ring's output signal with a continuous-wave reference laser at each round trip. The laser delivering the injected pulse and used as a reference in the local oscillator has a coherence length spanning hundreds of microseconds, significantly exceeding the duration of each recorded time trace. This ensures stable interference contrast over multiple cycles.

Upon introducing a narrow square pulse of 1.4 ns into the long ring α , we recorded the calibration shot intensity optical beating between the outputs of both fiber

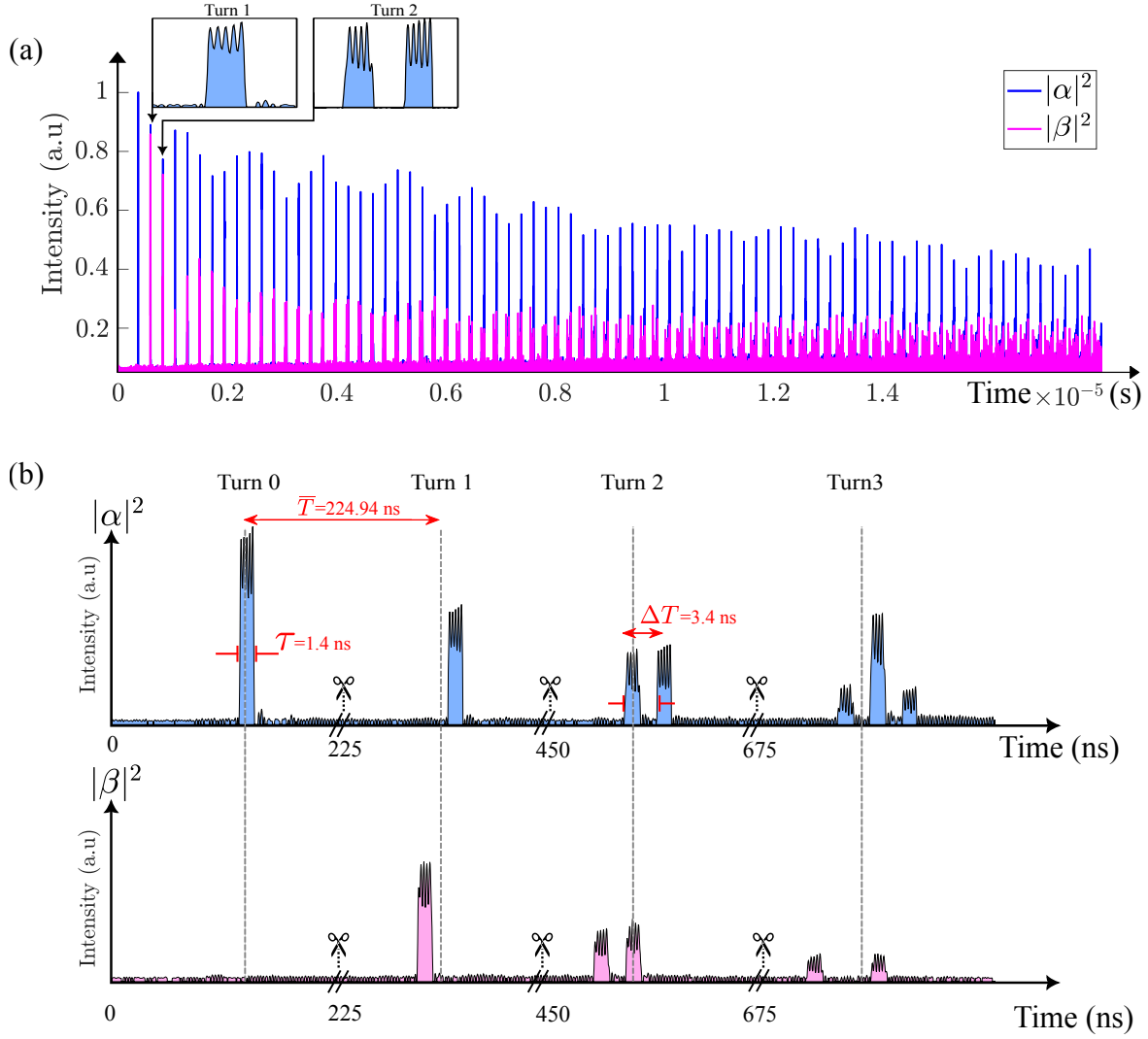


Figure 3.1: (a) Measured signal intensity of the optical beating between the output of both fiber loops (α & β) and the local oscillator's reference field shifted by 3 GHz away from the laser frequency. Four oscillations at the top of each pulse depict the beating. (b) Zoom on the first four turns of the recorded intensity signal within each ring, α in blue and β in pink.

loops (α and β) and the local oscillator as a function of time on the oscilloscope, as shown in Fig. 3.1.a. The introduced pulse has a width of 1.4 ns, and the local oscillator's reference field is shifted by 3 GHz from the laser frequency. Thus, the beating is visible at the top of the pulses, showing nearly 4 oscillations within their 1.4 ns duration, as shown in the zoomed-in view in Fig. 3.1.a.

Zooming on the first four-round trips, as presented in Fig. 3.1.b, we observe a series of groups of pulses separated by the average round-trip time inside the loops $\bar{T} = 224.94$ ns. Each pulse has a temporal width of $\tau = 1.4$ ns and it is separated from adjacent pulses in the same group at a time interval $\Delta T = 3.4$ ns, corresponding to the length difference between the two fiber loops. Moreover, the width of each pulse must be less than the time difference between the two rings ($\tau < \frac{\Delta T}{2}$) in order to witness distinct pulse sequences without any overlap.

The experimentally recorded intensity of Fig. 3.1 and the numerical simulation of Fig. 1.7 in Chapter. 1 reveals a high degree of similarity, with the primary difference being the presence of oscillations on top of each pulse in the experimental data. These oscillations are a direct consequence of the beating signal and hold crucial phase information, which is essential for accessing the phase information and consequently measuring the band structure along with their eigenvectors.

3.1.2 Spatiotemporal diagrams

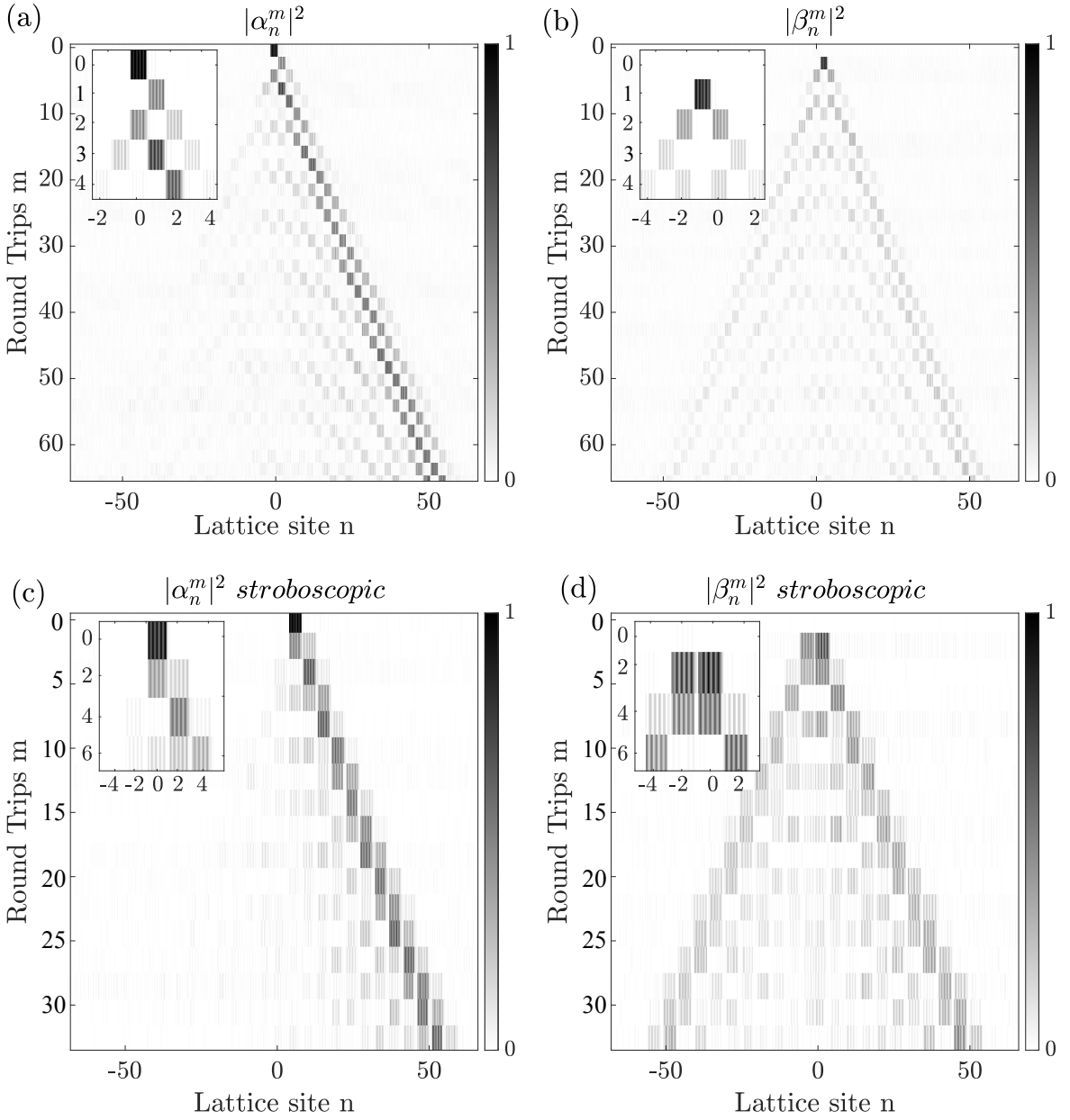


Figure 3.2: (a)-(b) Experimental spatiotemporal diagram of the long α and short β loops, respectively, when a short pulse of 1.4 ns is introduced to the long loop. (c)-(d) Corresponding stroboscopic spatiotemporal dynamics of each ring by keeping only odd round trips with odd site positions.

To reconstruct the spatiotemporal diagrams of the evolution of light intensity as a function of position and time in the α and β rings, we cut each recorded time trace after the arrival of the injected pulse into equal time segments of duration \bar{T} , (see Fig. 3.1.b). The segments are then arranged in lines corresponding to each round-trip time m , the spatial position n denoting the relative time of each pulse within each segment, as depicted in Fig. 3.2.

Figures. 3.2.a-b illustrate the normalized spatiotemporal diagrams in grayscale over 66 round trips and expand over 132 sites in the rings α and β , respectively. Figures. 3.2.c-d display the corresponding stroboscopic spatiotemporal diagrams of Figs. 3.2.a-b, achieved by keeping only odd time steps with odd site positions, which align with the temporal and spatial periodicity of the lattice. Notably, the observed oscillations on top of each pulse, appear as constructive and destructive fringes in the zoomed-in views of each subplot in Fig. 3.2.

The experimental spatiotemporal diagram in Fig. 3.2 exhibits a significant resemblance to the numerical spatiotemporal diagram in Fig. 1.9. This agreement demonstrates that the theoretical model accurately describes the light intensity evolution within the double-ring system.

3.1.3 Measuring the band structure

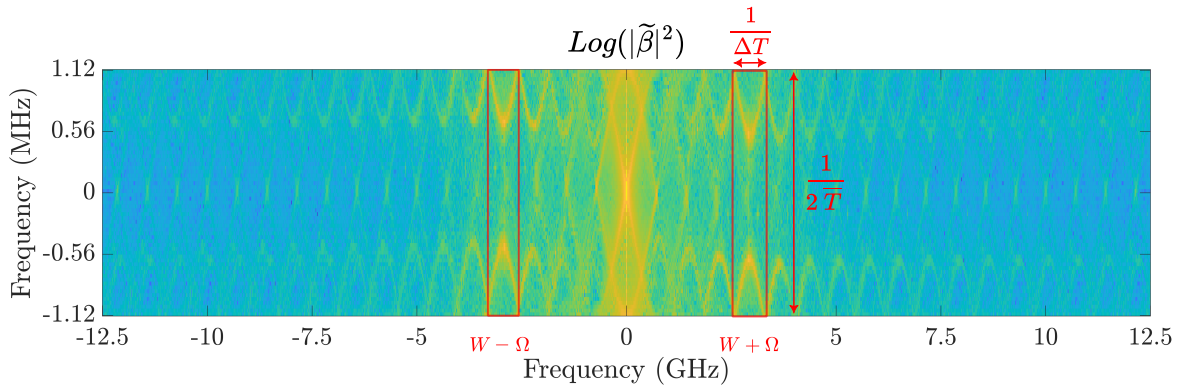


Figure 3.3: The two-dimensional Fourier transform in log scale of the stroboscopic spatiotemporal diagram shown in Fig. 3.2.d, reveals a prominent band structure at the heterodyne beating frequency $(W \pm \Omega) = \pm 3$ GHz, as highlighted by the red rectangle marking the Brillouin zone.

The band structure is obtained by applying a two-dimensional Fourier transform to the measured stroboscopic spatiotemporal diagram shown in Figs. 3.2.c-d. Figure. 3.3 displays in log scale the resulting spectrum of the short ring β , which spans horizontally from -12.5 GHz to 12.5 GHz, corresponding to a total range of 25 GHz. The 25 GHz frequency range of the spectrum corresponds to the inverse of the 40 ps sampling interval of the oscilloscope, which represents the minimum

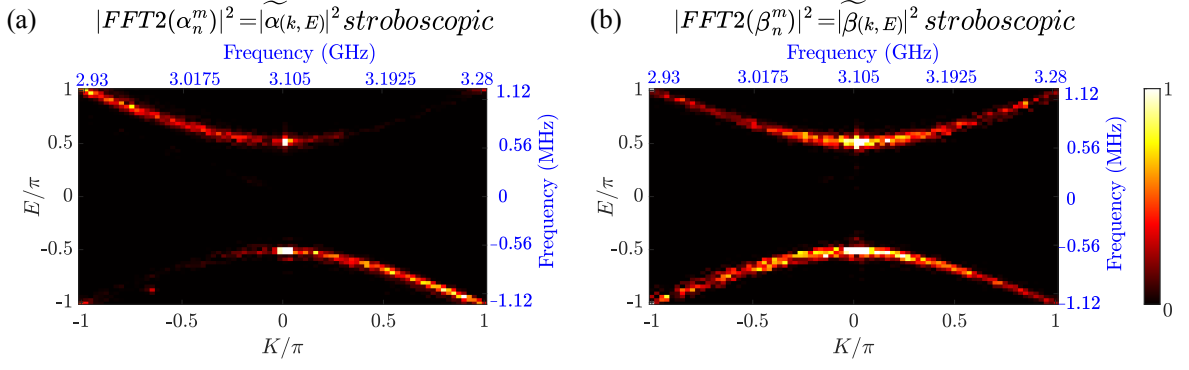


Figure 3.4: (a)-(b) Measured band structures of the long α and short β rings, respectively, within a single Brillouin zone at the heterodyne beating frequency of 3 GHz.

time resolution between data points on the horizontal axis of the stroboscopic spatiotemporal diagram. Similarly, the vertical axis of the spectrum in Fig. 3.3 spans from -1.12 MHz to 1.12 MHz, covering a total range of 2.24 MHz. This frequency range corresponds to the inverse of the resolution along the vertical axis of the stroboscopic spatiotemporal diagram, which, in our case, is two round trips ($2\bar{T}$), with $\bar{T} = 224.94$ ns.

The Fourier spectrum exhibits a localized feature at 0 Hz, which corresponds to the low frequencies derived from the two-dimensional Fourier transform of the intensity. It also features several visible Brillouin zones with band structures ranging from -6 GHz to 6 GHz, despite the spectrum horizontal frequency ranging from -12.5 GHz to 12.5 GHz. This limitation is due to the rapid diminishing of higher-order sidebands as they deviate from the carrier frequency.

A prominent band structure, highlighted by the red rectangle marking the Brillouin zone in Fig. 3.3, is observed at the heterodyne beating frequency $(W \pm \Omega) = \pm 3$ GHz. Our analysis will concentrate on a single Brillouin zone at a frequency $(W + \Omega) = 3$ GHz, as depicted in Fig. 3.4. Figures 3.4.a-b presents the normalized measured band structures of the long and short rings, respectively. The measured bands are quite similar to the analytical and numerical dispersion relation shown in Fig. 1.10 of Chapter. 1. Additionally, the horizontal and vertical frequency axes represent the conjugate of the pulse lattice site (n), corresponding to a specific physical time, and the time step (m), respectively. We can relate from $-\pi \rightarrow \pi$ the horizontal and vertical frequency axes to the normalized axes of quasimomentum k and quasienergy E , respectively, for a clearer examination of the experimental band structure.

We notice two symmetrical spectral bands. These bands center around $k = 0$ (3.1 GHz) on the horizontal axis and $E = 0$ (0 MHz) on the vertical axis. One might wonder why this center frequency is 3.1 GHz and not exactly 3 GHz. Because the observed bands result from a beating effect between the local oscillator reference field at 3 GHz and the laser frequency of the output from both fiber loops.

However, the acoustic optical modulator placed before the double ring introduces a slight 110 MHz shift to the laser frequency, causing this deviation. Additionally, an insignificant signature of beating is observed at $k = 0$ (3.1 GHz) as a bright notch. The narrow spectral width of this signature, confined to a single pixel, does not disrupt the measurement.

The 1.4 ns pulse injected into the double ring corresponds to a broad spectral region of 0.71 GHz in Fourier space. However, the observed window of the Brillouin zone in Fig. 3.4 ranges from 2.93 GHz to 3.23 GHz on the horizontal axis, resulting in a narrower span of 0.31 GHz, which is half of the expected spectral width. This discrepancy arises because the analyzed spectrum is the Fourier transform of a stroboscopic spatiotemporal diagram, rather than the complete spatiotemporal diagram. Thus, the fact that the observed window is exactly half of the expected one confirms that the injected pulse fully excites the Brillouin zone.

From shot to shot, due to variations in laser wavelength and fiber length not fully compensated by the piezo stabilization protocol, the band structure experiences slight shifts. To address this, we employ a correlation technique to align the measured calibration band structure with the analytical calibration dispersion relation. Once the Brillouin zone window is established for the calibration shot, we assume it remains the same for 10 ms (fluctuation timescale), providing sufficient time to study the science shot, in which different values of the splitting angle and phase modulators are engineered to study different topological properties of the lattice. This approach is one of the reasons for designing the experiment with this double injection protocol, as described in Section. 2.2.3. The correlation technique is an essential step, as manually fine-center the Brillouin zone window for each phase modulator value $\varphi \in [-\pi, \pi]$ becomes impractical for constructing the two-dimensional eigenvalue and eigenvector tomography, particularly when studying topological properties (discussed in greater detail in Chapter. 4).

Note: This section outlines the method for extracting the band structure of the calibration shot within the two-step model. In the four-step model, a similar approach is used. Specifically, the stroboscopic spatiotemporal diagram is obtained by selecting either odd or even round trips every four turns and either odd or even site positions. A 2D Fourier transform is then applied to this stroboscopic spatiotemporal diagram to extract the band structure.

To sum up, utilizing a heterodyne method, we successfully measured the dispersion relation of the calibration shot in the two-step model during a single acquisition. This method involved optical beating between the outputs of both fiber loops and the local oscillator, resulting in oscillations within each pulse that encode phase information. By rearranging the recorded time trace of the double ring's impulse response and applying a two-dimensional Fourier transform to the stroboscopic spatiotemporal diagram, we accessed the spectral information, revealing

the band structure that matches exactly the numerical and the analytical photonic bands discussed in Chapter. 1. As we will demonstrate in the following section, accessing the spectral information enables not only the measurement of the photonic band structure but also the determination of the system's eigenstates.

3.2 Measurement of eigenstates

My PhD research builds upon the foundational work of the former PhD student C. Lechevalier, who focused on measuring the eigenvalues and eigenvectors of a double-ring system in his thesis [17]. His research laid the groundwork for my doctoral study, which seeks to quantify specific topological properties. Leveraging his methodologies, we now proceed to extract the eigenvectors from the power and the phase of the spectral distribution. The method is first demonstrated through a numerical simulation of the calibration shot within the two-step model, followed by an application to experimental data.

3.2.1 Numerical eigenstate analysis

To extract the complex amplitudes of the eigenstates, we must accurately determine their Floquet-Bloch eigenvalues from the quasienergy-quasimomentum diagram derived from the measured spatiotemporal dynamics. We begin by conducting a numerical simulation replicating the calibration shot within the two-step model ($\theta = \pi/4$, $\varphi = 0$), where a narrow pulse is injected into the long ring α . For each quasimomentum k of the dispersion relation presented in α and β ring of Figs. 3.5.a-b, respectively. We use the analytical band structure of equation. 1.21 corresponding to the two-step calibration shot as a reference [blue line in Figs. 3.5.a-b]. This reference allows us to locate the maximum intensity of the numerical bands ($|\tilde{\alpha}^\pm(k, E)|^2$ & $|\tilde{\beta}^\pm(k, E)|^2$) [cyan line in Figs. 3.5.a-b]. This identification is accomplished by scanning two pixels in quasienergy above and below the analytical bands [yellow line, Figs. 3.5.a-b]. Other more general methods based exclusively on the location of the maxima of intensity extracted from the experiment without the use of the analytical expression are also successful.

Once the band's maximum intensity is identified, we extract the eigenvectors $|\psi(k)_\alpha^\pm\rangle$ and $|\psi(k)_\beta^\pm\rangle$ for each quasimomentum k within the upper (+) and lower (-) bands of both rings α and β . This is achieved by taking the complex amplitude of the Fourier mode ($\tilde{\alpha}^\pm(k, E(k)^\pm)$ and $\tilde{\beta}^\pm(k, E(k)^\pm)$), where $E(k)^\pm$ denotes the peak of the spectral energy density corresponding to the band's maximum intensity position [cyan line in Figs. 3.5.a-b].

The spectral phase distribution $\varphi_\alpha^\pm(k)$ and $\varphi_\beta^\pm(k)$ in each ring α and β for the upper and lower bands are showcased with blue and red lines, respectively, in

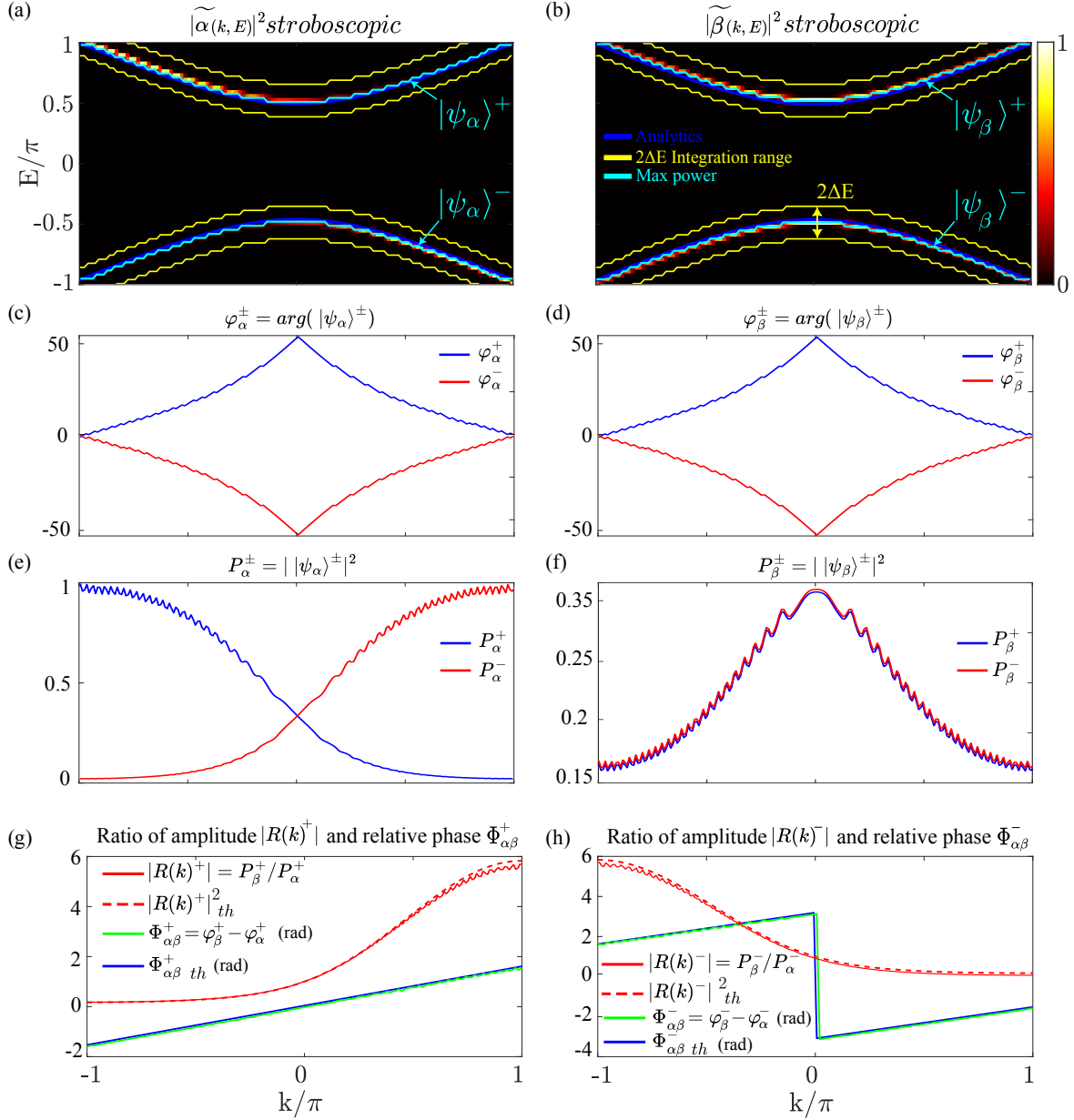


Figure 3.5: Numerical simulation of the calibration shot. (a-b) Dispersion relation of the α and β rings, respectively. For each ring, we present the following for both the upper and lower bands: (c-d) The spectral phase distribution. (e-f) The spectral power distribution. (g-h) The numerical (analytical) ratio of amplitude $|R(k)|$ in solid (dashed) red, along with the relative phase $\Phi_{\alpha\beta}$ in green (blue) line.

Figs. 3.5.c-d. The phase is determined by the argument of the Fourier mode at the peak of each band's spectral energy density along the k axis. This is expressed as:

$$\begin{cases} \varphi_\alpha^\pm(k) = \arg(\tilde{\alpha}^\pm(k, E^\pm(k))) \\ \varphi_\beta^\pm(k) = \arg(\tilde{\beta}^\pm(k, E^\pm(k))) \end{cases} \quad (3.2)$$

The numerical spectral phase distributions within the long and short rings exhibit nearly identical, yet not entirely equal behavior for the calibration shot, as

illustrated in Figs. 3.5.c-d. However, the phase of the upper (blue) band is a mirror image of the lower (red) band with respect to the k -axis.

Due to the finite number of points in the numerical simulation, the band intensity along the quasimomentum k is not confined to a single pixel. Thus, the measurement of the spectral power distribution ($P_\alpha^\pm(k)$ & $P_\beta^\pm(k)$) given by equation. 3.3 for each quasimomentum k involves integrating the identified maximum intensity in quasienergy over a width of $2\Delta E$, corresponding to two pixels below and above the band's peak [yellow line Figs. 3.5.a-b]. This integration also helps to reduce noise in the measurement.

$$\begin{cases} P_\alpha^\pm(k) = \frac{1}{2\Delta E} \int_{E(k)^\pm - \Delta E}^{E(k)^\pm + \Delta E} |\tilde{\alpha}^\pm(k, E(k)^\pm)|^2 dE \\ P_\beta^\pm(k) = \frac{1}{2\Delta E} \int_{E(k)^\pm - \Delta E}^{E(k)^\pm + \Delta E} |\tilde{\beta}^\pm(k, E(k)^\pm)|^2 dE \end{cases} \quad (3.3)$$

Figure. 3.5.a reveals asymmetric population in the upper (lower) bands of the α ring when a single site is excited in the long ring at round trip $m = 0$. This asymmetry is apparent in the normalized power distribution shown in Fig. 3.5.e, where the blue (red) curves for the upper (lower) band are concentrated on the negative (positive) side of the k axis. In contrast, the symmetrical population of modes observed in the upper (lower) bands of the β ring, depicted in Fig. 3.5.b, results in a symmetrical normalized power distribution around $k = 0$ in Fig. 3.5.f, with blue (red) curves for the upper (lower) band. The normalization is performed relative to the long loop in both Fig. 3.5.e and Fig. 3.5.f.

Once the power and the phase of spectral distribution are obtained, the numerical eigenstates of a specific band structure corresponding to the analytical normalized eigenvectors $|\psi^\pm(k)\rangle$ formula of the two-step model in equation. 1.22 and 1.23 (see Appendix. A) are straightforward established by the ratio of amplitudes $|R(k)^\pm| = P_\beta^\pm(k)/P_\alpha^\pm(k)$, and $\Phi_{\alpha\beta}^\pm(k) = \varphi_\beta^\pm(k) - \varphi_\alpha^\pm(k)$, denoting the relative phase between the two sublattice sites associated with the eigenvector with quasimomentum k within the first Brillouin zone. Figures. 3.5.g and 3.5.h demonstrate a good agreement between the numerical and analytical eigenstates $|\psi(k)^\pm\rangle$ for the upper and lower bands, respectively. The numerical (analytical) amplitude ratio $|R(k)^\pm|$ is represented by solid (dashed) red lines, while the numerical (analytical) relative phase $\Phi(k)_{\alpha\beta}^\pm$ is depicted by straight, increasing lines in green (blue) from $-\pi/2 \rightarrow \pi/2$ across the Brillouin zone.

A minor difference between the analytical and the numerical results is observed, attributable to the finite time step resolution of the simulation. To enhance the agreement, increasing the number of time steps and expanding the integration region ΔE for spectral power is necessary.

Note: The maximum intensity of the numerical bands for the two-step model's calibration shot was identified by scanning in quasienergy around the analytical bands defined in equation 1.21. This approach can also be extended to the four-step model, where the analytical bands defined by equation 1.26, corresponding to the nominal splitting angle and external phase modulator, serve as a reference to locate the maxima of the numerical bands for both calibration and science shots. Thus, for each scenario, we apply the relevant analytical band structure.

3.2.2 Experimental eigenstate analysis

In the preceding subsection, we detailed the extraction of the eigenstate from a numerical simulation replicating the calibration process. We will now apply the same methodology to the experimental calibration shot to extract the corresponding experimental eigenstate, as illustrated in Fig. 3.6.

Figures. 3.6.a and 3.6.b illustrate the normalized dispersion relation from the experimental two-step model calibration shot, when a narrow pulse is introduced into the long ring α . The corresponding analytical dispersion relation (blue line) shows excellent agreement with the experimental band structure. Consistent with previous methodologies in Subsection. 3.2.1, the analytic bands are utilized as a reference to pinpoint the maximum intensity of the experimental bands ($|\tilde{\alpha}^\pm(k, E)|^2$ & $|\tilde{\beta}^\pm(k, E)|^2$) [cyan line in Fig. 3.6.a-b]. This process involves scanning two pixels in quasienergy above and below the analytic bands [yellow line, Figs. 3.6.a-b].

The spectral phase distribution $\varphi_\alpha^\pm(k)$ and $\varphi_\beta^\pm(k)$ for each of the extracted eigenvector $|\psi(k)_\alpha^\pm\rangle$ and $|\psi(k)_\beta^\pm\rangle$ of the α and β ring, across both the upper and lower bands, are illustrated in blue and red in Figs. 3.6.c-d, respectively. A comparison of the numerical phase distribution shown in Figs. 3.5.c-d with the experimental phase presented in Figs. 3.6.c-d reveals a good resemblance between the two. However, for even greater accuracy, one could utilize heterodyne measurements with a higher frequency beating, such as 10 GHz, as demonstrated in the work of C. Lechevalier [17], combined with a higher resolution oscilloscope with a 65 GHz bandwidth.

Figures. 3.6.e and 3.6.f showcase the power distributions $P_\alpha^\pm(k)$ and $P_\beta^\pm(k)$ for the α and β rings, respectively, across both the upper and lower bands, represented by blue and red lines. The experimental power distribution in Figs. 3.6.e-f deviates from the simulated one Figs. 3.5.e-f and exhibits a noisy profile due to several factors. Firstly, this disparity arises from the imperfect replication of the simulation's sharply defined initial conditions in the experiment. Unlike the simulation's precise square pulse with sharp edges, the experimentally injected pulse

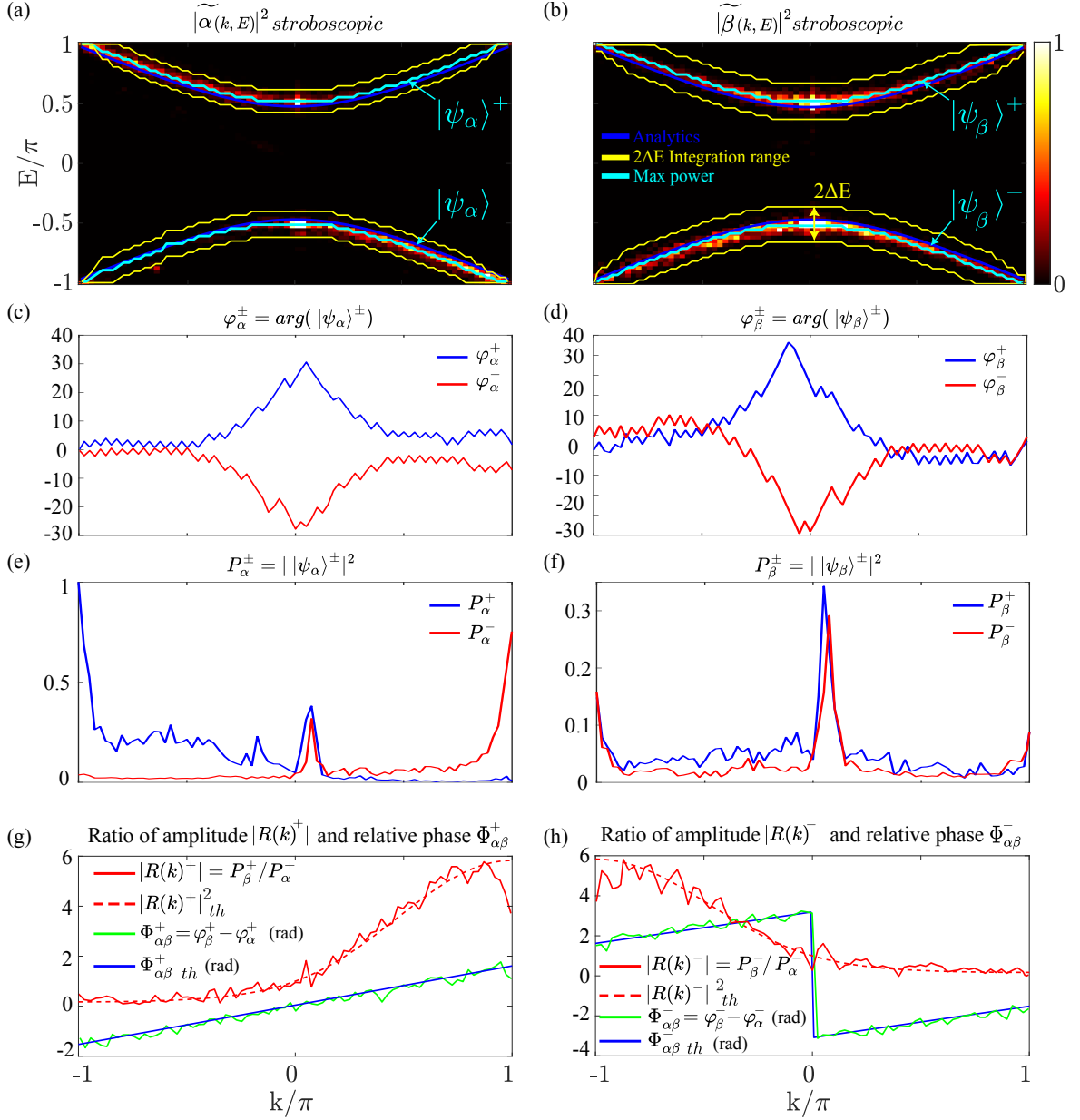


Figure 3.6: Experimental calibration shot. (a-b) Dispersion relation of the α and β rings, respectively. For each ring, we present the following for both the upper and lower bands: (c-d) the spectral phase distribution. (e-f) the spectral power distribution. (g-h) the experimental (analytical) ratio of amplitude $|R(k)|$ in solid (dashed) red, along with the relative phase $\Phi_{\alpha\beta}$ in green (blue) line.

possesses a certain width with less defined edges and an uncontrolled phase profile. Secondly, the spectral power distribution across both the upper and lower bands at $k = \pm\pi$ shows a sharp peak in Figs. 3.6.e-f. This is due to the band structure intersecting the Brillouin zone boundary at points $(k, E) = (\pm\pi, \pm\pi)$, as depicted in Figs. 3.6.a-b. This intersection limits our ability to integrate the experimental power distribution, as two pixels in quasienergy above and below the analytical bands $2\Delta E$ exceed the matrix size [yellow line in Figs. 3.6.a-b]. Lastly, the narrow peak observed at $k = 0\pi$ in the spectral power is attributable to the local oscillator, which manifests as a bright spot on the experimental band structure in

each ring, as shown in Figs. 3.6.a-b. This disturbance has a relatively minor impact on the overall measurement data.

Regarding the discrepancies in spectral power distribution between the experimental and simulated data, as well as the limited resolution of the spectral phase, the experimental eigenstate is effectively characterized by the magnitude amplitude ratio $|R(k)^\pm|$ and the relative phase $\Phi_{\alpha\beta}^\pm(k)$. Figures. 3.6.g and 3.6.h illustrate that the experimental amplitude ratio (red solid line) and the relative phase (green line) for the upper and lower bands, respectively, closely match the analytical amplitude ratio (red dashed line) and the relative phase (blue line).

Despite the active locking of the length of the rings, the phase profile of the light field within the double-ring system exhibits variations from shot to shot due to minor differences in the lengths of the fiber components in the experiment. One effective method to address the issue is to precisely align the relative phase to a reference value, as we will discuss now.

The experimental and analytical relative phase associated with the upper band, as shown in Fig. 3.6.g, follows a well-defined linear distribution given by $\Phi_{\alpha\beta}^+(k) = k/2$ across all quasimomentum values k . For each measured calibration shot, we precisely align the upper band experimental relative phase $\Phi_{\alpha\beta}^+(k = -\pi)$ to $-\pi/2$ via a correlation comparison algorithm with the analytical relative phase. In other words, we introduce an offset to all the measured phase difference values to ensure that the measured phase difference aligns as closely as possible with the analytically expected relative phase, forming a straight, increasing line from $-\pi/2$ to $\pi/2$ across the Brillouin zone. When processing the science part of the recorded time trace, we apply the phase rigid shift found in the calibration shot to the science shot. This ensures an unambiguous phase reference for the measured $\Phi_{\alpha\beta}(k)$ in the science bands. This process is essential for accurately characterizing the two-dimensional relative phase $\Phi_{\alpha\beta}(k, \varphi)$ in the science shots, which requires developing a tomography along the second parametric dimension, the phase modulator φ , by conducting separate measurements for different values of $\varphi \in [-\pi, \pi]$. To ensure consistency in the values of $\Phi_{\alpha\beta}(k, \varphi)$ across different φ , it is critical to use the calibration shot phase as a reference. This necessity underscores the importance of the double-injection protocol in our experimental design.

In summary, despite the slight disparity in the spectral power distribution between the experimental and simulated data, as well as the limited resolution of the spectral phase, we successfully extracted the experimental eigenstate and confirmed its close agreement with theoretical predictions.

3.3 Conclusion

Chapter. 3.1 demonstrates a novel technique for comprehensively characterizing the eigenvalues and eigenvectors. This method was initially been proposed by *A.M. Tikan* for measuring the dispersion relation [143], and it has been successfully implemented for the first time by *C. Lechevalier* [17, 118].

Our heterodyne approach enables the efficient acquisition of the double-ring system's dispersion relation within a single measurement. By encoding phase information within each pulse through optical beating between the local oscillator reference field and the outputs of both fiber loops. Subsequently, by rearranging the impulse response's recorded time trace and applying a two-dimensional Fourier transform to the stroboscopic spatiotemporal diagram, we obtained the band structure that accurately matches the numerical and analytical dispersion relations discussed in (Chapter. 1).

Furthermore, despite the spectral power distribution limitation and the spectral phase resolution, we successfully extracted the experimental eigenstate and confirmed its close agreement with theoretical results. Finally, the extracted eigenvector tomography enables the quantification of topological properties such as Berry curvature and Chern number, which will be the main focus of the next chapter.

BULK TOPOLOGICAL PROPERTIES OF THE TWO-STEP MODEL

Having explored the eigenvalue and the eigenvector extraction in the preceding chapter, we now turn our attention to quantifying the bulk topological invariants of the two-step model, such as the Chern number from the measured eigenvector tomography data. Furthermore, we investigate the extraction of the topological charge at the band structure gap-closing points during a topological phase transitions between distinct regions of the two-step model phase diagram.

4.1 Computing the Berry curvature

Since the discovery of topological phases of matter, the direct measurement of topological invariants in lattice systems has been one of the most difficult experimental challenges. Synthetic systems have opened the possibility of directly measuring the topological invariants in engineered lattices from bulk observables. In one dimension, it has been possible to measure the Zak phase using a lattice for cold atoms [144] and the dipolar displacements in photonic systems [145–148], which are directly related to the bulk invariants. In two dimensions, the Berry curvature (BC) has been determined in lattices of ultracold atoms and in time-multiplexed photonic lattices by measuring the anomalous velocity of a wavepacket adiabatically accelerated across the Brillouin zone [89, 149–151], as previously discussed in Section. 1.4.1, and illustrated in Fig. 1.22.

Berry curvature is related to the geometric phase acquired by a quantum state when external parameters are varied. It is analogous to the effect of a magnetic field on a particle moving in a closed trajectory, where the particle gains a phase proportional to the magnetic flux [152, 153]. In Chapter. 1, Section. 1.1.3, we introduced the Berry curvature as a geometric phase of the two-dimensional band structure, defined by the curl of the Berry connection, $\nabla_{\vec{k}} \times A(\vec{k})_n$, where $A(\mathbf{k})$ is a function of the eigenvectors. To circumvent the challenges posed by the derivatives of the eigenvector field, which can be particularly noisy in experimental conditions, we adopt an alternative approach for calculating the Berry curvature of a specific two-dimensional photonic band. This method leverages the natural discretization of the Brillouin zone inherent in the experimental data to extract

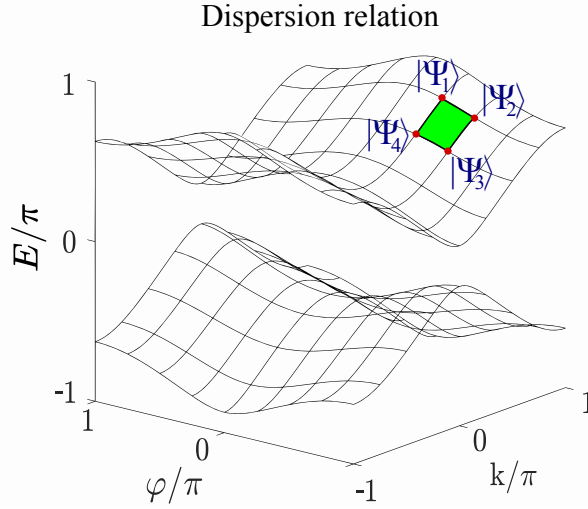


Figure 4.1: Discretization of the two dimensions dispersion relation over the Brillouin zone to compute the Berry curvature.

the Berry curvature (BC). This is achieved by computing the product of the eigenvectors at the four corners of a square within the discretized Brillouin zone [154], as detailed in equation. 4.1 and visualized in Fig. 4.1.

$$BC = -\text{Im} \log [\langle \psi_1 | \psi_2 \rangle \langle \psi_2 | \psi_3 \rangle \langle \psi_3 | \psi_4 \rangle \langle \psi_4 | \psi_1 \rangle]. \quad (4.1)$$

Shiing-Shen Chern introduced in mathematics in the mid-XXth century the concept of the Chern number, a topological invariant that characterizes the topology of a vector field. These concepts were brought into solid-state physics in the 1980s by Thouless, Kohmoto, den Nijs, and Nightingale to describe the topological invariants associated with the energy bands of a two-dimensional electron gas, which result in a surprisingly robust quantization of transport in the quantum Hall effect [155, 156]. Later, these ideas were extended to topological insulators based on the quantum spin Hall effect [157, 158]. The Chern number of a band n is computed by integrating the Berry curvature over the entire Brillouin zone.

$$C^n = \frac{1}{2\pi} \int_{\text{BZ}} BC \, d\vec{k}_x \, d\vec{k}_y. \quad (4.2)$$

4.2 Two-step model bulk topological invariants

We begin this section with a brief overview of the two-step model, previously discussed in Section. 1.3.1 of Chapter. 1. Subsequently, we present numerical and experimental measurements of bulk topological invariants (Berry curvature and Chern number)

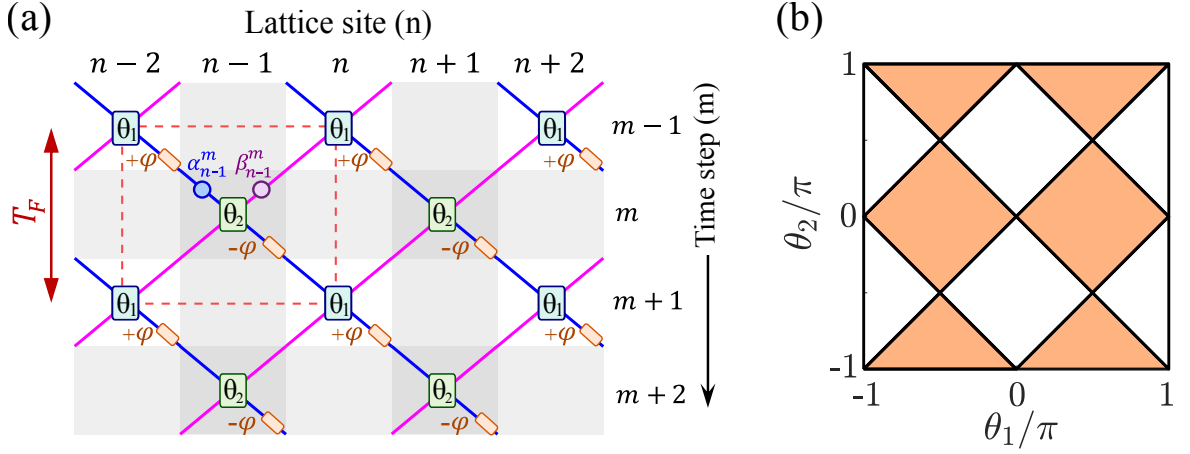


Figure 4.2: (a) A synthetic split-step lattice demonstrating a two-step periodic modulation of the beam splitter's coupling angle, alternating between θ_1 and θ_2 , and the phase modulator's applied phase φ , switching between $+\varphi$ and $-\varphi$ at odd and even time steps, the unit cell holds two sublattices α_{n-1}^m and β_{n-1}^m is presented in a dashed red square. (b) Two-step model phase diagram that features two distinct gapped phases, presented in white and orange.

In the two-step model, the coupling angle θ and the phase modulator φ demonstrate cyclic behavior, each alternating between two distinct values at subsequent time steps within a single Floquet period. The coupling angle alternates between two values, θ_1 and θ_2 , and the phase modulator between $\varphi_1 = +\varphi$ and $\varphi_2 = -\varphi$ at odd and even time steps, as illustrated in the synthetic split-step lattice in Fig. 4.2.a. As a result, Fig. 4.2.b showcases the two-step model phase diagram that features two distinct gapped phases presented in white and orange. These phases are separated by black lines, which indicate the simultaneous closure of the 0- and π -gaps. This occurs when $\theta_1 \pm \theta_2 = n\pi$, with $n \in \mathbb{Z}$.

The two-step model exhibits double periodicity: spatial (every two sites n) and temporal (every two-time steps m), as shown by the unit cell (red dashed square) in Fig. 4.2.a. The normalized eigenvectors $|\psi^\pm(k)\rangle$ and their corresponding eigenvalues $E^\pm(k)$ are defined by equations. 4.3, 4.4 and 4.5 (details in Appendix. A).

$$|\psi^\pm(k)\rangle = \begin{pmatrix} \tilde{\alpha}(k) \\ \tilde{\beta}(k) \end{pmatrix}^\pm = \frac{1}{\sqrt{1 + |R^\pm|^2}} \begin{pmatrix} 1 \\ |R^\pm| e^{i\Phi_{\alpha\beta}^\pm} \end{pmatrix} \quad (4.3)$$

$$R(k)^\pm = |R^\pm| e^{i\Phi_{\alpha\beta}^\pm} = \frac{[e^{iE(k)^\pm} - \cos \theta_2 \cos \theta_1 e^{-ik} e^{i(\varphi_1 + \varphi_2)} + \sin \theta_2 \sin \theta_1 e^{i\varphi_2}]}{[i \cos \theta_2 \sin \theta_1 e^{-ik} e^{i(\varphi_1 + \varphi_2)} + i \sin \theta_2 \cos \theta_1 e^{i\varphi_2}]} \quad (4.4)$$

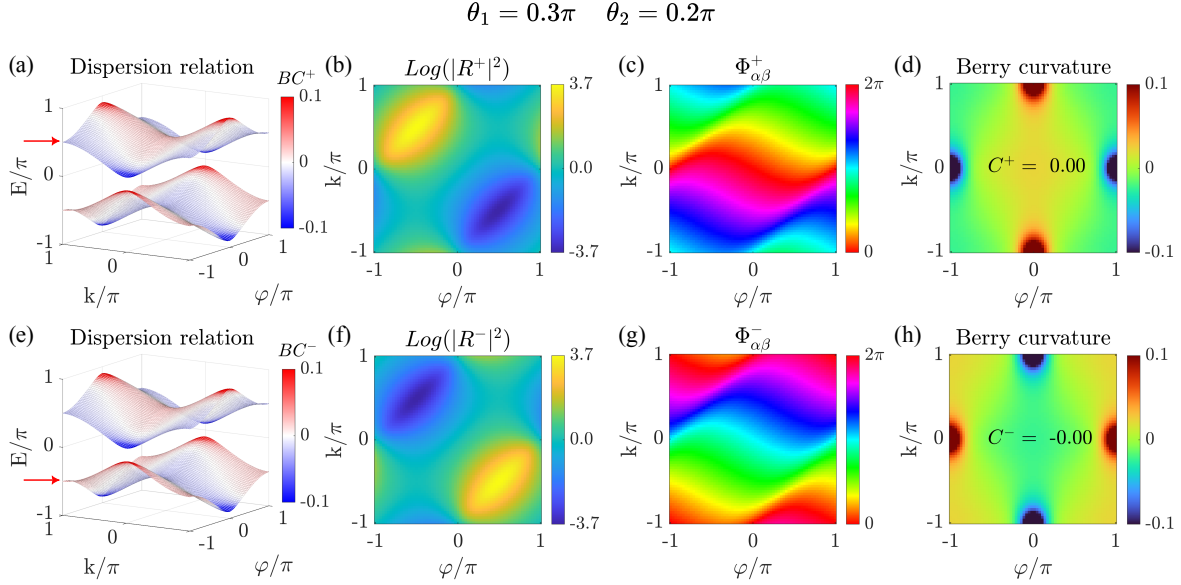


Figure 4.3: Analytical results of the two-step model for $(\theta_1, \theta_2) = (0.3, 0.2)\pi$. The first and second rows display the upper and lower 2D eigenvalues, respectively, along with their corresponding amplitude ratios in (b) and (f), relative phases in (c) and (g), and Berry curvatures with trivial Chern numbers in (d) and (h).

$$E^\pm(k, \varphi_1, \varphi_2, \theta_1, \theta_2) = \pm \cos^{-1} \left[\cos \theta_2 \cos \theta_1 \cos \left(\frac{\varphi_1 + \varphi_2}{2} - k \right) - \sin \theta_2 \sin \theta_1 \cos \left(\frac{\varphi_1 - \varphi_2}{2} \right) \right] + \frac{\varphi_1 + \varphi_2}{2} \quad (4.5)$$

Figure 4.3 displays the analytical solutions of the two-step model, for a set of coupling angles $(\theta_1, \theta_2) = (0.3, 0.2)\pi$ and a phase modulator value $\varphi \in [-\pi, \pi]$. The first and second rows present the upper and lower eigenvalues, as described by equation 4.5, respectively. These are accompanied by their corresponding eigenvectors, as given by equation 4.4, Berry curvature as defined by equation 4.1, and the Chern number obtained from equation 4.2. Figures 4.3.b-c characterize the two-dimensional eigenvectors through the amplitude ratio $|R|^+$ and the relative phase $\Phi_{\alpha\beta}^+$, respectively, of the upper band, as indicated by the red arrow in the dispersion relation in Fig. 4.3.a. The values of $|R|^+$ exhibit a dipole shape, with a high weight in the upper-left corner of the Brillouin zone and a low weight in the lower-right corner. Interestingly, the relative phase $\Phi_{\alpha\beta}^+$ winds between 0 and 2π along the k direction. In contrast, Figs. 4.3.f-g characterize the amplitude ratio $|R|^-$ and the relative phase $\Phi_{\alpha\beta}^-$, respectively, of the lower band, as indicated by the red arrow in the dispersion relation in Fig. 4.3.e. The values of $|R|^-$ exhibit a dipole shape that is opposite to that of the upper band.

Upon fully characterizing the eigenvectors via the amplitude ratio $|R|$ and the relative phase $\Phi_{\alpha\beta}$, we can readily discern the Berry curvature for the upper band at each point of the Brillouin zone using the formula in equation 4.1. This is demonstrated in Fig. 4.3.d, where strong positive and negative Berry curvature,

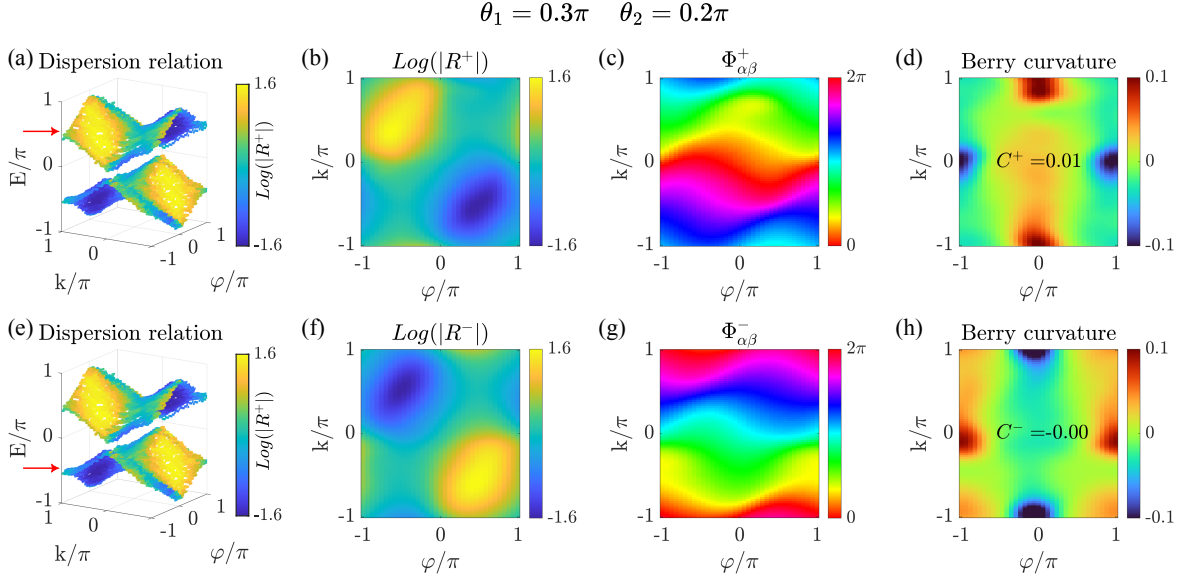


Figure 4.4: Experimental measurements replicating the numerical simulation of Fig. 4.3.

shown in red and blue, is evident around the gap-closing points at energy 0 and π , located at $(k, \varphi) = (0, \pm\pi)$ and $(k, \varphi) = (\pm\pi, 0)$, respectively. For clearer visualization, Fig. 4.3.a and 4.3.e overlays in colors the Berry curvature of the upper (Fig. 4.3.d) and lower band (Fig. 4.3.h) on their corresponding band structures, highlighting the increased concentration of positive and negative Berry curvature as the bands approach each other. A similar analysis of the lower band reveals a Berry curvature distribution opposite in sign to that of the upper band, as illustrated in Fig. 4.3.h. The Chern number is derived by simply integrating the Berry curvature over the Brillouin zone, which equals zero.

Figure. 4.4 presents experimental measurements that closely replicate the numerical simulations shown in Fig. 4.3, utilizing identical parameters. In the simulations, the dipole-shaped weight values of the two-dimensional amplitude ratio $|R|^\pm$ span a logarithmic scale from $[-3.7, 3.7]$ for both the upper and lower bands, as illustrated in Figs. 4.3.b and 4.3.f. However, the experimental amplitude ratio reveals a more constrained range of $[-1.6, 1.6]$, as depicted in Figs. 4.4.b and 4.4.f. This discrepancy arises from the smoothing method that may alter the amplitude ratio weighting, along with the white noise of the electronic devices and light disturbances. Despite this, a comparison of the analytical and experimental results across Figs. 4.3 and 4.4 demonstrate a strong correspondence in the two-dimensional eigenvalues $E(k, \varphi)^\pm$, amplitude ratio (R^\pm), relative phase ($\Phi_{\alpha\beta}^\pm$), Berry curvature (BC^\pm), and Chern number (C^\pm), indicating an excellent agreement between theory and experiment.

To achieve a more accurate measurement of the Berry curvature with reduced fluctuations and noise, we average the measured eigenvector data over five to ten experimental repetitions for each value of the phase modulator φ . This averaging

is performed within the two-dimensional amplitude ratio $R(k, \varphi)$ and the relative phase $\Phi_{\alpha\beta}(k, \varphi)$ tomography. To further enhance data smoothness, we apply Gaussian averaging using Matlab's 'smoothdata' function (refer to Appendix. D).

4.3 Topological charge associated with the phase transition

The two-step model phase diagram exhibits two distinct gapped phases. A transition between these gapped phases requires the closing and reopening of at least one energy gap. As we will see below, this transition is described by the topological charge Q , which is associated with the singularities in the quasi-energies at the gap-closing points. In this section, we present both numerical and experimental measurements of the topological charge corresponding to these singularities during the phase transition.

4.3.1 Phase transition

Figure 4.5.f presents the phase diagram of the two-step model, highlighting five points (a, b, c, d, and e). Points (a) and (b), located within the white region, correspond to coupling angles $(\theta_1, \theta_2) = (0.16, 0.34)\pi$ and $(0.2, 0.3)\pi$, respectively. Point (c) lies at the boundary between the white and orange regions, with a splitting angle set of $(\theta_1, \theta_2) = (0.25, 0.25)\pi$. In the orange region, points (d) and (e) are positioned at $(\theta_1, \theta_2) = (0.3, 0.2)\pi$ and $(0.34, 0.16)\pi$, respectively. The transition under analysis involves the smooth tuning of coupling parameters from point (a) in the white region to point (e) in the orange region.

The upper panels in Figs. 4.5.a-e show the measured two-dimensional quasienergy bands that correspond to the five different points (a, b, c, d, and e) in the phase diagram in panel (f), respectively. Figure. 4.5.a reveals two distinct energy gaps centered around $E = 0$ and $E = \pi$. By smoothly tuning the coupling parameters until they reach $(\theta_1, \theta_2) = (0.25, 0.25)\pi$, the two bands start to converge until they intersect. At this point, both the middle and upper gaps close simultaneously at the gap-closing points M_φ and M_k , located at $(k, \varphi) = (0, \pm\pi)$ and $(k, \varphi) = (\pm\pi, 0)$, respectively, as depicted in Fig. 4.5.c. Subsequently, the energy gap reopens in the orange phase. As the splitting angles set (θ_1, θ_2) deviates further from the black line representing the boundary between the two regions, the band structure progressively flattens, leading to an increase in the energy gap, as demonstrated in Figs. 4.5.d-e.

The second and third panels in Figs. 4.5.a-e present the measured tomography of the eigenvectors of the upper band through the measured ratio of amplitudes $|R|$ and phase difference $\Phi_{\alpha\beta}$ between the two sublattices for each point in the Brillouin

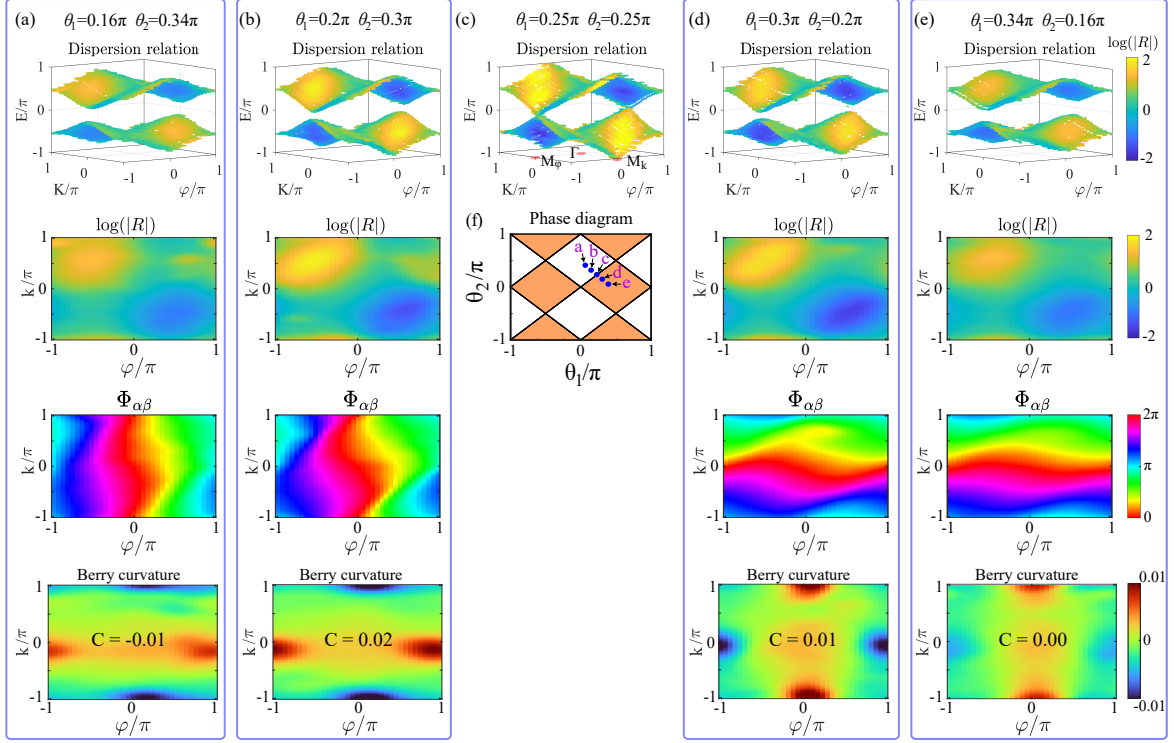


Figure 4.5: (a)-(b) Measured bands, ratio of amplitudes $|R|$, and phase difference $\Phi_{\alpha\beta}$ of the sublattice components of the upper band eigenvectors in the white phase in panel (f): (a) $(\theta_1, \theta_2) = (0.16, 0.34)\pi$; (b) $(\theta_1, \theta_2) = (0.2, 0.3)\pi$. The color code in the uppermost panels depicts the measured value of $|R|$ in log scale. The lowermost panels display the measured Berry curvature of the upper band. (c) Measured bands at the point where the $E = 0$ and $E = \pi$ gaps close ($\theta_1 = \theta_2 = 0.25\pi$). (d)-(e) Same as (a)-(b) for $(\theta_1, \theta_2) = (0.3, 0.2)\pi$ and $(\theta_1, \theta_2) = (0.34, 0.16)\pi$, respectively, in the orange phase. (f) Phase diagram of the system as a function of the splitting angles θ_1 and θ_2 . Black lines indicate the simultaneous closure of the 0- and π -gaps, which happens for $\theta_1 \pm \theta_2 = n\pi$, with $n \in \mathbb{Z}$.

zone. The values of $|R|$ exhibit a dipole shape, with eigenvectors possessing a high weight in the β sublattice in the upper left corner of the Brillouin zone and a low weight in the lower right corner. As the set of the coupling angle approaches the boundary, the dipole weight value increases. Interestingly, within the white region (panels (a)-(b)), the relative phase $\Phi_{\alpha\beta}$ winds along the φ direction, while in the orange phase corresponding to panels (d)-(e), it winds along the k direction. The difference in the winding of the sublattice phase between the two regions is directly linked to the presence of edge states for specific edge realizations, as we will see in Chapter. 5.

The lower panels of Fig. 4.5 depict the measured Berry curvature for the upper band in panels (a)-(b) and (d)-(e). We observe that the Berry curvature around the gap-closing points M_φ and M_k at $(k, \varphi) = (0, \pm\pi)$ and $(k, \varphi) = (\pm\pi, 0)$, respectively, intensifies as the set of coupling angles (θ_1, θ_2) approaches the boundary in the phase diagram, as indicated by the blue points in Fig.4.5.f. Additionally, upon

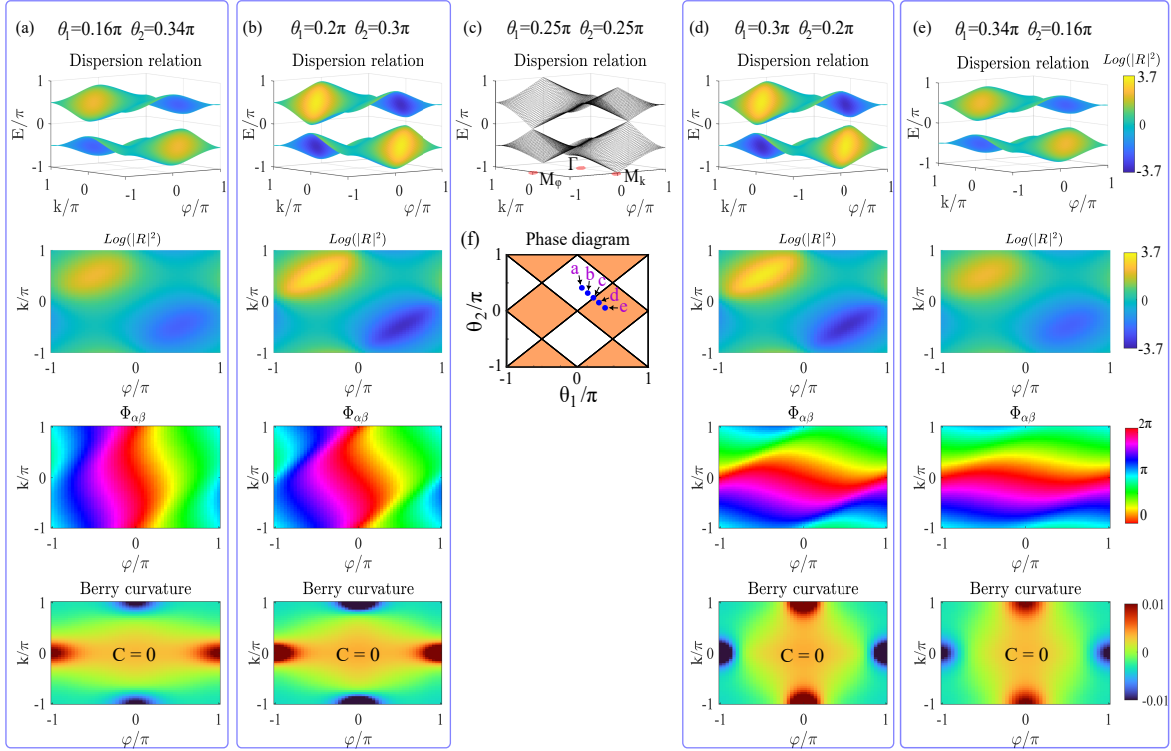


Figure 4.6: Analytical eigenvalues (top row), and the relative amplitude and phase difference between the two sublattices for the eigenvectors corresponding to the upper band under the same conditions of Fig. 4.5. The bottom row displays the Berry curvature computed from the analytic eigenvalues.

crossing the gap-closing transition, the Berry curvature exhibits a sign change, as depicted in panels (b) and (d). Conversely, the Berry curvature is not defined at the gap-closing point. The measured Chern number is approximately zero in all cases, with values of -0.01 in (a), 0.02 in (b), 0.01 in (d), and 0.00 in (e).

Figure. 4.6 presents the analytical values given by equations. 4.1, 4.4 and 4.5 that accurately replicate the experimental measurements shown in Fig. 4.5. Additionally, the analytical results reveal a Chern number of zero across all regions of the phase diagram for coupling angles $\theta \in [-\pi, \pi]$. However, our experimental investigations were constrained to a narrower range of coupling angle $\theta \in [0, \pi/2]$, due to limitations in the amplification voltage as previously explained in Chapter. 2.

Despite the zero Chern number in both phases (white and orange), the change of sign of the Berry curvature around the gap-closing points M_φ and M_k across the gap-closing transition in Figs. 4.5 and 4.6 is a direct manifestation of the topological nature of this transition between two distinct regions. This feature is captured by the topological charge, which we will explore in the next subsection.

4.3.2 Topological charge

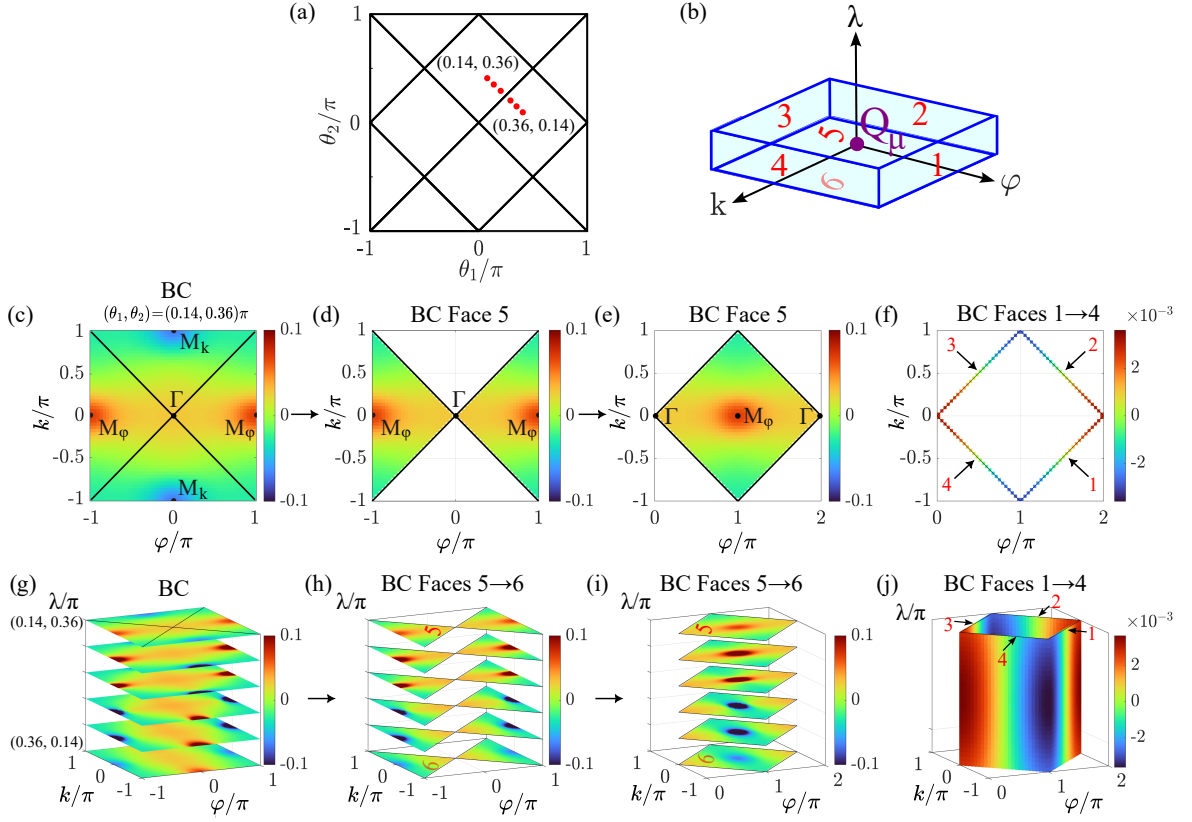


Figure 4.7: (a) Topological phase diagram showing six distinct points across two regions. (b) Cuboid in parameter space (k, φ, λ) , where λ tracks the evolution of the splitting amplitudes θ_1 and θ_2 during the phase transition. (c) Numerical simulation of the Berry curvature at $(\theta_1, \theta_2) = (0.14, 0.36)$. (d) Transversal Berry flux at face 5 of the cuboid. (e) Shifted version of (d) along the φ axis. (f) Lateral Berry flux through faces 1-4. (g-j) Corresponding tomography of panels (c-f), illustrating the variation of parameters (θ_1, θ_2) across the phase transition from the upper side (5) to the lower side (6) of the cuboid.

During a phase transition, the topological charge Q_μ associated with a specific band (upper or lower) is determined by summing the Berry flux B_μ^λ outgoing from each face of the cuboid that surrounds the gap-closing point μ of the quasi-energies [89, 159], as shown in Fig. 4.7.b and given by equation. 4.6. In analogy with the Chern number, the Berry flux defined by equation. 4.7 describes the integral of the Berry curvature over a surface in parameter space, while the Chern number accounts for the entire Brillouin zone.

$$Q_\mu = \sum_{i=1}^6 B_\mu^{\text{Face } i} \quad (4.6)$$

$$B_\mu^\lambda = \int_S BC dS \quad (4.7)$$

The cuboid is centered at the band touching singularity at the phase transition, spans a part of quasimomentum space (k, φ) , and consists of two transversal faces (5 and 6) along with four lateral faces (1-4). The third dimension, $\lambda = (\theta_1, \theta_2)$, captures the evolution of the splitting amplitude angles as the system transitions from Phase I at layer 5 of the cuboid to Phase II at layer 6. The outgoing transversal Berry flux through faces 5 (upper) and 6 (lower) of the cuboid in Fig. 4.7.b can be directly extracted from the integration of the Berry curvature around the high symmetry point M_φ or M_k , at which the band touching point takes place.

The Berry flux through the lateral faces (1-4) represents the border of the extracted transversal Berry flux and can be neglected if $\Delta\lambda$ is sufficiently small, that is, if the Berry curvature in momentum space is measured at points sufficiently close to the phase transition. In such a scenario, the topological charge at the μ gap can be expressed as follows:

$$Q_\mu = B_\mu^{\text{Face 5}} + B_\mu^{\text{Face 6}} = B_\mu^{\text{Phase I}} - B_\mu^{\text{Phase II}} \quad (4.8)$$

The prefactor -1 before the term $B_\mu^{\text{Phase II}}$ in equation. 4.8 comes from the fact that we evaluate the flux exiting the cuboid through the lower face, which is opposite to the orientation of the λ axis. Therefore, the topological charge is determined by evaluating the difference between the Berry flux B_μ^λ just before (Phase I) and just after (Phase II) the phase transition, surrounding the gap-closing point μ . This topological charge Q_μ thus corresponds to a local Chern number, which is different from the band Chern number obtained from the Berry flux through the first Brillouin zone, which vanishes here. For the other band, the topological charge associated with the gap-closing transition has an opposite sign.

To gain a better understanding of the transversal and lateral Berry flux, we will now consider a simple numerical simulation. Imagine a transition from a red point in Phase I at coordinates $(\theta_1, \theta_2) = (0.14, 0.36)$ to another red point in Phase II at $(0.36, 0.14)$, as shown in Fig. 4.7.a. Along this path, we can pick six distinct points located at $[(0.14, 0.36), (0.17, 0.33), (0.2, 0.3), (0.3, 0.2), (0.33, 0.17), \text{ and } (0.14, 0.36)]$. The initial point $(0.14, 0.36)$ in Phase I corresponds to the upper face (5) of the cuboid, while the final point of the phase transition represents the lower face (6). The Berry curvature of the initial point is presented in Fig. 4.7.c. By diving The Berry curvature along the first Brillouin zone into four regions, as depicted by the black lines in Fig. 4.7.c and extracting only the Berry flux surrounding one of the gap-closing points, in this example, we select the gap-closing point M_φ , located at $(k, \varphi) = (\pm\pi, 0)$, we obtain the transversal Berry flux at layer 5 of the cuboid, as depicted in Fig. 4.7.d. To enhance visualization, Fig. 4.7.e presents a shifted version of Fig. 4.7.d along the φ direction from $[-\pi, \pi]$ to $[0, 2\pi]$. The lateral Berry flux outgoing throughout the faces (1-4) is derived from the border of the transversal Berry flux at layer 5, as highlighted in Fig. 4.7.f.

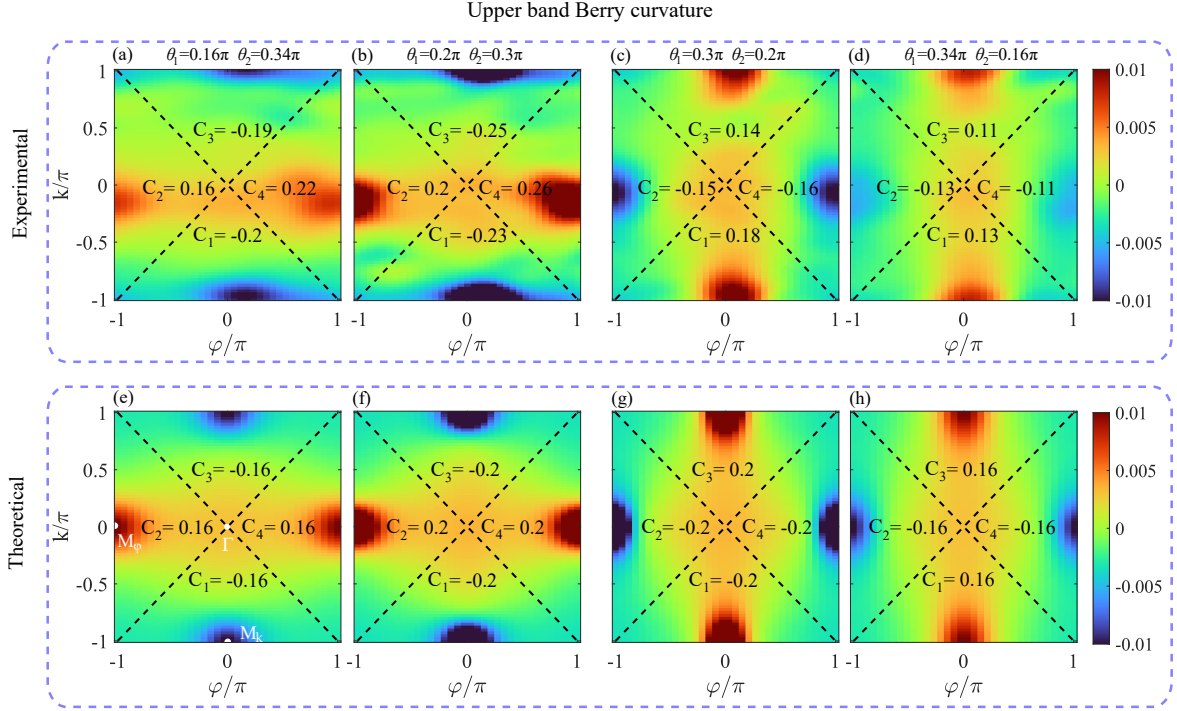


Figure 4.8: Measured (upper panels) and analytically (lower panels) computed Berry curvature for the upper band at points in the phase diagram displayed in Fig. 4.5.f. Each Berry curvature is divided into four regions, the numbers in each quadrant show the integrated Berry curvature in the quadrant.

By applying the same procedure to each of the six points corresponding to a specific splitting amplitude (θ_1, θ_2) , the Berry curvature tomography is visualized as a 3D representation in parameter space (k, φ, λ) , as depicted in Fig. 4.7.g. This is achieved by varying the parameters (θ_1, θ_2) across the phase transition from the upper face (5) to the lower face (6) of the cuboid, while stacking the Berry curvature associated with each point. Subsequently, the transversal Berry flux tomography was constructed by extracting the Berry flux surrounding the gap-closing points M_φ , as demonstrated in Fig. 4.7.h and the shifted version in Fig. 4.7.i. Finally, the outgoing flux through the lateral faces (1-4) of the cuboid, as displayed in Fig. 4.7.j, is deduced by smoothly varying the set of coupling angles (θ_1, θ_2) from $(0.14, 0.36)\pi$ to $(0.36, 0.14)\pi$ across 100 intermediate points. The evaluated Berry flux through each of the lateral faces is zero.

Having analyzed the phase transitions, and the outgoing flux through the cuboid, we can now proceed to measure experimentally and analytically the topological charge Q_μ at the gap-closing points M_φ and M_k . Figure. 4.8 upper and lower panels present the experimental and analytical Berry curvature across the phase transition, corresponding to the earlier results presented in the lower panels of Fig. 4.5 and Fig. 4.6, respectively.

To determine the topological charge at the $\mu = 0$ gap, we divide the Brillouin zone into four regions as indicated by the dashed lines in Fig. 4.8 and integrate the

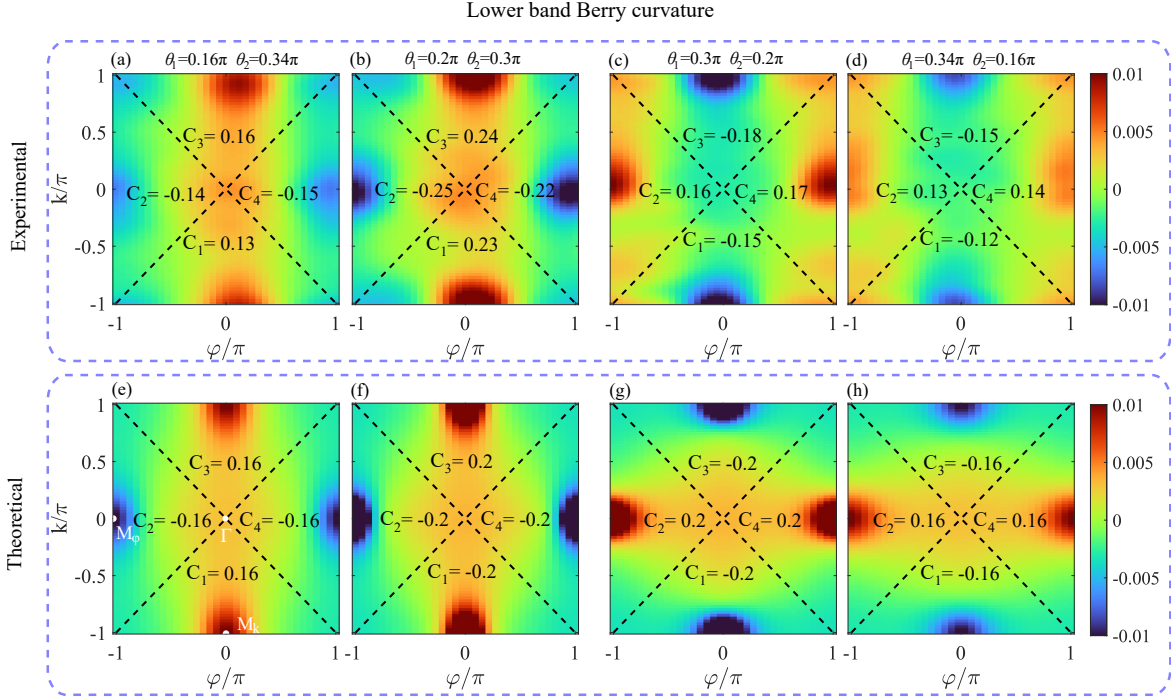


Figure 4.9: Measured (upper panels) and analytically (lower panels) computed Berry curvature for the lower band at points in the phase diagram displayed in Fig. 4.5.f. Each Berry curvature is divided into four regions, the numbers in each quadrant show the integrated Berry curvature in the quadrant.

measured Berry curvature over regions 2 and 4, which surround the M_φ point. The white region side (Phase I) in Fig. 4.5.f corresponds to the upper face of the cuboid. Close to the phase transition, the outgoing Berry flux is $B_{\mu=0}^{Phase I} = (C_2 + C_4) = 0.46$ as depicted in Fig. 4.8.b. At the orange side (Phase II) depicted in Fig. 4.8.c, $B_{\mu=0}^{Phase II} = -0.31$. The total measured flux is $B_{\mu=0}^{Phase I} - B_{\mu=0}^{Phase II} = 0.77$, close to the value of 0.80 computed from the analytic eigenvectors and represented in Figs. 4.8.f-g. The expected value of the topological charge is 1. Nevertheless, the analytic Berry flux through the lateral faces is zero (see Fig. 4.7.j). Therefore, the difference with the measured values stems from the spread of the Berry curvature associated with the M_φ point at finite gap sizes. By studying the Berry flux at points closer to the phase transition, analytic calculations show that the value of $Q_{\mu=0}$ extracted from the Berry flux approaches 1. To study a situation with a smaller gap, experimentally we are limited by the resolution of the quasienergy bands, which is given by the number of accessible round trips (66 in our case).

Similar to the $\mu = 0$ gap, we can calculate the Berry flux around the gap-closing point for $\mu = \pi$. To maintain consistent sign conventions, we must evaluate the Berry flux on the lower band around the M_k point at $(k, \varphi) = (\pm\pi, 0)$. Our experimental measurements, obtained by integrating the measured Berry curvature over regions 1 and 3, yielded $B_{\mu=\pi}^{Phase I} - B_{\mu=\pi}^{Phase II} = (0.24 + 0.23) - (-0.18 - 0.15) = 0.80$ (Figs. 4.9.b-c). This value aligns perfectly with the theoretical value of 0.80 computed from the analytic eigenvectors (Figs. 4.9.f-g). While the measured Berry

fluxes may deviate slightly from the ideal value of 1 for the topological charge at the transition, they are significantly different from zero, allowing for definitive identification of the topological nature of the phase transition.

A similar analysis was recently done in an ultracold atoms experiment implementing a two-band, two-dimensional lattice subject to periodic shaking [89]. In that case, the studied topological phases involved phase transitions with the closure of a single gap at a time, and a change of the number of edge states in that specific gap through the transition. To determine the topological charge related to the gap-closing singularity, the Berry flux was computed across the whole Brillouin zone, that is, via the change of Chern number in the bands across the transition. In our case, both gaps close and open simultaneously, and the Chern number of the bands is zero in all topological regions. Our study shows that a local analysis of the Berry flux around each gap closing point allows an accurate characterization of the local topological charge.

In this section, we investigated the topological phase transition between two distinct gapped topological phases by smoothly adjusting the splitting angles θ_1 and θ_2 . A topological phase transition between gapped phases requires the closing and reopening of at least one energy gap. We characterized this transition using the topological charge Q_μ , which we determined by calculating the difference between the outgoing Berry flux just before and after the gap-closing point.

4.4 Interface State

The non-trivial topological charge is a direct consequence of the Berry curvature changing sign locally at the gap-closing points in quasimomentum space. This topological property manifests the emergence of an interface state when lattices in the two different topological regions are pasted together, as depicted in Fig. 4.10.b. We implement a lattice with two different spatial regions by engineering the splitting angle properly on either side of the boundary [160]. Figure. 4.10.b shows a sketch of the employed lattice: the left part belongs to the white phase with $(\theta_1, \theta_2) = (0.2, 0.3)\pi$ (red dot in Fig. 4.10.a), while the right part belongs to the orange phase with $(\theta_1, \theta_2) = (0.3, 0.2)\pi$ (Blue dot in Fig. 4.10.a). By precisely injecting an initial pulse at the interface site of the long ring α and setting the phase modulator to $\varphi = \pi$, numerical simulations reveal that a portion of the light remains localized at the interface in both the long and short rings, as shown in Figs. 4.10.c and 4.10.g, respectively. Figures. 4.10.d and 4.10.h present the corresponding stroboscopic spatiotemporal diagrams for panels (c) and (g), respectively, by considering only odd site positions (n) and round trips (m).

Applying a two-dimensional Fourier transform to Figs. 4.10.d and 4.10.h, the dispersion relation is uncovered, displaying a localized state at energy 0, as de-

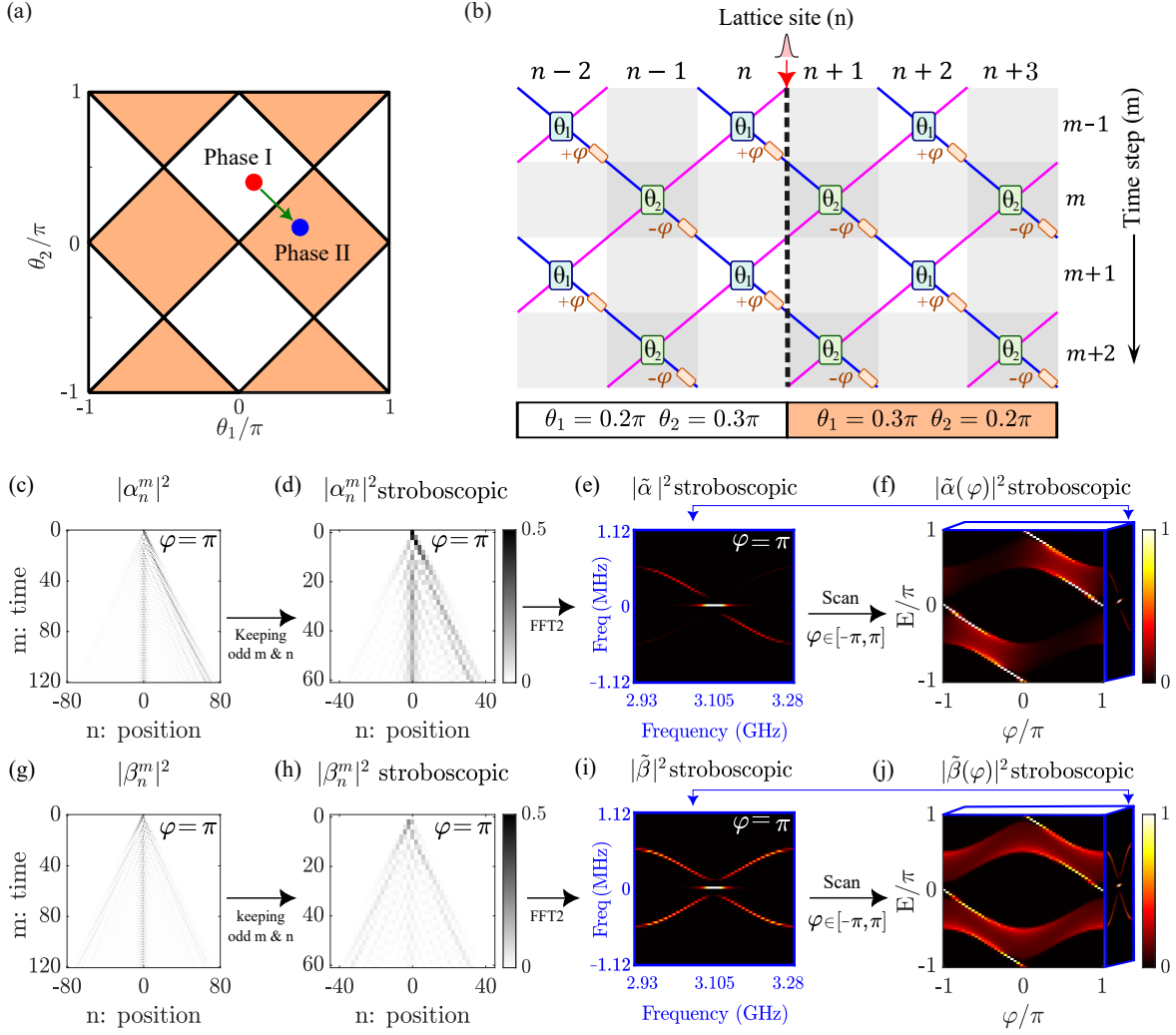


Figure 4.10: Numerical simulations. (a) A two-step model phase diagram illustrating two distinct topological regions, with a red dot in the white region at $(\theta_1, \theta_2) = (0.2, 0.3)\pi$ and a blue dot in the orange region at $(\theta_1, \theta_2) = (0.3, 0.2)\pi$. (b) A custom-designed synthetic photonic lattice with a specific splitting angle, created by merging two different topological regions. (c)-(g) Spatiotemporal dynamics of the long and short rings, respectively. (d) and (h) Corresponding stroboscopic spatiotemporal diagrams of panels (c) and (g). (e) and (i) Two-dimensional Fourier transforms of panels (d) and (h), revealing the dispersion relation with a localized state at energy level 0. (f) and (j) Band structure tomography when scanning φ from $-\pi$ to π .

picted in Figs. 4.10.e and 4.10.i. Due to the non-periodic modulation along the horizontal axis, representing the lattice site (n) in Fig. 4.10.b, the unit cell presented previously by a red dashed line in Fig. 4.2 is no longer defined. The typical quasi-momentum (k) and quasi-energy (E) axes associated with the dispersion relation are replaced with frequency axes, as illustrated by the blue frequency axes in Figs. 4.10.e and 4.10.i. To simulate the band along these frequency axes, a new numerical simulation strategy was employed by modulating the absolute amplitude of the pulse described in the equation. 1.19 with a 3 GHz reference field. This accurately replicates the experimental heterodyne procedure, which consisted of two

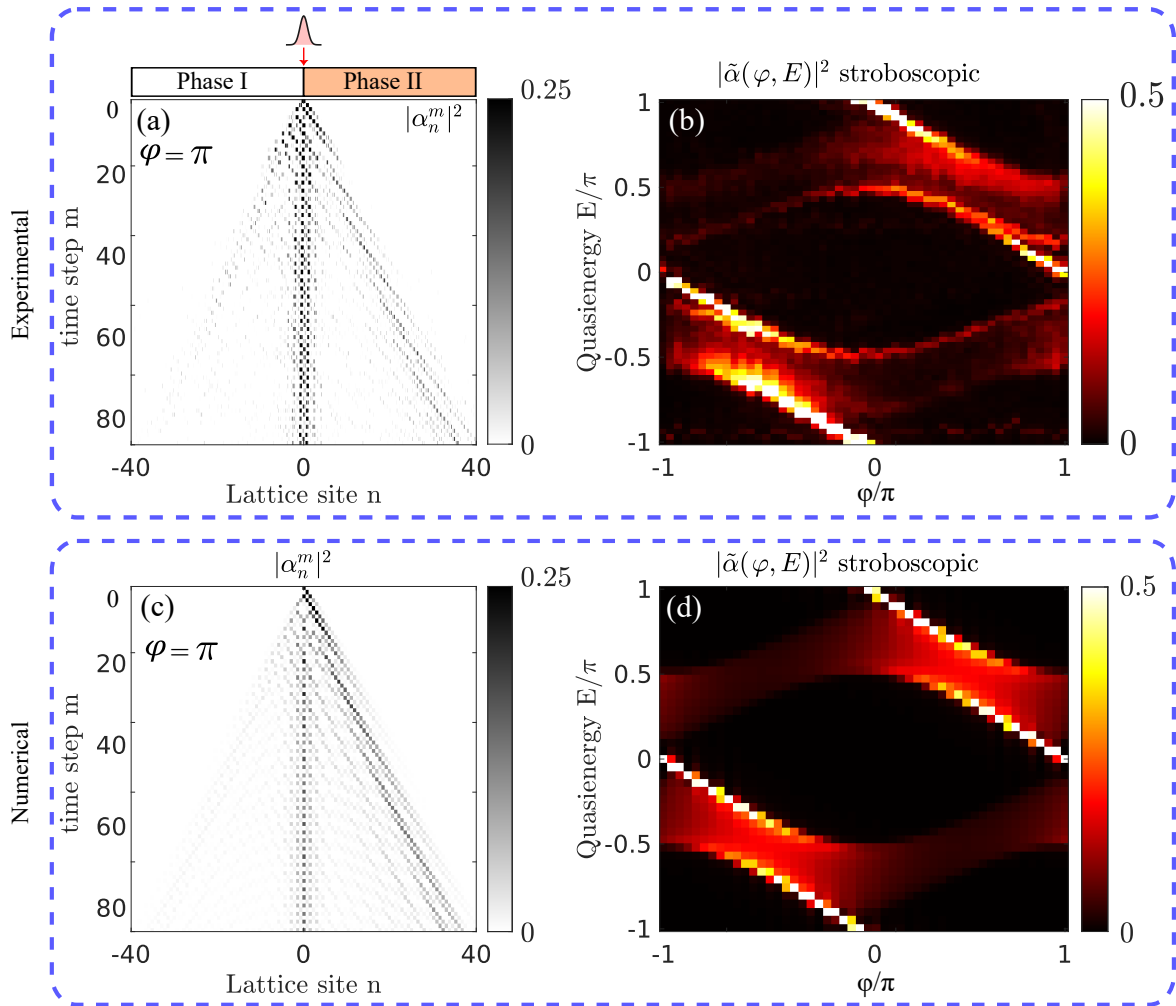


Figure 4.11: Experiments. (a) Measured step walk when exciting a single site at the interface between a lattice in the white region $(\theta_1, \theta_2) = (0.2, 0.3)\pi$ and a lattice in the orange region $(\theta_1, \theta_2) = (0.3, 0.2)\pi$ for $\varphi = \pi$. (b) Measured band structure as a function of φ showing an interface state traversing both gaps. (c) and (d) Numerical simulation of equation. 1.12 in the conditions of the experiment.

sequential numerical shots: a calibration shot and a science shot. By identifying the excited spectral regions within specific frequency windows, corresponding to the numerically calibrated bands, we were able to effectively analyze the interface scenario. This approach is identical to the technique used to extract the measured eigenvalues in Chapter. 3.

The subsequent results in Figs. 4.10.e and 4.10.i correspond to a specific phase modulator value. To provide a complete view of the edge state, we repeat the same numerical computation for all the phase modulator values φ from $-\pi$ to π while maintaining the injection at the interface. By stacking the resulting band structures for each value of φ , we obtain the band tomography shown in Figs. 4.10.f and 4.10.j. Each gap is crossed by a single band of interface states, exhibiting a group velocity with the same sign. This behavior corresponds to an anomalous topological phase.

The numerical simulation in Fig. 4.10 is now compared with the experimental measurement, as presented in Fig. 4.11, demonstrating the system's behavior when exciting a single site in the long ring α at the interface between two lattices: one in the white region $(\theta_1, \theta_2) = (0.2, 0.3)\pi$ and the other in the orange region $(\theta_1, \theta_2) = (0.3, 0.2)\pi$. Figure. 4.11.a highlights the measured spatiotemporal dynamics, constrained to the range $[0, 0.25]$, to enhance visualization within the long ring α for $\varphi = \pi$, where part of the light remains localized at the interface state. The measured band's tomography, obtained by scanning φ values from $-\pi$ to π , is shown in Fig. 4.11.b. The upper panels of Fig. 4.11 display the experimental results and show excellent agreement with the corresponding numerical simulations in the lower panels.

4.5 Conclusion

Reflecting on the findings presented in this chapter, we have investigated the bulk topological properties of the static two-step model system (without temporal modulation). Our results indicate that all regions in the phase diagram exhibit a zero Chern number. Nevertheless, locally, the Berry curvature changes sign at the gap-closing points, revealing non-trivial topological properties characterized by a topological charge associated with the phase transitions. These properties are evidenced through the existence of interface states when two lattices belonging to two adjacent regions of the phase diagram are pasted together.

Questions:

- 1- Are there any topological properties associated with time-dependent modulations within the two-step model? and how do they influence the behavior of edge states?
- 2- Can we distinguish between trivial and anomalous regions in the two-step model phase diagram?

These questions are explored in further detail in the next Chapter. 5.

EDGE DEPENDENT TOPOLOGY OF THE TWO-STEP MODEL

In our previous chapter, we experimentally observed that the anomalous topology of our lattice is revealed by the non-trivial topological charge at the gap-closing singularities. However, we have not yet fully characterized the topological phases within this system. In this chapter, we shed light on these distinct phases by examining edge states using two distinct approaches. The first method emphasizes the influence of lattice geometry on the presence of edge states, which is dictated by the choice of boundary condition. This choice is not only related to the selection of the bulk unit cell, as it is in certain static Hamiltonian systems (e.g., the SSH Hamiltonian), but also to a specific time frame in discrete step walks. To capture this interplay, we introduce a topological invariant that takes into account the choice of unit cell/time frame associated with the specific boundary conditions developed by our collaborator, Álvaro Gómez-León [1]. Our second approach utilizes extrinsic topology, which demonstrates that, owing to the topological properties of the boundaries, gapless boundary states can arise even when the bulk bands are topologically trivial. Finally, we demonstrate that our experimental platform paves the way for advanced edge-state engineering by introducing arbitrary unitary operators at the edge sites and dynamically controlling the variable beam splitter and phase modulator. This precise manipulation allows us to suppress or induce edge states.

5.1 Edge dependent topological invariant

Anomalous topological phases [7–9], where edge states coexist with topologically trivial Chern bands ($C=0$), can only appear in periodically driven lattices. When the driving is smooth and continuous, the bulk-edge correspondence is guaranteed by the existence of a bulk invariant known as the winding number. Unlike Floquet systems, whose dynamics are governed by continuous time-modulations of a Hamiltonian [83], recent discussions have shown that quantum walk systems offer richer topological phases due to their discrete time evolution. Notably, the presence of edge states, particularly in anomalous topological phases, cannot be fully explained by bulk invariants alone but also depends on the topology of the edges (extrinsic topology) [10, 161, 162].

Experimentally, Floquet anomalous topological phases, have been realized in one-dimensional discrete step walks [11–14] and in two-dimensional photonic lattices with continuous time evolution [15, 16]. However, no previous work has studied the anomalous topological phases in a two-dimensional discrete step walk. In this section, we delve into this intriguing case, in particular, we show that the specific choice of boundaries affects the existence of edge states and provides a suitable expression that defines the winding numbers that we directly measure in the experiment.

5.1.1 Bulk topology

The dynamics of the amplitude and phase of light pulses in the rings are described by the evolution equations at each time-step (m) and lattice site (n):

$$\begin{cases} \alpha_n^{m+1} = [\alpha_{n-1}^m \cos(\theta_{n-1}^m) + i\beta_{n-1}^m \sin(\theta_{n-1}^m)] e^{i\varphi_{n-1}^m} \\ \beta_n^{m+1} = i\alpha_{n+1}^m \sin(\theta_{n+1}^m) + \beta_{n+1}^m \cos(\theta_{n+1}^m) \end{cases} \quad (5.1)$$

For our two-step protocol, we can write the equations of motion describing the time evolution during each full period as:

$$\begin{cases} \alpha_n^{m+2} = [-\alpha_n^m \sin(\theta_n^m) + i\beta_n^m \cos(\theta_n^m)] \sin(\theta_{n-1}^{m+1}) e^{i\varphi_{n-1}^{m+1}} \\ \quad + [\alpha_{n-2}^m \cos(\theta_{n-2}^m) + i\beta_{n-2}^m \sin(\theta_{n-2}^m)] \cos(\theta_{n-1}^{m+1}) e^{i(\varphi_{n-2}^m + \varphi_{n-1}^{m+1})} \\ \beta_n^{m+2} = [i\alpha_n^m \cos(\theta_n^m) - \beta_n^m \sin(\theta_n^m)] \sin(\theta_{n+1}^{m+1}) e^{i\varphi_n^m} \\ \quad + [i\alpha_{n+2}^m \sin(\theta_{n+2}^m) + \beta_{n+2}^m \cos(\theta_{n+2}^m)] \cos(\theta_{n+1}^{m+1}) \end{cases} \quad (5.2)$$

In a stroboscopic framework, the evolution of the two-step model at discrete intervals is characterized by the Floquet operator, which is the product of two unitary operators and describes the evolution after each one of the two steps: $U_{\text{QW}} = U_2 U_1$. The complete time evolution of the initial state over many periods is described by the successive application of these operators, leading to the general form of the evolution operator:

$$U = \dots U_2 U_1 U_2 U_1 U_2 U_1 \dots \quad (5.3)$$

The bulk topology under periodic boundary conditions (PBC)¹ can be determined from the Floquet operator $U_{\text{QW}}(\mathbf{q})$ in reciprocal space. The latter can be written in the form of equation. 5.4, which describes one period of the quantum walk, and it is obtained by applying the Fourier transform to the equation. 5.2 for the two-step protocol.

¹ PBC is a type of boundary condition, where the edges or ends of a finite system are effectively connected to each other, forming a loop.

$$U_{\text{QW}}(\mathbf{q}) = v_0(\mathbf{q})\sigma_0 + i\mathbf{v}(\mathbf{q}) \cdot \boldsymbol{\sigma} \quad (5.4)$$

With $\mathbf{q} = (k, \varphi)$ a two-dimensional vector, $\boldsymbol{\sigma} = (\sigma_x, \sigma_y, \sigma_z)$ denote the Pauli matrices and σ_0 being the identity matrix. The components of the vector $\mathbf{v}(\mathbf{q})$ can be expressed in the following form:

$$\begin{cases} v_0 = J_1 \cos(k) - m_1 \cos(\varphi) \\ v_x = J_2 \cos(k) + m_2 \cos(\varphi) \\ v_y = J_2 \sin(k) + m_2 \sin(\varphi) \\ v_z = -J_1 \sin(k) + m_1 \sin(\varphi) \end{cases} \quad \text{with} \quad \begin{cases} J_1 = \cos(\theta_1) \cos(\theta_2) \\ J_2 = \sin(\theta_1) \cos(\theta_2) \\ m_1 = \sin(\theta_1) \sin(\theta_2) \\ m_2 = \cos(\theta_1) \sin(\theta_2) \end{cases} \quad (5.5)$$

The four parameters (J_1 , J_2 , m_1 , and m_2) being functions of the angles $\theta_{1,2}$ of the variable beamsplitter are not independent (only $\theta_{1,2}$ are) due to the unitarity of the time-evolution operator that imposes the constraints $J_1 m_1 = J_2 m_2$ and $J_1^2 + J_2^2 + m_1^2 + m_2^2 = 1$.

Importantly, to write this Floquet operator, we fixed the reference frame by assuming that U_1 acts before U_2 . This implies that during the first and second-time steps, the beamsplitter angles are set to θ_1 and θ_2 , respectively. Additionally, the synthetic dimension is generated by imposing the condition $\varphi_m = -\varphi_{m+1} = \varphi$. This allows us to identify the two-step stroboscopic evolution generated by $U_{\text{QW}}(\mathbf{q})$ with the blue time-slices in the schematic of Fig. 5.1.a. However, due to time-periodicity, another perfectly valid choice would have been to consider a shifted time frame in which the beamsplitter is set to θ_2 and θ_1 during the first and second-time steps, respectively. We will refer to this alternative choice as $\tilde{U}_{\text{QW}}(\mathbf{q})$, which corresponds to the red time-slices of the evolution in Fig. 5.1.a. Their matrix representation differs, but they are connected by the swap of the angles $\theta_1 \leftrightarrow \theta_2$, plus an additional sign change in the quasimomentum $\varphi \rightarrow -\varphi$. Their equivalence becomes more clear when one checks that their quasienergy spectrum is identical, and therefore, $\tilde{U}_{\text{QW}}(\mathbf{q})$ and $U_{\text{QW}}(\mathbf{q})$ have identical Floquet bands.

To study the bulk topology, it's necessary to examine the symmetry class of $U_{\text{QW}}(\mathbf{q})$. This is done by checking for the presence of particle-hole symmetry (PHS), which is defined as:

$$\mathcal{C}U_{\text{QW}}(\mathbf{q})\mathcal{C}^{-1} = U_{\text{QW}}(-\mathbf{q}) \quad (5.6)$$

with $\mathcal{C} = \sigma_z K$ being the anti-unitary operator associated to particle-hole symmetry, K the conjugation operation and σ_z the third Pauli matrix. Also, the PHS operator fulfills $\mathcal{C}^2 = +1$, placing the Floquet operator in class D in two dimensions (sys-

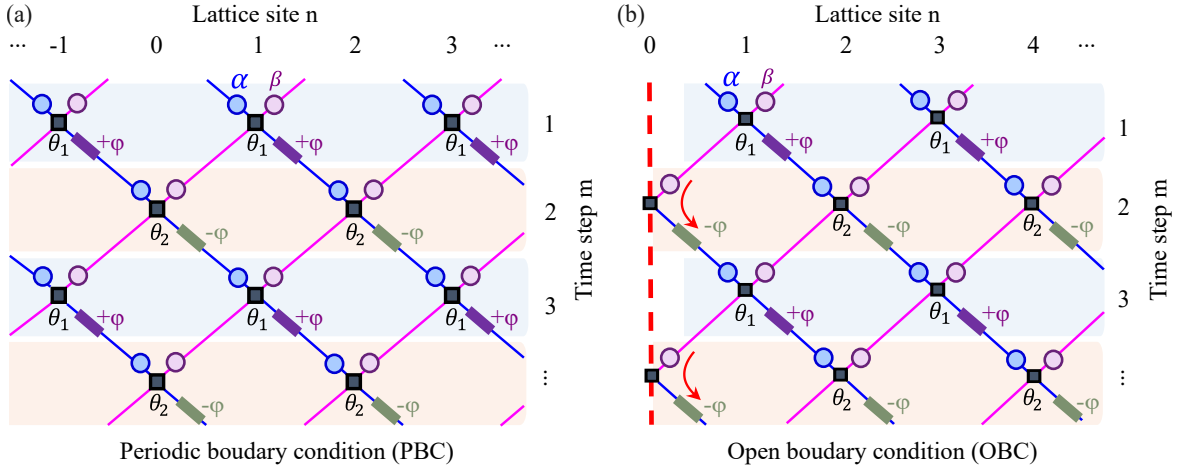


Figure 5.1: (a) Schematic of the quantum walk with periodic boundary conditions (PBC) applied along both the spatial and synthetic dimensions. (b) Schematics of the quantum walk with open boundary conditions (OBC) with the vacuum along the spatial coordinate at site $n=0$ and (PBC) along the synthetic dimension φ .

tems exhibiting particle-hole symmetry but no time-reversal or chiral symmetry) in the Altland-Zirnbauer (AZ) classification [10, 163]. This implies that the bulk invariant describing our system is the Chern number [164]. The numerical calculation of the Berry curvature distribution perfectly aligns with the one measured in the experiment, as previously shown in Chapter. 4, Fig. 4.8, and vanishes when summed over the whole Brillouin zone, for all values of θ_1 and θ_2 . Hence, the Chern number of the Floquet bands is zero, indicating that only trivial or anomalous phases are possible in our system. However, we have experimentally demonstrated above that the two phases separated by a gap closure are topologically distinct because chiral edge states develop at their interface (see Fig. 4.11). Therefore, despite the vanishing Chern number, the phase diagram must include at least one anomalous Floquet phase. This phase is characterized by a different topological property, distinct from the Chern number, that arises from the time-dependent modulations, which we will explore in more detail in the next subsection.

5.1.2 Reference frames and open boundary conditions

To identify experimentally each phase of the phase diagram independently, we implement open boundary conditions (OBC)² with the vacuum along the spatial coordinate (i.e., we end the lattice at a sharp edge) and periodic boundary conditions (PBC) along the synthetic one. OBC is implemented by dynamically changing the variable beamsplitter (VBS) at the edge, and setting its value to full reflectance as presented in the quantum walk lattice in Fig. 5.1.b.

² OBC is a type of boundary condition where the system is not fully enclosed or periodic.

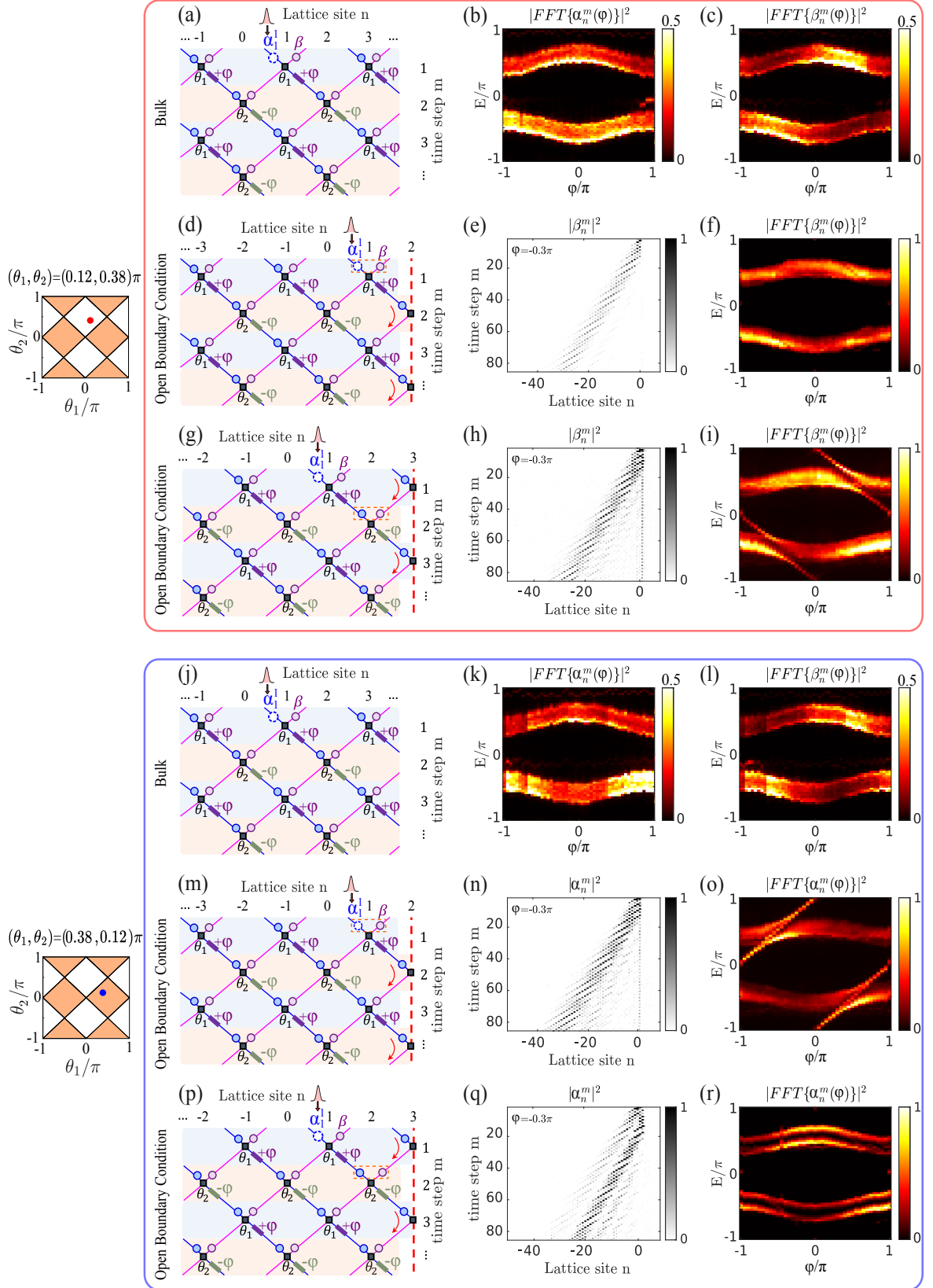


Figure 5.2: Upper (red) and lower (blue) boxes correspond to $(\theta_1, \theta_2) = (0.12, 0.38)$ and $(\theta_1, \theta_2) = (0.38, 0.12)$ respectively. Each box shows the experimental dispersion relations without boundary conditions of each ring in the first row, and OBC in the second and third rows at sites $n=2$ and 3 , respectively.

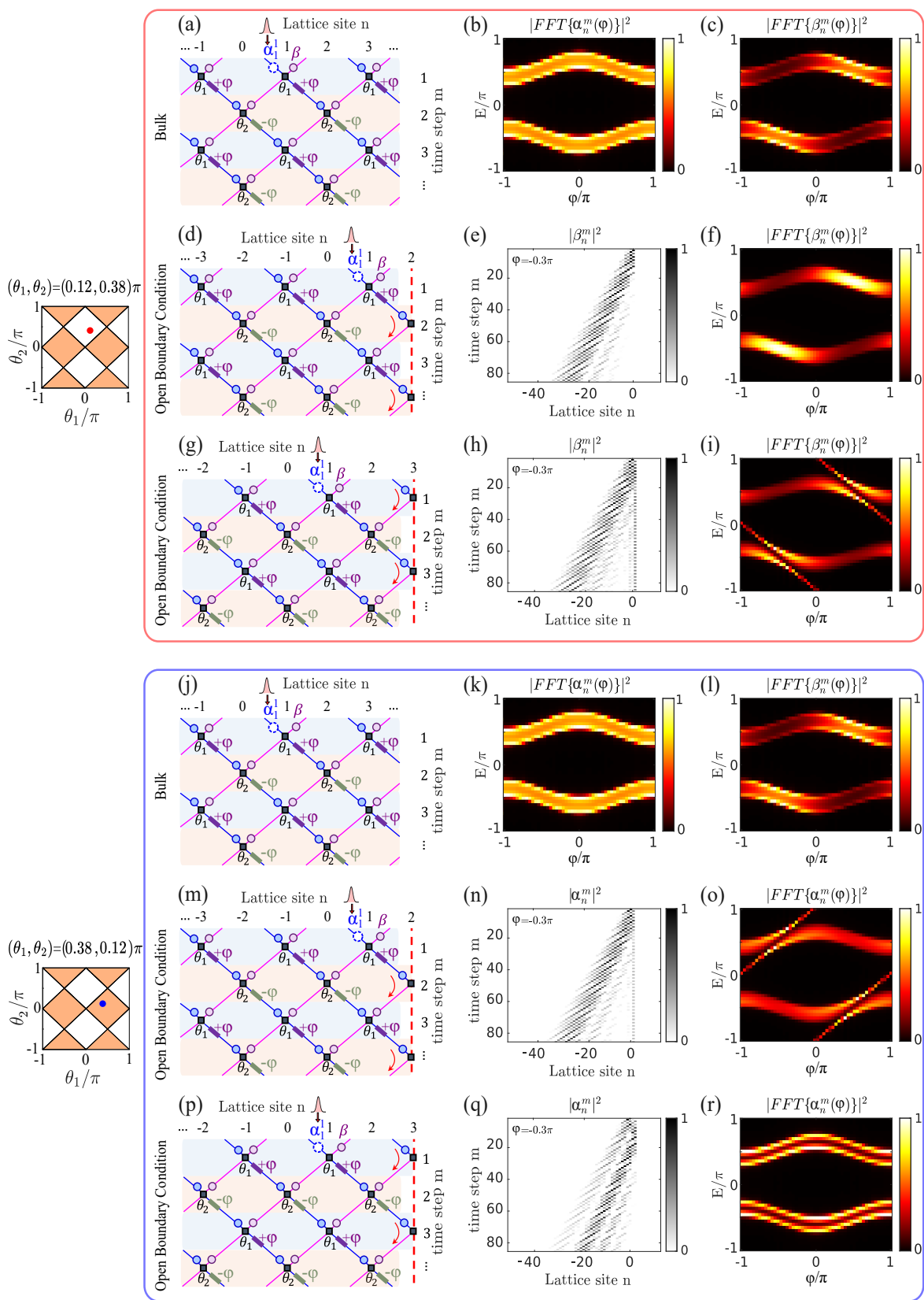


Figure 5.3: Numerical simulation replicating the experimental results of Fig. 5.2

Figure 5.2 depicts two vertically stacked boxes, red and blue, corresponding to two distinct points, plotted in red and blue, located in two different regions (white and orange) of the two-step model phase diagram for coupling angles $(\theta_1, \theta_2) = (0.2, 0.3)$ and $(\theta_1, \theta_2) = (0.3, 0.2)$, respectively. Each box contains three rows: the first row shows the experimental two-dimensional dispersion relation tomography when injecting the initial pulse in the bulk, far from the edge, for the rings α and β (see Figs. 5.2.a and 5.2.j). The second and third rows present results under open boundary conditions (OBC) at site positions $n = 2$ and $n = 3$, respectively.

Comparing the second row of each box (see Figs. 5.2.d-f and 5.2.m-o), when the VBS is set to full reflectance at site $n = 2$ and a pulse is introduced at site $n = 1$, as shown in the quantum walk lattices (see Figs. 5.2.d and 5.2.m), only the orange region exhibits partial light localization at the boundary in the spatiotemporal diagram for $\varphi = -0.3\pi$ (see Fig. 5.2.n) along with the emergence of robust chiral edge states traversing both gaps (see Fig. 5.2.o). In contrast, the white region shows neither light localization nor the presence of edge states (see Figs. 5.2.e-f). Numerical simulations of the equation 5.1 confirmed the experimental observations (see Fig. 5.3). This behavior indicates that the white panels of the phase diagram can be identified with the trivial phase, while the orange panels with the anomalous phase.

Nevertheless, this appears to be in contradiction with the time translation invariance between $U_{\text{QW}}(\mathbf{q})$ and $\tilde{U}_{\text{QW}}(\mathbf{q})$ previously discussed. The reason is that the two phases considered in Figs. 5.2.e-f and 5.2.n-o are related by the swap $\theta_1 \leftrightarrow \theta_2$. Hence, they are described by equivalent Floquet operators whose only difference is a shift in the reference frame by one step of the protocol and this should not change the bulk topology. That is, one would expect the two phases to be identical because they are related by a symmetry of the system and hence, no edge states at their interface. This is consistent with the fact that the Chern number remains zero at both sides of the quasienergies gap closure. We now resolve this contradiction by demonstrating the crucial role played by the boundaries.

To understand the role of the boundaries on the presence of edge states, notice that the choice of a stroboscopic time-frame in Fig. 5.2.d can be linked to a boundary choice when OBC is considered. For example, $U_{\text{QW}}(\mathbf{q})$ characterizes the stroboscopic evolution at the blue time-slices. The bipartite unit cell (α_n, β_n) , in this case, is marked by a dashed orange rectangle in Fig. 5.2.d. There is nothing special about this unit cell, as far as PBC is considered along the spatial dimension. However, once the fully reflecting edge is fixed at $n = 2$, the evolution can be interpreted as the stroboscopic evolution of a chain of dimers with a β -site termination within the blue time-slices. Instead, if one chooses the Floquet operator $\tilde{U}_{\text{QW}}(\mathbf{q})$ to characterize the stroboscopic evolution (red time-slices in Fig. 5.2.d), for a boundary at the same site, this corresponds to a dimer chain with a α -site termination. This implies that for OBC, a change in the boundary termination is equivalent to

a shift in the reference frame of the Floquet operator. This is shown schematically in Fig. 5.2.d, where the shift in one time-step (change of color in the time-slice) is equivalent to a change of boundary.

As a confirmation that our interpretation is correct regarding the importance of boundaries and that there is nothing special about the choice of $U_{\text{QW}}(\mathbf{q})$ or $\tilde{U}_{\text{QW}}(\mathbf{q})$ (i.e., they have identical bulk topology), we demonstrate in the third row of each box in Figs. 5.2.g-i and 5.2.p-r that altering the boundary to a fully reflecting edge at the site $n = 3$ for the same values of θ_j and injection position reverses the two-step model phase diagram. In this configuration, both the light localization at the boundary in the spatiotemporal diagram (see Fig. 5.2.h) and the emergence of Chiral edge states across the band (see Fig. 5.2.i) are now confined to the white region. Consequently, the white region corresponds to the anomalous phase, while the orange region represents the trivial phase.

Chiral edge states are obtained for any value of θ_j , this confirms that the system can actually be topological for all values of θ_j , and that the appearance of the chiral edge states is linked to the particular boundaries fixed in the experimental realization. Also, notice that the direction of the group velocity is associated with the edge state in Fig. 5.2.i is reversed with respect to the case with a boundary at site $n = 2$ in Fig. 5.2.o. The reason is that, as we discussed earlier, the time translation relating the two frames is not only implemented by the swap $\theta_1 \leftrightarrow \theta_2$, but it also involves the reflection of the quasimomentum $\varphi \rightarrow -\varphi$. Therefore, as changing the boundary site must be equivalent to a reference frame shift, the phase diagram not only reverses the phases but also the chiral edge states change their direction of propagation.

If we carefully account for the choice of the unit cell that defines a particular time frame and termination, it is possible to compute a topological invariant that describes the existence of the anomalous phases we have just shown. The computation of the topological invariant has been carried out by our collaborators Alvaro Gomez-Leon and Pierre Delplace and can be found in the appendix of our paper [1]. The invariant is expressed as a winding number ν_μ , defined as:

$$\begin{aligned} \nu_{\mu=0} &= \frac{1}{2} [1 - \text{sgn}(J_2 + m_2) \text{sgn}(m_2 - J_2)] \\ &= \frac{1}{2} [1 - \text{sgn}[\sin(\theta_1 + \theta_2)] \text{sgn}[\sin(\theta_2 - \theta_1)]] \end{aligned} \quad (5.7)$$

This equation predicts the existence of edge states across an energy gap $\mu = 0$ for a specific boundary condition. This winding number corresponds to the blue time frame in Fig. 5.2.d that defines the evolution operator $U_{\text{QW}}(\mathbf{q})$ when OBC are applied along the spatial coordinate at site $n=2$. In this frame, the orange phases with edge states reveal a winding number of $\nu_{\mu=0} = 1$, and the white phase, lacking edge states, corresponds to a winding of $\nu_{\mu=0} = 0$.

In this section, we experimentally demonstrated that modifying the boundary conditions enables the emergence or disappearance of chiral edge states under the same parameter θ_j . Furthermore, we presented a topological invariant that both predicts the existence of these edge states and corroborates our experimental findings. A second approach, which explores edge state existence through the lens of extrinsic topology [10], will be discussed in detail in the following section.

5.2 Extrinsic topology

5.2.1 Edge unitary

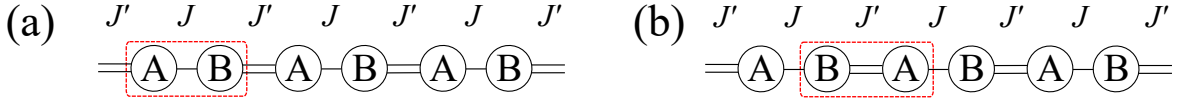


Figure 5.4: (a) The Su-Schrieffer-Heeger (SSH) model consists of a 1D chain with two sublattices (B and A) in each unit cell, as illustrated by the red dashed line. (b) SSH model with a unit cell arrangement of (B-A).

The topology of our double ring system seems to share some similarities with that of a chain of dimers (SSH model) [165, 166] in the sense that the existence of edge states is linked to the type of considered boundary [167]. Discussing this apparent similarity will allow us to place our results within the framework of extrinsic topology and explicitly show how edge unitaries affect the global topology of the system.

The Su-Schrieffer-Heeger (SSH) model consists of a periodic 1D chain with two sublattices (A and B) per unit cell. The sublattices are coupled through alternating hopping amplitudes: intra-cell hopping (J) within a unit cell and inter-cell hopping (J') between adjacent unit cells, as demonstrated in Fig. 5.4.a. The tight-binding Hamiltonian within the n -th unit cell for the SSH model is written as:

$$H = \sum_n [J |n, B\rangle \langle n, A| + J' |n+1, A\rangle \langle n, B| + \text{h.c.}] \quad (5.8)$$

The unit cell choice of A-B or B-A atoms in a chain of static dimers, as illustrated in Figs. 5.4.a-b respectively, is similar to the choice of the order of time steps in our setup. In both cases, this choice only fixes the spatial or temporal reference frame, respectively, which is unimportant for the physics of the bulk system. When OBC are considered, the two cases become different. In a chain of static dimers, a non-vanishing winding number implies that an unpaired state is present at the edge of a chain. The winding number is now unambiguously defined for the particular choice of the unit cell corresponding to the dimer at the edge. The existence of

the edge state is then explained by the bulk-boundary correspondence of chiral symmetric Hermitian Hamiltonian in dimension one [165, 168], and the value of the invariant is linked to the choice of termination (i.e., the unit cell)

However, for the case treated in this thesis, there is an important difference due to the Floquet dynamics. The discrete nature of the time periodicity in our lattice enriches the topology with the possibility of the winding of the quasienergy spectrum. Mathematically, this is related to the fact that in Floquet physics, one must deal with a unitary operator—the time-evolution operator—and not a Hermitian one. Recently, the group of T. Bessho et al. [169] demonstrated that in this context, it is possible to define a winding number associated with the unitary operator acting on the edge of the lattice. In this case, the topological characterization requires not only an understanding of the bulk topologies but also the invariants associated with the edge operator (v_{edge}). The full topological description is thus provided by both the bulk and the edge, a scenario referred to as extrinsic topology. In our case, the unitaries at the edge are effectively determined by the choice of time step (even or odd, or equivalently θ_1 and θ_2) at which the spatial unit cell is cut by the edge. In Fig. 5.2.d, the edge unit cell is cut at even site ($n = 2$), implicitly imposing the blue time reference frame (odd time steps m) for the determination of the edge unitaries. The opposite reference frame is imposed in Fig. 5.2.g.

To determine the edge unitaries, we consider a finite lattice with open boundary conditions (OBC) applied at sites $n = 2$ and $n = 2N$, where $N \in \mathbb{N}$. After one Floquet period, the evolution of the system in real space can be written as $\Psi(m+2) = U_F \Psi(m)$, with $\Psi = [\alpha_{n=2}^m \beta_{n=2}^m \alpha_{n=4}^m \beta_{n=4}^m \dots \alpha_{n=2N}^m \beta_{n=2N}^m]^T$. Thus, the complex amplitude sublattices α_n^m and β_n^m are derived from equation. 5.2, evolve according to the Floquet operator U_F . This operator governs a two-step walk and has a matrix form similar to that of the dimer chain.

$$\underbrace{\begin{pmatrix} [\alpha_{n=2}^{m+2} \beta_{n=2}^{m+2}]^T \\ [\alpha_{n=4}^{m+2} \beta_{n=4}^{m+2}]^T \\ [\alpha_{n=6}^{m+2} \beta_{n=6}^{m+2}]^T \\ [\alpha_{n=8}^{m+2} \beta_{n=8}^{m+2}]^T \\ \vdots \\ [\alpha_{n=2N}^{m+2} \beta_{n=2N}^{m+2}]^T \end{pmatrix}}_{\Psi(m+2)} = \underbrace{\begin{pmatrix} U_L & U_+ & 0 & 0 & 0 & 0 \\ U_- & U_0 & U_+ & 0 & 0 & \ddots & 0 \\ 0 & U_- & U_0 & U_+ & \ddots & 0 & 0 \\ 0 & 0 & U_- & \ddots & U_+ & 0 & 0 \\ 0 & 0 & \ddots & U_- & U_0 & U_+ & 0 \\ 0 & \ddots & 0 & 0 & U_- & U_0 & U_+ \\ 0 & 0 & 0 & 0 & 0 & U_- & U_R \end{pmatrix}}_{\text{Floquet operator } U_F} \underbrace{\begin{pmatrix} [\alpha_{n=2}^m \beta_{n=2}^m]^T \\ [\alpha_{n=4}^m \beta_{n=4}^m]^T \\ [\alpha_{n=6}^m \beta_{n=6}^m]^T \\ [\alpha_{n=8}^m \beta_{n=8}^m]^T \\ \vdots \\ [\alpha_{n=2N}^m \beta_{n=2N}^m]^T \end{pmatrix}}_{\Psi(m)}$$

The Floquet operator U_F is a unitary matrix can be seen as a combination of the bulk unitaries (U_{bulk}) and edge unitaries (U_{edge}), such that $U_F = (U_{edge} \oplus U_{bulk})$.

Where the different blocks of the bulk unitaries are given by equation. 5.9, and the edge unitaries by equation. 5.10:

$$\left\{ \begin{array}{l} U_0 = \sin(\theta_2) \begin{pmatrix} -e^{-i\varphi} \sin(\theta_1) & ie^{-i\varphi} \cos(\theta_1) \\ ie^{i\varphi} \cos(\theta_1) & -e^{i\varphi} \sin(\theta_1) \end{pmatrix} \\ U_+ = \cos(\theta_2) \begin{pmatrix} 0 & 0 \\ i \sin(\theta_1) & \cos(\theta_1) \end{pmatrix} \\ U_- = \cos(\theta_2) \begin{pmatrix} \cos(\theta_1) & i \sin(\theta_1) \\ 0 & 0 \end{pmatrix}. \end{array} \right. \quad (5.9)$$

$$\left\{ \begin{array}{l} U_L = \begin{pmatrix} -e^{-i\varphi} \sin(\theta_1) & ie^{-i\varphi} \cos(\theta_1) \\ ie^{i\varphi} \cos(\theta_1) \sin(\theta_2) & -e^{i\varphi} \sin(\theta_1) \sin(\theta_2) \end{pmatrix} \\ U_R = \begin{pmatrix} -e^{-i\varphi} \sin(\theta_1) \sin(\theta_2) & ie^{-i\varphi} \cos(\theta_1) \sin(\theta_2) \\ ie^{i\varphi} \cos(\theta_1) & -e^{i\varphi} \sin(\theta_1) \end{pmatrix} \end{array} \right. \quad (5.10)$$

The edge blocks U_L and U_R are different from the bulk blocks U_- , U_+ , and U_0 due to the condition of full reflection at the edges. In this case, the matrix U_F can be interpreted as a unitary version of a dimerized lattice, with couplings between neighboring dimers given by U_{\pm} .

The dimer chain consists of a series of bipartite unit cells (α_n, β_n) , it is useful to examine the different limits of dimerization by isolating the unit cell at the edge from its neighbors along the chain. This is achieved by considering a stripe (see Fig. 5.5.d). The simplest approach is to analyze two extreme scenarios: when $(\theta_1, \theta_2) = (0, \pi/2)$ and $(\theta_1, \theta_2) = (\pi/2, 0)$. In these scenarios, the dimer chain behaves as a collection of independent dimers, resulting in $U_{L,R} = U_{edge}$.

In the previous Section. 5.1.2, we computed the topological invariants based on the choice of the unit cell compatible with the edge termination. Here, we will compute the edge topological invariant associated with the edge operator. For the first case, when $(\theta_1, \theta_2) = (0, \pi/2)$, the edge blocks simplify to equation. 5.11. To determine the winding number of these unitaries, as defined in equation. 5.12, we can utilize the formula provided in the work of Bessho et al. [169]. Upon calculation, we find that the winding number of the unitary edge blocks for this particular case is zero.

$$U_{L,R} = \begin{pmatrix} 0 & ie^{-i\varphi} \\ ie^{i\varphi} & 0 \end{pmatrix} \quad (5.11)$$

$$\nu_{edge}[U_{edge}(\varphi)] = \int_0^{2\pi} \frac{d\varphi}{2\pi} \text{tr}[U_{edge}(\varphi)^{-1} i \partial_{\varphi} U_{edge}(\varphi)] \quad (5.12)$$

In contrast, for $(\theta_1, \theta_2) = (\pi/2, 0)$, the edge and bulk blocks correspond to equations. 5.13 and 5.14, respectively, and they are not unitary. The corresponding Floquet operator U_F is given by equation. 5.15 and 5.16.

$$U_L = \begin{pmatrix} -e^{-i\varphi} & 0 \\ 0 & 0 \end{pmatrix}, U_R = \begin{pmatrix} 0 & 0 \\ 0 & -e^{i\varphi} \end{pmatrix} \quad (5.13)$$

$$U_- = \begin{pmatrix} 0 & i \\ 0 & 0 \end{pmatrix}, U_+ = \begin{pmatrix} 0 & 0 \\ i & 0 \end{pmatrix}, U_0 = \mathbf{0} = \begin{pmatrix} 0 & 0 \\ 0 & 0 \end{pmatrix} \quad (5.14)$$

$$U_F = \begin{pmatrix} \begin{pmatrix} -e^{-i\varphi} & 0 \\ 0 & 0 \end{pmatrix} & \begin{pmatrix} 0 & 0 \\ i & 0 \end{pmatrix} & \mathbf{0} & \mathbf{0} & \mathbf{0} & \cdots & \mathbf{0} \\ \begin{pmatrix} 0 & i \\ 0 & 0 \end{pmatrix} & \begin{pmatrix} 0 & 0 \\ 0 & 0 \end{pmatrix} & \begin{pmatrix} 0 & 0 \\ i & 0 \end{pmatrix} & \mathbf{0} & \mathbf{0} & \cdots & \mathbf{0} \\ \mathbf{0} & \begin{pmatrix} 0 & i \\ 0 & 0 \end{pmatrix} & \begin{pmatrix} 0 & 0 \\ 0 & 0 \end{pmatrix} & \begin{pmatrix} 0 & 0 \\ i & 0 \end{pmatrix} & \mathbf{0} & \cdots & \mathbf{0} \\ \vdots & \ddots & \ddots & \ddots & \ddots & \begin{pmatrix} 0 & 0 \\ 0 & 0 \end{pmatrix} & \begin{pmatrix} 0 & 0 \\ i & 0 \end{pmatrix} \\ \mathbf{0} & \mathbf{0} & \mathbf{0} & \mathbf{0} & \mathbf{0} & \begin{pmatrix} 0 & i \\ 0 & 0 \end{pmatrix} & \begin{pmatrix} 0 & 0 \\ 0 & -e^{i\varphi} \end{pmatrix} \end{pmatrix} \quad (5.15)$$

$$U_F = \begin{pmatrix} -e^{-i\varphi} & 0 & 0 & 0 & 0 & 0 & 0 \\ 0 & 0 & i & 0 & 0 & \cdots & 0 \\ 0 & i & 0 & 0 & \cdots & 0 & 0 \\ 0 & 0 & 0 & \cdots & 0 & 0 & 0 \\ 0 & 0 & \cdots & 0 & 0 & i & 0 \\ 0 & \cdots & 0 & 0 & i & 0 & 0 \\ 0 & 0 & 0 & 0 & 0 & 0 & -e^{i\varphi} \end{pmatrix} \quad (5.16)$$

Note that the terms $-e^{-i\varphi}$ and $-e^{i\varphi}$, which appear in the U_L and U_R blocks, respectively, are fully decoupled from the bulk in equation.5.16. In this specific case, $U_L = -e^{-i\varphi}$ and $U_R = -e^{i\varphi}$, both of which are unitary and exhibit a winding number of 1. This winding number is directly influenced by the phase modulator φ . This exemplifies the meaning of edge unitaries in discretized time-step walks and how their topology (extrinsic) complements the bulk topology. It is important to stress that this result explicitly shows that the topology of the two-step walk is richer than that of a dimers chain. In particular, the fact that we are dealing with driven systems, characterized by unitary operators rather than Hermitian ones, is what makes possible the existence of chiral edge states crossing both gaps.

Extrinsic topology plays a role analogous to micromotion in continuously driven Floquet Hamiltonian, where chiral edge states can exist even when the bulk bands are topologically trivial. Unlike the Floquet topology in continuously driven systems, where anomalous phases are characterized by a bulk invariant [83], the extrinsic topology, is governed by edge unitaries. These unitaries can be manipulated to control the presence of chiral edge modes without altering the position of the edge, providing a means to suppress or induce these states as needed. This aspect will be explored in greater detail in the next section.

5.2.2 Edge state engineering

In this section, we investigate the role of edge unitaries in shaping the overall system topology, focusing on two distinct regions of the phase diagram: $(\theta_1, \theta_2) = (0.12, 0.38)\pi$ and $(\theta_1, \theta_2) = (0.38, 0.12)\pi$. This analysis is conducted by a carefully designed voltage sequence applied to the phase modulator.

5.2.2.1 *Extrinsic topology for $(\theta_1, \theta_2) = (0.12, 0.38)\pi$*

Figure. 5.5 shows a comparison between the numerical (a-i) and experimental (j-r) results in the upper and lower black boxes, respectively, when a narrow pulse is introduced into the long ring α at site $n = 1$, with a set of coupling angles $(\theta_1, \theta_2) = (0.12, 0.38)\pi$. Each box is composed of three rows, each containing three subplots.

Starting with the numerical results, the first row illustrates the scenario of an open boundary condition (OBC). In this configuration, the VBS is set to full reflectance at site $n = 0$, while alternating between θ_1 and θ_2 for the remaining lattice sites n . Simultaneously, the phase modulator alternates between $+\varphi$ and $-\varphi$ across all sites at odd and even time steps, as depicted in the quantum lattice of Fig. 5.5.a. Accompanying this, Figs. 5.5.b-c present the dispersion relation tomography of rings α and β , respectively. The resulting band structure of the ring exhibits no edge states, indicating a trivial topological phase.

The second row presents the scenario of a stripe configuration. This setup isolates the edge unit cell from the bulk by imposing full reflectance, $\theta_2 = \pi/2$, at sites $n = 0$ and $n = 2$, while maintaining the injection at site $n = 1$. Nevertheless, the edge unitary remains dependent on the phase modulator parameter. To modulate this parameter, we alternate the phase between odd and even time steps, setting $\phi_1 = +\varphi$ and $\phi_2 = 0\varphi$ (see Fig. 5.5.d), ensuring a non-zero net phase winding, $\phi_1 + \phi_2 \neq 0$, within one Floquet period. Figures 5.5.e-f show the corresponding Fourier stripe mode tomography of rings α and β , where we observe a single band of edge states winding through the entire Brillouin zone, from $(E, k) = (-\pi, -\pi)$ to (π, π) , with a positive group velocity throughout.

The final row demonstrates the combined configurations of the stripe and the bulk, as shown in Fig. 5.5.g. This is accomplished by first establishing the stripe configuration. At site $n = 0$, θ_2 is set to $\pi/2$, and the phase modulator alternates between $\phi_1 = +\varphi$ and $\phi_2 = 0$ at sites $n = 0$ and $n = 1$. For the remaining sites n , corresponding to the bulk, the VBS alternates between θ_1 and θ_2 , while the phase modulator alternates between $+\varphi$ and $-\varphi$ at odd and even time steps. In this scenario, the edge state associated with the stripe hybridizes with the bulk band, as depicted in Figs. 5.5.h-i. Each gap is traversed by a single intense band of edge states, all exhibiting a positive group velocity with the same sign. Thus, by manipulating the phase modulator at the boundary of the lattice in the case of an OBC, we introduced an edge state into the band.

Regarding the experimental results shown in Figs. 5.5.j-r, each row —representing the cases of the OBC, stripe, and hybridization—exhibits remarkable agreement with the expected numerical results presented in Figs. 5.5.a-i. However, upon closer inspection of the experimental data, we observe some imperfections because the average period time $\bar{T} = 224.94$ ns is not an exact integer multiple of the 40 ps resolution of the AWG7000B that generates the voltage signal. Consequently, after each round trip, the voltage sequence is slightly shifted by almost 20 ps. This shift becomes crucial after nearly 66 round trips, as it corresponds to the size of one site (1.4 ns). Since the extrinsic topology requires the application of a specific voltage for each lattice site, maintaining perfect synchronization proves to be challenging.

The non-zero net phase winding at the boundaries at the site ($n = 0$ and $n = 1$) of an OBC can introduce edge states. This raises the question: how would the system behave if the phase winding was applied at additional sites?

Building on the conditions established in Fig. 5.5, Figures. 5.6.a-c simulate the hybridization between the bulk and a single stripe. In contrast, Figs. 5.6.d-f numerically depict the hybridization involving two stripes, where a non-zero net phase winding $\phi_1 = +\varphi$ and $\phi_2 = 0$ is applied at sites $n = 0, 1, 2$, as illustrated in Fig. 5.6.d. Furthermore, Figs. 5.6.e-f show that each gap within both the long and short rings, respectively, is now crossed by two edge states instead of one. Thus, hybridizing the bulk with multiple stripes introduces additional edge states proportional to the number of stripes. Comparing the numerical results observed in Figs. 5.6.a-f align closely with the experimental findings presented in Figs. 5.6.g-l.

Moreover, when a non-trivial phase winding is applied across the entire lattice site n , our results align with Adiyatullin et al. [121], where gapless tilted band structure tomography absent of crossings was obtained in trivial phases.

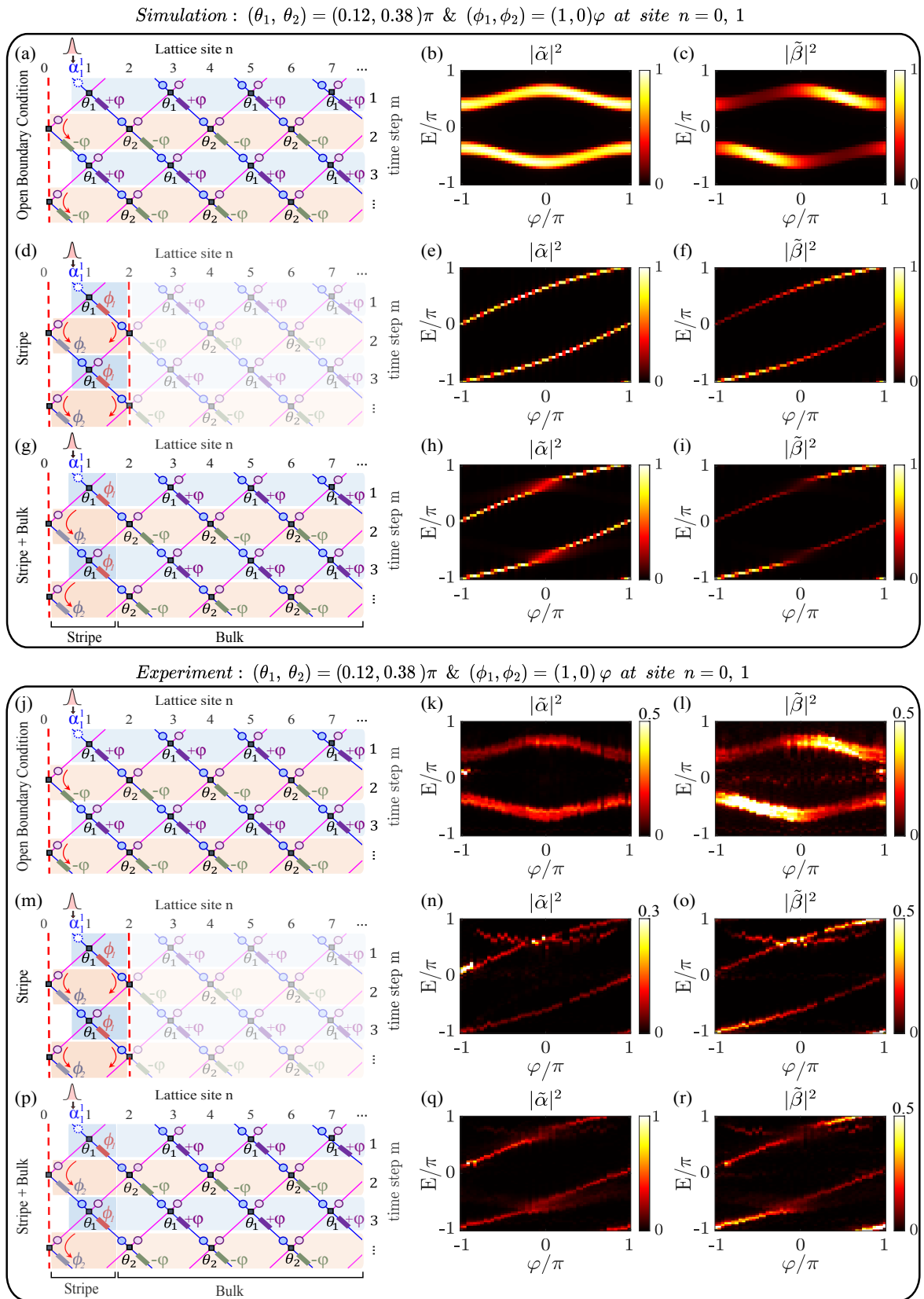


Figure 5.5: Comparison of numerical (a-i) and experimental (j-r) results for OBC, stripe, and their hybridization, when $(\theta_1, \theta_2) = (0.12, 0.38)\pi$ and $(\phi_1, \phi_2) = (1, 0)\varphi$.

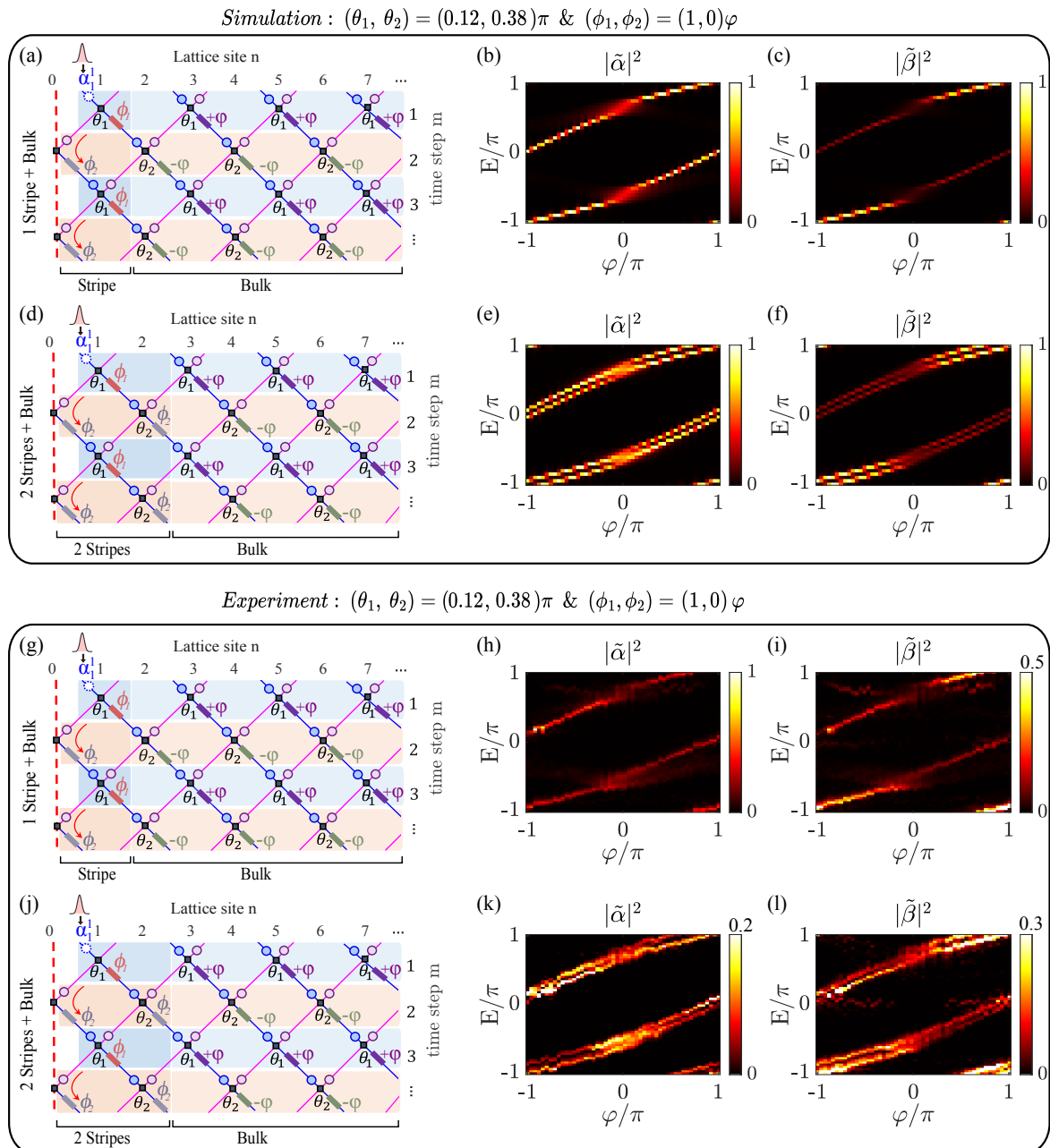


Figure 5.6: The upper (simulation) and lower (experiment) boxes compare the hybridization of the bulk with one and two stripes.

5.2.2.2 *Extrinsic topology for $(\theta_1, \theta_2) = (0.38, 0.12)\pi$*

We now explore the behavior of extrinsic topology in another region of the phase diagram. Our focus shifts to examining the interplay between edge states associated with stripes and those arising from bulk topology.

Figure. 5.7 replicates Fig. 5.5 and presents a side-by-side comparison of the numerical (upper panels a-i) and the experimental results (lower panels j-r) when a narrow pulse is introduced into the α ring at site $n = 1$ and the coupling angles are set to $(\theta_1, \theta_2) = (0.38, 0.12)\pi$. Figures. 5.7.a-c display the quantum walk lattice and the dispersion relation in rings α and β , respectively, under the OBC scenario, where each gap is traversed by an edge state with a negative group velocity, reflecting the underlying topological properties of the bulk system. Figure. 5.7.d highlights the stripe configuration, featuring a non-zero net phase winding of $\phi_1 = 0\varphi$ and $\phi_2 = +\varphi$ applied at sites 0 and 1. The Fourier stripe modes of the rings α and β unveil edge states with a positive group velocity (see Fig. 5.7.e-f). Engineering the quantum walk lattice to merge the stripe and bulk configurations, as illustrated in Fig. 5.7.g, facilitates the hybridization of edge states associated with both the bulk topology and the stripe. These states have opposing group velocities, leading to the opening of a gap at the point in which they anticross, as demonstrated in the dispersion relation of the long and short ring in Figs. 5.7.h-i, respectively. The edge states no longer traverse the gap between the bands, indicating a topologically trivial situation. The predicted numerical results in the upper panels (Figs. 5.7.a-i) align perfectly with the experimental results in the lower panels (Figs. 5.7.j-r).

Figure. 5.8 represent the inverted phase winding of Fig. 5.7, achieved by setting $(\phi_1, \phi_2) = (0, -1)\varphi$. This inversion causes the edge states of the stripe in the reciprocal space to have the same group velocity as those from the bulk topology, as seen in the second rows of both the numerical and experimental panels. Consequently, hybridizing the bulk and stripe cases leads to the merging of their edge states, resulting in a constructive superposition rather than a cancellation, as depicted numerically and experimentally in Figs. 5.8.g-i and 5.8.p-r, respectively.

Proceeding even further, doubling the non-trivial phase winding of Fig. 5.8 by setting $(\phi_1, \phi_2) = (0, -2)\varphi$, the edge states associated with the stripe wind twice across the entire Brillouin zone (see Fig. 5.9.e-f and 5.9.n-o), exhibiting the same group velocity as in Fig. 5.8.e-f. The corresponding numerical and experimental hybridization case of the α and β ring is demonstrated in Fig. 5.9.h-i and 5.9.q-r, respectively, and shows three edge states traversing each gap in the α ring, while two in β ring due to the sublattice's negligible weight.

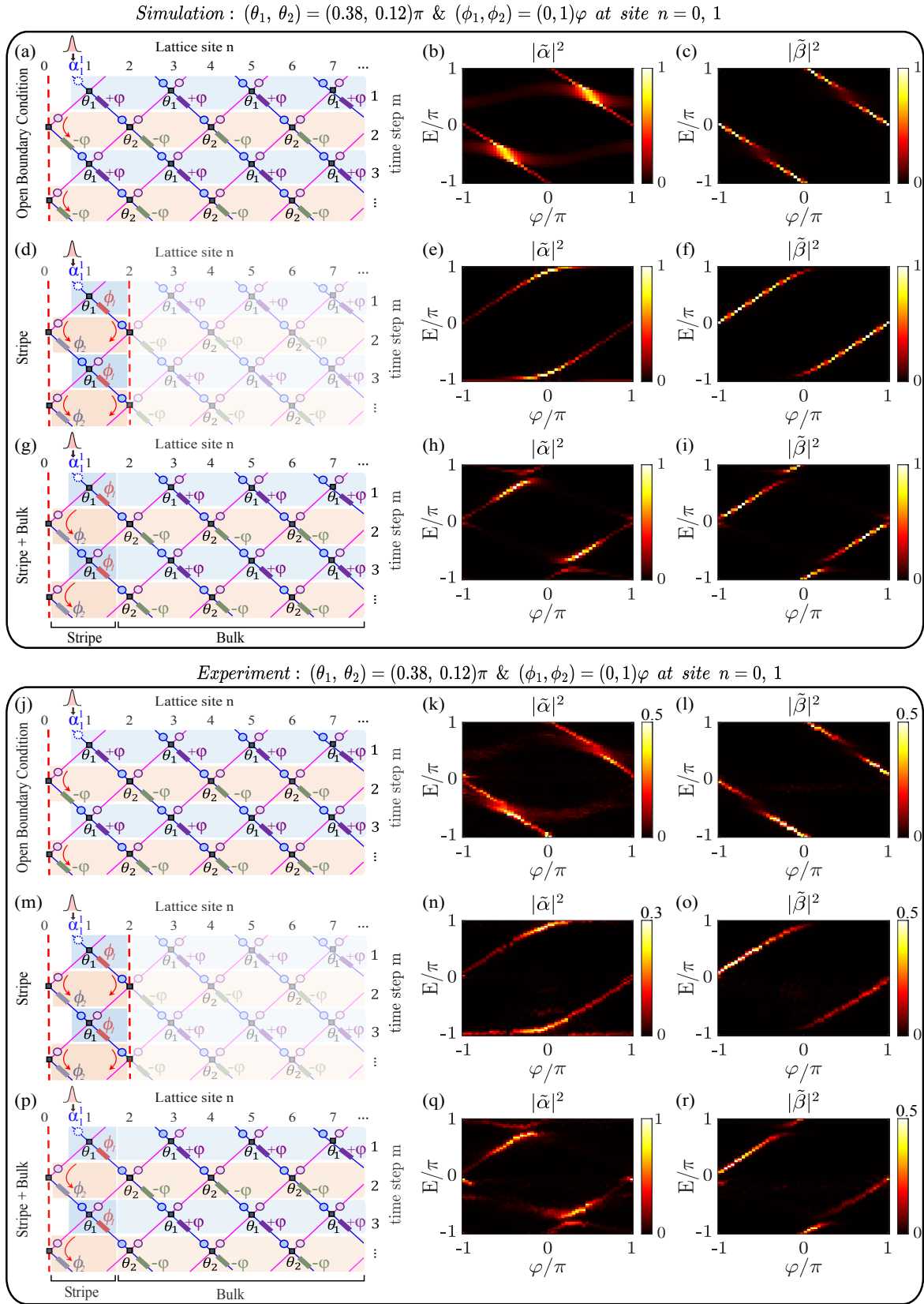


Figure 5.7: Comparison of numerical (a-i) and experimental (j-r) results for OBC, stripe, and their hybridization, when $(\theta_1, \theta_2) = (0.38, 0.12)\pi$ and $(\phi_1, \phi_2) = (0, +1)\varphi$.

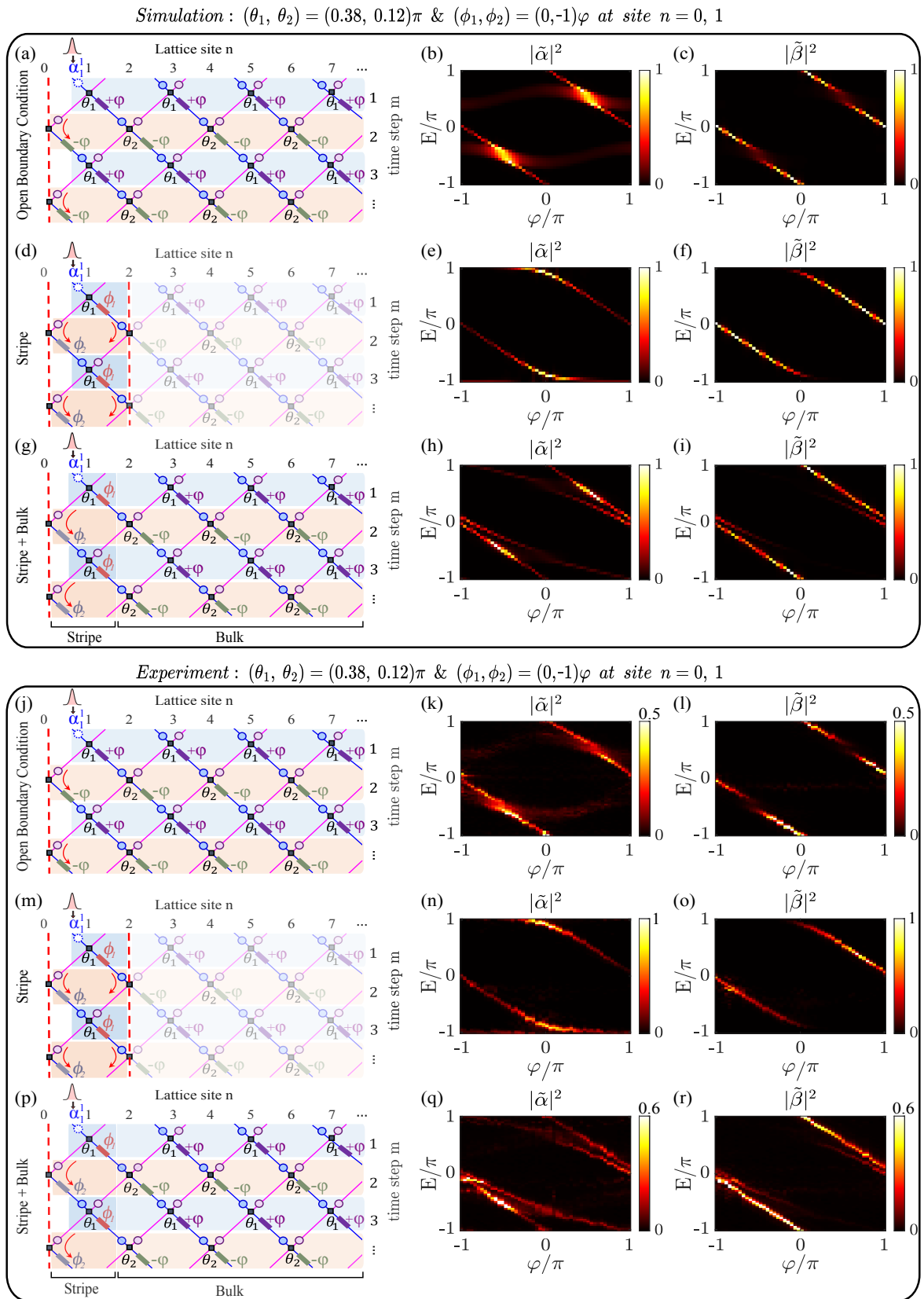


Figure 5.8: Comparison of numerical (a-i) and experimental (j-r) results for OBC, stripe, and their hybridization, when $(\theta_1, \theta_2) = (0.38, 0.12)\pi$ and $(\phi_1, \phi_2) = (0, -1)\varphi$.

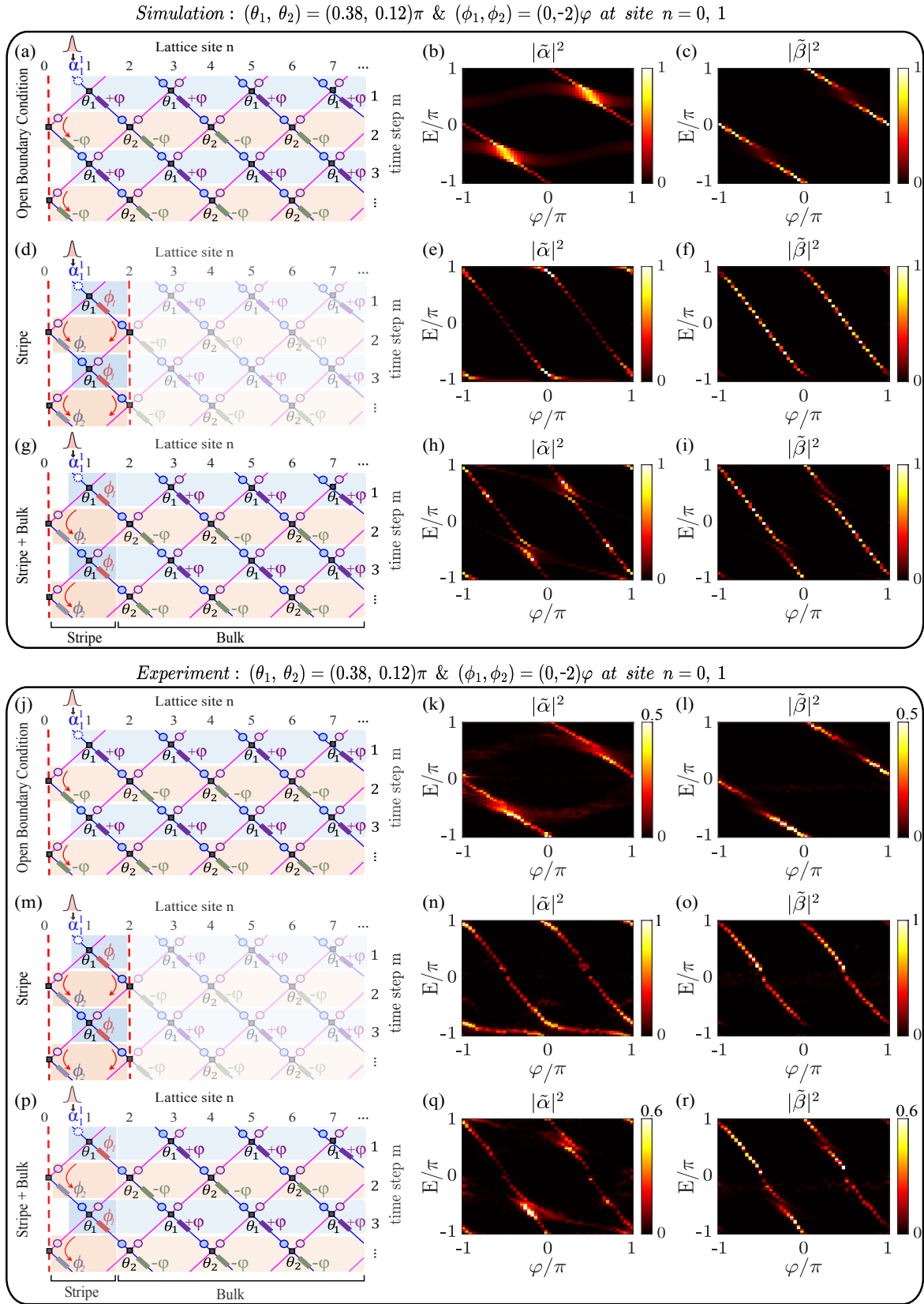


Figure 5.9: Comparison of numerical (a-i) and experimental (j-r) results for OBC, stripe, and their hybridization, when $(\theta_1, \theta_2) = (0.38, 0.12)\pi$ and $(\phi_1, \phi_2) = (0, -2)\varphi$.

5.3 Conclusion

Anomalous topological phases, where edge states coexist with topologically trivial Chern bands ($C=0$) were never studied in a two-dimensional discrete step walk. In this chapter, we delved into this intriguing case via two approaches:

The first approach underscores the pivotal role of lattice geometry in determining the existence of edge states, governed by the selected boundary conditions. Experimentally, this is realized through time-dependent modulation, enabling us to set the variable beam splitter at a specific site to full reflection, thereby establishing a boundary. By shifting this boundary by a single site, we can precisely control the presence of edge states within the same coupling parameter θ_j . Therefore, each region within the two-step model phase diagram can be either trivial or anomalous, depending on the initial conditions we implement. Additionally, we provided a topological invariant that defines the existence of these edge states.

The second approach delves into extrinsic topology, illustrating how the topological properties of the boundaries (edge unitaries) can impact the global topology of the system, leading to the emergence of gapless boundary states even when the bulk bands are topologically trivial. This phenomenon is experimentally validated by manipulating the phase modulator at the boundary with a specifically designed sequence, which can effectively suppress or induce these edge states.

Questions:

1- Chapter. 5 explored the influence of extrinsic topology on the system's topology when the Chern number vanishes. This naturally raises the question: how does extrinsic topology influence the system when the Chern number is non-zero? The detailed answer to this question is provided in the next Chapter. 6.

2- Having observed that time-dependent modulation can generate edge states, we now inquire: How will the system's dynamics evolve under quasi-periodic modulation (Fibonacci sequence) across both lattice site n and time step m ? This question is addressed in Appendix. E.

TOPOLOGICAL PROPERTIES OF THE FOUR-STEP MODEL

This chapter deals with the four-step model. Through theoretical and experimental analysis, we examine the bulk and edge topology, revealing a richer phase diagram featuring both trivial and non-trivial Chern numbers. Furthermore, we present diverse methodologies for determining the Chern number. Additionally, we explore the impact of extrinsic topology on the overall topological system in both trivial and non-trivial Chern band scenarios.

6.1 Four steps model bulk topology

Throughout this thesis, we investigated the bulk and edge topologies in models displaying bands with zero Chern number, we now turn our attention to exploring non-trivial Chern bands using the four-step model. Before proceeding, let's briefly recap the four-step model, previously detailed in Section 1.3.2 of Chapter 1. In such a scenario, the system possesses a double-periodic structure with a spatial period of two sites and a temporal period of four steps. During one Floquet period, the coupling angle θ alternating between four distinct values $[\theta_1, \theta_2, \theta_3, \theta_4]$ and the phase modulator between $[\varphi_1, \varphi_2, \varphi_3, \varphi_4] = [+ \varphi, - \varphi, + \varphi, - \varphi]$, as presented in the red dashed unit cell in Fig. 6.1.a.

To construct the phase diagram of the four-step model, we fix the coupling parameters at $[\theta_1, \theta_2] = [4\pi/32, 8\pi/32]$ and vary $[\theta_3, \theta_4]$ from 0 to $\pi/2$. Similarly to the two-step model, the system has two bands separated by two gaps at $E=0$ (g_0) and at $E=\pi$ (g_π). We can experimentally characterize the phase diagram by measuring the value of the two gaps as a function of the couplers at time steps θ_3 and θ_4 . The result is shown in Figs. 6.1.b-c, respectively. The gap distances range from 0 (white) to 1.25π (black). A value of 1.25π indicates maximum separation, while 0 signifies complete closure. Combining the gap closures at gap 0 and π (black dashed lines in Figs. 6.1.b-c), we arrive at the phase diagram of the four-step model (see Fig. 6.1.c). The latter is divided into nine regions, labeled from 1 \rightarrow 9, and the gaps at energy 0 and π do not necessarily close simultaneously. To differentiate between these events, we have marked the boundaries of the regions

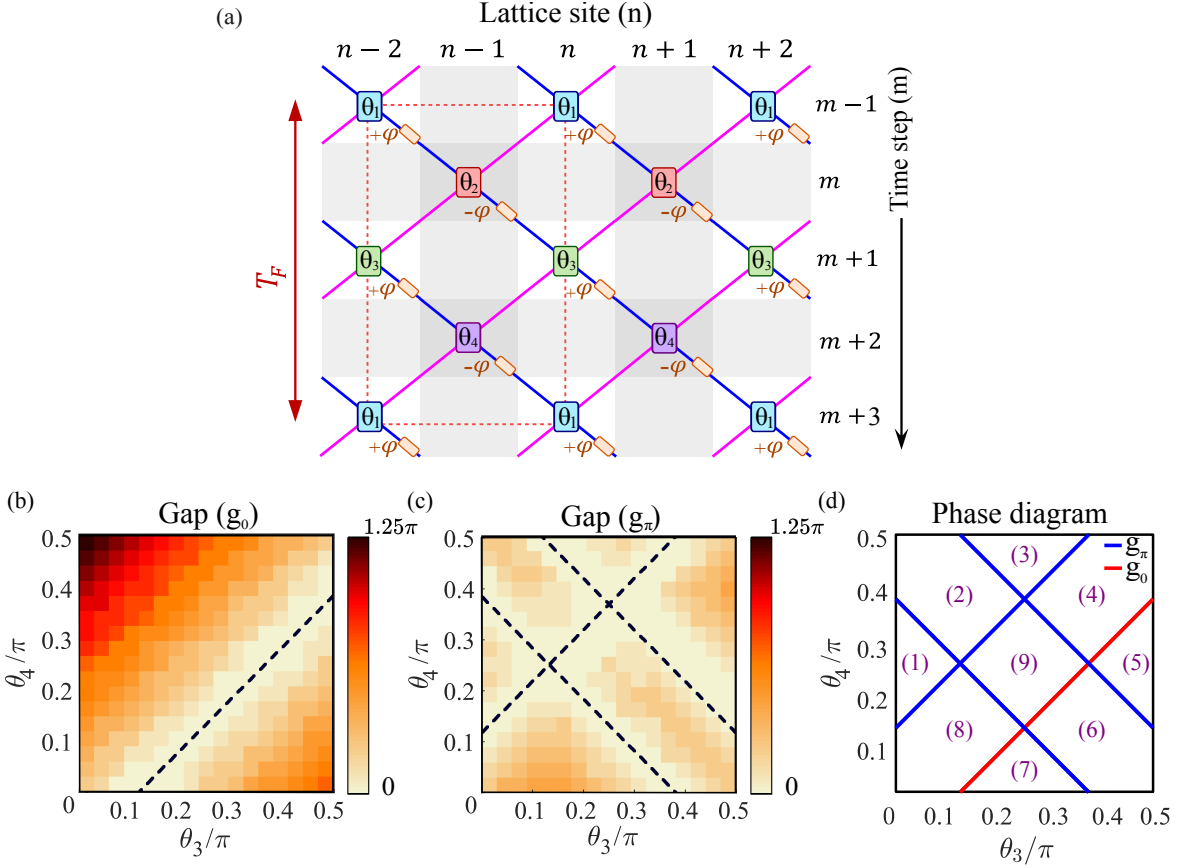


Figure 6.1: Four-step model. (a) Synthetic photonic lattice. (b)-(c) Measurement of the gap distance at energies 0 and π , respectively. (d) Phase diagram obtained by setting $[\theta_1, \theta_2] = [4\pi/32, 8\pi/32]$ and varying $[\theta_3, \theta_4]$ from 0 to $\pi/2$.

where each gap closes using blue and red lines. The red lines indicate the closure of the 0-gap, while the blue lines represent the closure of the π -gap.

The eigenvalues and eigenvectors describing the four-step model, are given by equations. 6.1, 6.2, and 6.3, respectively (see Appendix. B).

$$\begin{aligned}
 E^\pm(k, \varphi_{1 \rightarrow 4}) = & \pm \cos^{-1} \left[T_1 T_2 T_3 T_4 \cos\left(2k - \frac{\phi}{2}\right) + R_1 R_2 R_3 R_4 \cos\left(\varphi_{13} - \frac{\phi}{2}\right) \right. \\
 & + R_1 R_3 T_2 T_4 \cos\left(\varphi_{12} - \frac{\phi}{2}\right) + R_2 R_4 T_1 T_3 \cos\left(\varphi_{14} - \frac{\phi}{2}\right) \\
 & + R_1 R_2 T_3 T_4 \cos\left(\varphi_1 + k - \frac{\phi}{2}\right) + R_2 R_3 T_1 T_4 \cos\left(\varphi_2 + k - \frac{\phi}{2}\right) \\
 & \left. + R_3 R_4 T_1 T_2 \cos\left(\varphi_3 + k - \frac{\phi}{2}\right) + R_1 R_4 T_2 T_3 \cos\left(\varphi_4 + k - \frac{\phi}{2}\right) \right] + \frac{\phi}{2}
 \end{aligned} \tag{6.1}$$

$$|\psi(k)\rangle^\pm = \begin{pmatrix} \tilde{\alpha}(k) \\ \tilde{\beta}(k) \end{pmatrix}^\pm = \frac{1}{\sqrt{1 + |R^\pm|^2}} \begin{pmatrix} 1 \\ |R^\pm| e^{i\Phi_{\alpha\beta}^\pm} \end{pmatrix} \tag{6.2}$$

$$R(k)^\pm = |R^\pm| e^{i\Phi_{\alpha\beta}^\pm} = \frac{e^{iE(k)^\pm} - A}{B} \quad (6.3)$$

with

$$\begin{cases} T_m = \cos \theta_m \\ R_m = i \sin \theta_m \end{cases} \quad \begin{cases} \varphi_{ij} = \varphi_i + \varphi_j \\ \varphi_{ijz} = \varphi_i + \varphi_j + \varphi_z \\ \phi = \sum_{i=1}^4 \varphi_i = \varphi_1 + \varphi_2 + \varphi_3 + \varphi_4 \end{cases}$$

$$\begin{aligned} A = & [T_4 T_3 T_2 T_1 e^{i(-2k+\phi)} + T_4 T_3 R_2 R_1 e^{i(-k+\varphi_{234})} + T_4 R_3 T_2 R_1 e^{i\varphi_{34}} + T_4 R_3 R_2 T_1 e^{i(-k+\varphi_{134})} \\ & + R_4 T_3 T_2 R_1 e^{i(k+\varphi_4)} + R_4 T_3 R_2 T_1 e^{i\varphi_{14}} + R_4 R_3 T_2 T_1 e^{i(-k+\varphi_{124})} + R_4 R_3 R_2 R_1 e^{i\varphi_{24}}] \end{aligned} \quad (6.4)$$

$$\begin{aligned} B = & [T_4 T_3 T_2 R_1 e^{i(-2k+\phi)} + T_4 T_3 R_2 T_1 e^{i(-k+\varphi_{234})} + T_4 R_3 T_2 T_1 e^{i\varphi_{34}} + T_4 R_3 R_2 R_1 e^{i(-k+\varphi_{134})} \\ & + R_4 T_3 T_2 T_1 e^{i(k+\varphi_4)} + R_4 T_3 R_2 R_1 e^{i\varphi_{14}} + R_4 R_3 T_2 R_1 e^{i(-k+\varphi_{124})} + R_4 R_3 R_2 T_1 e^{i\varphi_{24}}] \end{aligned} \quad (6.5)$$

After reviewing the four-step model, we will delve into its bulk topology. Figures 6.2 and 6.3 correspond to the upper and lower bands, respectively, and include a 9x5 configuration of subplots. Each row represents a distinct region of the phase diagram, illustrating the 2D analytical eigenvalues, eigenvectors ($|R|$ & $\Phi_{\alpha\beta}$), Berry curvature, and Chern number, derived from equations 6.1, 6.2, 4.1, and 4.2.

These figures reveal several key observations. First, even-numbered regions (2), (4), (6), and (8) exhibit zero Chern numbers, while odd-numbered regions (1), (3), (5), (7), and (9) possess non-trivial Chern numbers of +2 and -2. Compared to the two-step model, the four-step model displays greater complexity and diversity, with trivial and non-trivial Chern numbers. Second, for the same coupling angles $[\theta_3, \theta_4]$ within each region, the upper and lower bands exhibit contrasting amplitude ratios ($|R^+|^2 = -|R^-|^2$), with a positive (yellow) and negative (blue) peaks of equal magnitude, and a relative phase difference of π ($\Phi_{\alpha\beta}^- - \Phi_{\alpha\beta}^+ = \pi$). Their Berry curvatures and Chern numbers possess opposite signs ($C^+ = -C^-$). Third, in regions with non-vanishing Chern numbers, the amplitude ratio $|R|^\pm$ reveals two pairs of singularity points with high and low amplitudes outlined in yellow and blue, respectively. These peaks coincide precisely with the positions of the two pairs of vortex-antivortex structures observed in the relative phase $\Phi_{\alpha\beta}^\pm$.

To validate our analytical findings, the experimental results depicted in Figs. 6.4 and 6.5, corresponding to the upper and lower bands, respectively, align with the theoretical predictions in Figs. 6.2 and 6.3, yielding Chern numbers that match exactly, despite the low resolution caused by a limited number of turns, which is 66 and results in 16 stroboscopic round trips. These experimental results have been validated through multiple independent measurements, consistently demonstrating the same outcomes.

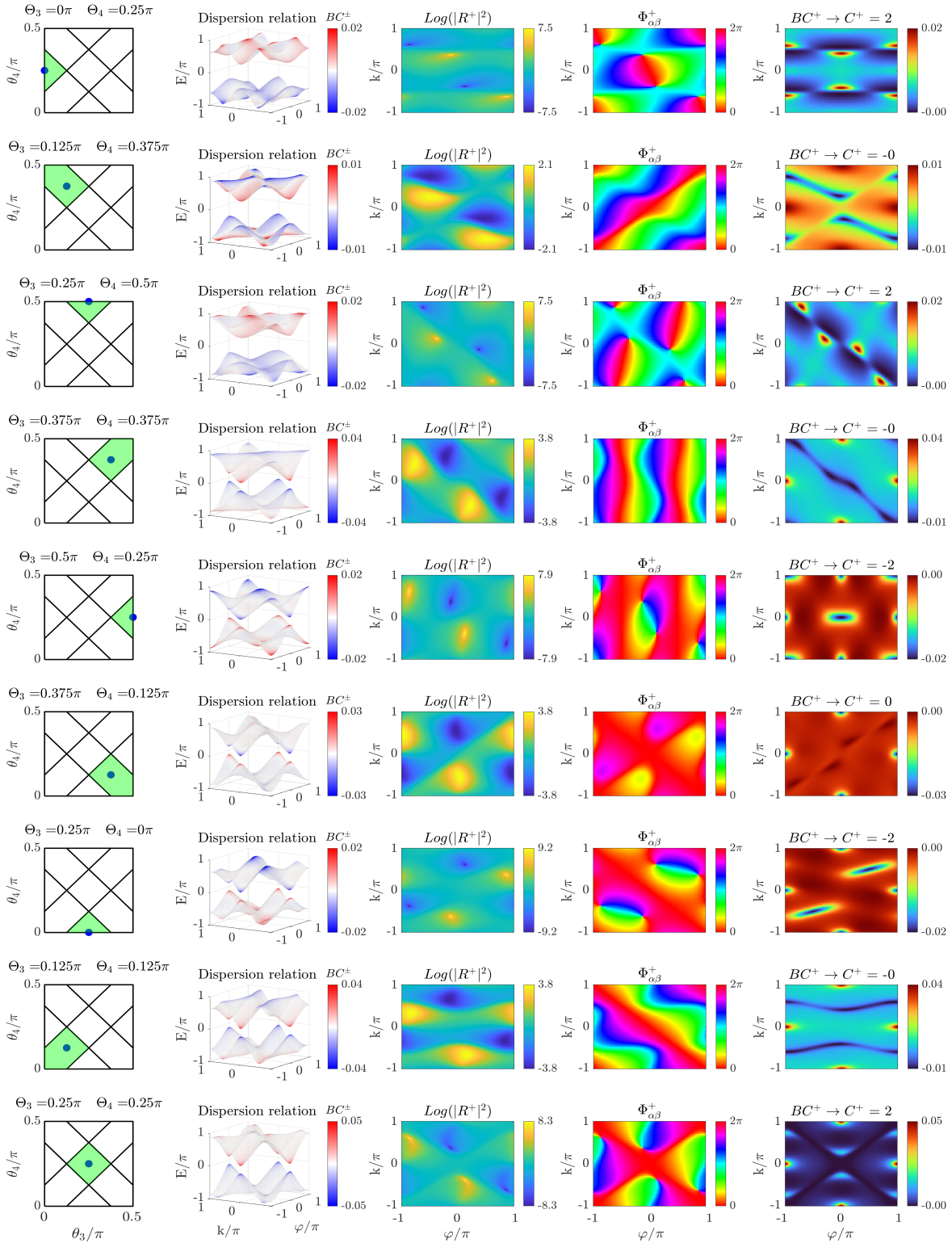


Figure 6.2: Numerical simulation illustrating, for each point in the four-step phase diagram, the dispersion band, amplitude ratio $|R|$, relative phase $\Phi_{\alpha\beta}$, and Berry curvature (BC) along with the Chern number (C) of the upper band.

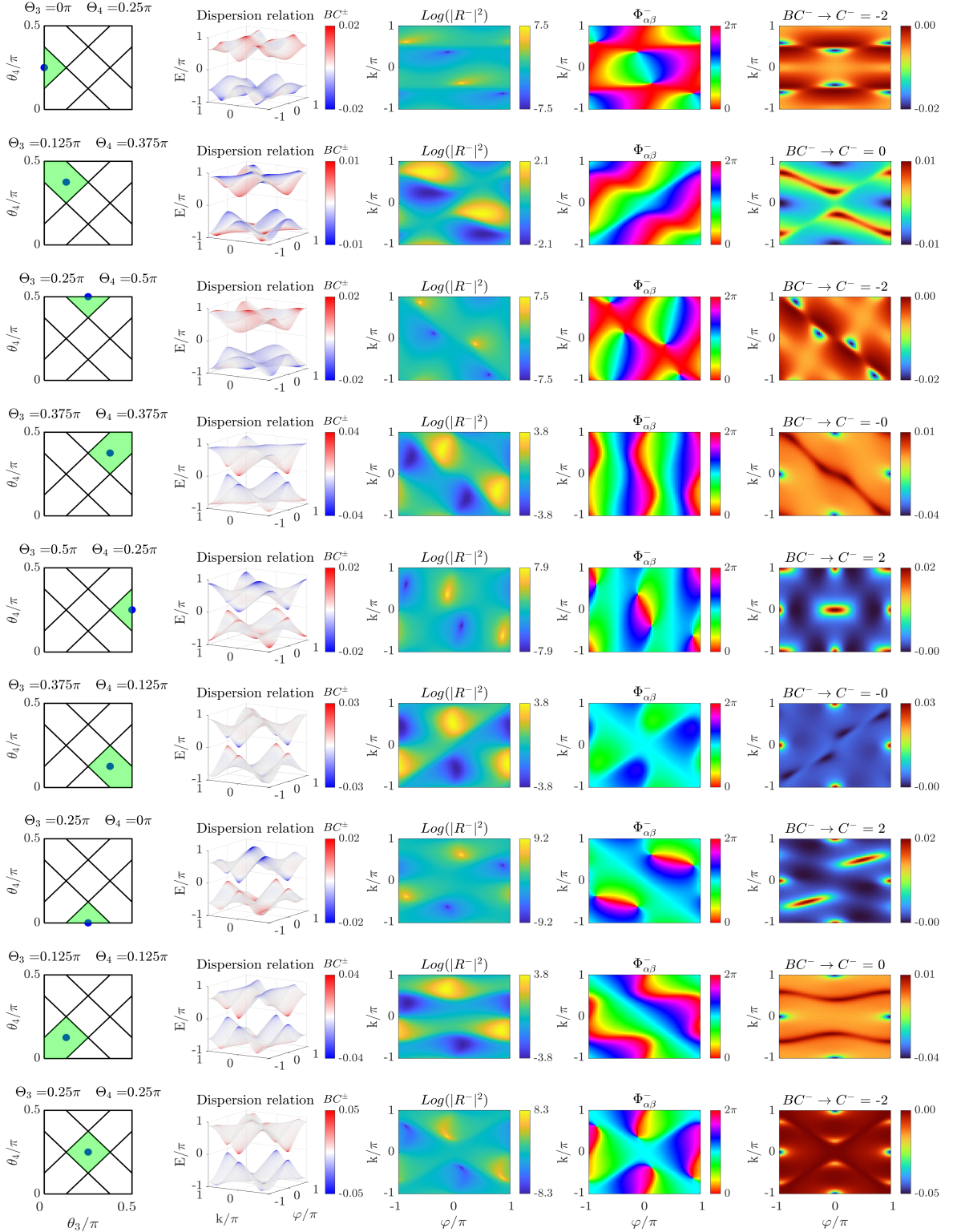


Figure 6.3: Numerical simulation illustrating, for each point in the four-step phase diagram, the dispersion band, amplitude ratio $|R|$, relative phase $\Phi_{\alpha\beta}$, and Berry curvature (BC) along with the Chern number (C) of the lower band.

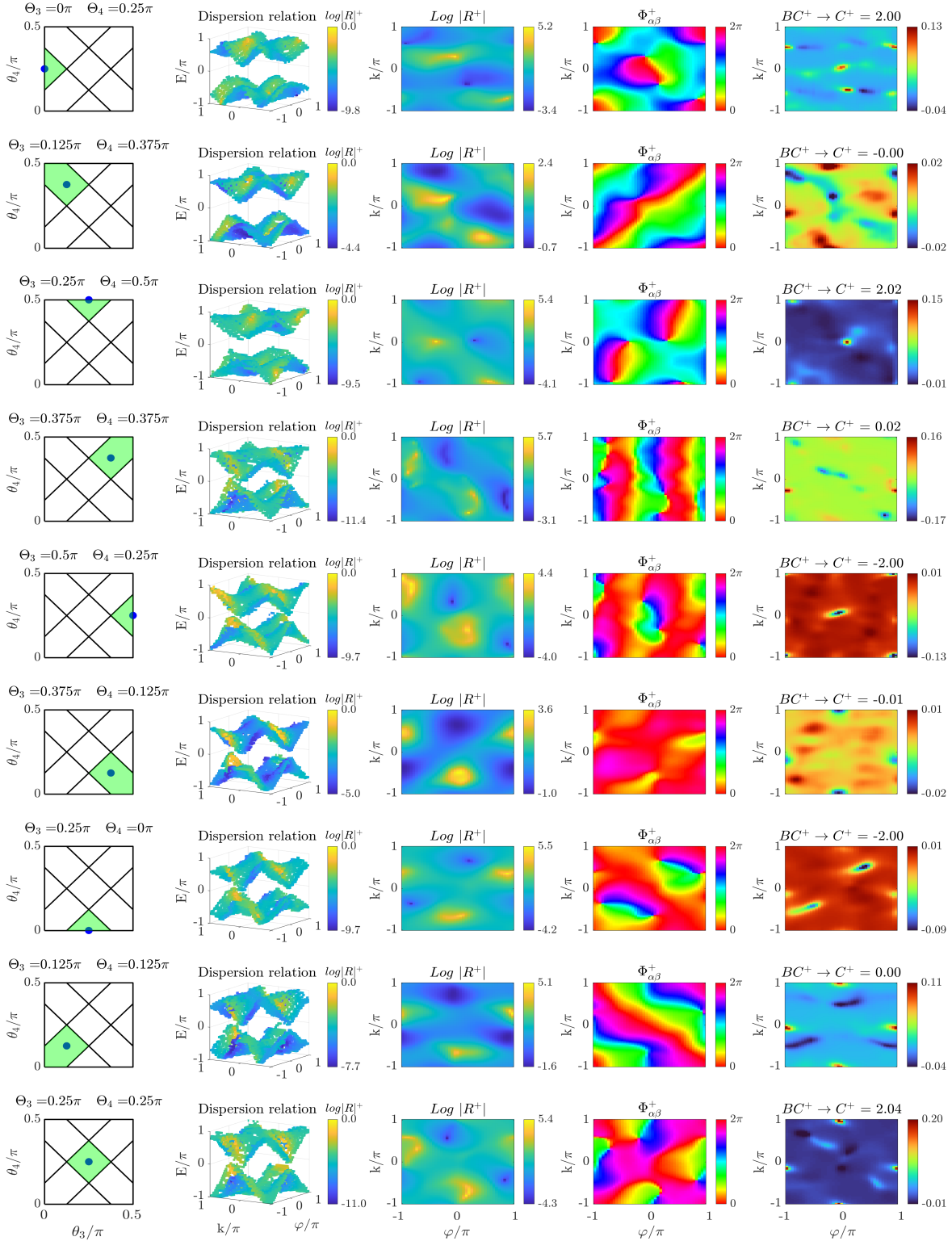


Figure 6.4: Experimental results, for each point in the four-step phase diagram, the dispersion band, amplitude ratio $|R|$, relative phase $\Phi_{\alpha\beta}$, and Berry curvature (BC) along with the Chern number (C) of the upper band.

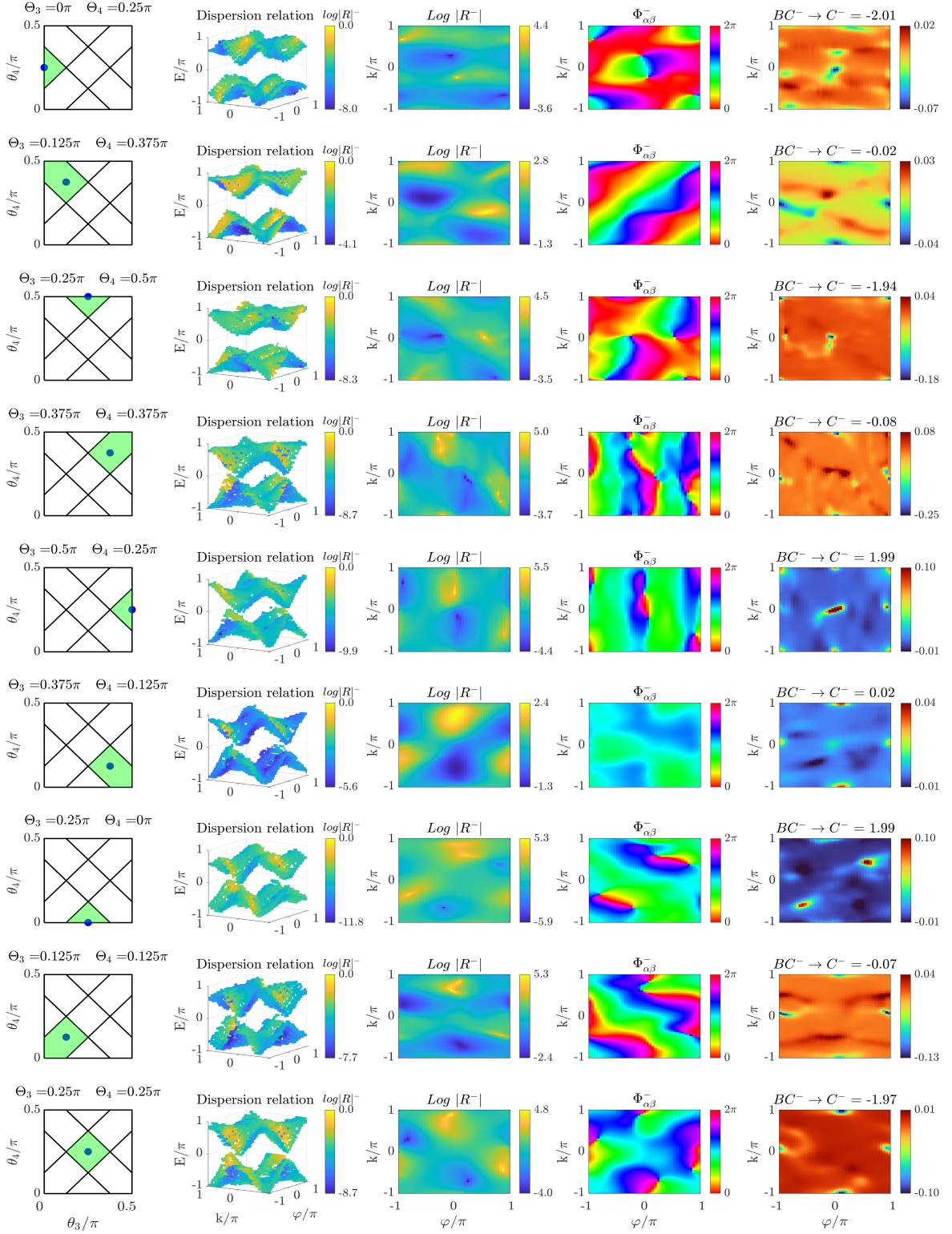


Figure 6.5: Experimental results, for each point in the four-step phase diagram, the dispersion band, amplitude ratio $|R|$, relative phase $\Phi_{\alpha\beta}$, and Berry curvature (BC) along with the Chern number (C) of the lower band.

6.2 Bulk-edge correspondence

Having identified in the previous section regions with trivial and non-trivial Chern numbers in the phase diagram, we now proceed to investigate the bulk-edge correspondence. The latter refers to a fundamental principle in topological physics that relates the topological invariants that characterize the bulk of a system (such as the Chern number in 2D systems) to the existence or absence of localized edge states at their boundaries or edges.

Figure 6.6 displays a numerical simulation illustrating the bulk-edge correspondence within the phase diagram of the four-step model. This is achieved by introducing a narrow pulse into the long ring α at site $n=1$, and alternating the coupling angle between four distinct values $[\theta_1, \theta_2, \theta_3, \theta_4]$ during one Floquet period, and the phase modulator between $+\varphi$ and $-\varphi$ at odd and even time steps. At site $n = 0$, we impose an open boundary condition (OBC) by setting the variable beam splitter to full reflectance ($\theta_{n=0}^m = \pi/2$). The phase diagram is divided into regions represented by white and orange, corresponding to trivial and non-trivial Chern numbers, respectively. For each region, the dispersion relation tomography for the (OBC) case is presented for a specific set of coupling angles $[\theta_3, \theta_4]$, marked by green dots, after selecting only the even stroboscopic round trips m .

In the odd-numbered orange regions (1), (3), and (9), the Chern numbers for the upper and lower bands are $C^+ = +2$ and $C^- = -2$, respectively. In each of these regions, two edge states cross the energy gap $\mu = \pi$, while no edge states cross the energy gap $\mu = 0$. The number of edge state mode traversing the band is $\nu_{\mu=\pi} = 2$ and $\nu_{\mu=0} = 0$. Conversely, regions (5) and (7) exhibit Chern numbers $C^+ = -2$ and $C^- = +2$. Both feature two edge states crossing the zero energy gap ($\nu_0 = 2$) but no edge states crossing the π gap. Notably, region (7) contains a localized state within the π energy gap, but since it does not traverse the gap, it does not have a topological origin and therefore cannot be considered as an edge state.

The even-numbered white regions, (2), (4), and (8), have zero Chern numbers ($C^\pm = 0$) and no edge states crossing the gap ($\nu_0 = \nu_\pi = 0$). In contrast, region (6) also has a zero Chern number ($C^\pm = 0$), but features two edge states crossing both gaps ($\nu_0 = \nu_\pi = 2$), representing an anomalous topological phase.

Based on our analysis of the bulk-edge correspondence, we can derive the Chern number from the number of edge states, expressed as follows [83]:

$$C^\pm = \pm(\nu_\pi - \nu_0) \quad (6.6)$$

The Chern number for a specific band is obtained by computing the difference between the number of edge states above the band and those below it.

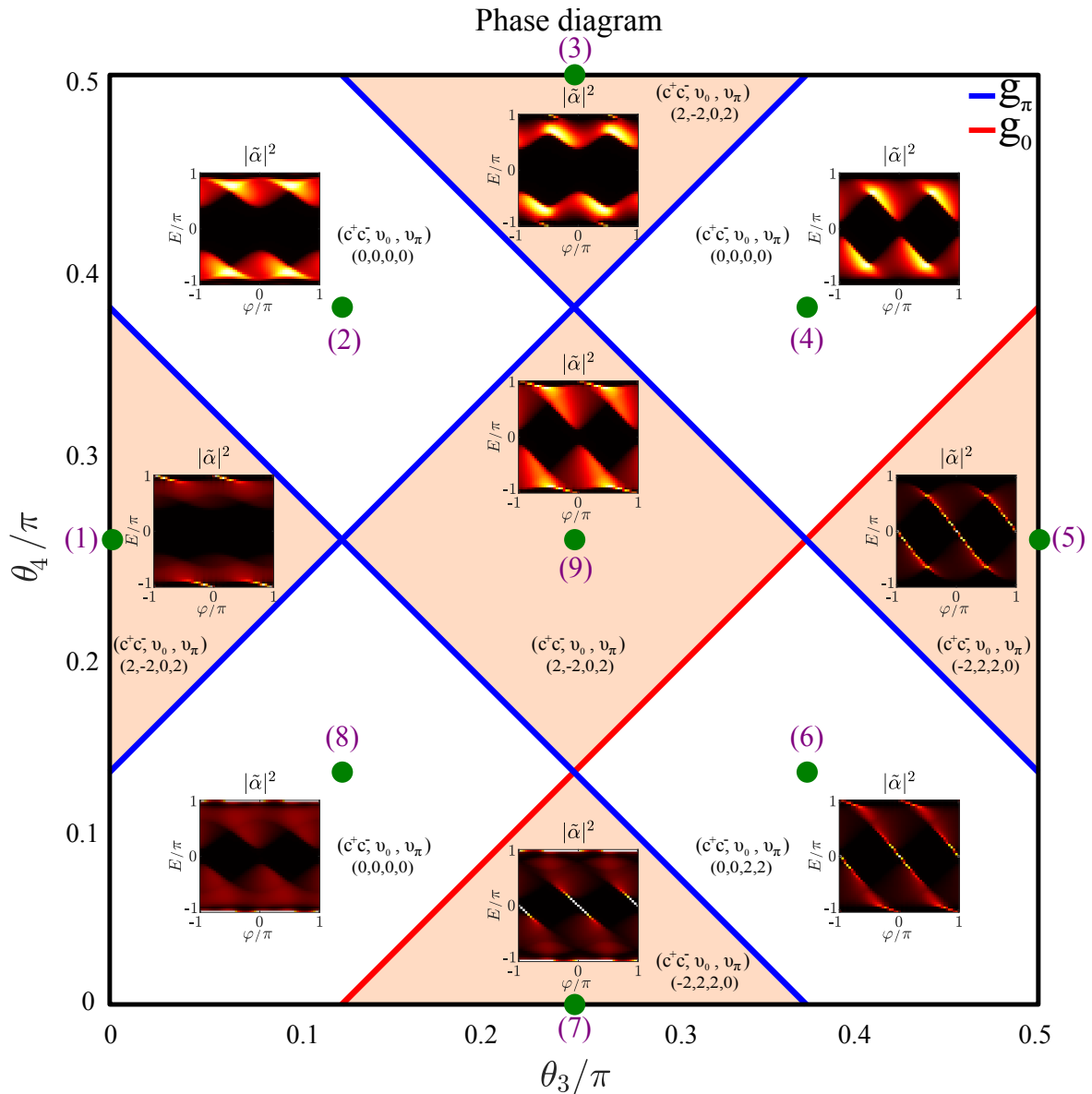


Figure 6.6: Numerical simulation illustrating the bulk-edge correspondence within the phase diagram of the four-step model. White and orange regions correspond to trivial and non-trivial Chern numbers, respectively. For each region, the dispersion relation tomography is conducted when an OBC is implemented at the site $n = 0$ for a specific set of coupling angles $[\theta_3, \theta_4]$, indicated by green dots.

6.3 Extrinsic topology

Similar to the two-step model in Chapter. 5, we aim now to examine in the case of the four-step model the influence of the extrinsic topology on the overall topological system in both trivial and non-trivial Chern bands scenarios by engineering properly the winding of the unitary operators acting on the edge sites.

Figure. 6.7 features upper (green) and lower (blue) boxes, each representing distinct points within the four-step model phase diagram. The green box illustrates

a point in the white region (4) with $(\theta_3, \theta_4) = (14/32, 14/32)\pi$, corresponding to a trivial Chern band. Conversely, the blue box denotes a point in the orange region (5) with $(\theta_3, \theta_4) = (1/2, 1/4)\pi$, which features non-zero Chern bands.

6.3.0.1 *Trivial Chern bands*

The first row of the green box (see Figs. 6.7.a-c), illustrates an OBC under the same conditions outlined in Fig. 6.6, as depicted in the quantum walk lattice in Fig. 6.7.a. Figures 6.7.b and 6.7.c provide a side-by-side comparison of the numerical and experimental dispersion relation tomography of the α ring, demonstrating a strong match and showcasing two distinct gapped bands with no edge states, indicating a zero Chern number and the absence of anomalous topological phases.

The second row (see Figs. 6.7.d-f) presents the hybridization scenarios (stripe + bulk). A boundary condition is imposed at site $n = 0$ by setting the coupling angles to full reflectance ($\theta_{n=0}^m = \pi/2$). Additionally, the phase modulator at sites $n = 0$ and 1 alternates between four distinct values $[\phi_1, \phi_2, \phi_3, \phi_4] = [1, 0, 0, 0]\varphi$, ensuring a non-zero net phase winding, $\sum_{i=1}^4 \phi_i = 1$, within one Floquet period. As a consequence, each gap is traversed by a single band of edge states, all exhibiting a positive group velocity, as depicted numerically and experimentally in Figs. 6.7.e and 6.7.c, respectively. Moreover, defining $([\phi_1, \phi_2, \phi_3, \phi_4] = [1, 0, 1, 0]\varphi$, the total phase winding becomes $\sum_{i=1}^4 \phi_i = 2$. As a result, each gap is now crossed by two bands of edge states with positive group velocity (see Figs. 6.7.h-i).

6.3.0.2 *Non-trivial Chern bands*

Figures. 6.7.j-l replicate Figs. 6.7.a-c and showcase an OBC for a point located at $(\theta_3, \theta_4) = (1/2, 1/4)\pi$ in region (5), characterized by $C^\pm = \mp 2$. The bands feature two edge states associated to the bulk topology with negative group velocity traversing the 0-gap, while no edge states cross the π -gap (see Figs. 6.7.k-l)

Figures. 6.7.m-o facilitates the hybridization scenarios when $[\phi_1, \phi_2, \phi_3, \phi_4] = [1, 0, 1, 0]\varphi$ and $(\theta_3, \theta_4) = (1/2, 1/4)\pi$. With this arrangement, the unitary operators acting on the edge sites exhibit a winding of +2 along the quasimomentum ϕ direction. This winding has an opposite sign to the winding of the Chern edge states displayed in Figs. 6.7.k-l. The hybridization of the Chern edge states with the winding of the edge operators results in the cancellation of the edge states at the 0-gap, as evidenced by a wavy localized state in Figs. 6.7.n-o that does not traverse 0-gap. Simultaneously, the winding of the edge operators introduces two edge states traversing the π -gap (see Figs. 6.7.n-o). Setting $[\phi_1, \phi_2, \phi_3, \phi_4] = [-1, 0, -1, 0]\varphi$ aligns the group velocities of the edge winding and the Chern edge states. This situation leads to the appearance of four edge states traversing the 0-gap and two traversing the π -gap, as demonstrated numerically and experimentally in Figs. 6.7.q-r, respectively. The low experimental resolution results from having only 16 stroboscopic turns.

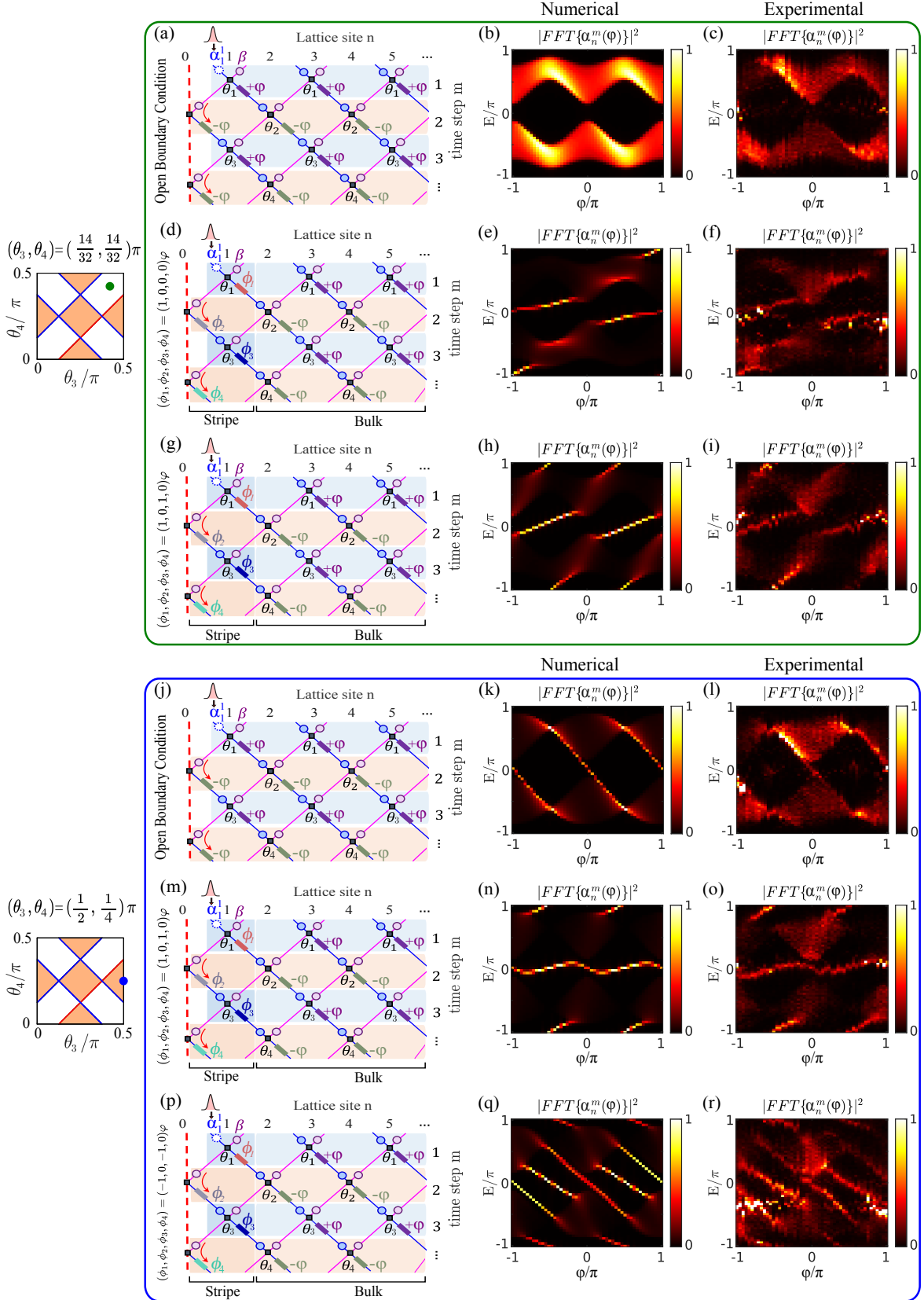


Figure 6.7: Numerical and experimental comparison is presented for OBC and various hybridization (stripe+bulk) cases, when $(\theta_3, \theta_4) = (14/32, 14/32)$ and $(1/2, 1/4)$, corresponding to the upper (green) and lower (blue) boxes, respectively.

6.4 Conclusion

This chapter presents a comprehensive theoretical and experimental analysis of both bulk and edge topology within the four-step model.

Beginning with bulk topology, our experimental measurements of the Berry curvature aligned with analytical predictions, allowing us to determine the exact Chern number. We observed both trivial and non-trivial Chern numbers, underscoring the richer phase diagram of the four-step model compared to its two-step counterpart. Additionally, we provided a second method for extracting the Chern number of a specific band by calculating the difference between the number of edge states above and below the band under open boundary conditions.

Finally, we examined the influence of extrinsic topology in systems with both zero and non-zero Chern numbers. Our findings indicate the potential to close and open specific gaps by effectively suppressing or inducing edge states, despite the low-resolution limitations imposed by the restricted number of round trips in the system.

Questions:

Is there a potential correlation between the Chern number and the number of vortex-antivortex pairs present in the relative phase $\Phi_{\alpha\beta}$? This hypothesis is currently under investigation in collaboration with our physics and mathematics colleagues.

CONCLUSION & PERSPECTIVE

7.1 Conclusion

Periodically driven lattices, commonly referred to as Floquet systems, exhibit a spectrum of modes that is both periodic in space and quasienergy. This phenomenon allows the emergence of bands featuring topological chiral edge states traversing the gap, even while exhibiting trivial Chern indices ($C=0$). Such phases are referred to as anomalous topological phases [7–9]. In cases where the driving is smooth and continuous, the bulk-edge correspondence is guaranteed by the existence of a bulk invariant, known as the winding number [83]. However, recent theoretical works show that 2D lattices subject to periodic discrete step walks result in a richer topological phase diagram, where the existence of chiral edge states does not only depend on the bulk invariant but also on an invariant associated with the specific edge termination "extrinsic" topology" [10]. This manuscript presents a comprehensive numerical and experimental analysis of both trivial and non-trivial topological phases, through simultaneous measurements of edge and bulk invariants in a 2D synthetic photonic lattice subjected to a discrete step-walk [120].

The 1D+1 lattice is implemented using time multiplexing of light pulses in two coupled fiber rings, characterized by a minor disparity in length and coupled with a variable beamsplitter (VBS). A second parametric synthetic dimension appears in the system when one of the rings incorporates an external phase modulator (PM), introducing a phase φ . The time evolution of light pulses in the rings is described by two mathematical equations. Each time step corresponds to a complete round trip of light within the rings. The split-step walk can be engineered to exhibit a periodicity of two or four round trips. In these cases, the models are referred to as the "two-step" and "four-step" models, respectively. Numerically, applying a 2D Fourier transform to the stroboscopic spatiotemporal diagram of the system's impulse response, we can access spectral information and presents a comprehensive characterization of the double-ring system eigenvalues and eigenvectors (from both power and phase spectral distributions). Experimentally, this is achieved within a single measurement by leveraging a heterodyne method [118]: a coherent beating between the extracted wavefield of the double rings, and the narrow bandwidth

of the local oscillator's reference field that is shifted by 3 GHz from the laser frequency.

In the case of the two-step model, the bulk topology is characterized by measuring the system's eigenstates, allowing for the determination of the Berry curvature and confirming a zero Chern number for the bands across all regions of the phase diagram. Additionally, the local Berry curvature changes sign at the gap-closing points during a phase transition, revealing a non trivial topological charge Q that indicates the presence of two distinct topological phases. This is evidenced through the existence of interface states when two distinct topological regions are pasted together. In the study of edge/extrinsic topology, an expression for the winding number is derived, demonstrating that the emergence of edge states is tied to a specific geometrical boundary. This relationship implies that irrespective of the coupling angle θ of the VBS, any region within the phase diagram can exhibit topological behavior. Furthermore, we elucidate how the topological properties of the boundaries can significantly influence the global topology of the system. This phenomenon is experimentally validated by manipulating the phase modulator at the boundary using a carefully designed sequence, enabling precise control over the suppression or induction of these edge states.

Building upon the two-step model, we conclude this thesis by examining the four-step model, which presents a richer topological phase diagram with both trivial and non-trivial Chern numbers. We explore various methods for extracting the Chern number, including Berry curvature and edge state analysis. Furthermore, we investigate the interplay between extrinsic topology and non-trivial Chern bands, providing deeper insights into the system's complex topological properties

7.2 Perspective

Our experimental platform establishes a foundation for investigating genuine step walk topology, including the potential observation of extrinsic topological phases when arbitrary unitary operators are introduced at the edge site [10]. These unitary operators can be designed to have local windings (i.e., at edge sites) by simply applying an appropriate voltage sequence to the phase modulator already present in one of the rings. This is not only interesting from a fundamental point of view but also paves the way for several practical investigations, such as exploring the robustness and lifetime of extrinsic edge states alongside those originating from bulk topology in the presence of disorder. Furthermore, this platform allows for the production of topological phases on demand, in situations in which the control of the bulk topology can be challenging. It could be of potential use to switch on and off topological channels via local actions at the edges of a two-dimensional metamaterial.

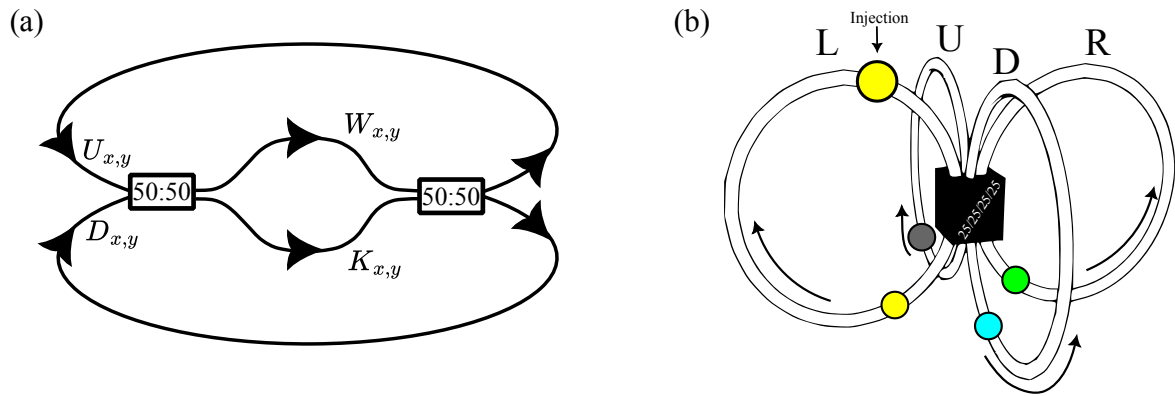


Figure 7.1: (a) A 2D system employing two consecutive coupled 2x2 beam splitters of 50/50 splitting ratios [170, 171]. (b) My proposed 2D system consists of four optical fiber rings interconnected by a 4x4 beam splitter of 25/25/25/25 splitting ratios.

Another promising direction for future research would involve exploring the eigenstates, eigenvalues, and topological invariants of a 2D system where the second dimension exists in real space rather than in a parameter space, as in our current study. Such a system has been implemented by A. Muniz et al. [170, 171], employing two consecutive 2x2 beam splitters with 50/50 splitting ratios, as illustrated in Fig. 7.1.a. In this configuration, the light pulse is first split along the horizontal spatial axis by the initial beam splitter, followed by a split along the vertical spatial axis by the second beam splitter. A novel alternative for obtaining a 2D system is my "Quadra-Ring" configuration, consisting of four optical fiber rings labeled U, D, L, and R (representing upward, downward, leftward, and rightward directions) interconnected by a 4x4 beam splitter with a 25/25/25/25 splitting ratio, as shown in Fig. 7.1.b. The numerical and analytical framework for this system is detailed in Appendix F, while experimental validation of this proposed configuration remains a goal for future research.

We anticipate that the results and insights presented in this manuscript, coupled with the accompanying perspectives, will serve as a catalyst for continued exploration and innovation within the field of fiber-based photonic lattices.

TWO-STEP MODEL

A.1 Eigenvector computation

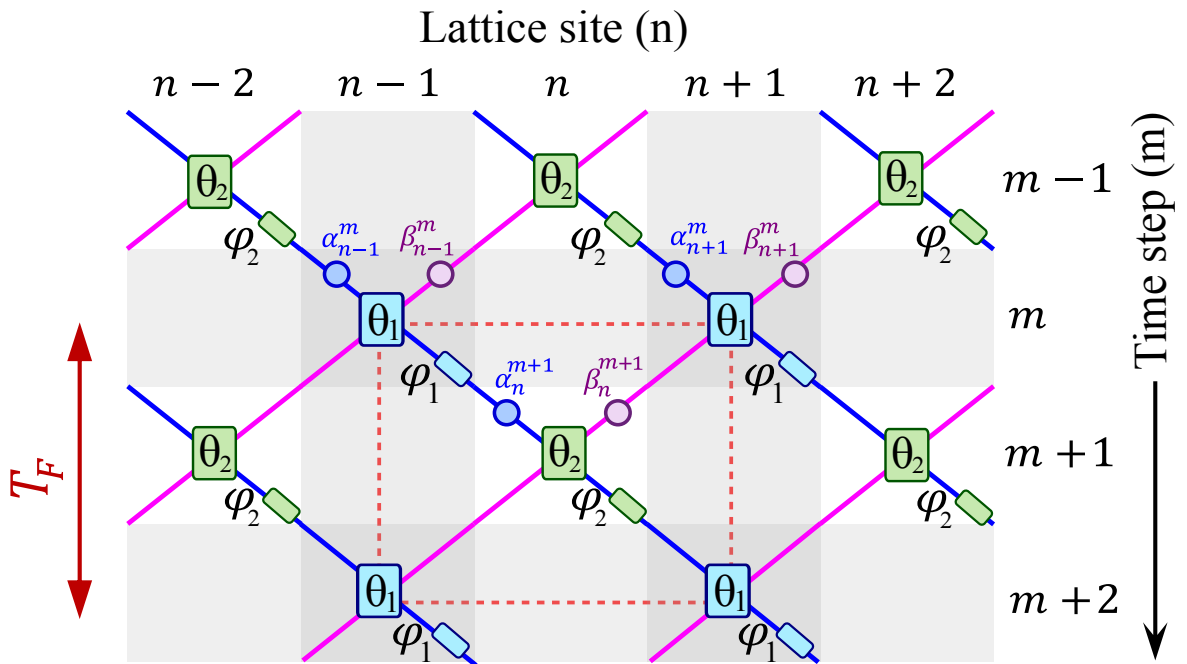


Figure A.1: Two-step model: the coupling angle alternates between two values, θ_1 and θ_2 , and the phase modulator between φ_1 and φ_2 at odd (m) and even ($m+1$) steps, the synthetic split step lattice spans in discrete steps along the position site n and time step m . The red dashed square defines the unit cell of the system that exhibits a double periodicity, a spatial periodicity with a period of two sites along the horizontal axis, and a temporal periodicity, with a period of two round trips along the vertical axis.

In the two-step model, the coupling angle θ and phase modulator demonstrate cyclic behavior, each alternating between two distinct values within a single Floquet period. The two-step model exhibits double periodicity: spatial (every two sites n) and temporal (every two-time steps m), as shown by the unit cell (red dashed square) in Fig. A.1. The lattice system has two sublattices α_n^m (blue) and β_n^m (purple) circles corresponding to the α and β rings.

The eigenvectors $|\psi\rangle^\pm$ are represented as a linear combination of the two complex amplitude eigenmodes $\tilde{\alpha}^\pm(k)$ and $\tilde{\beta}^\pm(k)$ corresponding to the α and β rings respectively.

$$|\psi(k)\rangle^\pm = \begin{pmatrix} \tilde{\alpha}(k) \\ \tilde{\beta}(k) \end{pmatrix}^\pm = \begin{pmatrix} |\tilde{\alpha}|e^{i\varphi_\alpha} \\ |\tilde{\beta}|e^{i\varphi_\beta} \end{pmatrix}^\pm \quad (\text{A.1})$$

We express the normalized eigenvector as the following expression:

$$\begin{aligned} |\psi(k)\rangle_{\text{norm}}^\pm &= \frac{1}{\sqrt{|\tilde{\alpha}|^2 + |\tilde{\beta}|^2}} \begin{pmatrix} |\tilde{\alpha}|e^{i\varphi_\alpha} \\ |\tilde{\beta}|e^{i\varphi_\beta} \end{pmatrix}^\pm \\ |\psi(k)\rangle_{\text{norm}}^\pm &= \frac{1}{|\tilde{\alpha}|\sqrt{1 + \frac{|\tilde{\beta}|^2}{|\tilde{\alpha}|^2}}} \begin{pmatrix} |\tilde{\alpha}|e^{i\varphi_\alpha} \\ |\tilde{\alpha}|e^{i\varphi_\beta} \end{pmatrix}^\pm \\ |\psi(k)\rangle_{\text{norm}}^\pm &= \frac{1}{|\tilde{\alpha}|\sqrt{1 + \frac{|\tilde{\beta}|^2}{|\tilde{\alpha}|^2}}} |\tilde{\alpha}| \begin{pmatrix} 1 \\ \frac{|\tilde{\beta}|}{|\tilde{\alpha}|}e^{i(\varphi_\beta - \varphi_\alpha)} \end{pmatrix}^\pm \\ |\psi(k)\rangle_{\text{norm}}^\pm &= \frac{1}{\sqrt{1 + |R^\pm|^2}} \begin{pmatrix} 1 \\ |R^\pm|e^{i\Phi_{\alpha\beta}^\pm} \end{pmatrix} \end{aligned} \quad (\text{A.2})$$

The magnitude $|R^\pm|$ and the argument $\Phi_{\alpha\beta}^\pm$ of the ratio of amplitude amplitudes $R^\pm(k)$ between the two sublattice sites for each quasimomentum eigenvector of each band are given by the following equation:

$$\begin{cases} R(k)^\pm = |R^\pm|e^{i\Phi_{\alpha\beta}^\pm} = \frac{\tilde{\beta}^\pm}{\tilde{\alpha}^\pm} \\ |R^\pm| = \frac{|\tilde{\beta}^\pm|}{|\tilde{\alpha}^\pm|} \\ \Phi_{\alpha\beta}^\pm = \varphi_\beta^\pm - \varphi_\alpha^\pm = \arg(\tilde{\beta}^\pm) - \arg(\tilde{\alpha}^\pm) \end{cases} \quad (\text{A.3})$$

The dynamics of the amplitude and phase of light pulses in the rings can be mapped into a coherent step evolution in the one-dimensional synthetic lattice depicted in Fig. A.1, governed by the following equations:

$$\begin{cases} \alpha_n^{m+1} = \left(\cos \theta_{n-1}^m \alpha_{n-1}^m + i \sin \theta_{n-1}^m \beta_{n-1}^{m-1} \right) e^{i\varphi_{n-1}^m} \\ \beta_n^{m+1} = i \sin \theta_{n+1}^m \alpha_{n+1}^m + \cos \theta_{n+1}^m \beta_{n+1}^m \end{cases} \quad (\text{A.4})$$

Let's consider that the coupling angle alternates between two values, θ_1 and θ_2 , and the phase modulator between φ_1 and φ_2 at odd (m) and even ($m+1$) time steps, as presented in equation A.5 and illustrated in Fig. A.1.

$$\varphi_n^m = \begin{cases} \varphi_1 & \forall n \text{ at odd time steps} \\ \varphi_2 & \forall n \text{ at even time steps} \end{cases} \quad \theta_n^m = \begin{cases} \theta_1 & \forall n \text{ at odd time steps} \\ \theta_2 & \forall n \text{ at even time steps} \end{cases} \quad (\text{A.5})$$

$$\alpha_n^{m+1} = (\cos \theta_1 \alpha_{n-1}^m + i \sin \theta_1 \beta_{n-1}^m) e^{i\varphi_1} \quad (\text{A.6})$$

$$\beta_n^{m+1} = i \sin \theta_1 \alpha_{n+1}^m + \cos \theta_1 \beta_{n+1}^m \quad (\text{A.7})$$

$$\alpha_{n-1}^{m+2} = (\cos \theta_2 \alpha_{n-2}^{m+1} + i \sin \theta_2 \beta_{n-2}^{m+1}) e^{i\varphi_2} \quad (\text{A.8})$$

$$\beta_{n-1}^{m+2} = i \sin \theta_2 \alpha_n^{m+1} + \cos \theta_2 \beta_n^{m+1} \quad (\text{A.9})$$

Due to the system's double periodicity, equations A.6 and A.7 can be solved using the Floquet-Bloch ansatz equation.

$$\begin{pmatrix} \alpha_n^m \\ \beta_n^m \end{pmatrix} = \begin{pmatrix} \tilde{\alpha}(k) \\ \tilde{\beta}(k) \end{pmatrix} e^{i\frac{E_m}{2}} e^{i\frac{kn}{2}} \quad (\text{A.10})$$

The temporal evolution of the sublattices complex amplitudes (α_m^n & β_m^n) at any stroboscopic time in real space can be expressed as a superposition of all the eigenmodes in reciprocal space, with $\tilde{\alpha}$ and $\tilde{\beta}$ being the complex amplitude of the eigenmodes at the sites corresponding to the α and β rings respectively.

One Floquet period is 2 round trips, we express α^{m+2} or β^{m+2} in the function of α^m and β^m to find the eigenvector. We start by replacing equations A.6 and A.7 in equation A.8, as we will demonstrate.

Starting with equation A.8:

$$\alpha_{n-1}^{m+2} = (\cos \theta_2 \alpha_{n-2}^{m+1} + i \sin \theta_2 \beta_{n-2}^{m+1}) e^{i\varphi_2}$$

$$\alpha_{n-1}^{m+2} = (\cos \theta_2 [\cos \theta_1 \alpha_{n-3}^m + i \sin \theta_1 \beta_{n-3}^m] e^{i\varphi_1} + i \sin \theta_2 [i \sin \theta_1 \alpha_{n-1}^m + \cos \theta_1 \beta_{n-1}^m]) e^{i\varphi_2}$$

$$\begin{aligned} \alpha_{n-1}^{m+2} &= \cos \theta_2 \cos \theta_1 \alpha_{n-3}^m e^{i(\varphi_1 + \varphi_2)} + i \cos \theta_2 \sin \theta_1 \beta_{n-3}^m e^{i(\varphi_1 + \varphi_2)} \\ &\quad - \sin \theta_2 \sin \theta_1 \alpha_{n-1}^m e^{i\varphi_2} + i \sin \theta_2 \cos \theta_1 \beta_{n-1}^m e^{i\varphi_2} \end{aligned} \quad (\text{A.11})$$

Substituting equation. A.10 in equation. A.11

$$\begin{aligned}\tilde{\alpha} e^{\frac{iE(m+2)}{2}} e^{\frac{ik(n-1)}{2}} &= \cos \theta_2 \cos \theta_1 \tilde{\alpha} e^{\frac{iE(m)}{2}} e^{\frac{ik(n-3)}{2}} e^{i(\varphi_1+\varphi_2)} \\ &+ i \cos \theta_2 \sin \theta_1 \tilde{\beta} e^{\frac{iE(m)}{2}} e^{\frac{ik(n-3)}{2}} e^{i(\varphi_1+\varphi_2)} \\ &- \sin \theta_2 \sin \theta_1 \tilde{\alpha} e^{\frac{iE(m)}{2}} e^{\frac{ik(n-1)}{2}} e^{i\varphi_2} \\ &+ i \sin \theta_2 \cos \theta_1 \tilde{\beta} e^{\frac{iE(m)}{2}} e^{\frac{ik(n-1)}{2}} e^{i\varphi_2}\end{aligned}$$

$$\begin{aligned}\tilde{\alpha} e^{\frac{iE(m)}{2}} e^{\frac{i2E}{2}} e^{\frac{ik(n-1)}{2}} &= \cos \theta_2 \cos \theta_1 \tilde{\alpha} e^{\frac{iE(m)}{2}} e^{\frac{ik(n-1)}{2}} e^{\frac{-2ik}{2}} e^{i(\varphi_1+\varphi_2)} \\ &+ i \cos \theta_2 \sin \theta_1 \tilde{\beta} e^{\frac{iE(m)}{2}} e^{\frac{ik(n-1)}{2}} e^{\frac{-2ik}{2}} e^{i(\varphi_1+\varphi_2)} \\ &- \sin \theta_2 \sin \theta_1 \tilde{\alpha} e^{\frac{iE(m)}{2}} e^{\frac{ik(n-1)}{2}} e^{i\varphi_2} \\ &+ i \sin \theta_2 \cos \theta_1 \tilde{\beta} e^{\frac{iE(m)}{2}} e^{\frac{ik(n-1)}{2}} e^{i\varphi_2}\end{aligned}$$

$$\begin{aligned}\tilde{\alpha} e^{iE} &= \cos \theta_2 \cos \theta_1 \tilde{\alpha} e^{-ik} e^{i(\varphi_1+\varphi_2)} + i \cos \theta_2 \sin \theta_1 \tilde{\beta} e^{-ik} e^{i(\varphi_1+\varphi_2)} \\ &- \sin \theta_2 \sin \theta_1 \tilde{\alpha} e^{i\varphi_2} + i \sin \theta_2 \cos \theta_1 \tilde{\beta} e^{i\varphi_2}\end{aligned}$$

$$\begin{aligned}\tilde{\alpha} e^{iE} &= \tilde{\alpha} [\cos \theta_2 \cos \theta_1 e^{-ik} e^{i(\varphi_1+\varphi_2)} - \sin \theta_2 \sin \theta_1 e^{i\varphi_2}] \\ &+ \tilde{\beta} [i \cos \theta_2 \sin \theta_1 e^{-ik} e^{i(\varphi_1+\varphi_2)} + i \sin \theta_2 \cos \theta_1 e^{i\varphi_2}]\end{aligned}\tag{A.12}$$

$$R(k)^\pm = |R^\pm| e^{i\Phi_{\tilde{\alpha}\tilde{\beta}}^\pm} = \frac{\tilde{\beta}^\pm}{\tilde{\alpha}^\pm} = \frac{[e^{iE^\pm} - \cos \theta_2 \cos \theta_1 e^{-ik} e^{i(\varphi_1+\varphi_2)} + \sin \theta_2 \sin \theta_1 e^{i\varphi_2}]}{[i \cos \theta_2 \sin \theta_1 e^{-ik} e^{i(\varphi_1+\varphi_2)} + i \sin \theta_2 \cos \theta_1 e^{i\varphi_2}]} \tag{A.13}$$

Equation. A.13 shows the eigenvector derived by substituting equations. A.6 and A.7 into equation. A.8, and then applying equation. A.10 to the result. Alternatively, the same eigenvector can be obtained by substituting equations. A.6 and A.7 into equation. A.9, as we will demonstrate.

Starting with equation. A.9:

$$\beta_{n-1}^{m+2} = i \sin \theta_2 \alpha_n^{m+1} + \cos \theta_2 \beta_n^{m+1} \tag{A.14}$$

$$\begin{aligned}\beta_{n-1}^{m+2} &= i \sin \theta_2 \cos \theta_1 \alpha_{n-1}^m e^{i\varphi_1} - \sin \theta_2 \sin \theta_1 \beta_{n-1}^m e^{i\varphi_1} \\ &+ i \cos \theta_2 \sin \theta_1 \alpha_{n+1}^m + \cos \theta_2 \cos \theta_1 \beta_{n+1}^m\end{aligned}\tag{A.15}$$

Substituting equation. A.10 in equation. A.15

$$\begin{aligned} \tilde{\beta} e^{\frac{iE(m+2)}{2}} e^{\frac{ik(n-1)}{2}} &= i \sin \theta_2 \cos \theta_1 \tilde{\alpha} e^{\frac{iE(m)}{2}} e^{\frac{ik(n-1)}{2}} e^{i\varphi_1} - \sin \theta_2 \sin \theta_1 \tilde{\beta} e^{\frac{iE(m)}{2}} e^{\frac{ik(n-1)}{2}} e^{i\varphi_1} \\ &\quad + i \cos \theta_2 \sin \theta_1 \tilde{\alpha} e^{\frac{iE(m)}{2}} e^{\frac{ik(n+1)}{2}} + \cos \theta_2 \cos \theta_1 \tilde{\beta} e^{\frac{iE(m)}{2}} e^{\frac{ik(n+1)}{2}} \end{aligned}$$

$$\begin{aligned} \tilde{\beta} e^{\frac{iE(m)}{2}} e^{\frac{i2E}{2}} e^{\frac{ik(n-1)}{2}} &= i \sin \theta_2 \cos \theta_1 \tilde{\alpha} e^{\frac{iE(m)}{2}} e^{\frac{ik(n-1)}{2}} e^{i\varphi_1} - \sin \theta_2 \sin \theta_1 \tilde{\beta} e^{\frac{iE(m)}{2}} e^{\frac{ik(n-1)}{2}} e^{i\varphi_1} \\ &\quad + i \cos \theta_2 \sin \theta_1 \tilde{\alpha} e^{\frac{iE(m)}{2}} e^{\frac{ik(n-1)}{2}} e^{\frac{i2k}{2}} + \cos \theta_2 \cos \theta_1 \tilde{\beta} e^{\frac{iE(m)}{2}} e^{\frac{ik(n-1)}{2}} e^{\frac{i2k}{2}} \end{aligned}$$

$$\tilde{\beta} e^{iE} = i \sin \theta_2 \cos \theta_1 \tilde{\alpha} e^{i\varphi_1} - \sin \theta_2 \sin \theta_1 \tilde{\beta} e^{i\varphi_1} + i \cos \theta_2 \sin \theta_1 \tilde{\alpha} e^{ik} + \cos \theta_2 \cos \theta_1 \tilde{\beta} e^{ik}$$

$$\tilde{\beta} e^{iE} = \tilde{\alpha} i [\sin \theta_2 \cos \theta_1 e^{i\varphi_1} + \cos \theta_2 \sin \theta_1 e^{ik}] + \tilde{\beta} [-\sin \theta_2 \sin \theta_1 e^{i\varphi_1} + \cos \theta_2 \cos \theta_1 e^{ik}] \quad (\text{A.16})$$

$$\tilde{\beta} [e^{iE} + \sin \theta_2 \sin \theta_1 e^{i\varphi_1} - \cos \theta_2 \cos \theta_1 e^{ik}] = \tilde{\alpha} [i \sin \theta_2 \cos \theta_1 e^{i\varphi_1} + i \cos \theta_2 \sin \theta_1 e^{ik}]$$

$$R(k)^\pm = |R^\pm| e^{i\Phi_{\tilde{\alpha}\tilde{\beta}}^\pm} = \frac{\tilde{\beta}^\pm}{\tilde{\alpha}^\pm} = \frac{[i \sin \theta_2 \cos \theta_1 e^{i\varphi_1} + i \cos \theta_2 \sin \theta_1 e^{ik}]}{[e^{iE^\pm} + \sin \theta_2 \sin \theta_1 e^{i\varphi_1} - \cos \theta_2 \cos \theta_1 e^{ik}]} \quad (\text{A.17})$$

A.2 Eigenvalue computation

To determine the eigenvalue, we can use one of two methods: either by solving the equation given in A.13 set equal to the expression in A.17, or by solving the evolution operator. In the following section, we will focus on solving the evolution operator.

From equation. A.12 we have:

$$\begin{aligned} \tilde{\alpha} e^{iE} &= \tilde{\alpha} [\cos \theta_2 \cos \theta_1 e^{-ik} e^{i(\varphi_1+\varphi_2)} - \sin \theta_2 \sin \theta_1 e^{i\varphi_2}] \\ &\quad + \tilde{\beta} [i \cos \theta_2 \sin \theta_1 e^{-ik} e^{i(\varphi_1+\varphi_2)} + i \sin \theta_2 \cos \theta_1 e^{i\varphi_2}] \end{aligned}$$

$$\begin{aligned} \tilde{\alpha} &= \underbrace{\tilde{\alpha} [\cos \theta_2 \cos \theta_1 e^{i(-k-E+\varphi_1+\varphi_2)} - \sin \theta_2 \sin \theta_1 e^{i(\varphi_2-E)}]}_A \\ &\quad + \underbrace{\tilde{\beta} [i \cos \theta_2 \sin \theta_1 e^{i(-k-E+\varphi_1+\varphi_2)} + i \sin \theta_2 \cos \theta_1 e^{i(-E+\varphi_2)}]}_B \end{aligned} \quad (\text{A.18})$$

From equation. A.16 we have:

$$\tilde{\beta} e^{iE} = \tilde{\alpha} i [\sin \theta_2 \cos \theta_1 e^{i\varphi_1} + \cos \theta_2 \sin \theta_1 e^{ik}] + \tilde{\beta} [-\sin \theta_2 \sin \theta_1 e^{i\varphi_1} + \cos \theta_2 \cos \theta_1 e^{ik}]$$

$$\begin{aligned} \tilde{\beta} = & \tilde{\alpha} \underbrace{i[\sin \theta_2 \cos \theta_1 e^{i(\varphi_1-E)} + \cos \theta_2 \sin \theta_1 e^{i(k-E)}]}_C \\ & + \tilde{\beta} \underbrace{[-\sin \theta_2 \sin \theta_1 e^{i(\varphi_1-E)} + \cos \theta_2 \cos \theta_1 e^{i(k-E)}]}_D \end{aligned} \quad (\text{A.19})$$

From equation. A.18 and A.19 we obtain:

$$\begin{cases} \tilde{\alpha} = \tilde{\alpha}A + \tilde{\beta}B \\ \tilde{\beta} = \tilde{\alpha}D + \tilde{\beta}C \end{cases}$$

$$\begin{pmatrix} \tilde{\alpha} \\ \tilde{\beta} \end{pmatrix} = \underbrace{\begin{bmatrix} A & B \\ C & D \end{bmatrix}}_{\text{Evolution operator}} \begin{pmatrix} \tilde{\alpha} \\ \tilde{\beta} \end{pmatrix}$$

$$\begin{pmatrix} \tilde{\alpha} \\ \tilde{\beta} \end{pmatrix} \left(\begin{bmatrix} A & B \\ C & D \end{bmatrix} - I \right) = 0$$

$$\det \begin{vmatrix} A - I & B \\ C & D - I \end{vmatrix} = 0$$

$$\begin{aligned} & - \cos \theta_2 \cos \theta_1 \sin \theta_2 \sin \theta_1 e^{i(-k-2E+2\varphi_1+\varphi_2)} + \cos^2 \theta_2 \cos^2 \theta_1 e^{i(-2E+\varphi_1+\varphi_2)} \\ & - \cos \theta_2 \cos \theta_1 e^{i(-k-E+\varphi_1+\varphi_2)} + \sin^2 \theta_2 \sin^2 \theta_1 e^{i(-2E+\varphi_1+\varphi_2)} - \sin \theta_2 \sin \theta_1 \cos \theta_2 \cos \theta_1 e^{i(\varphi_2-2E+k)} \\ & + \sin \theta_2 \sin \theta_1 e^{i(\varphi_2-E)} + \sin \theta_2 \sin \theta_1 e^{i(\varphi_1-E)} - \cos \theta_2 \cos \theta_1 e^{i(k-E)} + 1 \\ & + \sin \theta_2 \cos \theta_1 \cos \theta_2 \sin \theta_1 e^{i(-k-2E+2\varphi_1+\varphi_2)} + \sin^2 \theta_2 \cos^2 \theta_1 e^{i(-2E+\varphi_1+\varphi_2)} \\ & + \cos^2 \theta_2 \sin^2 \theta_1 e^{i(-2E+\varphi_1+\varphi_2)} + \cos \theta_2 \sin \theta_1 \sin \theta_2 \cos \theta_1 e^{i(\varphi_2-2E+k)} = 0 \end{aligned}$$

$$\begin{aligned} & - \cos \theta_2 \cos \theta_1 e^{i(-k-E+\varphi_1+\varphi_2)} + \sin \theta_2 \sin \theta_1 e^{i(\varphi_2-E)} + \sin \theta_2 \sin \theta_1 e^{i(\varphi_1-E)} - \cos \theta_2 \cos \theta_1 e^{i(k-E)} \\ & + e^{i(-2E+\varphi_1+\varphi_2)} \underbrace{[\cos^2 \theta_2 \cos^2 \theta_1 + \sin^2 \theta_2 \sin^2 \theta_1 + \sin^2 \theta_2 \cos^2 \theta_1 + \cos^2 \theta_2 \sin^2 \theta_1]}_1 + 1 = 0 \end{aligned}$$

$$\begin{aligned} & e^{-iE} [-\cos \theta_2 \cos \theta_1 e^{i(-k+\varphi_1+\varphi_2)} + \sin \theta_2 \sin \theta_1 e^{i\varphi_2} + \sin \theta_2 \sin \theta_1 e^{i\varphi_1} - \cos \theta_2 \cos \theta_1 e^{ik}] \\ & + e^{i(-2E+\varphi_1+\varphi_2)} + 1 = 0 \end{aligned}$$

$$- e^{-iE} [\cos \theta_2 \cos \theta_1 (e^{i(-k+\varphi_1+\varphi_2)} + e^{ik}) - \sin \theta_2 \sin \theta_1 (e^{i\varphi_2} + e^{i\varphi_1})] + e^{i(-2E+\varphi_1+\varphi_2)} + 1 = 0$$

$$\begin{aligned}
 & - e^{-iE} e^{i\frac{(\varphi_1+\varphi_2)}{2}} [\cos \theta_2 \cos \theta_1 (e^{-ik} e^{i\frac{(\varphi_1+\varphi_2)}{2}} + e^{ik} e^{-i\frac{(\varphi_1+\varphi_2)}{2}}) \\
 & - \sin \theta_2 \sin \theta_1 (e^{i\varphi_2} e^{-i\frac{(\varphi_1+\varphi_2)}{2}} + e^{i\varphi_1} e^{-i\frac{(\varphi_1+\varphi_2)}{2}})] + e^{-2iE} e^{i(\varphi_1+\varphi_2)} + 1 = 0 \\
 & - e^{-iE} e^{i\frac{(\varphi_1+\varphi_2)}{2}} [2 \cos \theta_2 \cos \theta_1 \cos\left(\frac{\varphi_1 + \varphi_2}{2} - k\right) - \sin \theta_2 \sin \theta_1 (e^{i\frac{(\varphi_2-\varphi_1)}{2}} + e^{i\frac{(\varphi_1-\varphi_2)}{2}})] \\
 & + e^{-2iE} e^{i(\varphi_1+\varphi_2)} + 1 = 0 \\
 & - e^{-iE} e^{i\frac{(\varphi_1+\varphi_2)}{2}} [2 \cos \theta_2 \cos \theta_1 \cos\left(\frac{\varphi_1 + \varphi_2}{2} - k\right) - 2 \sin \theta_2 \sin \theta_1 \cos\left(\frac{\varphi_1 - \varphi_2}{2}\right)] \\
 & + e^{-2iE} e^{i(\varphi_1+\varphi_2)} + 1 = 0 \\
 & \underbrace{e^{-iE} e^{i\frac{(\varphi_1+\varphi_2)}{2}}}_{\neq 0} [-[2 \cos \theta_2 \cos \theta_1 \cos\left(\frac{\varphi_1 + \varphi_2}{2} - k\right) - 2 \sin \theta_2 \sin \theta_1 \cos\left(\frac{\varphi_1 - \varphi_2}{2}\right)] \\
 & + e^{-iE} e^{i\frac{(\varphi_1+\varphi_2)}{2}} + e^{iE} e^{-i\frac{(\varphi_1+\varphi_2)}{2}}] = 0 \\
 & - 2 \cos \theta_2 \cos \theta_1 \cos\left(\frac{\varphi_1 + \varphi_2}{2} - k\right) - 2 \sin \theta_2 \sin \theta_1 \cos\left(\frac{\varphi_1 - \varphi_2}{2}\right) \\
 & + e^{-iE} e^{i\frac{(\varphi_1+\varphi_2)}{2}} + e^{iE} e^{-i\frac{(\varphi_1+\varphi_2)}{2}} = 0 \\
 & 2 \cos\left(\frac{\varphi_1 + \varphi_2}{2} - E\right) - 2 \cos \theta_2 \cos \theta_1 \cos\left(\frac{\varphi_1 + \varphi_2}{2} - k\right) - 2 \sin \theta_2 \sin \theta_1 \cos\left(\frac{\varphi_1 - \varphi_2}{2}\right) = 0 \\
 & \frac{\varphi_1 + \varphi_2}{2} - E = \pm \cos^{-1} [\cos \theta_2 \cos \theta_1 \cos\left(\frac{\varphi_1 + \varphi_2}{2} - k\right) - \sin \theta_2 \sin \theta_1 \cos\left(\frac{\varphi_1 - \varphi_2}{2}\right)]
 \end{aligned}$$

$$\begin{aligned}
 E^\pm(k, \theta_{1 \rightarrow 2}, \varphi_{1 \rightarrow 2}) = \pm \cos^{-1} & [\cos \theta_2 \cos \theta_1 \cos\left(\frac{\varphi_1 + \varphi_2}{2} - k\right) \\
 & - \sin \theta_2 \sin \theta_1 \cos\left(\frac{\varphi_1 - \varphi_2}{2}\right)] + \frac{\varphi_1 + \varphi_2}{2} \quad (\text{A.20})
 \end{aligned}$$

FOUR-STEP MODEL

B.1 Eigenvector computation

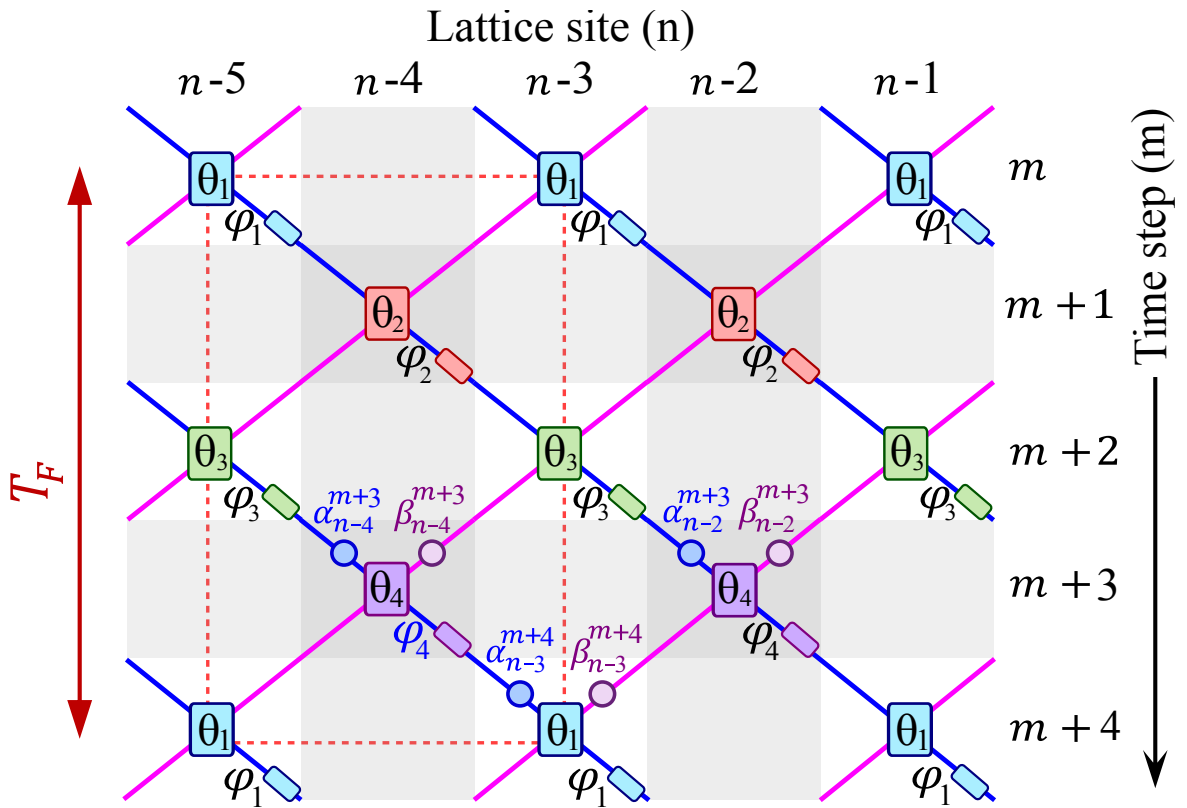


Figure B.1: Four-step model: the coupling angle θ and the phase modulator φ exhibit cyclic behavior, each alternating between four values. The coupling angle alternates among $\theta_1, \theta_2, \theta_3, \theta_4$, while the phase modulator alternates among $\varphi_1, \varphi_2, \varphi_3, \varphi_4$ at odd (m) and even ($m+1$) time steps. The synthetic split step lattice spans in discrete steps along the position site n and time step m . The red dashed square defines the unit cell of the system that exhibits a double periodicity, a spatial periodicity with a period of two sites along the horizontal axis, and a temporal periodicity, with a period of four round trips along the vertical axis.

In the four-step model, the coupling angle and phase modulator demonstrate cyclic behavior, each alternating between four distinct values within a single Floquet period. The four-step model exhibits double periodicity: spatial (every two

sites n) and temporal (every four-time steps m), as shown by the unit cell (red dashed square) in Fig. B.1. The lattice system has two sublattices α_n^m (blue) and β_n^m (purple) circles corresponding to the α and β rings.

The eigenvectors $|\psi\rangle^\pm$ are represented as a linear combination of the two complex amplitude eigenmodes $\tilde{\alpha}^\pm(k)$ and $\tilde{\beta}^\pm(k)$ corresponding to the α and β rings respectively.

$$|\psi(k)\rangle^\pm = \begin{pmatrix} \tilde{\alpha}(k) \\ \tilde{\beta}(k) \end{pmatrix}^\pm = \begin{pmatrix} |\tilde{\alpha}|e^{i\varphi_\alpha} \\ |\tilde{\beta}|e^{i\varphi_\beta} \end{pmatrix}^\pm \quad (\text{B.1})$$

We express the normalized eigenvector as the following expression:

$$\begin{aligned} |\psi(k)\rangle_{\text{norm}}^\pm &= \frac{1}{\sqrt{|\tilde{\alpha}|^2 + |\tilde{\beta}|^2}} \begin{pmatrix} |\tilde{\alpha}|e^{i\varphi_\alpha} \\ |\tilde{\beta}|e^{i\varphi_\beta} \end{pmatrix}^\pm \\ |\psi(k)\rangle_{\text{norm}}^\pm &= \frac{1}{|\tilde{\alpha}|\sqrt{1 + \frac{|\tilde{\beta}|^2}{|\tilde{\alpha}|^2}}} \begin{pmatrix} |\tilde{\alpha}|e^{i\varphi_\alpha} \\ |\tilde{\alpha}|e^{i\varphi_\beta} \end{pmatrix}^\pm \\ |\psi(k)\rangle_{\text{norm}}^\pm &= \frac{1}{|\tilde{\alpha}|\sqrt{1 + \frac{|\tilde{\beta}|^2}{|\tilde{\alpha}|^2}}} |\tilde{\alpha}| \begin{pmatrix} 1 \\ \frac{|\tilde{\beta}|}{|\tilde{\alpha}|}e^{i(\varphi_\beta - \varphi_\alpha)} \end{pmatrix}^\pm \\ |\psi(k)\rangle_{\text{norm}}^\pm &= \frac{1}{\sqrt{1 + |R^\pm|^2}} \begin{pmatrix} 1 \\ |R^\pm|e^{i\Phi_{\alpha\beta}^\pm} \end{pmatrix}^\pm \end{aligned} \quad (\text{B.2})$$

The magnitude $|R^\pm|$ and the argument $\Phi_{\alpha\beta}^\pm$ of the ratio of amplitude amplitudes $R^\pm(k)$ between the two sublattice sites for each quasimomentum eigenvector of each band are given by the following equation:

$$\begin{cases} R(k)^\pm = |R^\pm|e^{i\Phi_{\alpha\beta}^\pm} = \frac{\tilde{\beta}^\pm}{\tilde{\alpha}^\pm} \\ |R^\pm| = \frac{|\tilde{\beta}^\pm|}{|\tilde{\alpha}^\pm|} \\ \Phi_{\alpha\beta}^\pm = \varphi_\beta^\pm - \varphi_\alpha^\pm = \arg(\tilde{\beta}^\pm) - \arg(\tilde{\alpha}^\pm) \end{cases} \quad (\text{B.3})$$

The dynamics of the amplitude and phase of light pulses in the rings can be mapped into a coherent step evolution in the one-dimensional synthetic lattice depicted in Fig. B.1, governed by the following equations:

$$\alpha_{m+1}^n = \left(\cos \theta_m^{n-1} \alpha_m^{n-1} + i \sin \theta_m^{n-1} \beta_m^{n-1} \right) e^{i\varphi_m^{n-1}} \quad (\text{B.4})$$

$$\beta_{m+1}^n = i \sin \theta_m^{n+1} \alpha_m^{n+1} + \cos \theta_m^{n+1} \beta_m^{n+1} \quad (\text{B.5})$$

Let's consider that the coupling angle θ alternates between four values $[\theta_1, \theta_2, \theta_3, \theta_4]$, and the phase modulator φ between $[\varphi_1, \varphi_2, \varphi_3, \varphi_4]$ as follows:

$$\varphi_n^m = \begin{cases} \varphi_1 \\ \varphi_2 \\ \varphi_3 \\ \varphi_4 \end{cases} \quad \theta_n^m = \begin{cases} \theta_1 & \forall n \text{ if } m \bmod 4=1 \\ \theta_2 & \forall n \text{ if } m \bmod 4=2 \\ \theta_3 & \forall n \text{ if } m \bmod 4=3 \\ \theta_4 & \forall n \text{ if } m \bmod 4=0 \end{cases} \quad (\text{B.6})$$

Within the four-step model, the system exhibits a double periodicity, a spatial periodicity with a period of two sites, and a temporal periodicity, with a period of four round trips. Thus, equations. B.4 and B.5 can be solved using the Floquet-Bloch ansatz equation.

$$\begin{pmatrix} \alpha_m^n \\ \beta_m^n \end{pmatrix} = \begin{pmatrix} \tilde{\alpha}(k) \\ \tilde{\beta}(k) \end{pmatrix} e^{i\frac{Em}{4}} e^{i\frac{kn}{2}} = \begin{pmatrix} \tilde{\alpha}(k) \\ \tilde{\beta}(k) \end{pmatrix} e^{i\frac{E'm}{2}} e^{i\frac{kn}{2}} \quad \text{where } E' = \frac{E}{2} \quad (\text{B.7})$$

The temporal evolution of the sublattices complex amplitudes (α_m^n & β_m^n) at any stroboscopic time in real space can be expressed as a superposition of all the eigenmodes in reciprocal space, with α and β being the complex amplitude of the eigenmodes at the sites corresponding to the α and β rings respectively. We express the Floquet-Bloch ansatz equation as a function of E' to simplify the calculation.

Given that one Floquet period consists of four round trips, we express α_{m+4} from equation. B.4 as a function of α_m and β_m to determine the eigenvector. To simplify the calculations, we introduce a few abbreviations:

$$\begin{cases} T_m^n = \cos \theta_m^n \\ R_m^n = i \sin \theta_m^n \end{cases} \quad \begin{cases} \varphi_{ij} = \varphi_i + \varphi_j \\ \varphi_{ijz} = \varphi_i + \varphi_j + \varphi_z \\ \phi = \sum_{i=1}^4 \varphi_i = \varphi_1 + \varphi_2 + \varphi_3 + \varphi_4 \end{cases}$$

From equation. B.4 we have:

$$\begin{aligned} \alpha_{m+4}^{n-3} &= [T_{m+3}^{n-4} \alpha_{m+3}^{n-4} + R_{m+3}^{n-4} \beta_{m+3}^{n-4}] e^{i\varphi_{m+3}^{n-4}} = [T_4 \alpha_{m+3}^{n-4} + R_4 \beta_{m+3}^{n-4}] e^{i\varphi_4} \\ \alpha_{m+4}^{n-3} &= T_4 [T_3 \alpha_{m+2}^{n-5} + R_3 \beta_{m+2}^{n-5}] e^{i\varphi_{34}} + R_4 [T_3 \beta_{m+2}^{n-3} + R_3 \alpha_{m+2}^{n-3}] e^{i\varphi_4} \\ \alpha_{m+4}^{n-3} &= T_4 T_3 [T_2 \alpha_{m+1}^{n-6} + R_2 \beta_{m+1}^{n-6}] e^{i\varphi_{234}} + T_4 R_3 [T_2 \beta_{m+1}^{n-4} + R_2 \alpha_{m+1}^{n-4}] e^{i\varphi_{34}} \\ &\quad + R_4 T_3 [T_2 \beta_{m+1}^{n-2} + R_2 \alpha_{m+1}^{n-2}] e^{i\varphi_4} + R_4 R_3 [T_2 \alpha_{m+1}^{n-4} + R_2 \beta_{m+1}^{n-4}] e^{i\varphi_{24}} \end{aligned} \quad (\text{B.8})$$

$$\begin{aligned}
\alpha_{m+4}^{n-3} &= T_4 T_3 T_2 [T_1 \alpha_m^{n-7} + R_1 \beta_m^{n-7}] e^{i\phi} + T_4 T_3 R_2 [T_1 \beta_m^{n-5} + R_1 \alpha_m^{n-5}] e^{i\varphi_{234}} \\
&\quad + T_4 R_3 T_2 [T_1 \beta_m^{n-3} + R_1 \alpha_m^{n-3}] e^{i\varphi_{34}} + T_4 R_3 R_2 [T_1 \alpha_m^{n-5} + R_1 \beta_m^{n-5}] e^{i\varphi_{134}} \\
&\quad + R_4 T_3 T_2 [T_1 \beta_m^{n-1} + R_1 \alpha_m^{n-1}] e^{i\varphi_4} + R_4 T_3 R_2 [T_1 \alpha_m^{n-3} + R_1 \beta_m^{n-3}] e^{i\varphi_{14}} \\
&\quad + R_4 R_3 T_2 [T_1 \alpha_m^{n-5} + R_1 \beta_m^{n-5}] e^{i\varphi_{124}} + R_4 R_3 R_2 [T_1 \beta_m^{n-3} + R_1 \alpha_m^{n-3}] e^{i\varphi_{24}} \quad (\text{B.9})
\end{aligned}$$

Substituting equation. B.7 in equation. B.9

$$\begin{aligned}
\tilde{\alpha} e^{i2E'} &= [T_4 T_3 T_2 T_1 e^{i(-2k+\phi)} + T_4 T_3 R_2 R_1 e^{i(-k+\varphi_{234})} + T_4 R_3 T_2 R_1 e^{i\varphi_{34}} + T_4 R_3 R_2 T_1 e^{i(-k+\varphi_{134})} \\
&\quad + R_4 T_3 T_2 R_1 e^{i(k+\varphi_4)} + R_4 T_3 R_2 T_1 e^{i\varphi_{14}} + R_4 R_3 T_2 T_1 e^{i(-k+\varphi_{124})} + R_4 R_3 R_2 R_1 e^{i\varphi_{24}}] \tilde{\alpha} \\
&\quad \underbrace{\hspace{15em}}_A \\
&\quad + [T_4 T_3 T_2 R_1 e^{i(-2k+\phi)} + T_4 T_3 R_2 T_1 e^{i(-k+\varphi_{234})} + T_4 R_3 T_2 T_1 e^{i\varphi_{34}} + T_4 R_3 R_2 R_1 e^{i(-k+\varphi_{134})} \\
&\quad + R_4 T_3 T_2 T_1 e^{i(k+\varphi_4)} + R_4 T_3 R_2 R_1 e^{i\varphi_{14}} + R_4 R_3 T_2 R_1 e^{i(-k+\varphi_{124})} + R_4 R_3 R_2 T_1 e^{i\varphi_{24}}] \tilde{\beta} \\
&\quad \underbrace{\hspace{15em}}_B \quad (\text{B.10})
\end{aligned}$$

$$\tilde{\alpha} e^{i2E'} = \tilde{\alpha}[\dots] + \tilde{\beta}[\dots] = \tilde{\alpha}A + \tilde{\beta}B \quad (\text{B.11})$$

$$R(k)^\pm = |R^\pm| e^{i\Phi_{\alpha\beta}^\pm} = \frac{\tilde{\beta}^\pm}{\tilde{\alpha}^\pm} = \frac{e^{2iE'} - A}{B} \quad (\text{B.12})$$

Equation. B.12 shows the eigenvector derived by expressing α_{m+4} from equation. B.4 as a function of α_m and β_m . Alternatively, the same eigenvector can be obtained by expressing β_{m+4} from equation. B.5 as a function of α_m and β_m , as we will demonstrate now.

From equation. B.5 we have:

$$\begin{aligned}
\beta_{m+4}^{n-3} &= T_{m+3}^{n-2} \beta_{m+3}^{n-2} + R_{m+3}^{n-2} \alpha_{m+3}^{n-2} = T_4 \beta_{m+3}^{n-2} + R_4 \alpha_{m+3}^{n-2} \\
\beta_{m+4}^{n-3} &= T_4 [T_3 \beta_{m+2}^{n-1} + R_3 \alpha_{m+2}^{n-1}] + R_4 [T_3 \alpha_{m+2}^{n-3} + R_3 \beta_{m+2}^{n-3}] e^{i\varphi_3} \\
\beta_{m+4}^{n-3} &= T_4 T_3 [T_2 \beta_{m+1}^n + R_2 \alpha_{m+1}^n] + T_4 R_3 [T_2 \alpha_{m+1}^{n-2} + R_2 \beta_{m+1}^{n-2}] e^{i\varphi_2} \\
&\quad + R_4 T_3 [T_2 \alpha_{m+1}^{n-4} + R_2 \beta_{m+1}^{n-4}] e^{i\varphi_{23}} + R_4 R_3 [T_2 \beta_{m+1}^{n-2} + R_2 \alpha_{m+1}^{n-2}] e^{i\varphi_3} \\
\beta_{m+4}^{n-3} &= T_4 T_3 T_2 [T_1 \beta_m^{n+1} + R_1 \alpha_m^{n+1}] + T_4 T_3 R_2 [T_1 \alpha_m^{n-1} + R_1 \beta_m^{n-1}] e^{i\varphi_1} \\
&\quad + T_4 R_3 T_2 [T_1 \alpha_m^{n-3} + R_1 \beta_m^{n-3}] e^{i\varphi_{12}} + T_4 R_3 R_2 [T_1 \beta_m^{n-1} + R_1 \alpha_m^{n-1}] e^{i\varphi_2} \\
&\quad + R_4 T_3 T_2 [T_1 \alpha_m^{n-5} + R_1 \beta_m^{n-5}] e^{i\varphi_{123}} + R_4 T_3 R_2 [T_1 \beta_m^{n-3} + R_1 \alpha_m^{n-3}] e^{i\varphi_{23}} \\
&\quad + R_4 R_3 T_2 [T_1 \beta_m^{n-1} + R_1 \alpha_m^{n-1}] e^{i\varphi_3} + R_4 R_3 R_2 [T_1 \alpha_m^{n-3} + R_1 \beta_m^{n-3}] e^{i\varphi_{13}} \quad (\text{B.13})
\end{aligned}$$

Substituting equation. B.7 in equation. B.13

$$\begin{aligned}
\tilde{\beta}e^{i2E'} &= \tilde{\alpha}[T_4T_3T_2R_1e^{i(2k)} + T_4T_3R_2T_1e^{i(k+\varphi_1)} + T_4R_3T_2T_1e^{i\varphi_{12}} + T_4R_3R_2R_1e^{i(k+\varphi_2)} \\
&\quad + \underbrace{R_4T_3T_2T_1e^{i(-k+\varphi_{123})} + R_4T_3R_2R_1e^{i\varphi_{23}} + R_4R_3T_2R_1e^{i(k+\varphi_3)} + R_4R_3R_2T_1e^{i\varphi_{13}}}_{C}] \\
&\quad + \tilde{\beta}[T_4T_3T_2T_1e^{i(2k)} + T_4T_3R_2R_1e^{i(k+\varphi_1)} + T_4R_3T_2R_1e^{i\varphi_{12}} + T_4R_3R_2T_1e^{i(k+\varphi_2)} \\
&\quad + \underbrace{R_4T_3T_2R_1e^{i(-k+\varphi_{123})} + R_4T_3R_2T_1e^{i\varphi_{23}} + R_4R_3T_2T_1e^{i(k+\varphi_3)} + R_4R_3R_2R_1e^{i\varphi_{13}}}_{D}]
\end{aligned} \tag{B.14}$$

$$\tilde{\beta}e^{i2E'} = \tilde{\alpha}[\dots] + \tilde{\beta}[\dots] = \tilde{\alpha}C + \tilde{\beta}D \tag{B.15}$$

$$R(k)^\pm = |R^\pm|e^{i\Phi_{\alpha\beta}^\pm} = \frac{\tilde{\beta}^\pm}{\tilde{\alpha}^\pm} = \frac{C}{e^{2iE'} - D} \tag{B.16}$$

B.2 Eigenvalue computation

To determine the eigenvalue, we can use one of two methods: either by solving the equation given in B.12 set equal to the expression in B.16, or by solving the evolution operator. In the following section, we will focus on solving the evolution operator.

From equation. B.11 and B.15

$$\begin{cases} \tilde{\alpha}e^{i2E'} = \tilde{\alpha}A + \tilde{\beta}B \\ \tilde{\beta}e^{i2E'} = \tilde{\alpha}C + \tilde{\beta}D \end{cases}$$

$$\begin{cases} \tilde{\alpha} = \tilde{\alpha}^*A + \tilde{\beta}^*B \\ \tilde{\beta} = \tilde{\alpha}^*C + \tilde{\beta}^*D \end{cases}$$

$$A^* = Ae^{-2iE'} \quad B^* = Be^{-2iE'} \quad C^* = Ce^{-2iE'} \quad D^* = De^{-2iE'}$$

$$\begin{pmatrix} \tilde{\alpha} \\ \tilde{\beta} \end{pmatrix} = \underbrace{\begin{bmatrix} A^* & B^* \\ C^* & D^* \end{bmatrix}}_{\text{Evolution operator}} \begin{pmatrix} \tilde{\alpha} \\ \tilde{\beta} \end{pmatrix}$$

$$\begin{pmatrix} \tilde{\alpha} \\ \tilde{\beta} \end{pmatrix} \left(\begin{bmatrix} A^* & B^* \\ C^* & D^* \end{bmatrix} - I \right) = 0$$

$$\det \begin{vmatrix} *A - I & *B \\ *C & *D - I \end{vmatrix} = 0$$

```

1 % Matlab code to solve the determinant
  % we consider only in the matlab code that E is E'

clear all
clc

6
syms T1 T2 T3 T4 R1 R2 R3 R4 f1 f2 f3 f4 f k E
A= +T4*T3*T2*T1*exp(1i*(-2*k+f))      +T4*T3*R2*R1*exp(1i*(-k+f2+f3+f4))...
   +T4*R3*T2*R1*exp(1i*(f3+f4))      +T4*R3*R2*T1*exp(1i*(-k+f1+f3+f4))...
   +R4*T3*T2*R1*exp(1i*(k+f4))        +R4*T3*R2*T1*exp(1i*(f1+f4))...
11  +R4*R3*T2*T1*exp(1i*(-k+f1+f2+f4)) +R4*R3*R2*R1*exp(1i*(f2+f4));
A=A*exp(-2i*E);

B= +T4*T3*T2*R1*exp(1i*(2*-k+f))      +T4*T3*R2*T1*exp(1i*(-k+f2+f3+f4))...
   +T4*R3*T2*T1*exp(1i*(f3+f4))      +T4*R3*R2*R1*exp(1i*(-k+f1+f3+f4))...
16  +R4*T3*T2*T1*exp(1i*(k+f4))        +R4*T3*R2*R1*exp(1i*(f1+f4))...
   +R4*R3*T2*R1*exp(1i*(-k+f1+f2+f4)) +R4*R3*R2*T1*exp(1i*(f2+f4));
B=B*exp(-2i*E);

C= +T4*T3*T2*R1*exp(1i*(2*k))          +T4*T3*R2*T1*exp(1i*(k+f1))...
   +T4*R3*T2*T1*exp(1i*(f1+f2))      +T4*R3*R2*R1*exp(1i*(k+f2))...
21  +R4*T3*T2*T1*exp(1i*(-k+f1+f2+f3)) +R4*T3*R2*R1*exp(1i*(f2+f3))...
   +R4*R3*T2*R1*exp(1i*(k+f3))        +R4*R3*R2*T1*exp(1i*(f1+f3));
C=C*exp(-2i*E);

26 D= +T4*T3*T2*T1*exp(1i*(2*k))          +T4*T3*R2*R1*exp(1i*(k+f1))...
   +T4*R3*T2*R1*exp(1i*(f1+f2))      +T4*R3*R2*T1*exp(1i*(k+f2))...
   +R4*T3*T2*R1*exp(1i*(-k+f1+f2+f3)) +R4*T3*R2*T1*exp(1i*(f2+f3))...
   +R4*R3*T2*T1*exp(1i*(k+f3))        +R4*R3*R2*R1*exp(1i*(f1+f3));

31 D=D*exp(-2i*E);
M=(A-1)*(D-1)-B*C;
result = simplify(expand(M))

```

$$\begin{aligned}
& 1 + \underline{T_1^2 T_2^2 T_3^2 T_4^2 e^{i(-4E'+\phi)}} - \underline{T_1 T_2 T_3 T_4 e^{2i(-E'+k)}} - \underline{R_1 R_2 R_3 R_4 e^{i(-2E'+\varphi_{13})}} \\
& - \underline{R_1 R_2 R_3 R_4 e^{i(-2E'+\varphi_{24})}} - \underline{R_1 R_3 T_2 T_4 e^{i(-2E'+\varphi_{12})}} - \underline{R_2 R_4 T_1 T_3 e^{i(-2E'+\varphi_{14})}} \\
& - \underline{R_2 R_4 T_1 T_3 e^{i(-2E'+\varphi_{23})}} - \underline{R_1 R_3 T_2 T_4 e^{i(-2E'+\varphi_{34})}} - \underline{R_1 R_2 T_3 T_4 e^{i(-2E'+\varphi_1+k)}} \\
& - \underline{R_2 R_3 T_1 T_4 e^{i(-2E'+\varphi_2+k)}} - \underline{R_3 R_4 T_1 T_2 e^{i(-2E'+\varphi_3+k)}} - \underline{R_1 R_4 T_2 T_3 e^{i(-2E'+\varphi_4+k)}} \\
& - \underline{T_1 T_2 T_3 T_4 e^{i(-2E'+\phi-2k)}} - \underline{R_1 R_4 T_2 T_3 e^{i(-2E'+\varphi_{123}-k)}} - \underline{R_3 R_4 T_1 T_2 e^{i(-2E'+\varphi_{124}-k)}} \\
& - \underline{R_2 R_3 T_1 T_4 e^{i(-2E'+\varphi_{134}-k)}} - \underline{R_1 R_2 T_3 T_4 e^{i(-2E'+\varphi_{234}-k)}} + \underline{R_1^2 R_2^2 R_3^2 R_4^2 e^{i(-4E'+\phi)}} \\
& - \underline{R_1^2 R_2^2 R_3^2 T_4^2 e^{i(-4E'+\phi)}} - \underline{R_1^2 R_2^2 R_4^2 T_3^2 e^{i(-4E'+\phi)}} - \underline{R_1^2 R_3^2 R_4^2 T_2^2 e^{i(-4E'+\phi)}} \\
& - \underline{R_2^2 R_3^2 R_4^2 T_1^2 e^{i(-4E'+\phi)}} + \underline{R_1^2 R_2^2 T_3^2 T_4^2 e^{i(-4E'+\phi)}} + \underline{R_1^2 R_3^2 T_2^2 T_4^2 e^{i(-4E'+\phi)}} \\
& + \underline{R_1^2 R_4^2 T_2^2 T_3^2 e^{i(-4E'+\phi)}} + \underline{R_2^2 R_3^2 T_1^2 T_4^2 e^{i(-4E'+\phi)}} + \underline{R_2^2 R_4^2 T_1^2 T_3^2 e^{i(-4E'+\phi)}} \\
& + \underline{R_3^2 R_4^2 T_1^2 T_2^2 e^{i(-4E'+\phi)}} - \underline{R_2^2 T_1^2 T_3^2 T_4^2 e^{i(-4E'+\phi)}} - \underline{R_3^2 T_1^2 T_2^2 T_4^2 e^{i(-4E'+\phi)}} \\
& - \underline{R_4^2 T_1^2 T_2^2 T_3^2 e^{i(-4E'+\phi)}} - \underline{R_1^2 R_2 R_4 T_2 T_3 T_4 e^{i(-4E'+\phi+\varphi_{23}-2k)}} \\
& + \underline{R_1^2 R_2 R_3 T_2 T_3 T_4 e^{i(-4E'+\varphi_{134}+k)}} + \underline{R_1^2 R_3 R_4 T_2^2 T_3 T_4 e^{i(-4E'+\varphi_{124}+k)}} \\
& + \underline{R_2 R_4 T_1^2 T_2 T_3 T_4 e^{i(-4E'+\phi+\varphi_{23}-2k)}} - \underline{R_2 R_3 T_1^2 T_2 T_3 T_4 e^{i(-4E'+\varphi_{134}+k)}} \\
& - \underline{R_3 R_4 T_1^2 T_2 T_3 T_4 e^{i(-4E'+\varphi_{124}+k)}} - \underline{R_1^2 R_2 R_3 T_2 T_3 T_4 e^{i(-4E'+\phi+\varphi_2-k)}} \\
& - \underline{R_1^2 R_3 R_4 T_2^2 T_3 T_4 e^{i(-4E'+\phi+\varphi_3-k)}} + \underline{R_2 R_3 T_1^2 T_2 T_3 T_4 e^{i(-4E'+\phi+\varphi_2-k)}} \\
& + \underline{R_3 R_4 T_1^2 T_2 T_3 T_4 e^{i(-4E'+\phi+\varphi_3-k)}} + \underline{R_1^2 R_2 R_3 T_2 T_3 T_4 e^{i(-4E'+\phi+\varphi_2-k)}} \\
& + \underline{R_1^2 R_3 R_4 T_2^2 T_3 T_4 e^{i(-4E'+\phi+\varphi_3-k)}} + \underline{R_1^2 R_2 R_4 T_2 T_3 T_4 e^{i(-4E'+\phi+\varphi_{23}-2k)}} \\
& - \underline{R_2 R_3 T_1^2 T_2 T_3 T_4 e^{i(-4E'+\phi+\varphi_2-k)}} - \underline{R_3 R_4 T_1^2 T_2 T_3 T_4 e^{i(-4E'+\phi+\varphi_3-k)}} \\
& - \underline{R_2 R_4 T_1^2 T_2 T_3 T_4 e^{i(-4E'+\phi+\varphi_{23}-2k)}} - \underline{R_1^2 R_2 R_3 T_2 T_3 T_4 e^{i(-4E'+\varphi_{134}+k)}} \\
& - \underline{R_1^2 R_3 R_4 T_2^2 T_3 T_4 e^{i(-4E'+\varphi_{124}+k)}} + \underline{R_2 R_3 T_1^2 T_2 T_3 T_4 e^{i(-4E'+\varphi_{134}+k)}} \\
& + \underline{R_3 R_4 T_1^2 T_2 T_3 T_4 e^{i(-4E'+\varphi_{124}+k)}} - \underline{R_1^2 T_2^2 T_3^2 T_4^2 e^{i(-4E'+\phi)}} = 0
\end{aligned}$$

$$\begin{aligned}
& - e^{-2iE'} [T_1 T_2 T_3 T_4 [e^{2ik} + e^{i(\phi-2k)}] + R_1 R_2 R_3 R_4 [e^{i\varphi_{13}} + e^{i(\phi-\varphi_{13})}] \\
& + R_1 R_3 T_2 T_4 [e^{i\varphi_{12}} + e^{i(\phi-\varphi_{12})}] + R_2 R_4 T_1 T_3 [e^{i\varphi_{14}} + e^{i(\phi-\varphi_{14})}] \\
& + R_1 R_2 T_3 T_4 [e^{i(\varphi_1+k)} + e^{i(\phi-\varphi_1-k)}] + R_2 R_3 T_1 T_4 [e^{i(\varphi_2+k)} + e^{i(\phi-\varphi_2-k)}] \\
& + R_3 R_4 T_1 T_2 [e^{i(\varphi_3+k)} + e^{i(\phi-\varphi_3-k)}] + R_1 R_4 T_2 T_3 [e^{i(\varphi_4+k)} + e^{i(\phi-\varphi_4-k)}]] \\
& + e^{i(-4E'+\phi)} + 1 = 0
\end{aligned} \tag{B.17}$$

$$\begin{aligned}
& - e^{i(-2E'+\frac{\phi}{2})} [T_1 T_2 T_3 T_4 [e^{i(2k-\frac{\phi}{2})} + e^{i(\frac{\phi}{2}-2k)}] + R_1 R_2 R_3 R_4 [e^{i(\varphi_{13}-\frac{\phi}{2})} + e^{i(\frac{\phi}{2}-\varphi_{13})}] \\
& + R_1 R_3 T_2 T_4 [e^{i(\varphi_{12}-\frac{\phi}{2})} + e^{i(\frac{\phi}{2}-\varphi_{12})}] + R_2 R_4 T_1 T_3 [e^{i(\varphi_{14}-\frac{\phi}{2})} + e^{i(\frac{\phi}{2}-\varphi_{14})}] \\
& + R_1 R_2 T_3 T_4 [e^{i(\varphi_1+k-\frac{\phi}{2})} + e^{i(\frac{\phi}{2}-\varphi_1-k)}] + R_2 R_3 T_1 T_4 [e^{i(\varphi_2+k-\frac{\phi}{2})} + e^{i(\frac{\phi}{2}-\varphi_2-k)}] \\
& + R_3 R_4 T_1 T_2 [e^{i(\varphi_3+k-\frac{\phi}{2})} + e^{i(\frac{\phi}{2}-\varphi_3-k)}] + R_1 R_4 T_2 T_3 [e^{i(\varphi_4+k-\frac{\phi}{2})} + e^{i(\frac{\phi}{2}-\varphi_4-k)}]] \\
& + e^{i(-4E'+\phi)} + 1 = 0
\end{aligned} \tag{B.18}$$

$$\begin{aligned}
& - 2e^{i(-2E'+\frac{\phi}{2})} [T_1 T_2 T_3 T_4 \cos\left(2k - \frac{\phi}{2}\right) + R_1 R_2 R_3 R_4 \cos\left(\varphi_{13} - \frac{\phi}{2}\right) \\
& + R_1 R_3 T_2 T_4 \cos\left(\varphi_{12} - \frac{\phi}{2}\right) + R_2 R_4 T_1 T_3 \cos\left(\varphi_{14} - \frac{\phi}{2}\right) \\
& + R_1 R_2 T_3 T_4 \cos\left(\varphi_1 + k - \frac{\phi}{2}\right) + R_2 R_3 T_1 T_4 \cos\left(\varphi_2 + k - \frac{\phi}{2}\right) \\
& + R_3 R_4 T_1 T_2 \cos\left(\varphi_3 + k - \frac{\phi}{2}\right) + R_1 R_4 T_2 T_3 \cos\left(\varphi_4 + k - \frac{\phi}{2}\right)] \\
& + e^{i(-4E'+\phi)} + 1 = 0
\end{aligned} \tag{B.19}$$

$$1 + e^{i(-4E'+\phi)} - 2e^{i(-2E'+\frac{\phi}{2})} [\dots] = 0$$

$$\underbrace{e^{i(-2E'+\frac{\phi}{2})}}_{\neq 0} [e^{-i(-2E'+\frac{\phi}{2})} + e^{i(-2E'+\frac{\phi}{2})} - 2[\dots]] = 0$$

$$e^{-i(-2E'+\frac{\phi}{2})} + e^{i(-2E'+\frac{\phi}{2})} - 2[\dots] = 0$$

$$2 \cos\left(-2E' + \frac{\phi}{2}\right) - 2[\dots] = 0$$

$$\cos\left(-2E' + \frac{\phi}{2}\right) = [\dots]$$

$$-2E' + \frac{\phi}{2} = \pm \cos^{-1}([\dots])$$

$$E' = \pm \frac{1}{2} \cos^{-1}([\dots]) + \frac{\phi}{4} \quad \text{Nevertheless} \quad E' = \frac{E}{2}$$

$$E = \pm \cos^{-1}([\dots]) + \frac{\phi}{2}$$

$$\begin{aligned}
E^\pm(k, \varphi_{1 \rightarrow 4}) = & \pm \arccos[T_1 T_2 T_3 T_4 \cos\left(2k - \frac{\phi}{2}\right) + R_1 R_2 R_3 R_4 \cos\left(\varphi_{13} - \frac{\phi}{2}\right) \\
& + R_1 R_3 T_2 T_4 \cos\left(\varphi_{12} - \frac{\phi}{2}\right) + R_2 R_4 T_1 T_3 \cos\left(\varphi_{14} - \frac{\phi}{2}\right) \\
& + R_1 R_2 T_3 T_4 \cos\left(\varphi_1 + k - \frac{\phi}{2}\right) + R_2 R_3 T_1 T_4 \cos\left(\varphi_2 + k - \frac{\phi}{2}\right) \\
& + R_3 R_4 T_1 T_2 \cos\left(\varphi_3 + k - \frac{\phi}{2}\right) + R_1 R_4 T_2 T_3 \cos\left(\varphi_4 + k - \frac{\phi}{2}\right)] + \frac{\phi}{2}
\end{aligned} \tag{B.20}$$

Finally, the dispersion relation can be expressed as a function of $(k, \theta_{1 \rightarrow 4}, \varphi_{1 \rightarrow 4})$ by substituting T_m^n and R_m^n with $\cos(\theta_m^n)$ and $i \sin(\theta_m^n)$, respectively.

$$\begin{aligned}
E^\pm(k, \theta, \varphi) = & \pm \cos^{-1}[\\
& \cos(\theta_1) \cos(\theta_2) \cos(\theta_3) \cos(\theta_4) \cos\left(2k - \frac{\varphi_1 + \varphi_2 + \varphi_3 + \varphi_4}{2}\right) \\
& + \sin(\theta_1) \sin(\theta_2) \sin(\theta_3) \sin(\theta_4) \cos\left(\varphi_1 + \varphi_3 - \frac{\varphi_1 + \varphi_2 + \varphi_3 + \varphi_4}{2}\right) \\
& + \sin(\theta_1) \sin(\theta_3) \cos(\theta_2) \cos(\theta_4) \cos\left(\varphi_1 + \varphi_2 - \frac{\varphi_1 + \varphi_2 + \varphi_3 + \varphi_4}{2}\right) \\
& + \sin(\theta_2) \sin(\theta_4) \cos(\theta_1) \cos(\theta_3) \cos\left(\varphi_1 + \varphi_4 - \frac{\varphi_1 + \varphi_2 + \varphi_3 + \varphi_4}{2}\right) \\
& + \sin(\theta_1) \sin(\theta_2) \cos(\theta_3) \cos(\theta_4) \cos\left(\varphi_1 + k - \frac{\varphi_1 + \varphi_2 + \varphi_3 + \varphi_4}{2}\right) \\
& + \sin(\theta_2) \sin(\theta_3) \cos(\theta_1) \cos(\theta_4) \cos\left(\varphi_2 + k - \frac{\varphi_1 + \varphi_2 + \varphi_3 + \varphi_4}{2}\right) \\
& + \sin(\theta_3) \sin(\theta_4) \cos(\theta_1) \cos(\theta_2) \cos\left(\varphi_3 + k - \frac{\varphi_1 + \varphi_2 + \varphi_3 + \varphi_4}{2}\right) \\
& + \sin(\theta_1) \sin(\theta_4) \cos(\theta_2) \cos(\theta_3) \cos\left(\varphi_4 + k - \frac{\varphi_1 + \varphi_2 + \varphi_3 + \varphi_4}{2}\right)] \\
& + \frac{\varphi_1 + \varphi_2 + \varphi_3 + \varphi_4}{2}
\end{aligned} \tag{B.21}$$

COMPONENT POSITION

C.1 Phase modulator placement relative to beamsplitter

As emphasized in Chapter. 2, the component ordering is crucial to our experimental results. The positioning of the phase modulator (PM) relative to the 90/10 beam splitter drastically alters light behavior, necessitating a corresponding adjustment to the evolution equation. This section provides a thorough examination of these changes to enhance our understanding of the experimental process and facilitate accurate comparisons with experimental, numerical and analytical findings.

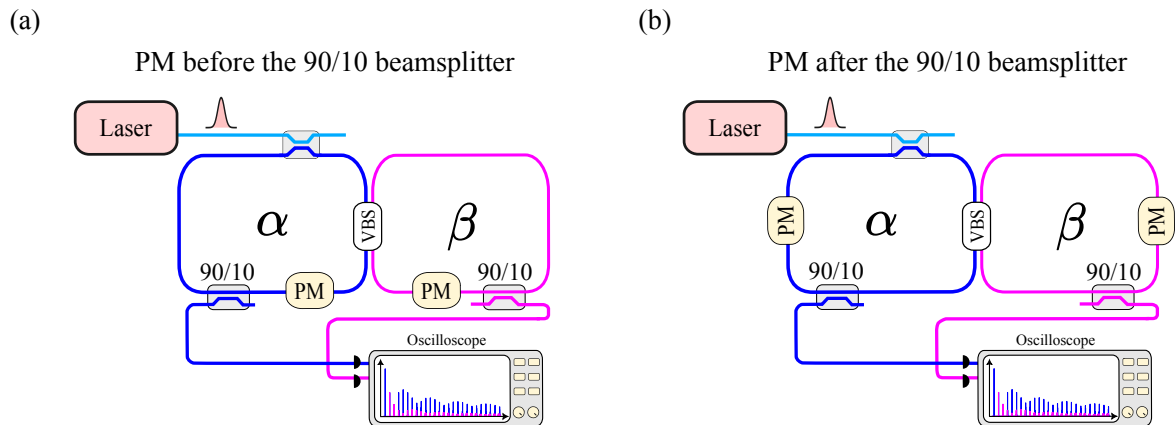


Figure C.1: Experimental setup with the phase modulator positioned: (a) before the beamsplitter, and (b) after the beamsplitter.

C.1.1 Phase modulator before the beamsplitter

When the phase modulator is placed before the 90/10 beamsplitter that directs 90% of the light towards the photodiode of the oscilloscope to do the measurement, as illustrated in the experimental setup of Fig. C.1.a. The dynamics of the amplitude and phase of light pulses in the rings can be mapped into a coherent step evolution in the one-dimensional synthetic lattice, governed by the following equations:

$$\begin{cases} \alpha_{m+1}^n = \left(\cos \theta_m^{n-1} \alpha_m^{n-1} + i \sin \theta_m^{n-1} \beta_m^{n-1} \right) e^{i\varphi_m^{n-1}} \\ \beta_{m+1}^n = i \sin \theta_m^{n+1} \alpha_m^{n+1} + \cos \theta_m^{n+1} \beta_m^{n+1} \end{cases} \quad (\text{C.1})$$

In this scenario, detailed eigenvectors and eigenvalues for the two-step and four-step models are provided in Appendices [A](#) and [B](#), respectively.

C.1.2 Phase modulator after the beamsplitter

In contrast to the previous case, positioning the phase modulator after the 90/10 beamsplitter, as illustrated in the experimental setup of Fig. [C.1.b](#), results in the following dynamics for the amplitude and phase of the light pulses:

$$\begin{cases} \alpha_{m+1}^n = \cos \theta_m^{n-1} \alpha_m^{n-1} e^{i\varphi_m^{n-1}} + i \sin \theta_m^{n-1} \beta_m^{n-1} \\ \beta_{m+1}^n = i \sin \theta_m^{n+1} \alpha_m^{n+1} e^{i\varphi_m^{n+1}} + \cos \theta_m^{n+1} \beta_m^{n+1} \end{cases} \quad (\text{C.2})$$

c.1.2.1 Two-step model when the phase modulator is after the beam splitter

Following the detailed step-by-step calculation in Appendix [A](#), we derive the general dispersion relation $E^\pm(k)$ in equation [C.3](#), along with the corresponding normalized eigenvectors formula $|\psi^+(k)\rangle$ and $|\psi^-(k)\rangle$ in equation [C.4](#) and [C.5](#), for the two-step model when the phase modulator is after the beamsplitter:

$$\begin{aligned} E^\pm(k, \varphi_1, \varphi_2, \theta_1, \theta_2) = \pm \cos^{-1} \left[\cos \theta_2 \cos \theta_1 \cos \left(-k - \frac{\varphi_2 + \varphi_1}{2} \right) \right. \\ \left. - \sin \theta_2 \sin \theta_1 \cos \left(\frac{\varphi_2 - \varphi_1}{2} \right) \right] + \frac{\varphi_1 + \varphi_2}{2} \end{aligned} \quad (\text{C.3})$$

$$|\psi^\pm(k)\rangle = \begin{pmatrix} \tilde{\alpha}(k) \\ \tilde{\beta}(k) \end{pmatrix}^\pm = \frac{1}{\sqrt{1 + |R^\pm|^2}} \begin{pmatrix} 1 \\ |R^\pm| e^{i\Phi_{\alpha\beta}^\pm} \end{pmatrix} \quad (\text{C.4})$$

$$R(k)^\pm = |R^\pm| e^{i\Phi_{\alpha\beta}^\pm} = \frac{[e^{iE(k)^\pm} - \cos \theta_2 \cos \theta_1 e^{-ik} + \sin \theta_2 \sin \theta_1 e^{i\varphi_1}]}{[i \cos \theta_2 \sin \theta_1 e^{i(-k+\varphi_2)} + i \sin \theta_2 \cos \theta_1 e^{i(\varphi_2+\varphi_1)}]} \quad (\text{C.5})$$

c.1.2.2 Four-step model when the phase modulator is after the beam splitter

Similarly, by following the detailed step-by-step calculation in Appendix [B](#), we derive the general dispersion relation $E^\pm(k)$ in equation [C.6](#), along with the corres-

ponding normalized eigenvectors formula $|\psi^+(k)\rangle$ and $|\psi^-(k)\rangle$ in equations. C.7 and C.8, for the four-step model when the phase modulator is after the variable beamsplitter (VBS):

To simplify the calculation, we introduce a few abbreviations:

$$\begin{cases} T_m = \cos \theta_m \\ R_m = i \sin \theta_m \end{cases} \quad \begin{cases} \varphi_{ij} = \varphi_i + \varphi_j \\ \varphi_{ijz} = \varphi_i + \varphi_j + \varphi_z \\ \phi = \sum_{i=1}^4 \varphi_i = \varphi_1 + \varphi_2 + \varphi_3 + \varphi_4 \end{cases}$$

$$\begin{aligned} E^\pm(k) = & \pm \cos^{-1} [T_1 T_2 T_3 T_4 \cos\left(-2k - \frac{\phi}{2}\right) + R_1 R_2 R_3 R_4 \cos\left(\varphi_{24} - \frac{\phi}{2}\right) \\ & + R_1 R_3 T_2 T_4 \cos\left(\varphi_{12} - \frac{\phi}{2}\right) + R_2 R_4 T_1 T_3 \cos\left(\varphi_{23} - \frac{\phi}{2}\right) \\ & + R_1 R_2 T_3 T_4 \cos\left(\varphi_3 - k - \frac{\phi}{2}\right) + R_2 R_3 T_1 T_4 \cos\left(\varphi_4 - k - \frac{\phi}{2}\right) \\ & + R_3 R_4 T_1 T_2 \cos\left(\varphi_1 - k - \frac{\phi}{2}\right) + R_1 R_4 T_2 T_3 \cos\left(\varphi_2 - k - \frac{\phi}{2}\right)] + \frac{\phi}{2} \end{aligned} \quad (\text{C.6})$$

$$|\psi(k)\rangle^\pm = \begin{pmatrix} \alpha(k) \\ \beta(k) \end{pmatrix}^\pm = \frac{1}{\sqrt{1 + |R^\pm|^2}} \begin{pmatrix} 1 \\ |R^\pm| e^{i\Phi_{\alpha\beta}^\pm} \end{pmatrix} \quad (\text{C.7})$$

$$R(k)^\pm = |R^\pm| e^{i\Phi_{\alpha\beta}^\pm} = \frac{e^{iE(k)^\pm} - A}{B} \quad (\text{C.8})$$

$$\begin{aligned} A = & [T_4 T_3 T_2 T_1 e^{i(-2k)} + T_4 T_3 R_2 R_1 e^{i(-k+\varphi_3)} + T_4 R_3 T_2 R_1 e^{i\varphi_{34}} + T_4 R_3 R_2 T_1 e^{i(-k+\varphi_4)} \\ & + R_4 T_3 T_2 R_1 e^{i(k+\varphi_{134})} + R_4 T_3 R_2 T_1 e^{i\varphi_{14}} + R_4 R_3 T_2 T_1 e^{i(-k+\varphi_1)} + R_4 R_3 R_2 R_1 e^{i\varphi_{13}}] \end{aligned} \quad (\text{C.9})$$

$$\begin{aligned} B = & [T_4 T_3 T_2 R_1 e^{i(-2k+\varphi_2)} + T_4 T_3 R_2 T_1 e^{i(-k+\varphi_{23})} + T_4 R_3 T_2 T_1 e^{i\varphi_{234}} + T_4 R_3 R_2 R_1 e^{i(-k+\varphi_{24})} \\ & + R_4 T_3 T_2 T_1 e^{i(k+\phi)} + R_4 T_3 R_2 R_1 e^{i\varphi_{124}} + R_4 R_3 T_2 R_1 e^{i(-k+\varphi_{12})} + R_4 R_3 R_2 T_1 e^{i\varphi_{123}}] \end{aligned} \quad (\text{C.10})$$

Figure. C.2 provides an analytical comparison of the two-dimensional eigenvectors, eigenvalues, and Berry curvature of the upper band when the phase modulator is placed before (first row) and after (second row) the beamsplitter. This comparison is made for a set of coupling angles $(\theta_1, \theta_2) = (0.2, 0.3)\pi$ and for

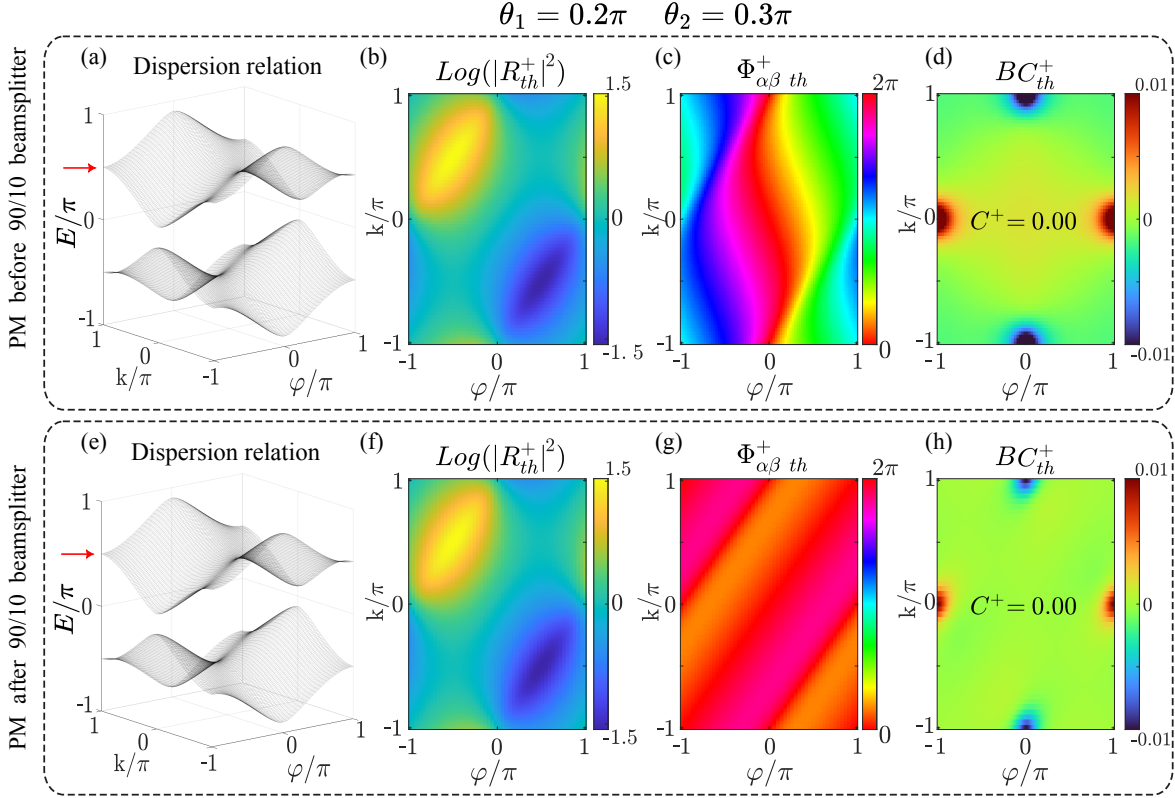


Figure C.2: Analytical comparison of the two-dimensional eigenvectors, eigenvalues, and Berry curvature when the phase modulator is placed before (first row) and after (second row) the beamsplitter. This comparison is made for a set of coupling angles $(\theta_1, \theta_2) = (0.2, 0.3)\pi$ and for $\varphi \in [-\pi, \pi]$ when a narrow pulse is introduced into the α ring. (a, e) Illustrate the two-dimensional dispersion relation. (b, f) Depict the two-dimensional amplitude ratio. (c, g) Show the two-dimensional relative phase. (d, h) Berry curvature with a trivial Chern number.

$\varphi \in [-\pi, \pi]$, after the introduction of a narrow pulse into the system that satisfies the condition in equation 1.13. The band structures in Figs. C.2.a-e and the upper band's amplitude ratio $|R|^+$ in Figs. C.2.b-f show excellent agreement regardless of whether the phase modulator is placed before or after the beamsplitter. However, the relative phase $\Phi_{\alpha\beta}$ in Figs. C.2.c-g exhibits distinct behavior, impacting the Berry curvature depicted in Figs. C.2.d-h. The concentrated blue and red flux of the Berry curvature in Fig. C.2.h is tilted compared to Fig. C.2.d. Despite these differences, integrating the Berry curvature yields a zero Chern number regardless of the phase modulator's position.

To validate our analytical and numerical models, Fig. C.3 provides an analytical, numerical, and experimental comparison of the two-dimensional eigenvectors, eigenvalues, and Berry curvature results for the upper band across its three rows respectively. A narrow pulse is injected into the long ring with a phase modulator positioned after the beam splitter. This comparison is performed for a set of coupling angles $(\theta_1, \theta_2) = (0.2, 0.3)\pi$ and $\varphi \in [-\pi, \pi]$. The excellent agreement between the

analytical, numerical, and experimental dispersion relations Figs. C.3.a, e, i, amplitude ratios Figs. C.3.b, f, j, relative phases Figs. C.3.c, g, k, and Berry curvatures with trivial Chern numbers Figs. C.3.d, h, l, respectively, confirms the reliability of our model.

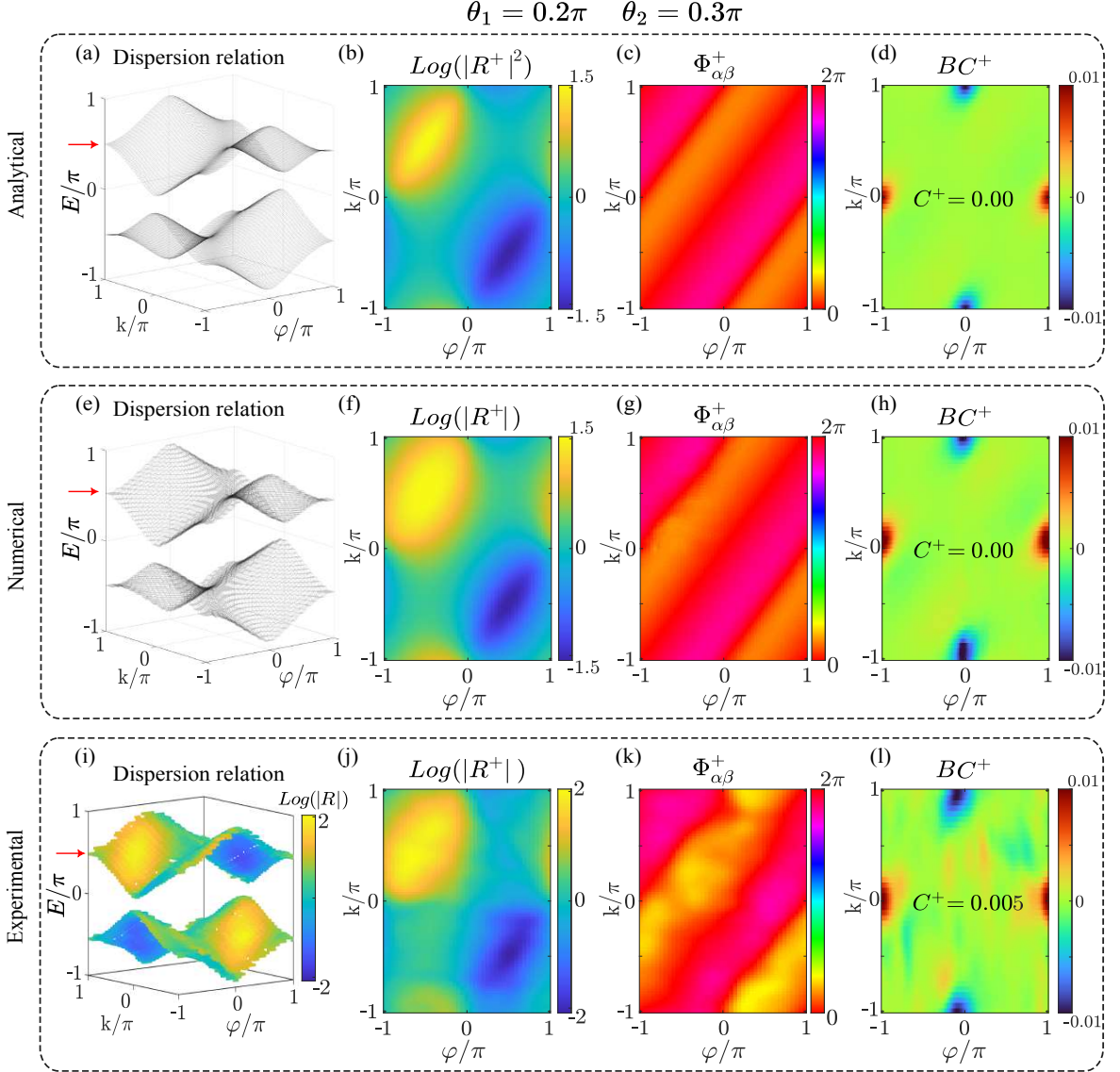


Figure C.3: A comparison of analytical, numerical, and experimental results is presented across the three rows of the figure. This comparison focuses on the upper band, considering a narrow pulse injected into the long ring with a phase modulator positioned after the beam splitter when the coupling angles are set to $(\theta_1, \theta_2) = (0.2, 0.3)\pi$ and $\varphi \in [-\pi, \pi]$. (a, e, i) Illustrate the two-dimensional dispersion relation. (b, f, j) Depict the two-dimensional amplitude ratio. (c, g, k) Show the two-dimensional relative phase. (d, h, l) Berry curvature with a trivial Chern number.

D

DATA SMOOTHING

Appendix. D demonstrates the smoothing techniques applied to the experimental data using a four-step model analytical example. We focus on two primary methods: the first employs the ‘smoothdata’ function in MATLAB, while the second involves refining the eigenvectors of the projector operator. Both approaches aim to reduce data fluctuations.

Figure. D.1 displays a 4x4 matrix of plots. The top row illustrates the two-dimensional eigenvectors $|\psi^+(k, \varphi)\rangle$ of the analytical upper band for the four-step model, derived from equations 1.27 and 1.28. This is shown when a narrow pulse, satisfying the condition of equation. 1.13, is introduced into the long ring α . The phase modulator value φ ranges from $[-\pi, \pi]$, and the coupling angles are set to $[\theta_1, \theta_2, \theta_3, \theta_4] = [4\pi/32, 8\pi/32, 0, 8\pi/32]$.

The first and second panels of the top row in Figs. D.1.a-b illustrate the two-dimensional amplitude ratio $|R|^+(k, \varphi)$ and the relative phase $\Phi_{\alpha\beta}^+(k, \varphi)$ of the upper band, respectively. The amplitude ratio $|R|^+(k, \varphi)$ displays high and low amplitude regions, depicted in yellow and blue, which correspond precisely to the positions of the vortex-antivortex pairs in the relative phase tomography $\Phi_{\alpha\beta}^+(k, \varphi)$. The third and fourth panels of the top row in Figs. D.1.c-d respectively depict the trajectories of $|R|^+(k, \varphi)$ and $\Phi_{\alpha\beta}^+(k, \varphi)$ on the Bloch sphere for $\varphi = 0$. The slice is depicted by a white dashed line in Figs. D.1.a-b. The analytical examples in the first row represent the ideal, fluctuation-free model. The aim is to apply smoothing techniques to noisy data, aligning it as closely as possible with these analytical results.

The second row presents noisy versions of the analytical results in the first row, intentionally added to simulate the fluctuations and noise typically observed in the experimental data. This random noise can blur the amplitude ratio and the relative phase (see Figs. D.1.e-f), consequently distorting the eigenvector’s trajectory on the Bloch sphere (see Figs. D.1.g-h).

The third row demonstrates the first smoothing method. Due to the system’s double periodicity in time and space, this method involves constructing a large matrix for both the two-dimensional amplitude ratio $|R|^+(k, \varphi)$ and the relative

phase $\Phi_{\alpha\beta}^+(k, \varphi)$ by replicating each matrix three times horizontally and vertically. This replication is essential to apply MATLAB's Gaussian *smoothdata* function effectively, ensuring that the entire two-dimensional ratio of amplitude $|R|^+(k, \varphi)$ and relative phase $\Phi_{\alpha\beta}^+(k, \varphi)$ are smoothed, including at the matrix borders, with a Gaussian smoothing window's size of 15 pixels that is equal to 3 times the standard deviation in each direction. Given the nature of Gaussian functions, the tails of the window effectively diminish to negligible values beyond the standard deviation range of 5 pixels. Figures D.1.i and D.1.j display the final smoothed results of the amplitude ratio $|R|^+(k, \varphi)$ and the relative phase $\Phi_{\alpha\beta}^+(k, \varphi)$, respectively, which are obtained by taking out the central third of the processed matrices. Compared to Figs. D.1.e–f, these results show a decrease in random noise fluctuations. However, the high and low amplitude associated with the singularity point, highlighted in yellow and blue in Fig. D.1.i, are both broader and less prominent than the expected analytical result of Fig. D.1.a. This smoothing method alters the weight distribution specifically around singularity points, consequently influencing the eigenvector trajectory on the Bloch sphere (see Figures. D.1.k-l).

One approach to mitigate this issue involves smoothing the noise in Cartesian coordinates and subsequently recalculating the eigenvector via the projector operator. This methodology was developed by Martin Guillot, a PhD student at the C2N group, at Paris-Saclay University.

Consider a 2D noisy normalized eigenvector $|\psi(k, \varphi)\rangle$ given by equation. D.1, as a linear combination of the two complex amplitude eigenmodes $\tilde{\alpha}(k, \varphi)$ and $\tilde{\beta}(k, \varphi)$ corresponding to the α and β rings respectively. The corresponding bra vector $\langle\psi(k, \varphi)|$ in equation. D.2 is the complex conjugate transpose of $|\psi(k, \varphi)\rangle$.

$$|\psi(k, \varphi)\rangle = \begin{pmatrix} \tilde{\alpha}(k, \varphi) \\ \tilde{\beta}(k, \varphi) \end{pmatrix} \quad (\text{D.1})$$

$$\langle\psi(k, \varphi)| = \left(\tilde{\alpha}^*(k, \varphi) \quad \tilde{\beta}^*(k, \varphi) \right) \quad (\text{D.2})$$

The projector operator \hat{P} onto the state $|\psi\rangle$ is given by $\hat{P} = |\psi\rangle \langle\psi|$, such that:

$$\begin{aligned} \hat{P} &= |\psi(k, \varphi)\rangle \langle\psi(k, \varphi)| \\ &= \begin{pmatrix} \tilde{\alpha}(k, \varphi) \\ \tilde{\beta}(k, \varphi) \end{pmatrix} \left(\tilde{\alpha}^*(k, \varphi) \quad \tilde{\beta}^*(k, \varphi) \right) \\ &= \begin{bmatrix} \underbrace{\tilde{\alpha}(k, \varphi) \tilde{\alpha}^*(k, \varphi)}_{\hat{P}_{11}(k, \varphi)} & \underbrace{\tilde{\alpha}(k, \varphi) \tilde{\beta}^*(k, \varphi)}_{\hat{P}_{12}(k, \varphi)} \\ \underbrace{\tilde{\beta}(k, \varphi) \tilde{\alpha}^*(k, \varphi)}_{\hat{P}_{21}(k, \varphi)} & \underbrace{\tilde{\beta}(k, \varphi) \tilde{\beta}^*(k, \varphi)}_{\hat{P}_{22}(k, \varphi)} \end{bmatrix} \end{aligned} \quad (\text{D.3})$$

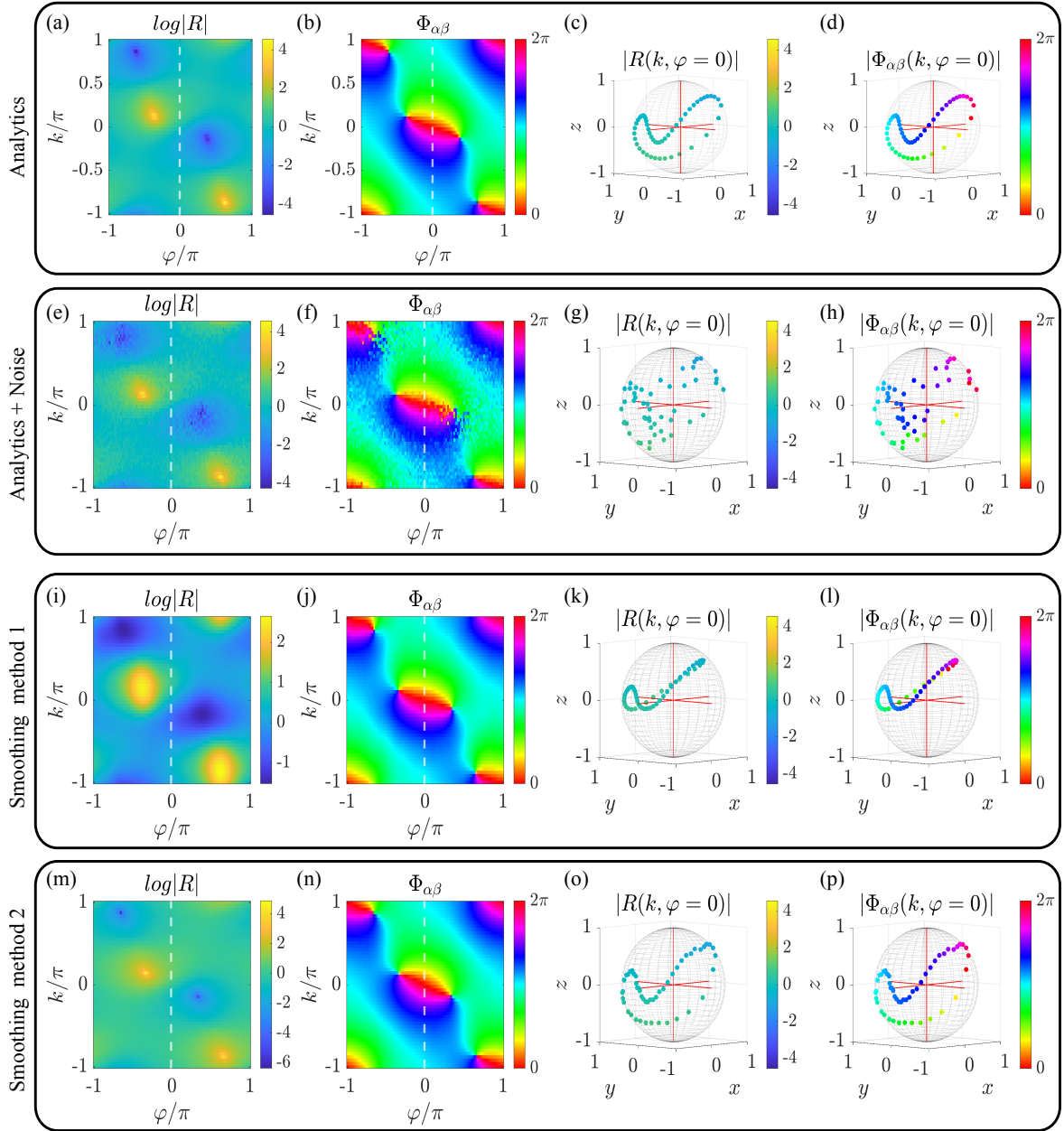


Figure D.1: Two-dimensional eigenvectors of the analytical upper band for the four-step model when a narrow pulse is introduced into the long ring α . The phase modulator value φ ranges from $[-\pi, \pi]$, and the coupling angles are set to $[\theta_1, \theta_2, \theta_3, \theta_4] = [4\pi/32, 8\pi/32, 0, 8\pi/32]$. Row 1: Analytical results showing in (a-b) the amplitude ratio $|R|^+(k, \varphi)$ and the relative phase $\Phi_{\alpha\beta}^+(k, \varphi)$, respectively, and their corresponding Bloch sphere representations (c-d) at a specific value of $\varphi = 0$. Row 2: Noisy versions of row 1. Row 3: First smoothing method of the noisy data in row 2. Row 4: Second smoothing method of the noisy data in row 2, impressively reducing noise fluctuations and aligning closely with the analytical results.

In quantum mechanics, any 2×2 Hermitian matrix (like \hat{P}), can be expressed as a linear combination of the identity matrix I and the three Pauli matrices σ_x , σ_y , and σ_z [172], as demonstrated by equation. D.4, where a , b , c , and d are matrices with real coefficients..

$$\begin{aligned} \hat{P} &= \begin{bmatrix} \hat{P}_{11}(k, \varphi) & \hat{P}_{12}(k, \varphi) \\ \hat{P}_{21}(k, \varphi) & \hat{P}_{22}(k, \varphi) \end{bmatrix} = \begin{bmatrix} a(k, \varphi) + d(k, \varphi) & b(k, \varphi) - ic(k, \varphi) \\ b(k, \varphi) + ic(k, \varphi) & a(k, \varphi) - d(k, \varphi) \end{bmatrix} \\ &= a(k, \varphi)I + b(k, \varphi)\sigma_x + c(k, \varphi)\sigma_y + d(k, \varphi)\sigma_z \end{aligned} \quad (\text{D.4})$$

The identity matrix I and the three Pauli matrices σ_x , σ_y , and σ_z are the following:

$$I = \begin{pmatrix} 1 & 0 \\ 0 & 1 \end{pmatrix} \quad \sigma_x = \begin{pmatrix} 0 & 1 \\ 1 & 0 \end{pmatrix} \quad \sigma_y = \begin{pmatrix} 0 & -i \\ i & 0 \end{pmatrix} \quad \sigma_z = \begin{pmatrix} 1 & 0 \\ 0 & -1 \end{pmatrix} \quad (\text{D.5})$$

Under ideal conditions (without noise), the eigenvector $|\psi\rangle$ is associated with a unitary eigenvalue of the projector operator \hat{P} . To demonstrate, applying \hat{P} to the normalized eigenvector $|\psi\rangle$ yields:

$$\hat{P}|\psi\rangle = (|\psi\rangle\langle\psi|)|\psi\rangle = |\psi\rangle(\langle\psi|\psi\rangle) = |\psi\rangle \cdot 1 = |\psi\rangle \quad (\text{D.6})$$

The matrices $a(k, \varphi)$, $b(k, \varphi)$, $c(k, \varphi)$, and $d(k, \varphi)$ are derived from the elements of the projector operator \hat{P} as follows:

$$a(k, \varphi) = \frac{1}{2} (\hat{P}_{11}(k, \varphi) + \hat{P}_{22}(k, \varphi)) \quad (\text{D.7})$$

$$d(k, \varphi) = \frac{1}{2} (\hat{P}_{11}(k, \varphi) - \hat{P}_{22}(k, \varphi)) \quad (\text{D.8})$$

$$b(k, \varphi) = \frac{1}{2} (\hat{P}_{12}(k, \varphi) + \hat{P}_{21}(k, \varphi)) \quad (\text{D.9})$$

$$c(k, \varphi) = -\frac{1}{2i} (\hat{P}_{12}(k, \varphi) - \hat{P}_{21}(k, \varphi)) \quad (\text{D.10})$$

To recover the smoothed eigenvector, we initially apply Gaussian smoothing to the Cartesian components (a, b, c, d) using MATLAB's 'smoothdata' function. The smoothed projector components (\hat{P}_{s11} , \hat{P}_{s12} , \hat{P}_{s21} , \hat{P}_{s22}) are subsequently derived from the smoothed matrices (a_s , b_s , c_s , d_s). We then compute the new eigenvalues and eigenvectors of the smoothed projector operator \hat{P}_s . Ideally, the equation $\hat{P}_s|\psi\rangle = \lambda|\psi\rangle$ should result in an eigenvalue of $\lambda = 1$. Therefore, we select the eigenvector associated with the biggest eigenvalue closest to 1, obtained by solving the determinant equation $\det(\hat{P}_s - \lambda I) = 0$.

The latest smoothing method presented in Figs. D.1.m-p, which involves determining the eigenvalue and eigenvector of the projector operator, produces impressive results aligning with the expected analytical values in Figs. D.1.a-d. By accurately accounting for amplitude weights associated with singularities, highlighted in yellow and blue in Fig. D.1.m, the eigenvector amplitude and phase trajectory on the Bloch sphere remains stable, as depicted in Figs. D.1.o-p and closely matches the anticipated analytical behavior of Figs. D.1.c-d. Furthermore, the novel smoothing technique (Method 2) effectively addresses both noisy amplitude ratios and relative phases through eigenvector recalculation. In contrast, the previous smoothing method (Method 1) applies smoothing individually to the amplitude ratio and relative phase.

In summary, while the first smoothing method directly uses Gaussian smoothing techniques to effectively mitigate noise, it can introduce distortions in the amplitude ratio and eigenvector trajectory around singularity points. The second smoothing approach, which involves eigenvector recalculation, addresses these limitations, yielding more precise outcomes that closely align with theoretical predictions.

QUASI PERIODIC MODULATION

A quasicrystal structure, represented by the one-dimensional Fibonacci chain presents a fractal energy spectrum with an infinite number of gaps [173, 174]. This appendix demonstrates that our double-ring system can also attain a fractal energy spectrum via quasiperiodic modulation in both time (m) and space (n).

E.1 Quasi periodic modulation in space

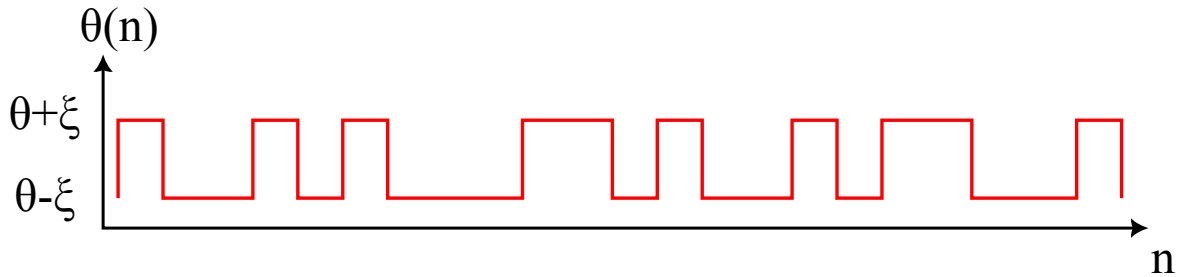


Figure E.1: The coupling angle θ alternates between the two values $\theta + \xi$ and $\theta - \xi$ in function of space (n), following a Fibonacci sequence, with $\xi \in [0, \pi]$.

The spatial quasi-periodic modulation is implemented by alternating the coupling angle of the (VBS) according to a Fibonacci sequence. This approach leverages the characteristic function presented in equation E.1, as proposed by [175].

$$\kappa(n) = \text{sign}[\cos(2\pi n/\sigma) - \cos(\pi/\sigma)] \quad (\text{E.1})$$

The characteristic function $\kappa(n)$ takes only two possible values, ± 1 , where n represents the lattice sites, and $\sigma = (1 + \sqrt{5})/2$ is the golden ratio.

The splitting angle θ , defined by equation E.2, alternates between the two values $\theta + \xi$ and $\theta - \xi$ in the function of lattice site (n), according to the characteristic function following a Fibonacci sequence, with $\xi \in [0, \pi]$ being a coefficient, as illustrated in Fig. E.1.

$$\theta(m, n) = \theta(m, n) + \xi\kappa(n) \quad (\text{E.2})$$

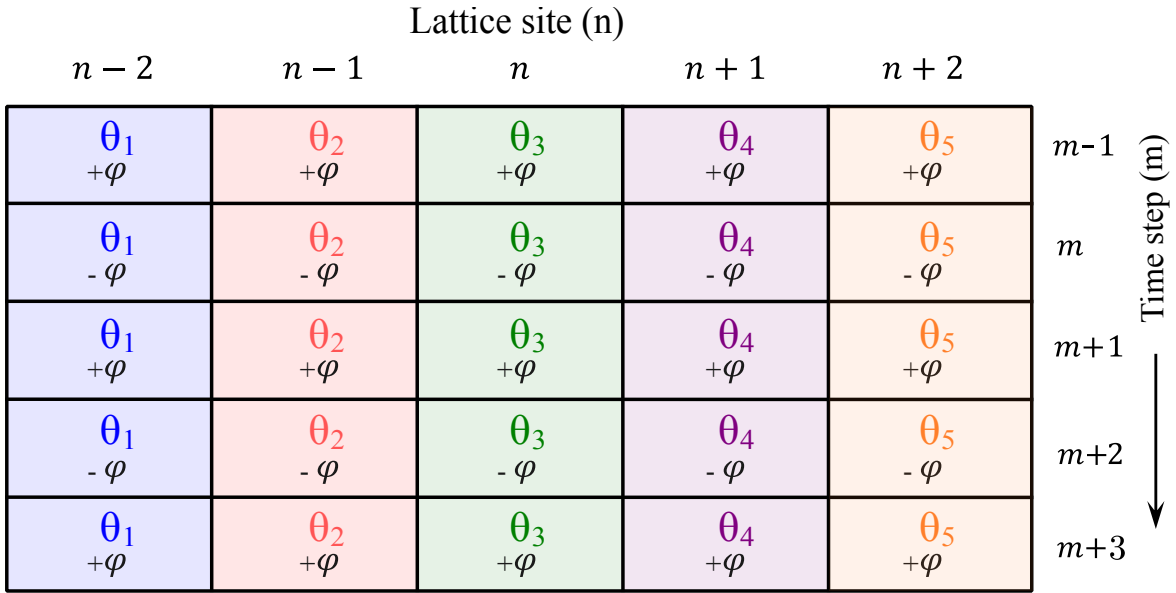


Figure E.2: Photonic mesh lattice showcasing the spatial quasi-periodic modulation. The coupling angle sequence, denoted as $\theta(m, n)$, is replicated every time step (m) but varies spatially based on site position. The phase modulator φ alternates between two values, $+\varphi$ and $-\varphi$, during odd and even time steps, respectively.

To visualize the manipulation of the coupling angle, Fig. E.2 presents the photonic mesh lattice discretized in time (vertical axis) and space (horizontal axis). The coupling angle sequence, denoted as $\theta(m, n)$, is replicated every time step (m) but varies spatially based on site position. The phase modulator φ alternates between two values, $+\varphi$ and $-\varphi$, during odd and even time steps, respectively.

Figure. E.3 presents a comprehensive non-stroboscopic spatiotemporal comparison of the experimental and numerical results for the rings α and β under spatial quasi-periodic modulation. The experimental results for rings α and β are depicted in panels (a) and (b), respectively, while the corresponding numerical results are shown in panels (c) and (d). The comparison involves introducing a narrow pulse of 1.4 ns into the long ring α with a baseline coupling angle of $\theta = \pi/4$ and a phase modulator value $\varphi = 0$. This splitting angle is spatially modulated between $\theta + \zeta$ and $\theta - \zeta$, where $\zeta = \pi/16$, by a Fibonacci sequence. The numerical and experimental results exhibit a remarkable similarity, demonstrating close agreement between the two.

The red dashed lines in the subplots of Fig. E.3 indicate a coupling angle $\theta = \pi/2$ at site position $n = \pm 32$, leading to full reflection. This configuration allows the light to circulate for up to 100 round trips without pulse overlap caused by beam splitter diffraction. Moreover, Increasing the number of round trips significantly enhances the resolution for observing the fractal energy spectrum. The same condition was applied in both experimental and numerical simulations to maintain consistency.

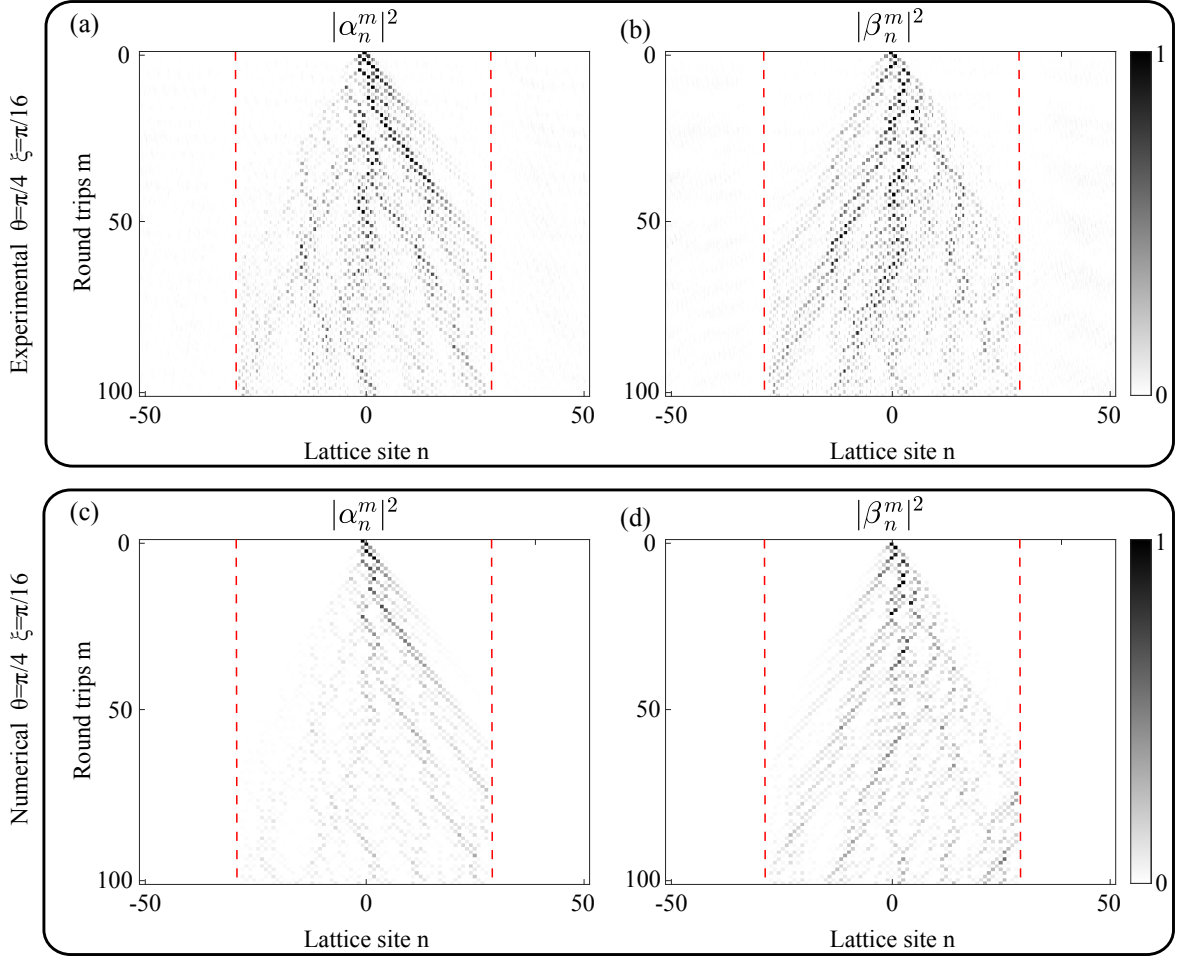


Figure E.3: A non-stroboscopic spatiotemporal comparison of experimental results (a-b) and numerical results (c-d) for the rings α and β , respectively, under spatial quasi-periodic modulation. The modulation involves introducing a narrow pulse of 1.4 ns into the long ring α , where the coupling angle θ is spatially varied between $\pi/4 + \xi$ and $\pi/4 - \xi$, with $\xi = \pi/16$ according to a Fibonacci sequence, while a non-active phase modulator is set to $\varphi = 0$. The red dashed lines indicate a coupling angle $\theta = \pi/2$ at site position $n = \pm 32$, leading to full reflection.

Figure E.4 displays 3x2 subplots. The first row shows the experimental excited energy spectrum of each of the rings α and β in panels (a) and (b), respectively, for the spatially non-modulated scenario. This case corresponds exactly to the calibration shot ($\theta = \pi/4$, $\varphi = 0$, and $\xi = 0$). The energy spectrum spans from 2.74 GHz to 3.45 GHz, with a bandwidth of 0.71 GHz, which is precisely the inverse of the 1.4 ns pulse width introduced into the long ring α . The spectrum is derived by applying a two-dimensional Fourier transform to the non-stroboscopic spatiotemporal diagram.

The second row presents the measured excited energy spectra for rings α and β in panels (c) and (d), respectively, under spatially quasi-periodic modulation with $\theta = \pi/4$ and $\xi = \pi/16$. Given the non-periodic nature of the modulation,

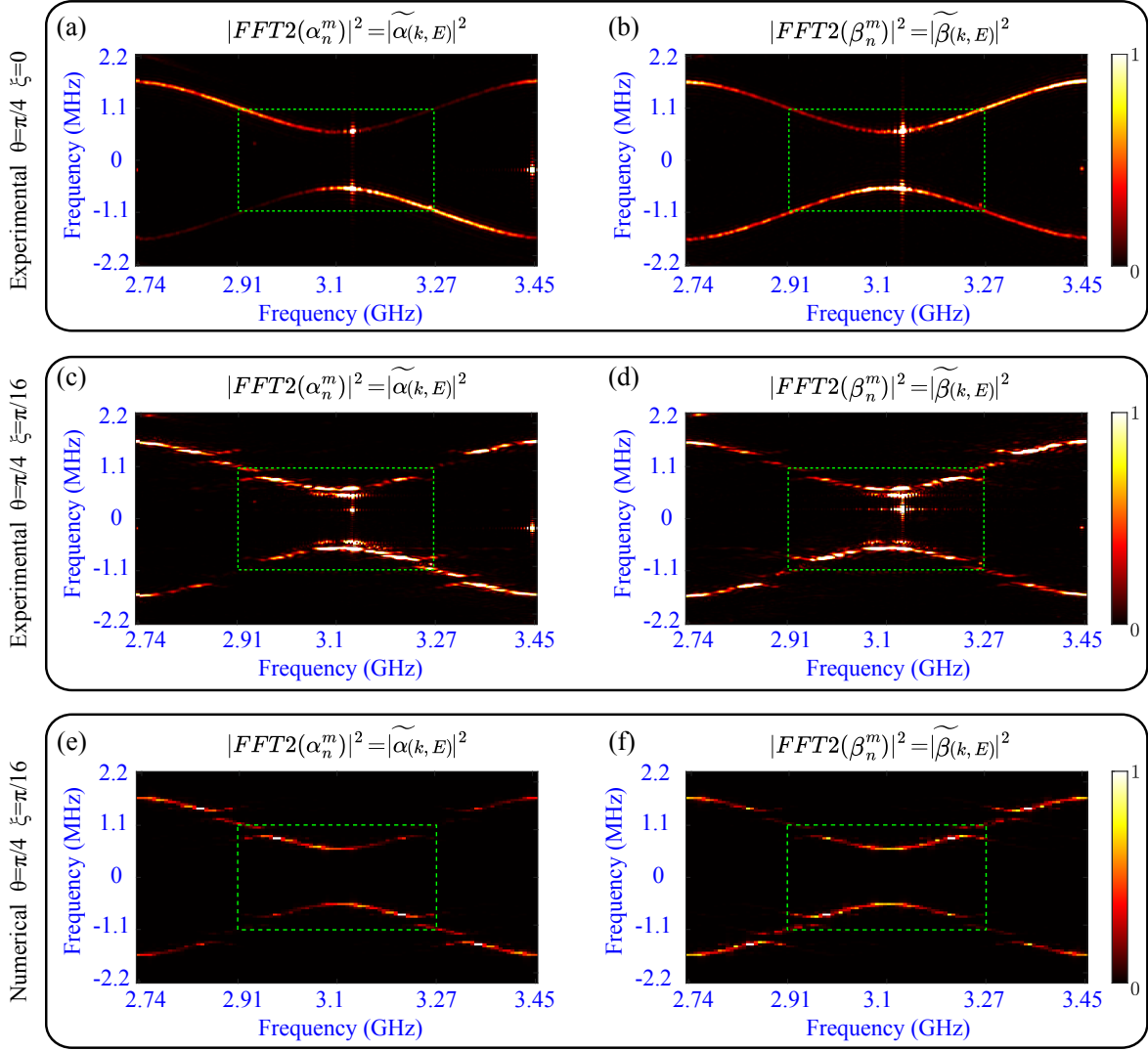


Figure E.4: The excited energy spectra for rings α and β are shown in panels (a) and (b) for the non-modulated case with $\theta = \pi/4$ (calibration shot). Panels (c) and (d) display the spectra under spatial modulation with $\theta = \pi/4$, $\varphi = 0$ and $\xi = \pi/16$. Panels (e) and (f) present the corresponding numerical simulations for the experimental spectra shown in panels (c) and (d).

along the horizontal axis, representing the lattice site (n), the unit cell is no longer defined. The typical quasi-momentum (k) and quasi-energy (E) axes are replaced with frequency axes, as illustrated by the blue frequency axes in Fig. E.4. This requires a non-stroboscopic spatiotemporal analysis. To identify the excited spectral regions corresponding to the band structures for the quasi-periodic modulation, we first use the analytical band structure from the calibration shot to pinpoint the experimental calibration bands within specific frequency windows. The identified spectral windows are then applied to analyze the quasi-periodic modulation scenario. The numerical quasi-periodic modulation in panels Figs. E.4.e and E.4.f, was performed by modulating the absolute amplitude of the pulse described in equation. 1.19 with a 3 GHz reference field. This replicated the experimental procedure, which consisted of two sequential shots: a calibration and a science shot.

The experimental fractal energy spectra in Figs. E.4.c and E.4.d exhibit excellent agreement with their corresponding numerical simulations in Fig. E.4.e and Fig. E.4.f. Notably, both experimental and numerical spectra reveal multiple gaps within each upper and lower band, forming a fractal pattern. The green dashed rectangle highlights the region corresponding to the previously studied Brillouin zone in the context of the two-step model.

E.2 Quasi periodic modulation in time

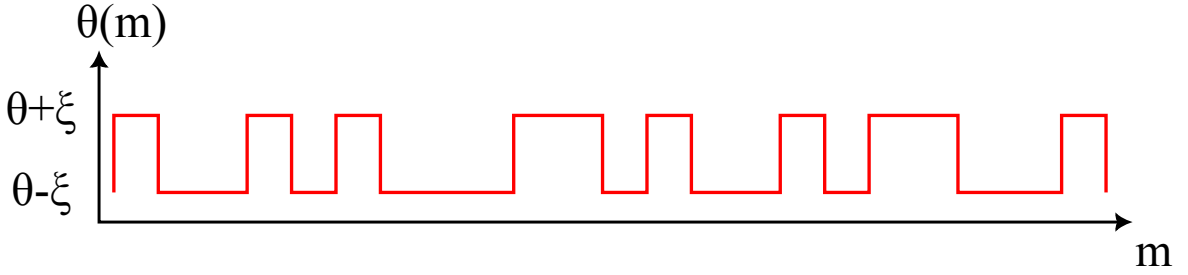


Figure E.5: The splitting angle θ alternates between the two values $\theta + \xi$ and $\theta - \xi$ in function of time steps (m), following a Fibonacci sequence, with $\xi \in [0, \pi]$.

Lattice site (n)					Time step (m)
$n - 2$	$n - 1$	n	$n + 1$	$n + 2$	
θ_1 $+\varphi$	θ_1 $+\varphi$	θ_1 $+\varphi$	θ_1 $+\varphi$	θ_1 $+\varphi$	$m-1$
θ_2 $-\varphi$	θ_2 $-\varphi$	θ_2 $-\varphi$	θ_2 $-\varphi$	θ_2 $-\varphi$	m
θ_3 $+\varphi$	θ_3 $+\varphi$	θ_3 $+\varphi$	θ_3 $+\varphi$	θ_3 $+\varphi$	$m+1$
θ_4 $-\varphi$	θ_4 $-\varphi$	θ_4 $-\varphi$	θ_4 $-\varphi$	θ_4 $-\varphi$	$m+2$
θ_5 $+\varphi$	θ_5 $+\varphi$	θ_5 $+\varphi$	θ_5 $+\varphi$	θ_5 $+\varphi$	$m+3$

Figure E.6: Photonic mesh lattice showcasing the temporal quasi-periodic modulation. The coupling angle varies in time steps (m) only.

Building upon the previous analysis of spatial quasi-periodic modulation, we now explore the effects of temporal quasi-periodic modulation.

The temporal quasi-periodic modulation is achieved by considering a nonactive phase modulator $\varphi = 0$ and alternating the splitting angle θ between $\theta + \xi$ and $\theta - \xi$ in the function of time steps (m), as outlined in equation. E.4 and illustrated in

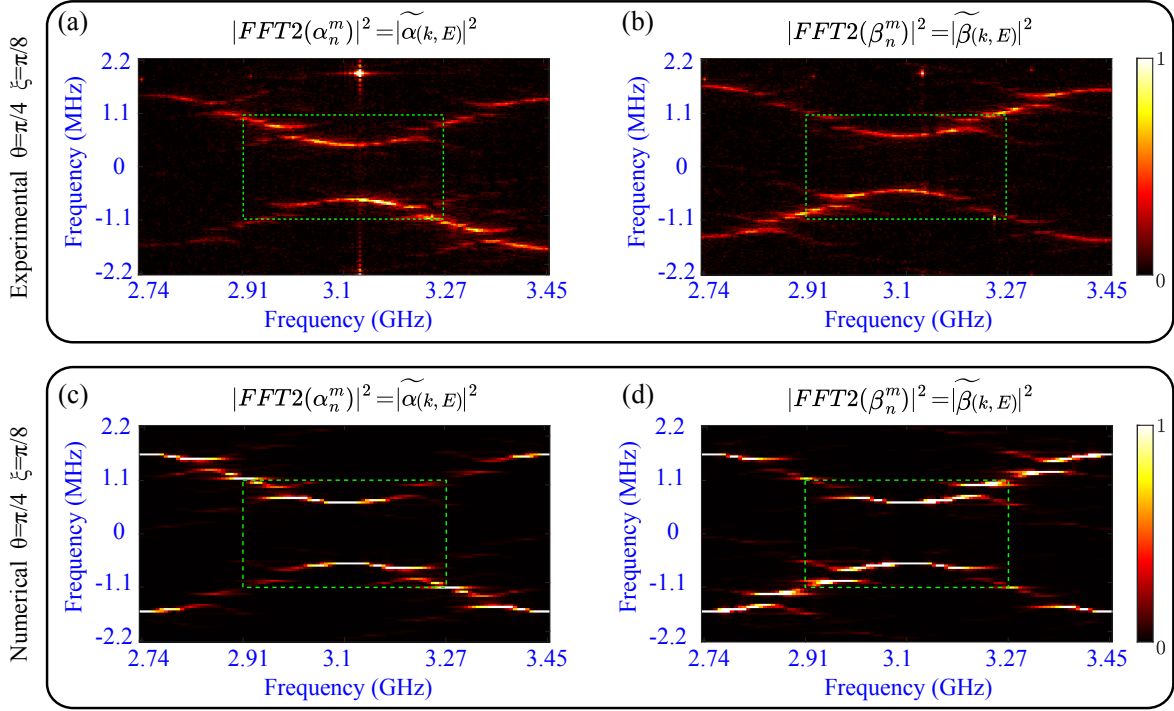


Figure E.7: The excited energy spectra for each of the rings α and β under temporal modulation with $\theta = \pi/4$ and $\xi = \pi/8$ are shown in panels (a) and (b) for the experimental results, respectively. Corresponding numerical simulations are presented in panels (c) and (d), respectively.

Fig. E.5. This modulation follows a Fibonacci sequence defined by the characteristic function in equation. E.3.

$$\kappa(m) = \text{sign}[\cos(2\pi m/\sigma) - \cos(\pi/\sigma)] \quad (\text{E.3})$$

$$\theta(m, n) = \theta(m, n) + \xi\kappa(m) \quad (\text{E.4})$$

The coupling angle modulation $\theta(m, n)$ is displayed in Fig. E.6 that presents the photonic mesh lattice discretized in time (vertical axis) and space (horizontal axis). The splitting angle $\theta(m, n)$ varies exclusively with time steps m , while the phase modulator φ alternates between two values, $+\varphi$ and $-\varphi$, during odd and even time steps, respectively.

Figures. E.7.a-b presents the experimentally obtained energy spectra for each of the rings α and β , respectively, under temporal quasi-periodic modulation with $\varphi = 0$, $\theta = \pi/4$ and $\xi = \pi/8$ when a narrow pulse of 1.4 ns is introduced into the long ring. These experimental fractal spectra show excellent agreement with the corresponding numerical simulations in panels (c) and (d). Both the experimental and numerical data reveal multiple gaps within the upper and lower band, forming a distinct fractal pattern.

The resulting bands from both spatial and temporal quasi-periodic modulation appear similar; however, the modulation parameters differ. In the spatial case,

$\tilde{\zeta} = \pi/16$, while in the temporal case, $\tilde{\zeta} = \pi/8$. This indicates that the spatial modulation is twice as sensitive to the changes in $\tilde{\zeta}$.

In summary, this appendix demonstrates that our double-ring system exhibits fractal energy spectra when subjected to temporal or spatial quasi-periodic modulation of the variable beam splitter, characterized by a Fibonacci sequence.

QUADRA-RING SYSTEM

Inspired by the groundbreaking work of Andre L. M. and H. Chalabi et al. [170, 176] on a real two-dimensional system employing two coupled 2x2 beam splitters, this appendix introduces my innovative two-dimensional system. The system consists of four optical fiber rings interconnected by a 4x4 beam splitter. While experimental validation of this proposed configuration remains a goal for future research, I am excited about the potential of this novel concept.

F.1 Quadra-ring temporal response

My novel real two-dimensional configuration termed the "Quadra-Ring System" consists of four optical fiber rings labeled U, D, L, and R, representing upward, downward, leftward, and rightward directions, respectively, and a 25/25/25/25 beam splitter. The rings are interconnected through a 25/25/25/25 beam splitter that divides the input wavefield into four equal amplitude components each time a pulse encounters the splitter, as illustrated in Fig. F.1.a. The beam splitter is symbolized by the red and green cube in the 2D synthetic photonic mesh lattice of Fig. F.1.b. The ring lengths are arranged in ascending order: $L_D < L_L < L_R < L_U$. Specifically, these lengths are defined as follows: $L_L = L_D + \Delta L_y$, $L_R = L_D + \Delta L_y + \Delta L_x$, and $L_U = L_D + 2\Delta L_y + \Delta L_x$, where ΔL_x and ΔL_y represent the differences in length between the rings, with $\Delta L_x < \Delta L_y$, and L_U , L_D , L_L , and L_R denote the lengths of the U, D, L, and R rings, respectively.

The dynamics of the complex amplitude of light pulses in the rings can be mapped into a coherent step evolution in the 2D synthetic lattice depicted in Fig. F.1.b, governed by the following equations:

$$\begin{cases} U_{x,y}^{m+1} = \frac{1}{\sqrt{4}} [U_{x,y-1}^m + (D_{x,y-1}^m + L_{x,y-1}^m + R_{x,y-1}^m)e^{i\pi}] \\ D_{x,y}^{m+1} = \frac{1}{\sqrt{4}} [D_{x,y+1}^m + (U_{x,y+1}^m + L_{x,y+1}^m + R_{x,y+1}^m)e^{i\pi}] \\ L_{x,y}^{m+1} = \frac{1}{\sqrt{4}} [L_{x+1,y}^m + (D_{x+1,y}^m + U_{x+1,y}^m + R_{x+1,y}^m)e^{i\pi}] \\ R_{x,y}^{m+1} = \frac{1}{\sqrt{4}} [R_{x-1,y}^m + (D_{x-1,y}^m + L_{x-1,y}^m + U_{x-1,y}^m)e^{i\pi}] \end{cases} \quad (\text{F.1})$$

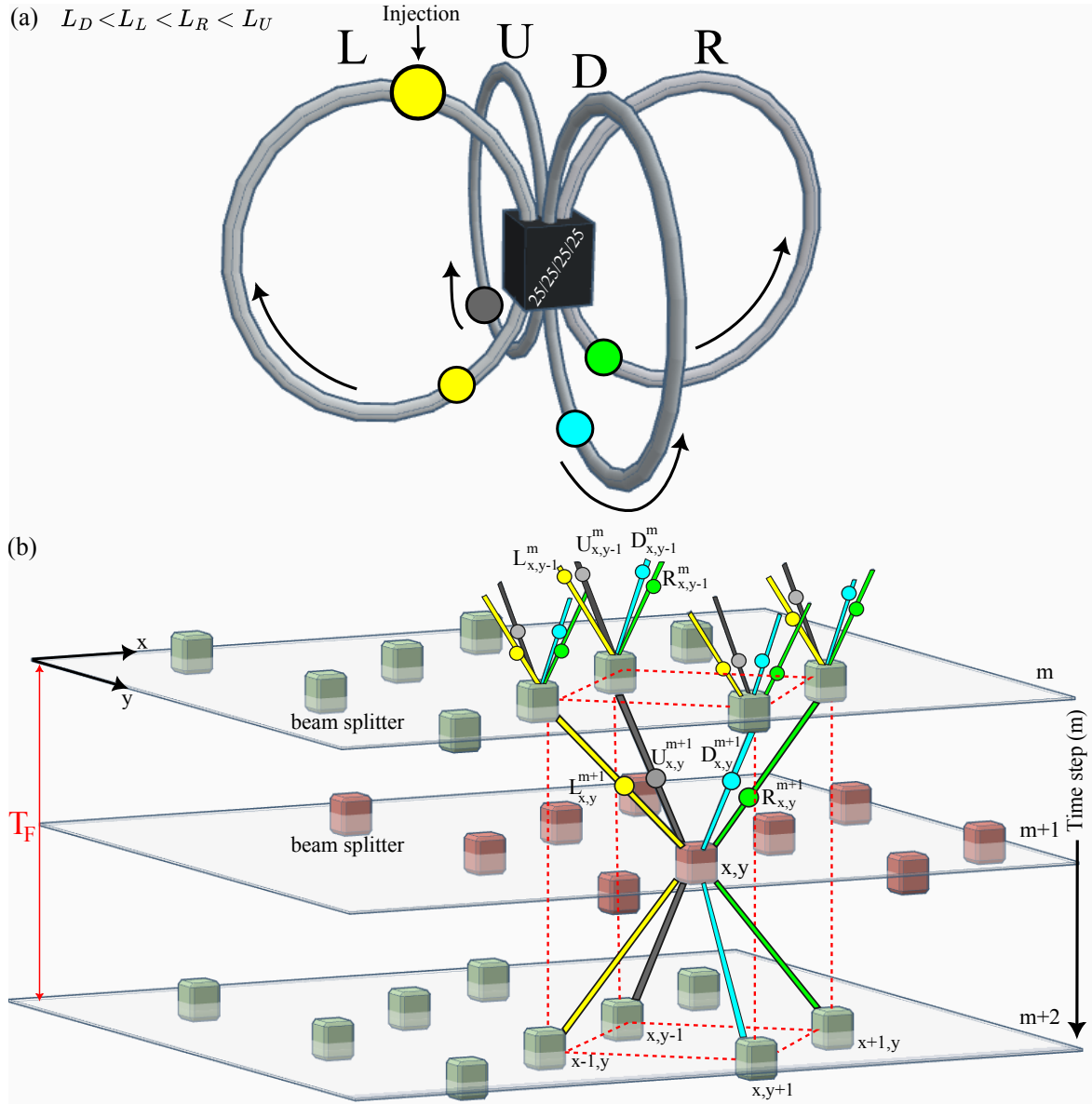


Figure F.1: (a) The four-ring system comprises five essential components: four optical fiber rings denoted U, D, L, and R and a 25/25/25/25 beam splitter. (b) A 2D synthetic photonic mesh lattice that describes the light diffraction along the x and y axes, with light propagation occurring along the vertical axis, representing discrete time steps (m).

$$\begin{cases} U_{x,y}^{m+1} = \frac{1}{2} [+U_{x,y-1}^m - D_{x,y-1}^m - L_{x,y-1}^m - R_{x,y-1}^m] \\ D_{x,y}^{m+1} = \frac{1}{2} [-U_{x,y+1}^m + D_{x,y+1}^m - L_{x,y+1}^m - R_{x,y+1}^m] \\ L_{x,y}^{m+1} = \frac{1}{2} [-U_{x+1,y}^m - D_{x+1,y}^m + L_{x+1,y}^m - R_{x+1,y}^m] \\ R_{x,y}^{m+1} = \frac{1}{2} [-U_{x-1,y}^m - D_{x-1,y}^m - L_{x-1,y}^m + R_{x-1,y}^m] \end{cases} \quad (\text{F.2})$$

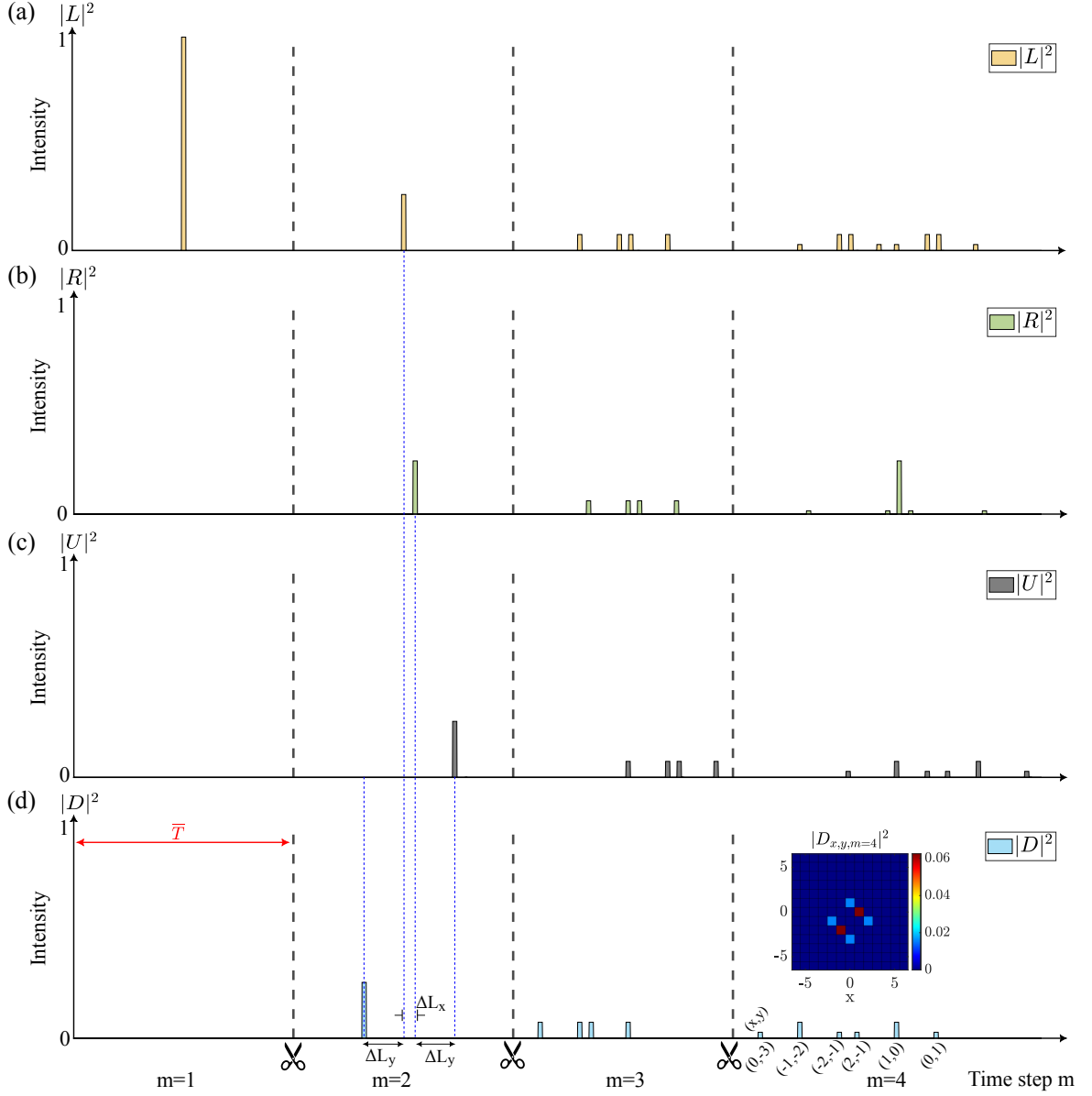


Figure F.2: Numerical simulation of the quadra-ring temporal response at the output of each ring (L , R , U , D) is shown in panels (a), (b), (c), and (d), respectively, when a narrow pulse is introduced into the Left ring L .

Equations. F.2 reveal that the output complex amplitudes of the wavefield for each ring at lattice site (x, y) during time step $(m + 1)$ result from a linear combination of the transmitted fields along the same optical fiber path and the reflected input amplitude fields from different paths at round trip (m) with a phase shift π .

The progression of the light dynamics is visualized in Fig. F.1.b via a 2D synthetic photonic mesh lattice. The x and y axes represent discrete spatial dimensions, while the vertical axis corresponds to discrete time steps (m). The four sublattices sites, depicted in black, blue, yellow, and green in Fig. F.1.b correspond to the complex amplitudes $U_{x,y}^m$, $D_{x,y}^m$, $L_{x,y}^m$ and $R_{x,y}^m$ respectively, for a specific round trip m and position (x, y) , return to the same site position after two-time steps. Thus one

Floquet period T_F corresponds to two round trips. Similarly, At a specific round trip (m), the four sublattices manifest by a spatial periodicity every two site positions. Thus, our system exhibits dual periodicity in both time and space, with a period corresponding to two round trips in time $m \rightarrow m + 2$ and two site positions in space $x \rightarrow x + 2$ and $y \rightarrow y + 2$. This defines the unit cell, represented as a cube, as illustrated by the red dashed outline in Fig. F.1.b.

Figure. F.2 presents a numerical simulation of the quadra-ring temporal response when a narrow pulse is introduced in the left ring L at round trip $m = 1$ and position site $(x, y) = (0, 0)$. The distribution of the signal intensity as a function of time step (m) at the output of each ring (L, R, U, D) is represented in (yellow, green, black, and blue), respectively. Initially, the pulse divides into four smaller pulses with equal amplitude within each ring once it reaches the 25/25/25/25 fiber coupler, as depicted at round trip $m = 2$. These pulses journey through their respective loops until they reunite at the beam splitter at different moments due to the length difference between the rings. Once again, each of the pulses within each ring split into four smaller pulses, as illustrated at round trip $m = 3$. Consequently, this continuous cyclic process generates multiple pulses with consistent time intervals during each round trip (red double arrows). Due to the length difference in the loops, the adjacent pulses within the same round trip in each ring are temporally separated, leading to their detection at specific physical times. We assign integer numbers to each pulse to represent a particular time coordinate, which can be equated to a position (x, y) in space, (see round trip $m=4$ in Fig. F.2.d).

The average time of one period \bar{T} is given by $\bar{T} = \bar{L}/v$, where \bar{L} denotes the average length of the rings, calculated as $\bar{L} = (L_U + L_D + L_L + L_R)/4$, and v represents the speed of light in the optical fiber. The temporal response of the quadra-ring system in Fig. F.2 is segmented into equal duration of \bar{T} , with each segment further divided into smaller time intervals of $\Delta L_y/v$. These smaller intervals within the same round trip are superimposed and reshaped into a two-dimensional discrete lattice slice, representing the corresponding x and y coordinates of the pulses within the rings, as depicted by the 2D slice at round trip $m = 4$ in Fig. F.2.d.

F.2 Quadra-ring dispersion relation

F.2.1 Numerical characterization of the band structure

The spatiotemporal diagram for each ring (L, R, U, D) is constructed by layering the 2D slices next to one another, as presented in Figs. F.3.a-d, respectively, which illustrates the progression of light from one round trip to the next one as a function of position (x, y) . Figures. F.3.e-f provides a magnified view of the first five round trips of each of the rings depicted in Figs. F.3.a-d, respectively. Due to the

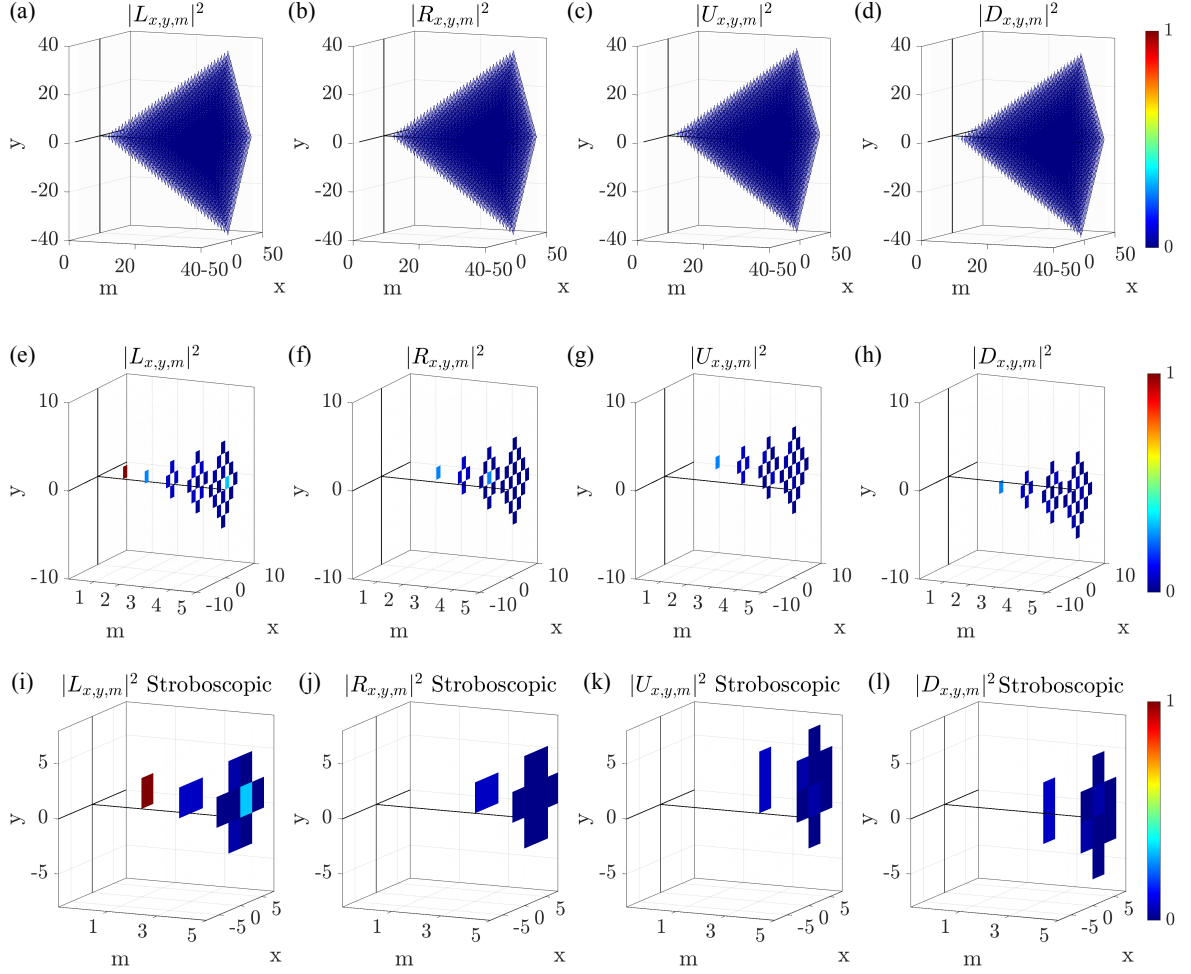


Figure F.3: Spatiotemporal diagrams of the rings (L, R, U, D) are presented in panels (a-d), respectively. (e-h) Magnified views of the first five round trips for each ring. (i-l) Stroboscopic spatiotemporal diagrams of the magnified views by keeping even site position (x, y) and odd time steps (m).

system's double periodicity in space and time, it is more convenient to consider the stroboscopic dynamics, as shown in the zoomed stroboscopic spatiotemporal diagram of Figs. F.3.i-j, by keeping even site position (x, y) and odd time steps (m).

To better understand the evolution of light within the spatiotemporal diagrams, we present 2D slices for each ring (L, R, U, D) in columns 1, 2, 3, and 4, respectively, of Fig. F.4. These slices are shown at round trips ($m = 1, 2, 3, 4, 5$, and 39), illustrating the temporal progression. Additionally, corresponding stroboscopic 2D slices are plotted in Fig. F.5. The 2D slice at round trip ($m=39$) of the spatiotemporal diagram in the right ring R (see Fig. F.4.v) shows a symmetrical light intensity pattern along both the x and y axes. In contrast, the left ring L exhibits a dominant distribution along the negative x -axis. The upper ring U has its intensity concentrated in the region where the x -axis is negative and the y -axis is positive. Finally, the lower ring D displays intensity confined to the bottom left corner, where both x and y are negative.

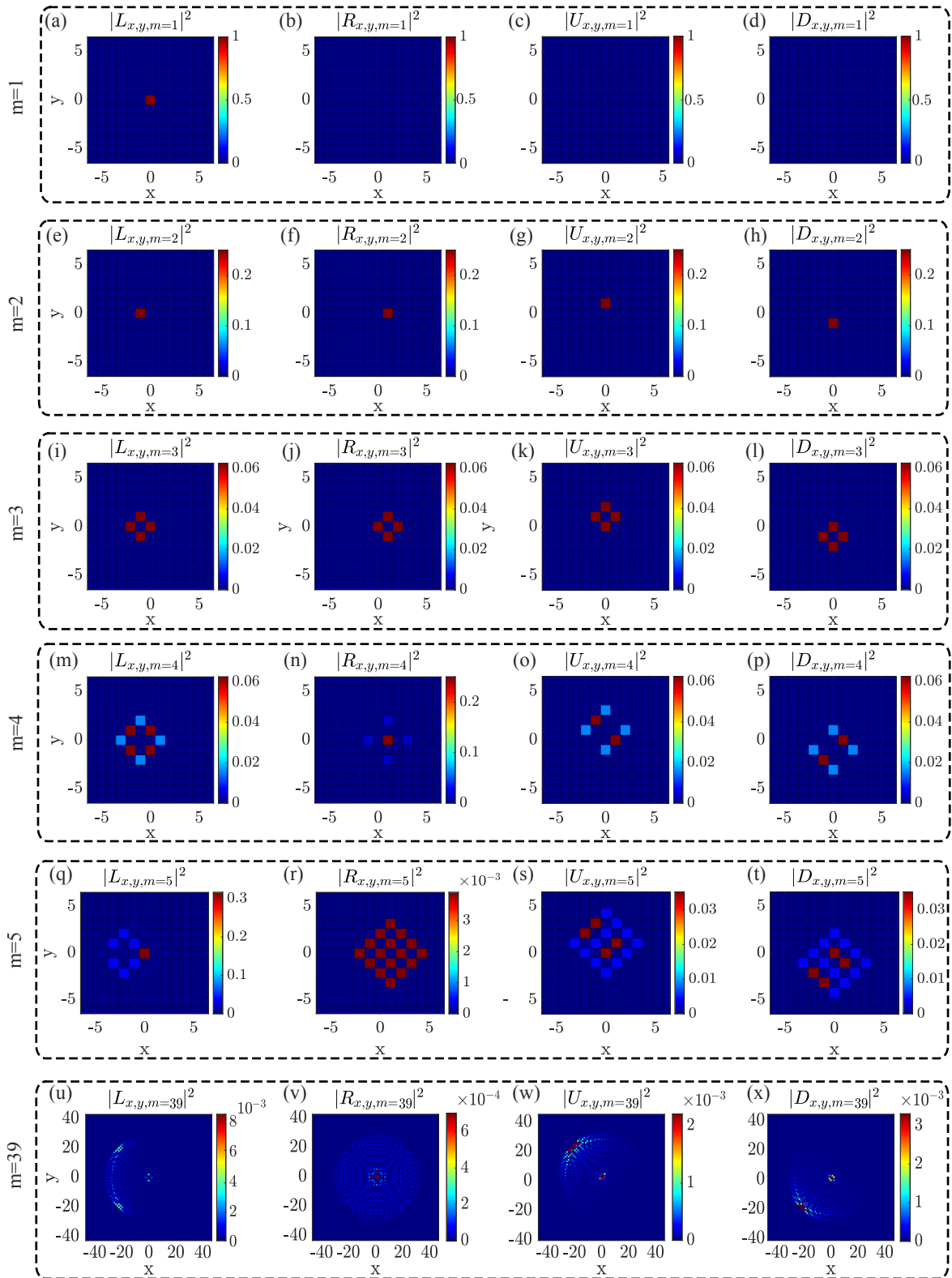


Figure F.4: 2D slices of the spatiotemporal diagrams in Fig. F.4 are presented for each ring (L , R , U , D) in columns 1, 2, 3, and 4, respectively. These slices are shown at round trips ($m = 1, 2, 3, 4, 5,$ and 39).

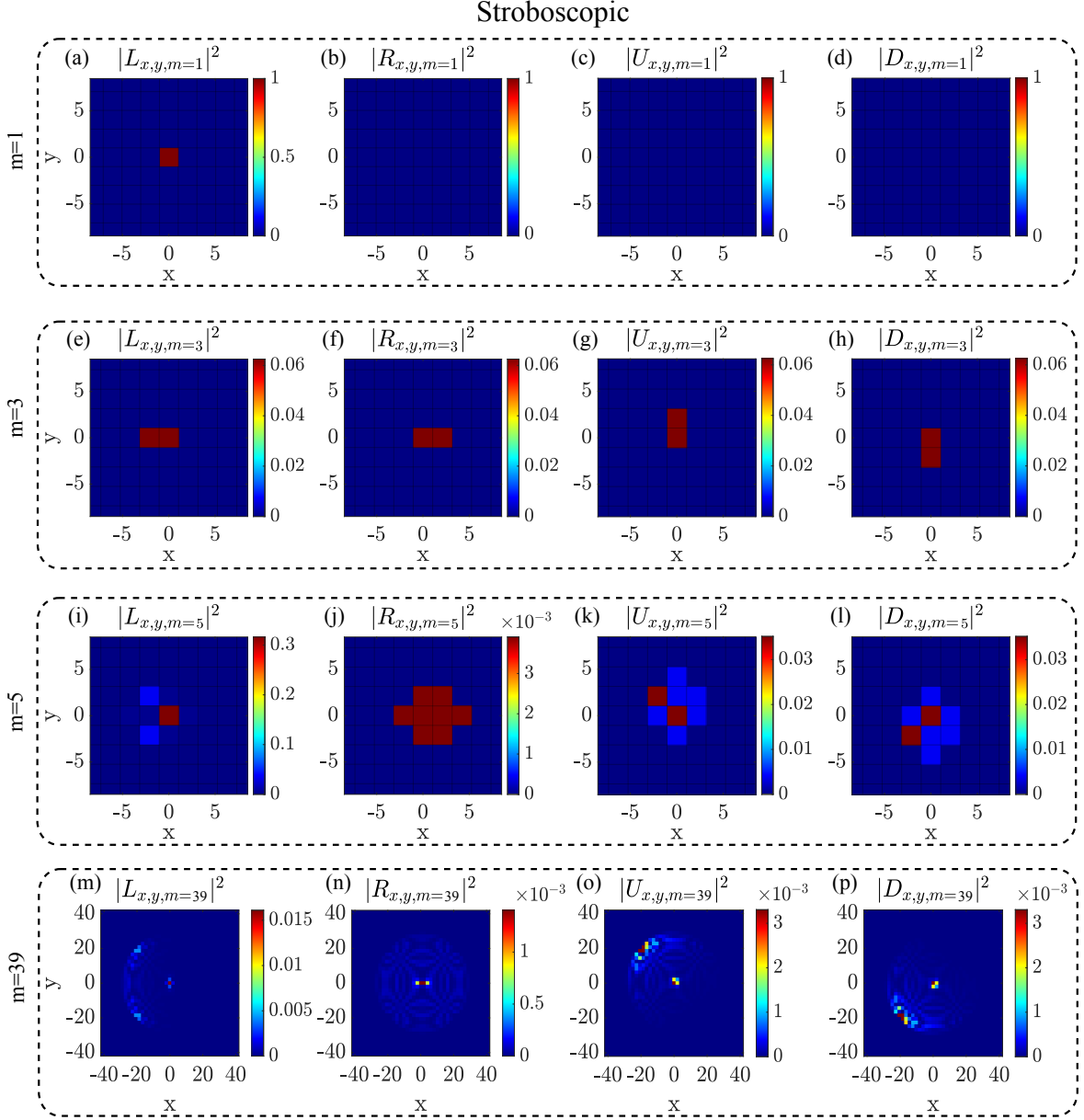


Figure F.5: Corresponding stroboscopic 2D slices of Fig. F.4 at round trips ($m = 1, 3, 5,$ and 39), obtained by keeping even site position (x,y) and odd time steps (m) .

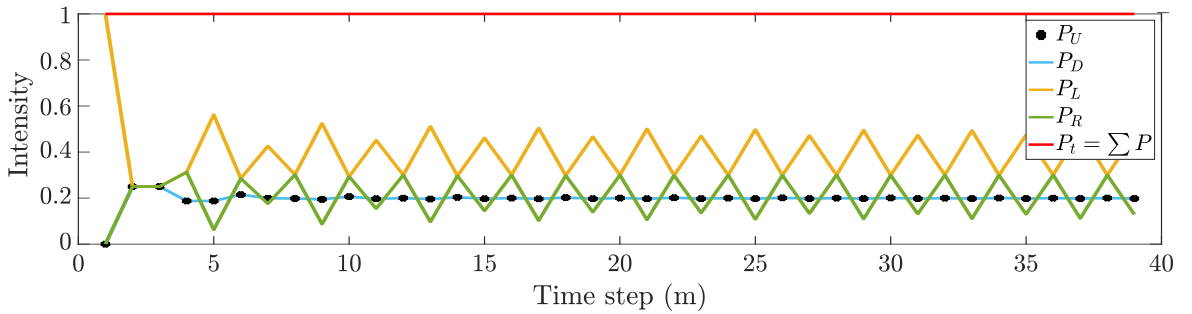


Figure F.6: The total power in each of the rings $U, D, L,$ and R is represented by black, blue, yellow, and green lines, respectively, as a function of the time step (m) . The red line illustrates that the sum of the total power across all rings remains constant at 1.

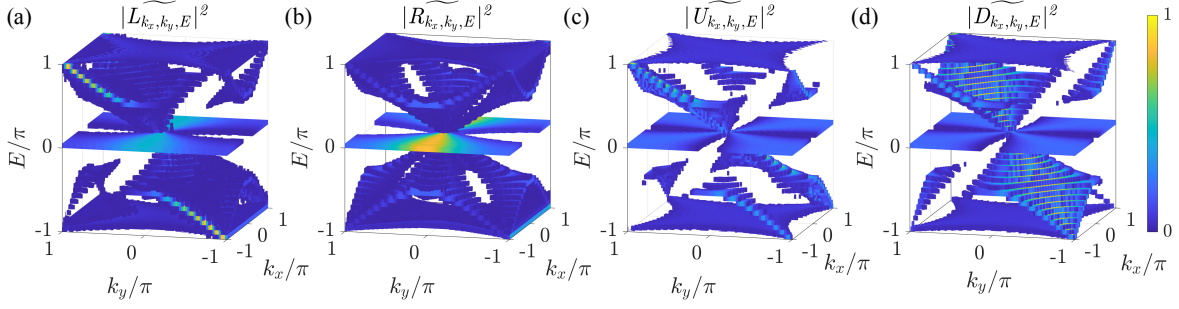


Figure F.7: The dispersion relation of the rings (L, R, U, D) are presented in panels (a, b, c, d) respectively. Each dispersion relation exhibits four bands: two flat bands at energy levels 0 and π , and two bands forming a gapless Dirac cone within the Brillouin zone spanning from $-\pi$ to π in both quasimomenta k_x and k_y , and quasienergy E .

Figure. F.6 illustrates the total power evolution within the rings $U, D, L,$ and R , depicted by black, blue, yellow, and green lines, respectively, as a function of time step (m). Each data point on these lines represents the cumulative power of all the pulses residing in the corresponding ring at a specific round trip (m) within a corresponding slice of the spatiotemporal diagram showcased in Fig. F.4. Initially, at round trip $m=1$, a single pulse with a power of 1 is injected into ring L , marked by a yellow dot. The other rings contain no power. At round trip $m=2$, this pulse divides into four equal pulses, each carrying a quarter of the initial power (0.25). The red line illustrates the total power across all rings ($P_t = P_U + P_D + P_L + P_R$), which remains constant at 1 over 40 round trips, signifying power conservation in the absence of losses within the numerical simulation. This conservation confirms the accuracy of the evolution equation. F.2 in describing our 4-ring system.

By performing a 3D Fourier transform on the stroboscopic spatiotemporal diagram, we derive the dispersion relations of each of the rings (L, R, U, D) in Figs. F.7.a-d, respectively. Each dispersion relation exhibits four bands within the Brillouin zone spanning from $-\pi$ to π in both quasimomenta k_x and k_y , and quasienergy E . These bands consist of two flat bands at energy levels 0 and π , and two bands forming a gapless Dirac cone, as exemplified in Fig. F.7.b. The excitation profile of the band structure energy spectrum mirrors the light intensity distribution in the stroboscopic spatiotemporal diagram. The symmetrical light intensity pattern in the ring R of Fig. F.5.n along x and y translates to a symmetrically excited numerical dispersion relation in quasimomentum k_x and k_y . In contrast, the asymmetrical light patterns in the other rings produce asymmetrical band excitations.

F.2.2 Analytical characterization of the band structure

The quadra-ring system exhibits a double periodicity: spatial (every two sites along x and y) and temporal (every two-time steps m), as shown by the

unit cell (red dashed cube) in Fig. F.1.b. The eigenvectors $|\psi(k_x, k_y)\rangle$ are represented as a linear combination of the four complex amplitude eigenmodes $\tilde{U}(k_x, k_y)$, $\tilde{D}(k_x, k_y)$, $\tilde{L}(k_x, k_y)$, $\tilde{R}(k_x, k_y)$ corresponding to the (U , D , L , R) rings respectively.

$$|\psi(k_x, k_y)\rangle = \begin{bmatrix} \tilde{U}(k_x, k_y) \\ \tilde{D}(k_x, k_y) \\ \tilde{L}(k_x, k_y) \\ \tilde{R}(k_x, k_y) \end{bmatrix} e^{\frac{i}{2}(Em+k_x x+k_y y)} \quad (\text{F.3})$$

The Bloch momentum (k_x, k_y) and the quasienergies E are conjugate variables associated with the spatial (x, y) and the temporal parameter m , respectively. Equation. F.3 highlights the system's double periodicity in both directions, with a period of two discrete steps. This periodicity is evident in the ansatz equation, where the exponents are scaled by a factor of $1/2$ with respect to both E and (k_x, k_y) .

To determine the eigenvalue, we substitute equation. F.3 into equation F.2, resulting in the following expression:

$$\begin{cases} \tilde{U}e^{i(E/2)} = \frac{e^{-ik_y/2}}{2} [\tilde{U} - \tilde{D} - \tilde{L} - \tilde{R}] \\ \tilde{D}e^{i(E/2)} = \frac{e^{ik_y/2}}{2} [-\tilde{U} + \tilde{D} - \tilde{L} - \tilde{R}] \\ \tilde{L}e^{i(E/2)} = \frac{e^{ik_x/2}}{2} [-\tilde{U} - \tilde{D} + \tilde{L} - \tilde{R}] \\ \tilde{R}e^{i(E/2)} = \frac{e^{-ik_x/2}}{2} [-\tilde{U} - \tilde{D} - \tilde{L} + \tilde{R}] \end{cases} \quad (\text{F.4})$$

$$\begin{bmatrix} \tilde{U} \\ \tilde{D} \\ \tilde{L} \\ \tilde{R} \end{bmatrix} = \underbrace{\begin{bmatrix} +\frac{e^{i(-k_y-E)/2}}{2} & -\frac{e^{i(-k_y-E)/2}}{2} & -\frac{e^{i(-k_y-E)/2}}{2} & -\frac{e^{i(-k_y-E)/2}}{2} \\ -\frac{e^{i(k_y-E)/2}}{2} & +\frac{e^{i(k_y-E)/2}}{2} & -\frac{e^{i(k_y-E)/2}}{2} & -\frac{e^{i(k_y-E)/2}}{2} \\ -\frac{e^{i(k_x-E)/2}}{2} & -\frac{e^{i(k_x-E)/2}}{2} & +\frac{e^{i(k_x-E)/2}}{2} & -\frac{e^{i(k_x-E)/2}}{2} \\ -\frac{e^{i(-k_x-E)/2}}{2} & -\frac{e^{i(-k_x-E)/2}}{2} & -\frac{e^{i(-k_x-E)/2}}{2} & +\frac{e^{i(-k_x-E)/2}}{2} \end{bmatrix}}_{\text{M=Evolution operator}} \begin{bmatrix} \tilde{U} \\ \tilde{D} \\ \tilde{L} \\ \tilde{R} \end{bmatrix} \quad (\text{F.5})$$

$$\begin{bmatrix} \tilde{U} \\ \tilde{D} \\ \tilde{L} \\ \tilde{R} \end{bmatrix} (M - I) = 0 \quad (\text{F.6})$$

$$\det(M - I) = 0 \quad (\text{F.7})$$

$$\begin{vmatrix} +\frac{e^{i(-k_y-E)/2}}{2} - 1 & -\frac{e^{i(-k_y-E)/2}}{2} & -\frac{e^{i(-k_y-E)/2}}{2} & -\frac{e^{i(-k_y-E)/2}}{2} \\ -\frac{e^{i(k_y-E)/2}}{2} & +\frac{e^{i(k_y-E)/2}}{2} - 1 & -\frac{e^{i(k_y-E)/2}}{2} & -\frac{e^{i(k_y-E)/2}}{2} \\ -\frac{e^{i(k_x-E)/2}}{2} & -\frac{e^{i(k_x-E)/2}}{2} & +\frac{e^{i(k_x-E)/2}}{2} - 1 & -\frac{e^{i(k_x-E)/2}}{2} \\ -\frac{e^{i(-k_x-E)/2}}{2} & -\frac{e^{i(-k_x-E)/2}}{2} & -\frac{e^{i(-k_x-E)/2}}{2} & +\frac{e^{i(-k_x-E)/2}}{2} - 1 \end{vmatrix} = 0 \quad (\text{F.8})$$

$$e^{-2iE} \left[e^{i2E} + \frac{e^{i(E-k_x)/2}}{2} + \frac{e^{i(E+k_x)/2}}{2} - \frac{e^{i(3E-k_x)/2}}{2} - \frac{e^{i(3E+k_x)/2}}{2} + \frac{e^{i(E-k_y)/2}}{2} + \frac{e^{i(E+k_y)/2}}{2} - \frac{e^{i(3E-k_y)/2}}{2} - \frac{e^{i(3E+k_y)/2}}{2} - 1 \right] = 0 \quad (\text{F.9})$$

$$\underbrace{e^{-2iE}}_{\neq 0} \left[e^{i2E} + \frac{e^{iE/2}}{2} (e^{-ik_x/2} + e^{ik_x/2}) - \frac{e^{i3E/2}}{2} (e^{-ik_x/2} + e^{ik_x/2}) + \frac{e^{iE/2}}{2} (e^{-ik_y/2} + e^{ik_y/2}) - \frac{e^{i3E/2}}{2} (e^{-ik_y/2} + e^{ik_y/2}) - 1 \right] = 0 \quad (\text{F.10})$$

$$\left[e^{i2E} + \frac{e^{iE/2}}{2} (\cos \frac{k_x}{2} + \cos \frac{k_y}{2}) - \frac{e^{i3E/2}}{2} (\cos \frac{k_x}{2} + \cos \frac{k_y}{2}) - 1 \right] = 0 \quad (\text{F.11})$$

$$\underbrace{e^{iE}}_{\neq 0} \left[e^{iE} + \frac{e^{-iE/2}}{2} (\cos \frac{k_x}{2} + \cos \frac{k_y}{2}) - \frac{e^{iE/2}}{2} (\cos \frac{k_x}{2} + \cos \frac{k_y}{2}) - e^{-iE} \right] = 0 \quad (\text{F.12})$$

$$e^{iE} - e^{-iE} + (\cos \frac{k_x}{2} + \cos \frac{k_y}{2}) \left(\frac{e^{-iE/2}}{2} - \frac{e^{iE/2}}{2} \right) = 0 \quad (\text{F.13})$$

$$2i \sin E - 2i \sin \frac{E}{2} (\cos \frac{k_x}{2} + \cos \frac{k_y}{2}) = 0 \quad \text{or} \quad \sin E = 2 \sin \frac{E}{2} \cos \frac{E}{2} \quad (\text{F.14})$$

$$4i \sin \frac{E}{2} \cos \frac{E}{2} - 2i \sin \frac{E}{2} (\cos \frac{k_x}{2} + \cos \frac{k_y}{2}) = 0 \quad (\text{F.15})$$

$$\underbrace{i \sin \frac{E}{2}}_{=0} \underbrace{\left[4 \cos \frac{E}{2} - 2(\cos \frac{k_x}{2} + \cos \frac{k_y}{2}) \right]}_{=0} = 0 \quad (\text{F.16})$$

$$\begin{cases} \sin \frac{E}{2} = 0 \\ \frac{E}{2} = \sin^{-1}(0) \\ E = 2n\pi \text{ (even)} \quad \text{and} \quad E = \pi - 2n\pi \text{ (odd)} \rightarrow E = n\pi \quad \text{with } n \in \mathbb{Z} \end{cases} \quad (\text{F.17})$$

$$\begin{cases} 4 \cos \frac{E}{2} - 2(\cos \frac{k_x}{2} + \cos \frac{k_y}{2}) = 0 \\ E = \pm 2 \cos^{-1}[\frac{1}{2}(\cos \frac{k_x}{2} + \cos \frac{k_y}{2})] \end{cases} \quad (\text{F.18})$$

$$E = n\pi \quad \& \quad E = \pm 2 \cos^{-1}[\frac{1}{2}(\cos \frac{k_x}{2} + \cos \frac{k_y}{2})] \quad \text{with } n \in \mathbb{Z} \quad (\text{F.19})$$

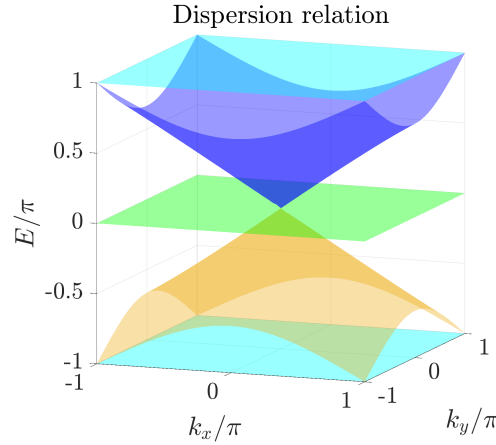


Figure F.8: The analytical dispersion relation for the quadra-ring system features four distinct bands: two flat bands at energy levels 0 and π , and two bands forming a gapless Dirac cone within the Brillouin zone, which spans from $-\pi$ to π in both quasimomenta k_x and k_y , as well as in quasienergy E

The analytical dispersion relation of the quadra-ring system is provided by equation. F.19 and is illustrated in Fig. F.8. The band structure features four distinct bands: two flat bands at energy levels 0 and π , and two bands forming a gapless Dirac cone within the Brillouin zone, which spans from $-\pi$ to π in both quasimomenta k_x and k_y , as well as in quasienergy E . The analytical results align perfectly with the numerical dispersion bands presented in Fig. F.7, which validates the reliability of the mathematical model.

In conclusion, this work introduces my novel real two-dimensional system comprising four optical fiber rings of distinct lengths interconnected by a 25/25/25/25 beam splitter. A detailed analysis of the system's impulse response was conducted. Moreover, a three-dimensional visualization of the spatiotemporal diagram was provided, from which the numerical band structure was extracted. Finally, the development of a mathematical framework yielded an analytical dispersion relation that demonstrates excellent agreement with the numerical results, thereby validating my model.

BIBLIOGRAPHY

- [1] R. El Sokhen et al., 'Edge-dependent anomalous topology in synthetic photonic lattices subject to discrete step walks,' *Phys. Rev. Res.*, vol. 6, p. 023282, 2 Jun. 2024. doi: [10.1103/PhysRevResearch.6.023282](https://doi.org/10.1103/PhysRevResearch.6.023282). (cit. on pp. [xi](#), [95](#), [102](#)).
- [2] L. Lu et al., 'Topological photonics,' *Nature Photonics*, vol. 8, no. 11, pp. 821–829, 2014. doi: [10.1038/nphoton.2014.248](https://doi.org/10.1038/nphoton.2014.248) (cit. on pp. [1](#), [10](#)).
- [3] T. Ozawa et al., 'Topological photonics,' *Rev. Mod. Phys.*, vol. 91, p. 015006, 1 Mar. 2019. doi: [10.1103/RevModPhys.91.015006](https://doi.org/10.1103/RevModPhys.91.015006). (cit. on pp. [1](#), [11](#)).
- [4] M. Z. Hasan et al., 'Colloquium: Topological insulators,' *Rev. Mod. Phys.*, vol. 82, pp. 3045–3067, 4 Nov. 2010. doi: [10.1103/RevModPhys.82.3045](https://doi.org/10.1103/RevModPhys.82.3045). (cit. on pp. [1](#), [11](#), [14](#)).
- [5] X.-L. Qi et al., 'Topological insulators and superconductors,' *Rev. Mod. Phys.*, vol. 83, pp. 1057–1110, 4 Oct. 2011. doi: [10.1103/RevModPhys.83.1057](https://doi.org/10.1103/RevModPhys.83.1057). (cit. on pp. [1](#), [11](#)).
- [6] K. v. Klitzing et al., 'New method for high-accuracy determination of the fine-structure constant based on quantized hall resistance,' *Phys. Rev. Lett.*, vol. 45, pp. 494–497, 6 Aug. 1980. doi: [10.1103/PhysRevLett.45.494](https://doi.org/10.1103/PhysRevLett.45.494). (cit. on pp. [1](#), [11](#)).
- [7] T. Kitagawa et al., 'Observation of topologically protected bound states in photonic quantum walks,' *Nature Communications*, vol. 3, no. 1, p. 882, 2012. doi: [10.1038/ncomms1872](https://doi.org/10.1038/ncomms1872) (cit. on pp. [1](#), [95](#), [129](#)).
- [8] T. Kitagawa et al., 'Exploring topological phases with quantum walks,' *Phys. Rev. A*, vol. 82, p. 033429, 3 Sep. 2010. doi: [10.1103/PhysRevA.82.033429](https://doi.org/10.1103/PhysRevA.82.033429). (cit. on pp. [1](#), [95](#), [129](#)).
- [9] T. Kitagawa, 'Topological phenomena in quantum walks: Elementary introduction to the physics of topological phases,' *Quantum Information Processing*, vol. 11, pp. 1107–1148, 2012. doi: [10.1007/s11128-012-0425-4](https://doi.org/10.1007/s11128-012-0425-4) (cit. on pp. [1](#), [95](#), [129](#)).
- [10] T. Bessho et al., 'Extrinsic topology of floquet anomalous boundary states in quantum walks,' *Phys. Rev. B*, vol. 105, p. 094306, 9 Mar. 2022. doi: [10.1103/PhysRevB.105.094306](https://doi.org/10.1103/PhysRevB.105.094306). (cit. on pp. [1](#), [2](#), [13](#), [14](#), [95](#), [98](#), [103](#), [129](#), [130](#)).
- [11] T. Kitagawa et al., 'Observation of topologically protected bound states in photonic quantum walks,' *Nat. Commun.*, vol. 3, p. 882, 2012. doi: [10.1038/ncomms1872](https://doi.org/10.1038/ncomms1872). (cit. on pp. [1](#), [12](#), [14](#), [15](#), [44](#), [96](#)).
- [12] S. Barkhofen et al., 'Measuring topological invariants in disordered discrete-time quantum walks,' *Phys. Rev. A*, vol. 96, no. 3, p. 033846, Sep. 2017, issn: 2469-9926, 2469-9934. doi: [10.1103/PhysRevA.96.033846](https://doi.org/10.1103/PhysRevA.96.033846). (visited on 02/04/2024) (cit. on pp. [1](#), [12](#), [14](#), [15](#), [44](#), [96](#)).
- [13] M. Bellec et al., 'Non-diffracting states in one-dimensional Floquet photonic topological insulators,' *EPL*, vol. 119, no. 1, p. 14003, 2017. doi: [10.1209/0295-5075/119/14003](https://doi.org/10.1209/0295-5075/119/14003). (cit. on pp. [1](#), [12](#), [14](#), [15](#), [44](#), [96](#)).
- [14] A. Bisianov et al., 'Stability of topologically protected edge states in nonlinear fiber loops,' *Phys. Rev. A*, vol. 100, no. 6, p. 063830, Dec. 2019, issn: 2469-9926, 2469-9934. doi: [10.1103/PhysRevA.100.063830](https://doi.org/10.1103/PhysRevA.100.063830). (visited on 10/09/2021) (cit. on pp. [1](#), [12](#), [14](#), [15](#), [28](#), [42](#), [44](#), [96](#)).
- [15] L. J. Maczewsky et al., 'Observation of photonic anomalous floquet topological insulators,' *Nature communications*, vol. 8, no. 1, p. 13756, 2017. doi: [10.1038/ncomms13756](https://doi.org/10.1038/ncomms13756) (cit. on pp. [1](#), [12](#), [14](#), [15](#), [44](#), [96](#)).

- [16] S. Mukherjee et al., 'Experimental observation of anomalous topological edge modes in a slowly driven photonic lattice,' *Nat. Commun.*, vol. 8, p. 13918, Jan. 2017, issn: 2041-1723. doi: [10.1038/ncomms13918](https://doi.org/10.1038/ncomms13918). (visited on 28/02/2017) (cit. on pp. 1, 12, 14, 15, 44, 96).
- [17] C. Lechevalier, 'Structure des bandes, états propres et dynamique non linéaire dans un réseau photonique fibré,' <https://theses.fr/2022ULILR070>, Ph.D. dissertation, Université de Lille, 2022 (cit. on pp. 2, 24, 26, 40, 42, 65, 71, 74, 77).
- [18] J. Joannopoulos et al., 'Photonic crystals: Putting a new twist on light,' *Nature*, vol. 386, no. 6621, pp. 143–149, Mar. 1997, issn: 1476-4687. doi: [10.1038/386143a0](https://doi.org/10.1038/386143a0). (cit. on p. 5).
- [19] J. N. e. a. Winn, 'Omnidirectional reflection from a one-dimensional photonic crystal,' *Opt. Lett.*, OL, vol. 23, no. 20, pp. 1573–1575, Oct. 1998. doi: [10.1364/OL.23.001573](https://doi.org/10.1364/OL.23.001573). (cit. on p. 5).
- [20] T. Pertsch et al., 'Anomalous refraction and diffraction in discrete optical systems,' *Physical Review Letters*, vol. 88, no. 9, p. 093901, 2002. doi: [10.1103/PhysRevLett.88.093901](https://doi.org/10.1103/PhysRevLett.88.093901) (cit. on pp. 5, 7).
- [21] S. Mukherjee et al., 'Experimental observation of anomalous topological edge modes in a slowly driven photonic lattice,' *Nature communications*, vol. 8, no. 1, p. 13918, 2017. doi: [10.1038/ncomms13918](https://doi.org/10.1038/ncomms13918) (cit. on p. 5).
- [22] G. P. Agrawal, *Fiber-optic communication systems*. John Wiley & Sons, 2012 (cit. on p. 5).
- [23] D. Marcuse, *Theory of dielectric optical waveguides*. Elsevier, 2013 (cit. on p. 5).
- [24] M. e. a. Bellec, 'Topological transition of dirac points in a microwave experiment,' *Phys. Rev. Lett.*, vol. 110, no. 3, p. 033902, Jan. 2013. doi: [10.1103/PhysRevLett.110.033902](https://doi.org/10.1103/PhysRevLett.110.033902). (cit. on p. 5).
- [25] M. Hafezi et al., 'Robust optical delay lines with topological protection,' *Nature Physics*, vol. 7, no. 11, pp. 907–912, 2011. doi: [10.1038/nphys2063](https://doi.org/10.1038/nphys2063) (cit. on p. 5).
- [26] P. Senellart et al., 'High-performance semiconductor quantum-dot single-photon sources,' *Nature Nanotechnology*, vol. 12, no. 11, pp. 1026–1039, 2017. doi: [10.1038/nnano.2017.218](https://doi.org/10.1038/nnano.2017.218) (cit. on p. 5).
- [27] T. Jacqmin et al., 'Direct observation of dirac cones and a flatband in a honeycomb lattice for polaritons,' *Physical review letters*, vol. 112, no. 11, p. 116402, 2014. doi: [10.1103/PhysRevLett.112.116402](https://doi.org/10.1103/PhysRevLett.112.116402) (cit. on p. 5).
- [28] N. Cooper et al., 'Topological bands for ultracold atoms,' *Reviews of modern physics*, vol. 91, no. 1, p. 015005, 2019. doi: [10.1103/RevModPhys.91.015005](https://doi.org/10.1103/RevModPhys.91.015005) (cit. on p. 5).
- [29] T. Ozawa et al., 'Topological photonics,' *Reviews of Modern Physics*, vol. 91, no. 1, p. 015006, 2019. doi: [10.1103/RevModPhys.91.015006](https://doi.org/10.1103/RevModPhys.91.015006) (cit. on p. 5).
- [30] G. Ma et al., 'Topological phases in acoustic and mechanical systems,' *Nature Reviews Physics*, vol. 1, no. 4, pp. 281–294, 2019. doi: [10.1038/s42254-019-0030-x](https://doi.org/10.1038/s42254-019-0030-x) (cit. on p. 5).
- [31] R. Süsstrunk et al., 'Classification of topological phonons in linear mechanical metamaterials,' *Proceedings of the National Academy of Sciences*, vol. 113, no. 33, E4767–E4775, 2016. doi: [10.1073/pnas.1605462113](https://doi.org/10.1073/pnas.1605462113) (cit. on p. 5).
- [32] S. O. Kasap, *Electronic materials and Devices*. McGraw-Hill New York, 2006 (cit. on p. 5).
- [33] I. L. Garanovich et al., 'Light propagation and localization in modulated photonic lattices and waveguides,' *Physics Reports*, vol. 518, no. 1, pp. 1–79, 2012, issn: 0370-1573. doi: [10.1016/j.physrep.2012.03.005](https://doi.org/10.1016/j.physrep.2012.03.005) (cit. on p. 5).
- [34] R. Morandotti et al., 'Experimental observation of linear and nonlinear optical bloch oscillations,' *Phys. Rev. Lett.*, vol. 83, no. 23, pp. 4756–4759, Dec. 1999. doi: [10.1103/PhysRevLett.83.4756](https://doi.org/10.1103/PhysRevLett.83.4756) (cit. on p. 5).

- [35] T. Pertsch et al., 'Optical bloch oscillations in temperature tuned waveguide arrays,' *Phys. Rev. Lett.*, vol. 83, no. 23, pp. 4752–4755, Dec. 1999. DOI: [10.1103/PhysRevLett.83.4752](https://doi.org/10.1103/PhysRevLett.83.4752) (cit. on p. 5).
- [36] K. Shandarova et al., 'Experimental observation of rabi oscillations in photonic lattices,' *Physical review letters*, vol. 102, no. 12, p. 123905, 2009. DOI: [10.1103/PhysRevLett.102.123905](https://doi.org/10.1103/PhysRevLett.102.123905) (cit. on p. 5).
- [37] Y. Lahini et al., 'Anderson localization and nonlinearity in one-dimensional disordered photonic lattices,' *Physical Review Letters*, vol. 100, no. 1, p. 013906, 2008. DOI: [10.1103/PhysRevLett.100.013906](https://doi.org/10.1103/PhysRevLett.100.013906) (cit. on p. 5).
- [38] K. Staliunas et al., 'Subdiffractive light in bi-periodic arrays of modulated fibers,' *Optics Express*, vol. 14, no. 22, pp. 10669–10677, 2006. DOI: [10.1364/OE.14.010669](https://doi.org/10.1364/OE.14.010669) (cit. on p. 5).
- [39] H. Eisenberg et al., 'Discrete spatial optical solitons in waveguide arrays,' *Physical Review Letters*, vol. 81, no. 16, p. 3383, 1998. DOI: [10.1103/PhysRevLett.81.3383](https://doi.org/10.1103/PhysRevLett.81.3383) (cit. on pp. 5, 6).
- [40] A. Dutt et al., 'Experimental band structure spectroscopy along a synthetic dimension,' *Nature communications*, vol. 10, no. 1, p. 3122, 2019. DOI: [10.1038/s41467-019-11117-9](https://doi.org/10.1038/s41467-019-11117-9) (cit. on p. 5).
- [41] D. N. Christodoulides et al., 'Discretizing light behaviour in linear and nonlinear waveguide lattices,' *Nature*, vol. 424, no. 6950, pp. 817–823, 2003. DOI: [10.1038/nature01936](https://doi.org/10.1038/nature01936) (cit. on pp. 5, 6).
- [42] T. Kitagawa et al., 'Observation of topologically protected bound states in a one dimensional photonic system,' *arXiv preprint arXiv:1105.5334*, 2011. DOI: [10.1038/ncomms1872](https://doi.org/10.1038/ncomms1872) (cit. on pp. 5, 14).
- [43] A. Boudrioua, 'Comprendre les structures guidantes,' *Photoniques*, no. 98, pp. 39–43, 2019. DOI: [10.1051/photon/20199839](https://doi.org/10.1051/photon/20199839) (cit. on p. 6).
- [44] A. Yariv, 'Coupled-mode theory for guided-wave optics,' *IEEE Journal of Quantum Electronics*, vol. 9, no. 9, pp. 919–933, 1973. DOI: [10.1109/JQE.1973.1077767](https://doi.org/10.1109/JQE.1973.1077767) (cit. on p. 6).
- [45] H. S. Eisenberg et al., 'Diffraction management,' *Phys. Rev. Lett.*, vol. 85, pp. 1863–1866, 9 Aug. 2000. DOI: [10.1103/PhysRevLett.85.1863](https://doi.org/10.1103/PhysRevLett.85.1863). (cit. on p. 6).
- [46] A. Szameit et al., 'Discrete optics in femtosecond laser written waveguide arrays,' in *Femtosecond Laser Micromachining*, Springer, 2011, pp. 351–388. DOI: [10.1007/978-3-642-23366-1_13](https://doi.org/10.1007/978-3-642-23366-1_13) (cit. on p. 6).
- [47] J. W. Fleischer et al., 'Spatial photonics in nonlinear waveguide arrays,' *Optics express*, vol. 13, no. 6, pp. 1780–1796, 2005. DOI: [10.1364/OPEX.13.001780](https://doi.org/10.1364/OPEX.13.001780) (cit. on p. 6).
- [48] A. Szameit et al., 'Discrete optics in femtosecond-laser-written photonic structures,' *Journal of Physics B: Atomic, Molecular and Optical Physics*, vol. 43, no. 16, p. 163001, 2010. DOI: [10.1088/0953-4075/43/16/163001](https://doi.org/10.1088/0953-4075/43/16/163001) (cit. on pp. 6, 7).
- [49] J. Vasiljević, 'Propagation, localization, and control of light in mathieu lattices,' Ph.D. dissertation, Univerzitet u Beogradu-Fizički fakultet, 2020 (cit. on p. 6).
- [50] S. Somekh et al., 'Channel optical waveguide directional couplers,' *Applied Physics Letters*, vol. 22, no. 1, pp. 46–47, Jan. 1973, ISSN: 0003-6951. DOI: [10.1063/1.1654468](https://doi.org/10.1063/1.1654468). eprint: [https://pubs.aip.org/aip/apl/article-pdf/22/1/46/18427152/46_1_online.pdf](https://pubs.aip.org/aip/apl/article-pdf/22/1/46/18427152/46%20_1_online.pdf). (cit. on p. 7).
- [51] H. Haus et al., 'Coupled multiple waveguide systems,' *IEEE Journal of Quantum Electronics*, vol. 19, no. 5, pp. 840–844, 1983. DOI: [10.1109/JQE.1983.1071950](https://doi.org/10.1109/JQE.1983.1071950) (cit. on p. 7).
- [52] A. L. Jones, 'Coupling of optical fibers and scattering in fibers,' *JOSA*, vol. 55, no. 3, pp. 261–271, 1965. DOI: [10.1364/JOSA.55.000261](https://doi.org/10.1364/JOSA.55.000261) (cit. on p. 7).

- [53] F. Lederer et al., 'Discrete solitons in optics,' *Physics Reports*, vol. 463, no. 1-3, pp. 1–126, 2008. doi: [10.1016/j.physrep.2008.04.004](https://doi.org/10.1016/j.physrep.2008.04.004) (cit. on p. 7).
- [54] D. Christodoulides et al., 'Discrete self-focusing in nonlinear arrays of coupled waveguides,' *Optics letters*, vol. 13, no. 9, pp. 794–796, 1988. doi: [10.1364/OL.13.000794](https://doi.org/10.1364/OL.13.000794) (cit. on p. 7).
- [55] J. Zak, 'Berry's phase for energy bands in solids,' *Phys. Rev. Lett.*, vol. 62, pp. 2747–2750, 23 Jun. 1989. doi: [10.1103/PhysRevLett.62.2747](https://doi.org/10.1103/PhysRevLett.62.2747) (cit. on p. 8).
- [56] A. Lyapunov, 'Sur une serie relative a la theorie des equations differentielles lineaires a coefficients periodiques,' *Compt. Rend*, vol. 123, no. 26, pp. 1248–1252, 1896. doi: [10.24033/asens.220](https://doi.org/10.24033/asens.220) (cit. on p. 8).
- [57] F. Bloch, 'Quantum mechanics of electrons in crystal lattices,' *Z. Phys*, vol. 52, pp. 555–600, 1928, <http://www.jstor.org/stable/95691> (cit. on p. 8).
- [58] G. Floquet, 'Sur les équations différentielles linéaires à coefficients périodiques,' <http://eudml.org/doc/80895>, vol. 12, 1883, pp. 47–88 (cit. on p. 9).
- [59] G. W. Hill, 'On the part of the motion of the lunar perigee which is a function of the mean motions of the sun and moon,' 1886, <https://ui.adsabs.harvard.edu/abs/1877opml.book....H> (cit. on p. 9).
- [60] F. H. M. Faisal et al., 'Floquet-bloch theory of high-harmonic generation in periodic structures,' *Phys. Rev. A*, vol. 56, pp. 748–762, 1 Jul. 1997. doi: [10.1103/PhysRevA.56.748](https://doi.org/10.1103/PhysRevA.56.748). (cit. on p. 9).
- [61] L. Lu et al., 'Topological photonics,' *Nature Photonics*, vol. 8, no. 11, pp. 821–829, Oct. 2014, Publisher: Nature Publishing Group, a division of Macmillan Publishers Limited. All Rights Reserved., ISSN: 1749-4885. doi: [10.1038/nphoton.2014.248](https://doi.org/10.1038/nphoton.2014.248). (visited on 01/10/2015) (cit. on p. 10).
- [62] J. Dalibard, 'La matière topologique et son exploration avec les gaz quantiques,' <https://hal.science/hal-03746131>, Ph.D. dissertation, Collège de France, France, 2018 (cit. on p. 10).
- [63] J. E. Avron et al., 'A topological look at the quantum hall effect,' *Physics Today*, vol. 56, no. 8, pp. 38–42, 2003. doi: [10.1063/1.1611351](https://doi.org/10.1063/1.1611351). (cit. on p. 10).
- [64] C. L. Kane et al., 'Quantum spin hall effect in graphene,' *Physical Review Letters*, vol. 95, no. 22, p. 226 801, 2005. doi: [10.1103/PhysRevLett.95.226801](https://doi.org/10.1103/PhysRevLett.95.226801) (cit. on p. 11).
- [65] M. Z. Hasan et al., 'Colloquium: Topological insulators,' *Rev. Mod. Phys.*, vol. 82, no. 4, pp. 3045–3067, Nov. 2010, ISSN: 0034-6861. doi: [10.1103/RevModPhys.82.3045](https://doi.org/10.1103/RevModPhys.82.3045). (visited on 11/07/2014) (cit. on p. 11).
- [66] K. von Klitzing, 'Essay: Quantum hall effect and the new international system of units,' *Phys. Rev. Lett.*, vol. 122, p. 200 001, 20 May 2019. doi: [10.1103/PhysRevLett.122.200001](https://doi.org/10.1103/PhysRevLett.122.200001). (cit. on p. 11).
- [67] L. Li et al., 'Topological phases of generalized Su-Schrieffer-Heeger models,' *Phys. Rev. B*, vol. 89, no. 8, p. 085 111, Feb. 2014. doi: [10.1103/PhysRevB.89.085111](https://doi.org/10.1103/PhysRevB.89.085111). (cit. on p. 11).
- [68] H. Zhao et al., 'Two-dimensional materials for nanophotonics application,' *Nanophotonics*, vol. 4, no. 2, pp. 128–142, 2015. doi: [doi:10.1515/nanoph-2014-0022](https://doi.org/10.1515/nanoph-2014-0022). (cit. on p. 11).
- [69] J. Bardeen et al., 'Theory of superconductivity,' *Physical Review*, vol. 108, no. 5, pp. 1175–1204, 1957. doi: [10.1103/PhysRev.108.1175](https://doi.org/10.1103/PhysRev.108.1175) (cit. on p. 11).
- [70] D. Xiao et al., 'Berry phase effects on electronic properties,' *Rev. Mod. Phys.*, vol. 82, pp. 1959–2007, 3 Jul. 2010. doi: [10.1103/RevModPhys.82.1959](https://doi.org/10.1103/RevModPhys.82.1959). (cit. on p. 11).
- [71] A. Dixon, '23 - review of solid state physics,' in *Solar Energy Conversion*, A. DIXON et al., Eds., Pergamon, 1979, pp. 773–784, ISBN: 978-0-08-024744-1. doi: <https://doi.org/10.1016/B978-0-08-024744-1.50028-0> (cit. on p. 11).

- [72] C. Kittel, *Introduction to Solid State Physics*, 8th. Wiley, 2005. doi: [10.1002/0471238961](https://doi.org/10.1002/0471238961) (cit. on p. 11).
- [73] Z. Gong et al., 'Topological Phases of Non-Hermitian Systems,' *Phys. Rev. X*, vol. 8, no. 3, p. 031079, Sep. 2018. doi: [10.1103/PhysRevX.8.031079](https://doi.org/10.1103/PhysRevX.8.031079). (cit. on p. 11).
- [74] N. H. Lindner et al., 'Floquet topological insulator in semiconductor quantum wells,' *Nat. Phys.*, vol. 7, no. 6, pp. 490–495, Jun. 2011, issn: 1745-2481. doi: [10.1038/nphys1926](https://doi.org/10.1038/nphys1926). (cit. on p. 11).
- [75] A. Gómez-León et al., 'Floquet-Bloch Theory and Topology in Periodically Driven Lattices,' *Phys. Rev. Lett.*, vol. 110, no. 20, p. 200403, May 2013. doi: [10.1103/PhysRevLett.110.200403](https://doi.org/10.1103/PhysRevLett.110.200403). (cit. on p. 11).
- [76] F. Harper et al., 'Topology and Broken Symmetry in Floquet Systems,' *Annu. Rev. Condens. Matter Phys.*, vol. 11, no. 1, pp. 345–368, Mar. 2020, issn: 1947-5454, 1947-5462. doi: [10.1146/annurev-conmatphys-031218-013721](https://doi.org/10.1146/annurev-conmatphys-031218-013721). (visited on 02/04/2024) (cit. on p. 11).
- [77] M. S. Rudner et al., 'Anomalous edge states and the bulk-edge correspondence for periodically-driven two dimensional systems,' 2012, <https://arxiv.org/abs/1212.3324v2> (cit. on p. 12).
- [78] N. Mostaan et al., 'Quantized topological pumping of solitons in nonlinear photonics and ultracold atomic mixtures,' *nature communications*, vol. 13, no. 1, p. 5997, 2022. doi: [10.1038/s41467-022-33478-4](https://doi.org/10.1038/s41467-022-33478-4) (cit. on p. 13).
- [79] D. J. Thouless, 'Quantization of particle transport,' *Phys. Rev. B*, vol. 27, pp. 6083–6087, 10 May 1983. doi: [10.1103/PhysRevB.27.6083](https://doi.org/10.1103/PhysRevB.27.6083). (cit. on p. 13).
- [80] D. J. Thouless et al., 'Quantized hall conductance in a two-dimensional periodic potential,' *Phys. Rev. Lett.*, vol. 49, pp. 405–408, 6 Aug. 1982. doi: [10.1103/PhysRevLett.49.405](https://doi.org/10.1103/PhysRevLett.49.405). (cit. on p. 13).
- [81] M. C. Rechtsman et al., 'Photonic floquet topological insulators,' *Nature*, vol. 496, no. 7444, pp. 196–200, 2013. doi: [10.1038/nature12066](https://doi.org/10.1038/nature12066) (cit. on p. 13).
- [82] T. Kitagawa et al., 'Topological characterization of periodically driven quantum systems,' *Phys. Rev. B*, vol. 82, no. 23, p. 235114, Dec. 2010, issn: 1098-0121, 1550-235X. doi: [10.1103/PhysRevB.82.235114](https://doi.org/10.1103/PhysRevB.82.235114). (visited on 16/12/2021) (cit. on p. 14).
- [83] M. S. Rudner et al., 'Anomalous Edge States and the Bulk-Edge Correspondence for Periodically Driven Two-Dimensional Systems,' *Phys. Rev. X*, vol. 3, no. 3, p. 031005, Jul. 2013. doi: [10.1103/PhysRevX.3.031005](https://doi.org/10.1103/PhysRevX.3.031005). (cit. on pp. 14, 15, 95, 107, 124, 129).
- [84] Á. Gómez-León et al., 'Engineering anomalous quantum hall plateaus and antichiral states with ac fields,' *Phys. Rev. B*, vol. 89, p. 205408, 20 May 2014. doi: [10.1103/PhysRevB.89.205408](https://doi.org/10.1103/PhysRevB.89.205408). (cit. on p. 14).
- [85] F. Nathan et al., 'Topological singularities and the general classification of Floquet–Bloch systems,' *New J. Phys.*, vol. 17, no. 12, p. 125014, 2015, issn: 1367-2630. doi: [10.1088/1367-2630/17/12/125014](https://doi.org/10.1088/1367-2630/17/12/125014). (cit. on pp. 14, 15).
- [86] Y.-G. Peng et al., 'Experimental demonstration of anomalous Floquet topological insulator for sound,' *Nat Commun*, vol. 7, no. 1, p. 13368, Nov. 2016, Peng2016, issn: 2041-1723. doi: [10.1038/ncomms13368](https://doi.org/10.1038/ncomms13368). (visited on 02/04/2024) (cit. on p. 14).
- [87] Q. Cheng et al., 'Observation of Anomalous π Modes in Photonic Floquet Engineering,' *Phys. Rev. Lett.*, vol. 122, no. 17, p. 173901, May 2019, issn: 0031-9007, 1079-7114. doi: [10.1103/PhysRevLett.122.173901](https://doi.org/10.1103/PhysRevLett.122.173901). (visited on 02/04/2024) (cit. on p. 14).
- [88] S. Afzal et al., 'Realization of Anomalous Floquet Insulators in Strongly Coupled Nanophotonic Lattices,' *Phys. Rev. Lett.*, vol. 124, no. 25, p. 253601, Jun. 2020, issn: 0031-9007, 1079-7114. doi: [10.1103/PhysRevLett.124.253601](https://doi.org/10.1103/PhysRevLett.124.253601). (visited on 12/04/2022) (cit. on pp. 14, 15).

- [89] K. Wintersperger et al., ‘Realization of an anomalous Floquet topological system with ultracold atoms,’ *Nat. Phys.*, vol. 16, no. 10, pp. 1058–1063, Oct. 2020, ISSN: 1745-2473, 1745-2481. DOI: [10.1038/s41567-020-0949-y](https://doi.org/10.1038/s41567-020-0949-y). (visited on 05/01/2022) (cit. on pp. 14, 79, 87, 91).
- [90] Á. Gómez-León, *Floquet topological phases: A new perspective*, 2023 (cit. on p. 14).
- [91] J.-Y. Zhang et al., ‘Tuning Anomalous Floquet Topological Bands with Ultracold Atoms,’ *Phys. Rev. Lett.*, vol. 130, no. 4, p. 043201, Jan. 2023, ISSN: 0031-9007, 1079-7114. DOI: [10.1103/PhysRevLett.130.043201](https://doi.org/10.1103/PhysRevLett.130.043201). (visited on 02/04/2024) (cit. on p. 14).
- [92] C. Braun et al., ‘Real-space detection and manipulation of topological edge modes with ultracold atoms,’ *Nature Physics*, pp. 1–7, 2024. DOI: [10.1038/s41567-024-02506-z](https://doi.org/10.1038/s41567-024-02506-z) (cit. on p. 14).
- [93] F. Nathan et al., ‘Topological singularities and the general classification of floquet–bloch systems,’ *New Journal of Physics*, vol. 17, no. 12, p. 125014, Dec. 2015. DOI: [10.1088/1367-2630/17/12/125014](https://doi.org/10.1088/1367-2630/17/12/125014). (cit. on p. 14).
- [94] F. Cardano et al., ‘Detection of zak phases and topological invariants in a chiral quantum walk of twisted photons,’ *Nature communications*, vol. 8, no. 1, p. 15516, 2017. DOI: [10.1038/ncomms15516](https://doi.org/10.1038/ncomms15516) (cit. on p. 14).
- [95] M. Bellec et al., ‘Non-diffracting states in one-dimensional floquet photonic topological insulators,’ *Europhysics Letters*, vol. 119, no. 1, p. 14003, 2017. DOI: [10.1209/0295-5075/119/14003](https://doi.org/10.1209/0295-5075/119/14003) (cit. on p. 14).
- [96] M. S. Rudner et al., ‘Anomalous edge states and the bulk-edge correspondence for periodically driven two-dimensional systems,’ *Phys. Rev. X*, vol. 3, p. 031005, 3 Jul. 2013. DOI: [10.1103/PhysRevX.3.031005](https://doi.org/10.1103/PhysRevX.3.031005). (cit. on p. 14).
- [97] J. K. Asbóth et al., ‘Bulk-boundary correspondence for chiral symmetric quantum walks,’ *Phys. Rev. B*, vol. 88, 121406(R), 12 Sep. 2013. DOI: [10.1103/PhysRevB.88.121406](https://doi.org/10.1103/PhysRevB.88.121406). (cit. on p. 14).
- [98] C. Cedzich et al., ‘The Topological Classification of One-Dimensional Symmetric Quantum Walks,’ *Ann. Henri Poincaré*, vol. 19, no. 2, pp. 325–383, Feb. 2018, ISSN: 1424-0637, 1424-0661. DOI: [10.1007/s00023-017-0630-x](https://doi.org/10.1007/s00023-017-0630-x). (visited on 02/04/2024) (cit. on p. 14).
- [99] K. Mochizuki et al., ‘Topological quantum walk with discrete time-glide symmetry,’ *Phys. Rev. B*, vol. 102, p. 035418, 3 Jul. 2020. DOI: [10.1103/PhysRevB.102.035418](https://doi.org/10.1103/PhysRevB.102.035418). (cit. on p. 14).
- [100] A. Grudka et al., ‘Topological invariants in quantum walks,’ *Phys. Rev. A*, vol. 107, p. 032201, 3 Mar. 2023. DOI: [10.1103/PhysRevA.107.032201](https://doi.org/10.1103/PhysRevA.107.032201). (cit. on p. 14).
- [101] S. Mukherjee et al., ‘Observation of Floquet solitons in a topological bandgap,’ *Science*, vol. 368, no. 6493, 856 LP–859, May 2020. DOI: [10.1126/science.aba8725](https://doi.org/10.1126/science.aba8725). (cit. on p. 15).
- [102] M. Sebabrata et al., ‘Observation of unidirectional solitonlike edge states in nonlinear floquet topological insulators,’ *Phys. Rev. X*, vol. 11, p. 041057, 4 Dec. 2021. DOI: [10.1103/PhysRevX.11.041057](https://doi.org/10.1103/PhysRevX.11.041057) (cit. on p. 15).
- [103] F. Galton, *Natural inheritance*. Macmillan, 1889, vol. 42 (cit. on pp. 15, 16).
- [104] J. Kempe, ‘Quantum random walks: An introductory overview,’ *Contemporary Physics*, vol. 44, no. 4, pp. 307–327, 2003. DOI: [10.1080/00107510902734722](https://doi.org/10.1080/00107510902734722) (cit. on pp. 15, 16).
- [105] H. C. Berg, *Random walks in biology*. Princeton University Press, 1993 (cit. on p. 15).
- [106] D. Bouwmeester et al., ‘Optical galton board,’ *Phys. Rev. A*, vol. 61, p. 013410, 1 Dec. 1999. DOI: [10.1103/PhysRevA.61.013410](https://doi.org/10.1103/PhysRevA.61.013410). (cit. on pp. 15, 16).
- [107] M. Wimmer, ‘Experiments on photonic mesh lattices,’ <https://open.fau.de/handle/openfau/10213>, Ph.D. dissertation, Friedrich-Alexander-Universität Erlangen-Nürnberg (FAU), 2018 (cit. on pp. 16, 17).

- [108] S. E. Venegas-Andraca, 'Quantum walks: A comprehensive review,' *Quantum Information Processing*, vol. 11, no. 5, pp. 1015–1106, 2012 (cit. on p. 16).
- [109] A. Regensburger et al., 'Photon propagation in a discrete fiber network: An interplay of coherence and losses,' *Phys. Rev. Lett.*, vol. 107, p. 233902, 23 Dec. 2011. doi: [10.1103/PhysRevLett.107.233902](https://doi.org/10.1103/PhysRevLett.107.233902). (cit. on p. 16).
- [110] S. Sang-Ngern et al., 'Electronic feedback system for stabilization of fiber ring resonator,' *ETRI journal*, vol. 32, no. 1, pp. 53–61, 2010. doi: [10.4218/etrij.10.0109.0320](https://doi.org/10.4218/etrij.10.0109.0320) (cit. on p. 16).
- [111] A. Schreiber, *Quantum walks in time*. Friedrich-Alexander-Universitaet Erlangen-Nuernberg (Germany), 2013 (cit. on p. 16).
- [112] A. Schreiber et al., 'Decoherence and disorder in quantum walks: From ballistic spread to localization,' *Phys. Rev. Lett.*, vol. 106, p. 180403, 18 May 2011. doi: [10.1103/PhysRevLett.106.180403](https://doi.org/10.1103/PhysRevLett.106.180403). (cit. on p. 16).
- [113] A. Schreiber et al., 'Photons walking the line: A quantum walk with adjustable coin operations,' *Phys. Rev. Lett.*, vol. 104, p. 050502, 5 Feb. 2010. doi: [10.1103/PhysRevLett.104.050502](https://doi.org/10.1103/PhysRevLett.104.050502). (cit. on p. 16).
- [114] A. Schreiber et al., 'A 2d quantum walk simulation of two-particle dynamics,' *Science*, vol. 336, no. 6077, pp. 55–58, 2012. doi: [10.1126/science.1218448](https://doi.org/10.1126/science.1218448) (cit. on p. 16).
- [115] A. Regensburger et al., 'Photon propagation in a discrete fiber network: An interplay of coherence and losses,' *Phys. Rev. Lett.*, vol. 107, p. 233902, 23 Dec. 2011. doi: [10.1103/PhysRevLett.107.233902](https://doi.org/10.1103/PhysRevLett.107.233902). (cit. on pp. 16, 17, 21).
- [116] A. Regensburger et al., 'Parity–time synthetic photonic lattices,' *Nature*, vol. 488, no. 7410, pp. 167–171, 2012. doi: [10.1038/nature11298](https://doi.org/10.1038/nature11298). (cit. on p. 17).
- [117] A. Bisianov et al., 'Stability of topologically protected edge states in nonlinear fiber loops,' *Phys. Rev. A*, vol. 100, p. 063830, 6 Dec. 2019. doi: [10.1103/PhysRevA.100.063830](https://doi.org/10.1103/PhysRevA.100.063830). (cit. on p. 18).
- [118] C. Lechevalier et al., 'Single-shot measurement of the photonic band structure in a fiber-based Floquet-Bloch lattice,' *Commun. Phys.*, vol. 4, no. 1, p. 243, Dec. 2021, issn: 2399-3650. doi: [10.1038/s42005-021-00750-w](https://doi.org/10.1038/s42005-021-00750-w). (visited on 21/11/2021) (cit. on pp. 21, 24, 28, 42, 47, 52, 65, 77, 129).
- [119] M. Wimmer, *Experiments on Photonic Mesh Lattices*, 2018 (cit. on p. 21).
- [120] M. Wimmer et al., 'Experimental measurement of the berry curvature from anomalous transport,' *Nature Physics*, vol. 13, no. 6, pp. 545–550, 2017. doi: [10.1038/nphys4050](https://doi.org/10.1038/nphys4050) (cit. on pp. 21, 40, 41, 129).
- [121] A. F. Adiyatullin et al., 'Topological properties of floquet winding bands in a photonic lattice,' *Phys. Rev. Lett.*, vol. 130, p. 056901, 5 Feb. 2023. doi: [10.1103/PhysRevLett.130.056901](https://doi.org/10.1103/PhysRevLett.130.056901). (cit. on pp. 21, 40, 47, 55, 108).
- [122] M. Wimmer et al., 'Experimental measurement of the berry curvature from anomalous transport,' *Nature Physics*, vol. 13, no. 6, pp. 545–550, 2017. doi: <https://doi-org.ressources-electroniques.univ-lille.fr/10.1038/nphys4050> (cit. on p. 28).
- [123] S. Weidemann et al., 'Topological funneling of light,' *Science*, vol. 368, no. 6488, pp. 311–314, Apr. 2020. doi: [10.1126/science.aaz8727](https://doi.org/10.1126/science.aaz8727). (cit. on p. 28).
- [124] T. Jacqmin et al., 'Direct Observation of Dirac Cones and a Flatband in a Honeycomb Lattice for Polaritons,' *Phys. Rev. Lett.*, vol. 112, no. 11, p. 116402, 2014. doi: [10.1103/PhysRevLett.112.116402](https://doi.org/10.1103/PhysRevLett.112.116402). (cit. on p. 32).
- [125] M. Wimmer et al., 'Observation of optical solitons in pt-symmetric lattices,' *Nature communications*, vol. 6, no. 1, p. 7782, 2015. doi: [10.1038/ncomms8782](https://doi.org/10.1038/ncomms8782) (cit. on p. 40).

- [126] A. L. M. Muniz et al., ‘2d solitons in \mathcal{PT} -symmetric photonic lattices,’ *Phys. Rev. Lett.*, vol. 123, p. 253 903, 25 Dec. 2019. doi: [10.1103/PhysRevLett.123.253903](https://doi.org/10.1103/PhysRevLett.123.253903). (cit. on p. 40).
- [127] M. Wimmer et al., ‘Observation of bloch oscillations in complex pt-symmetric photonic lattices,’ *Scientific reports*, vol. 5, no. 1, p. 17760, 2015. doi: [10.1038/srep17760](https://doi.org/10.1038/srep17760) (cit. on p. 40).
- [128] H. Chalabi et al., ‘Synthetic gauge field for two-dimensional time-multiplexed quantum random walks,’ *Physical Review Letters*, vol. 123, no. 15, p. 150 503, 2019. doi: [10.1103/PhysRevLett.123.150503](https://doi.org/10.1103/PhysRevLett.123.150503) (cit. on p. 40).
- [129] S. Weidemann et al., ‘Topological funneling of light,’ *Science*, vol. 368, no. 6488, pp. 311–314, 2020. doi: [10.1126/science.aaz8727](https://doi.org/10.1126/science.aaz8727). (cit. on pp. 40, 43).
- [130] M. Wimmer et al., ‘Superfluidity of light and its breakdown in optical mesh lattices,’ *Phys. Rev. Lett.*, vol. 127, p. 163 901, 16 Oct. 2021. doi: [10.1103/PhysRevLett.127.163901](https://doi.org/10.1103/PhysRevLett.127.163901). (cit. on p. 40).
- [131] M. Wimmer et al., ‘Optical diametric drive acceleration through action–reaction symmetry breaking,’ *Nature Physics*, vol. 9, no. 12, pp. 780–784, 2013. doi: [10.1038/nphys2777](https://doi.org/10.1038/nphys2777) (cit. on p. 40).
- [132] C. H. Lee et al., ‘Anatomy of skin modes and topology in non-hermitian systems,’ *Phys. Rev. B*, vol. 99, p. 201 103, 20 May 2019. doi: [10.1103/PhysRevB.99.201103](https://doi.org/10.1103/PhysRevB.99.201103). (cit. on p. 43).
- [133] S. Yao et al., ‘Edge states and topological invariants of non-hermitian systems,’ *Phys. Rev. Lett.*, vol. 121, p. 086 803, 8 Aug. 2018. doi: [10.1103/PhysRevLett.121.086803](https://doi.org/10.1103/PhysRevLett.121.086803). (cit. on p. 43).
- [134] W. P. Su et al., ‘Solitons in polyacetylene,’ *Phys. Rev. Lett.*, vol. 42, pp. 1698–1701, 25 Jun. 1979. doi: [10.1103/PhysRevLett.42.1698](https://doi.org/10.1103/PhysRevLett.42.1698). (cit. on p. 44).
- [135] J. K. Asbóth et al., *A Short Course on Topological Insulators*. 2015, <https://doi.org/10.1007/978-3-319-25607-8> (cit. on p. 44).
- [136] E. Udd et al., *Fiber optic sensors: an introduction for engineers and scientists*. John Wiley & Sons, 2024 (cit. on p. 50).
- [137] G. Keiser, *Optical Fiber Communications*, 4th. McGraw-Hill, 2011 (cit. on p. 51).
- [138] G. N. Watson, *A treatise on the theory of Bessel functions*. The University Press, 1922, vol. 2 (cit. on p. 52).
- [139] G. Hernández, *Fabry-perot interferometers*, 3. Cambridge University Press, 1988 (cit. on p. 54).
- [140] A. Regensburger et al., ‘Photon propagation in a discrete fiber network: An interplay of coherence and losses,’ *Phys. Rev. Lett.*, vol. 107, p. 233 902, 23 Dec. 2011. doi: [10.1103/PhysRevLett.107.233902](https://doi.org/10.1103/PhysRevLett.107.233902). (cit. on p. 61).
- [141] K. Şafak et al., ‘All fiber-coupled, long-term stable timing distribution for free-electron lasers with few-femtosecond jitter,’ *Structural Dynamics*, vol. 2, no. 4, p. 041 715, Jun. 2015. doi: [10.1063/1.4922747](https://doi.org/10.1063/1.4922747) (cit. on p. 62).
- [142] X. Chen et al., ‘Optical fiber sensor with stable operating point for ac magnetic field measurement,’ *Applied Sciences*, vol. 12, no. 14, 2022, issn: 2076-3417. doi: [10.3390/app12147049](https://doi.org/10.3390/app12147049). (cit. on p. 62).
- [143] A. M. Tikan et al., ‘Deriving eigenmode excitation spectrum of synthetic photonic lattices by means of optical heterodyning,’ *Laser Physics*, vol. 27, no. 2, p. 026 203, Jan. 2017. doi: [10.1088/1555-6611/aa4f59](https://doi.org/10.1088/1555-6611/aa4f59). (cit. on pp. 65, 77).
- [144] M. Atala et al., ‘Direct measurement of the Zak phase in topological Bloch bands,’ *Nat. Phys.*, vol. 9, no. 12, pp. 795–800, Nov. 2013, Publisher: Nature Research, issn: 1745-2473. doi: [10.1038/nphys2790](https://doi.org/10.1038/nphys2790). (visited on 01/03/2017) (cit. on p. 79).

- [145] F. Pellerin et al., 'Wave-function tomography of topological dimer chains with long-range couplings,' *Phys. Rev. Lett.*, vol. 132, p. 183 802, 18 May 2024. doi: [10.1103/PhysRevLett.132.183802](https://doi.org/10.1103/PhysRevLett.132.183802). (cit. on p. 79).
- [146] F. Cardano et al., 'Detection of Zak phases and topological invariants in a chiral quantum walk of twisted photons,' *Nat. Commun.*, vol. 8, p. 15 516, Jun. 2017, Publisher: Nature Publishing Group, ISSN: 2041-1723. doi: [10.1038/ncomms15516](https://doi.org/10.1038/ncomms15516). (visited on 21/11/2017) (cit. on p. 79).
- [147] Z.-Q. Jiao et al., 'Experimentally Detecting Quantized Zak Phases without Chiral Symmetry in Photonic Lattices,' *Phys. Rev. Lett.*, vol. 127, no. 14, p. 147 401, Sep. 2021, ISSN: 0031-9007, 1079-7114. doi: [10.1103/PhysRevLett.127.147401](https://doi.org/10.1103/PhysRevLett.127.147401). (visited on 26/10/2021) (cit. on p. 79).
- [148] P. St-Jean et al., 'Measuring Topological Invariants in a Polaritonic Analog of Graphene,' *Phys. Rev. Lett.*, vol. 126, no. 12, p. 127 403, Mar. 2021, ISSN: 0031-9007, 1079-7114. doi: [10.1103/PhysRevLett.126.127403](https://doi.org/10.1103/PhysRevLett.126.127403). (visited on 25/03/2021) (cit. on p. 79).
- [149] M. Aidelsburger et al., 'Measuring the Chern number of Hofstadter bands with ultracold bosonic atoms,' *Nature Physics*, vol. 11, pp. 162–166, 2015, Publisher: Nature Publishing Group. (cit. on p. 79).
- [150] M. Wimmer et al., 'Experimental measurement of the Berry curvature from anomalous transport,' *Nature Physics*, vol. 13, p. 545, Feb. 2017, Publisher: Nature Publishing Group. (cit. on p. 79).
- [151] C. Chen et al., 'Berry Curvature and Bulk-Boundary Correspondence from Transport Measurement for Photonic Chern Bands,' *Phys. Rev. Lett.*, vol. 131, no. 13, p. 133 601, Sep. 2023, ISSN: 0031-9007, 1079-7114. doi: [10.1103/PhysRevLett.131.133601](https://doi.org/10.1103/PhysRevLett.131.133601). (visited on 26/10/2023) (cit. on p. 79).
- [152] R. Skomski et al., 'Nonadiabatic Berry phase in nanocrystalline magnets,' *AIP Advances*, vol. 7, no. 5, p. 055 802, Dec. 2016, ISSN: 2158-3226. doi: [10.1063/1.4972804](https://doi.org/10.1063/1.4972804). (cit. on p. 79).
- [153] L. D. M. Peters et al., 'Berry population analysis: Atomic charges from the berry curvature in a magnetic field,' *Journal of Chemical Theory and Computation*, vol. 19, no. 4, pp. 1231–1242, 2023. doi: [10.1021/acs.jctc.2c01138](https://doi.org/10.1021/acs.jctc.2c01138) (cit. on p. 79).
- [154] M. Blanco de Paz et al., 'Tutorial: Computing topological invariants in 2d photonic crystals,' *Advanced Quantum Technologies*, vol. 3, no. 2, p. 1 900 117, 2020. doi: <https://doi.org/10.1002/qute.201900117>. (cit. on p. 80).
- [155] D. Thouless et al., 'Quantized Hall Conductance in a Two-Dimensional Periodic Potential,' *Phys. Rev. Lett.*, vol. 49, no. 6, pp. 405–408, Aug. 1982, ISSN: 0031-9007. doi: [10.1103/PhysRevLett.49.405](https://doi.org/10.1103/PhysRevLett.49.405). (visited on 10/01/2015) (cit. on p. 80).
- [156] Y. Hatsugai, 'Chern number and edge states in the integer quantum Hall effect,' *Phys. Rev. Lett.*, vol. 71, no. 22, pp. 3697–3700, Nov. 1993, Publisher: American Physical Society. doi: [10.1103/PhysRevLett.71.3697](https://doi.org/10.1103/PhysRevLett.71.3697). (cit. on p. 80).
- [157] C. L. Kane et al., 'Z₂ Topological Order and the Quantum Spin Hall Effect,' *Phys. Rev. Lett.*, vol. 95, no. 14, p. 146 802, Sep. 2005, ISSN: 0031-9007, 1079-7114. doi: [10.1103/PhysRevLett.95.146802](https://doi.org/10.1103/PhysRevLett.95.146802). (visited on 16/12/2021) (cit. on p. 80).
- [158] B. A. Bernevig et al., 'Quantum Spin Hall Effect and Topological Phase Transition in HgTe Quantum Wells,' *Science*, vol. 314, p. 1757, 2006. (cit. on p. 80).
- [159] F. N. Ünal et al., 'How to Directly Measure Floquet Topological Invariants in Optical Lattices,' *Phys. Rev. Lett.*, vol. 122, no. 25, p. 253 601, Jun. 2019, ISSN: 0031-9007, 1079-7114. doi: [10.1103/PhysRevLett.122.253601](https://doi.org/10.1103/PhysRevLett.122.253601). (visited on 27/05/2022) (cit. on p. 87).
- [160] A. F. Adiyatullin et al., 'Topological Properties of Floquet Winding Bands in a Photonic Lattice,' *Phys. Rev. Lett.*, vol. 130, no. 5, p. 056 901, Feb. 2023, ISSN: 0031-9007, 1079-7114. doi: [10.1103/PhysRevLett.130.056901](https://doi.org/10.1103/PhysRevLett.130.056901). (visited on 04/02/2023) (cit. on p. 91).

- [161] P. Delplace et al., 'Phase rotation symmetry and the topology of oriented scattering networks,' *Phys. Rev. B*, vol. 95, p. 205413, 20 May 2017. DOI: [10.1103/PhysRevB.95.205413](https://doi.org/10.1103/PhysRevB.95.205413). (cit. on p. 95).
- [162] P. Delplace, 'Topological chiral modes in random scattering networks,' *SciPost Phys.*, vol. 8, no. 5, p. 081, May 2020, ISSN: 2542-4653. DOI: [10.21468/SciPostPhys.8.5.081](https://doi.org/10.21468/SciPostPhys.8.5.081). (visited on 27/12/2020) (cit. on p. 95).
- [163] A. Altland et al., 'Nonstandard symmetry classes in mesoscopic normal-superconducting hybrid structures,' *Phys. Rev. B*, vol. 55, pp. 1142–1161, 2 Jan. 1997. DOI: [10.1103/PhysRevB.55.1142](https://doi.org/10.1103/PhysRevB.55.1142). (cit. on p. 98).
- [164] S. Ryu et al., 'Topological insulators and superconductors: Tenfold way and dimensional hierarchy,' *New J. Phys.*, vol. 12, no. 6, p. 065010, Jun. 2010. DOI: [10.1088/1367-2630/12/6/065010](https://doi.org/10.1088/1367-2630/12/6/065010). (cit. on p. 98).
- [165] P. Delplace et al., 'Zak phase and the existence of edge states in graphene,' *Phys. Rev. B*, vol. 84, no. 19, p. 195452, Nov. 2011, ISSN: 1098-0121. DOI: [10.1103/PhysRevB.84.195452](https://doi.org/10.1103/PhysRevB.84.195452). (visited on 06/01/2015) (cit. on pp. 103, 104).
- [166] B. Pérez-González et al., 'Interplay between long-range hopping and disorder in topological systems,' *Phys. Rev. B*, vol. 99, no. 3, p. 035146, 2019, ISSN: 2469-9950, 2469-9969. DOI: [10.1103/PhysRevB.99.035146](https://doi.org/10.1103/PhysRevB.99.035146). (cit. on p. 103).
- [167] B. A. Bernevig et al., Topological Insulators and Topological Superconductors. Princeton University Press, 2013 (cit. on p. 103).
- [168] L. Jezequel et al., 'Estimating bulk and edge topological indices in finite open chiral chains,' *J. Math. Phys.*, vol. 63, no. 12, p. 121901, Dec. 2022, ISSN: 0022-2488. DOI: [10.1063/5.0096720](https://doi.org/10.1063/5.0096720). (cit. on p. 104).
- [169] T. Bessho et al., 'Nielsen-ninomiya theorem with bulk topology: Duality in floquet and non-hermitian systems,' *Phys. Rev. Lett.*, vol. 127, p. 196404, 19 Nov. 2021. DOI: [10.1103/PhysRevLett.127.196404](https://doi.org/10.1103/PhysRevLett.127.196404). (cit. on pp. 104, 105).
- [170] A. L. M. Muniz et al., '2d solitons in \mathcal{PT} -symmetric photonic lattices,' *Phys. Rev. Lett.*, vol. 123, p. 253903, 25 Dec. 2019. DOI: [10.1103/PhysRevLett.123.253903](https://doi.org/10.1103/PhysRevLett.123.253903). (cit. on pp. 131, 171).
- [171] L. M. M. André et al., 'Collapse on the line – how synthetic dimensions influence nonlinear effects,' *Scientific Reports*, vol. 9, no. 1, p. 9518, Jul. 2019, ISSN: 2045-2322. DOI: [10.1038/s41598-019-46060-8](https://doi.org/10.1038/s41598-019-46060-8) (cit. on p. 131).
- [172] M. A. Nielsen et al., Quantum computation and quantum information. Cambridge university press, 2010 (cit. on p. 160).
- [173] D. Damanik et al., 'The fractal dimension of the spectrum of the fibonacci hamiltonian,' *Communications in Mathematical Physics*, vol. 280, no. 2, pp. 499–516, 2008. DOI: [10.1007/s00220-008-0451-3](https://doi.org/10.1007/s00220-008-0451-3) (cit. on p. 163).
- [174] F. Baboux et al., 'Measuring topological invariants from generalized edge states in polaritonic quasicrystals,' *Phys. Rev. B*, vol. 95, p. 161114, 16 Apr. 2017. DOI: [10.1103/PhysRevB.95.161114](https://doi.org/10.1103/PhysRevB.95.161114). (cit. on p. 163).
- [175] Y. E. Kraus et al., 'Topological equivalence between the fibonacci quasicrystal and the harper model,' *Phys. Rev. Lett.*, vol. 109, p. 116404, 11 Sep. 2012. DOI: [10.1103/PhysRevLett.109.116404](https://doi.org/10.1103/PhysRevLett.109.116404). (cit. on p. 163).
- [176] H. Chalabi et al., 'Guiding and confining of light in a two-dimensional synthetic space using electric fields,' *Optica*, vol. 7, no. 5, pp. 506–513, May 2020. DOI: [10.1364/OPTICA.386347](https://doi.org/10.1364/OPTICA.386347) (cit. on p. 171).